Gran Sasso Science Institute

ASTROPARTICLE PHYSICS DOCTORAL PROGRAMME

Cycle XXIX - AY 2013/2016

New Spectral Analysis of Solar ^{8}B Neutrino with the Borexino Detector

PHD CANDIDATE

Ilia Drachnev

PhD Thesis submitted
October 28, 2016

ADVISORS

Aldo Ianni
Laboratori Nazionali del Gran Sasso

Alexander Derbin
Petersburg Nuclear Physics Institute

TUTORS

Nicola Rossi
Laboratori Nazionali del Gran Sasso

Marcin Misiaszek
Jagiellonian University

GRAN SASSO SCIENCE INSTITUTE
SCHOOL OF ADVANCED STUDIES
Scuola Universitaria Superiore

SISSA
Scuola Internazionale Superiore di Studi Avanzati

Abstract

Solar neutrinos were first detected in the 1970's and have played since then a significant role in the studies related to the construction of the solar model as well as in studies of the intrinsic properties of these particles, such as the features of vacuum and matter-enhanced oscillations. The Borexino detector is a unique experimental apparatus which has spectral sensitivity to all solar neutrino components apart from hep neutrinos. The detector could cover the energy range from 150 keV to as much as 15 MeV and in some cases even higher, while the achieved radiopurity levels minimizes the interference with background components.

In this thesis spectral studies of the whole solar neutrino spectrum detected in Phase II with a duration of 1173 live days are reported. In particular, solar neutrinos from ^{8}B are studied from the lowest detection threshold ever used for this component of solar neutrino spectrum. Electrons produced by recoil of these neutrinos are detected above 2.17 MeV of visible energy with a measured total neutrino flux of $(5.5 \pm 0.4) \times 10^6\ cm^{-2}s^{-1}$ under assumption of Large Mixing Angle (LMA) solution of Mikheyev-Smirnov-Wolfenstein(MSW) theory, that is compatible with the Standard Solar Model(SSM) in the high metallicity case. The spectral shape shows statistical compatibility with MSW-LMA.

In this thesis it is shown that Borexino detector has *statistical sensitivity* to CNO and pep neutrino when the dedicated analysis here developed is applied. Central values are $(5.2 \pm 1.8_{stat}) \times 10^8\ cm^{-2}s^{-1}$ and $(1.31 \pm 0.35_{stat}) \times 10^9\ cm^{-2}s^{-1}$ respectively, compatible with expectations of high metallicity case of the SSM and MSW-LMA.

In spite of the low precision, these results, obtained using the data collected by the Borexino detector could pave the way to future solar neutrino studies aiming to improve our understanding of solar models and neutrino oscillations in matter.

Introduction

This thesis is devoted to solar neutrino studies with Borexino detector data, obtained in Phase II. Neutrino are of great interest for both experimental and theoretical physics since this light lepton is both not very well studied in its properties and still is already becoming a powerful tool for studying the universe. Neutrino interacts with matter very weakly that results in outstanding penetration of matter, thus it is a unique tool that allows to look inside the solar core since all other types of solar radiation do not exit it undistorted. At the same time neutrino properties remain not very well established, for instance, matter oscillations are demonstrated to be present, but the compound of modern experimental data still does not allow to establish matter oscillation properties, especially in the so-called "transition region" of 1 - 3 MeV where oscillation passes from vacuum regime to matter resonance regime. Solar and neutrino properties can't be decoupled in solar neutrino studies and thus it results in the necessity of studying them together, that makes us obtain maximum information available, both on fluxes and spectral shapes. Borexino is a unique detector that allows to obtain spectral information on solar neutrinos together with the possibility to measure fluxes of decoupled solar neutrino spectrum components. In Phase II the natural radioactivity background has been significantly decreased and this results in an increase of the precision of neutrino studies with respect to previous analysis as well as in a possibility to have a first glance into the transition region with usage of ^{8}B neutrino spectral studies with low threshold.

Experimental activity

The experimental activity presented in this thesis was performed in the Borexino collaboration during Phase II data analysis. My own activity started from the End of 2013 and lasted until the end of 2016.

My own contribution includes fluidodynamical simulations of the detector in simplified model of temperature distributions, that brought to a better understanding of the convective picture, development and support of so-called "effective quantum efficiencies" (see corresponding chapter), developement of the Three-fold coincidence algorithm (so-called LNGS TFC algorithm), partial participation in development of light collection nonuniformity corrections, development of likelihood minimization approach for pulse shape alpha/beta discrimination, as well as participation in all stages of studies devoted to the detection of neutrinos from ^{8}B, such as primary data selection, development of statistical subtraction of ex-

ternal background component, establishment of background composition including the discovery of neutron-induced gamma-background at high energies, background subtraction and energy scale establishment. The impact of the new approaches in low-energy analysis allowed to break some of internal correlations in the likelihood function allowing to increase the final precision achievable by the detector, while in the case of neutrinos from ^{8}B allowed to lower the threshold by the value of 0.83 MeV with respect to previous analysis.

Thesis layout

Chap. 1 serves as an introduction and describes the historical milestones that lead to appearance of the field of neutrino physics and establishes the solar neutrino problem.

Chap. 2 shows the main aspects of neutrino physics and establishes the theoretical framework under which neutrino physics experiments are operating.

Chap. 3 describes the main solar neutrino experiments performed so far and establishes the actual situation in neutrino physics without Borexino detector contribution, such as establishment of solar neutrino problem as well as the first discoveries on the way for a total understanding of its background.

Chap. 4 contains a description of the Borexino detector focusing on its construction, activity level and operation as well on the generic data analysis framework.

Chap. 5 describes the current status of low energy solar neutrino analysis and shows the current statistical sensitivity of the detector in the case of present analysis framework application and describes the basic approaches implied in the low-energy spectral studies.

Chap. 6 shows the analysis of neutrinos from ^{8}B, including counting and spectral analysis of the detector data and gives the current result of the detector sensitivity to this neutrino component.

Contents

Chapter 1

Introduction

1.1 Discovery of neutrino

The neutrino was discovered only in the middle of 20th century. This fact was preceded by a series of observations, problems and discoveries.

At the end of 19th century A.Bequerel discovered uranium radiation [1]. Later it was found that this radiation is composed of three types of radiation, that could be distinguished by different behavior in magnetic field, namely the beam that was going straight, was called γ-radiation, while two others declined to different sides were called α and β [2]. The discovery of neutrino is related to beta-radiation.

The first hints of neutrino existing were coming from the β-decay studies. After some studies it was established that in such process one observes a reaction, changing the particle charge and conserving its mass, such as ${}^{A}_{Z}X \rightarrow {}^{A}_{Z-1}X$ with two particles observed after the reaction, namely a nucleus and an electron, which were distinguished by mass/charge ratio with magnetic spectrometry. Taking into account mass-energy conservation, one would expect this reaction to have a constant energy release. The same time the spectrum of electrons appeared to be continuous [3], that meant either energy nonconservation in this process, either an unknown mechanism of energy release. Actually, the most popular solution was energy conservation violation, since there were no experimental nor theoretical reasons for energy conservation on the particle scale [1].

On the 4th of December 1930 W. Pauli proposed a "desperate way out" of this situation[4], introducing as a product of beta decay a new neutral particle having a mass of the same order of magnitude as an electron and large penetrative power that he called "neutron" [2], that might have appeared in this reaction and would

[1] the theoretical motivation, relating conservation laws with global space-time symmetries, appeared only in 1918, four years later than the discovery of beta-process

[2] After the detection of a massive neutral particle that also got the name "neutron" by

explain the anomalous energy loss. Actually, it was given more as a proposal for a discussion rather than a solution of the actual problem, since he would expect neutrino to be already discovered in case of its existence, but considered it worth the risk to search for any possible way to solve the mystery. The particle remained unobservable due to non-interacting in electromagnetic and strong interactions, the interactions which were at the moment used for particle detection, hence the search for such particle became a strong problem itself.

The next source of the problem was a later theory of the nuclear proton-neutron composition, proposed by Heisenberg in 1932, that automatically imposed the problem of electron source in beta-process. This problem solution was proposed by E. Fermi as a theory of beta-decay [5], that was in some sense analogous to proton radiation by excited atomic levels, where the emitted particle is created within the decay process itself, introducing a neutrino as one of the particles produced within the reaction and following all known conservation laws. Later it was understood that this theory "saved" not only energy conservation, but also momentum and rotational momentum conservation and became a strong motivation for neutrino acceptance even in case of lack of direct discovery.

1.2 First evidence

The first ideas of neutrino detection started to appear right after the first theory of beta-decay, but the predicted interaction rates were practically blocking neutrino from any kind of direct detection. The same time, one could think of measurement of global conservations laws that could bring some light to the neutrino problem, e.g. one could try to observe nuclear recoil and test the momentum conservation law. The first attempt of doing it was done in 1936 by Leipunsky [6] with beta-decay of ^{11}C, resulting in observation of recoil of ^{11}B together with a positron. The experiment was based on spectra comparison for positrons and recoil nucleus and gave a nonzero value of the total momentum of the system after the reaction, that was an indirect evidence of neutrino emission.

According to an idea of the soviet physicists A.Alichian and A Alichanov, numerical results were possible to reach in case of a reaction of K-capture. They proposed to perform the study on nucleus of ^{7}Be, which was decaying into ^{7}Li, leaving us with only the recoil nucleus as a detectable particle. According to the measurement performed in 1942 by G. Allen [7], the energy of the recoil nucleus was equal to (56.6$\pm$1) eV, that was practically equal to the theoretical prediction of 57.3 eV. Observation of a recoil nucleus with energy equal to the one that could be predicted by including a light neutrino into the decay according to existing theory

Chadwick the particle got the name of "neutrino"

lead to acceptance of neutrino despite all the difficulties related to its observation. Neutrino was still waiting for its moment of truth that was related to appearance of such a powerful radioactivity source as induced fission.

1.2.1 First experimental ideas

Since neutrino was predicted and was strongly evidenced by conservation laws that could be derived from global symmetries of our universe in a generic way and thus should exist the same way both in microscopic and macroscopic world. Since in macroscopic world they are strongly supported by entire experience of humanity expressed in classical physics, it became a very strong motivation to challenge an actual detection experiment that would put the final point in understanding of beta-decay. The process predicted by Fermi theory that would provide neutrino detection with an unique signature of neutrino detection appeared to be inverse beta-decay. It was proposed for such use already in 1934 by H. Bethe and R. Peierls [8]. But at that time an experiment based on such reaction looked to be impossible under consideration of expected interaction rate of neutrino with matter.

In 1946 B.Pontekorvo proposed an implementation of inverse beta-decay technique based on seeking a possibility to concentrate the products of inverse beta-decay from a large volume in order to perform a measurement of the activity that could be produced only by neutrino. A nucleus he proposed for such search was ^{37}Cl, that was inversely beta-decaying into argon, which, being a noble gas would be relatively easy to separate from the chlorine-containing substance and thus to obtain radioactive argon that could have been produced only by neutrino [9]. Regretfully, this remained just an idea for more than 20 years before it was actually used for neutrino detection. In any case, the start of the neutrino detection challenge was given.

1.2.2 First direct neutrino measurement attempt: Davis experiment at Brookhaven

The first attempt of neutrino direct detection was done by R. Davis in 1954 [10], even before a successful antineutrino detection, according to the original idea of B.M. Pontecorvo. The idea of neutrino detection was based on usage of chlorine detector, namely the reaction

$$^{37}Cl(\nu, e^-)^{37}Ar$$

This reaction should be able to detect neutrino by an unique process, practically without any background, while argon would be relatively easy to extract.

Registration of such process was performed by a relatively large target of 3900 liters of CCl_4, that was located at the depth of 6m below the ground just outside

the Brookhaven reactor and was irradiated within two months in order to obtain neutrino-produced argon. After that the fluid was stripped with helium gas and the argon atoms were trapped with two charcoal traps, cooled with solid carbon dioxide and liquid nitrogen respectively. Usage of less cooled trap was due to a need of krypton and radon removal, thus argon was trapped in the second trap, while vapors of carbon tetrachloride were passing through the condenser and returned to the target volume. The gas in the colder trap was extracted and desorbed at 200 °C to be put inside quench gas of a Geiger-Muller counter. Since argon decays within 34 days it was possible to perform calculation of the number of argon atoms obtained. The rate obtained was absolutely compatible with the expected cosmogenic production of ^{37}Ar and that allowed only to put a limit on the actual neutrino rate. One could be interested, why such an experiment was performed on a reactor. The answer is that it was not guaranteed that neutrino and antineutrino are different particles and thus that antineutrino does not take part in this interaction. So this experiment could be treated as the very first attempt of neutrino detection and a proof of no inverse beta-decay with neutrino and electron. Moreover, it gave an upper limit on the total solar neutrino flux of $10^{14} cm^{-2} s^{-1}$, that is of course much larger than any theoretical prediction, but was still a valuable limit at that time, even before the very first antineutrino detection.

1.2.3 Antineutrino discovery

Since all the previous experiments evidenced neutrino only in the production point, it was a great interest to discover neutrino by direct detection at some distance from it. A powerful tool that allowed neutrino detection was a new mechanism of neutrino production, a new mechanism of creating massive amounts of beta-decaying nuclides, a nuclear reactor. The very first reactor was created in 1942 by E. Fermi [11] and since than neutrino detection became possible. The reaction that would provide such detection, was the already proposed inverse beta-decay. Moreover, in 1949 L. Herford and H. Kallmann found and described scintillation in organic liquids [12], that allowed building a detector that would have needed size, that, together with high flux of a reactor, would give a sensitivity to neutrino.

The very first detection of antineutrino belongs to F. Reynes and C. Cowan [13]. The experiment, purposed to perform the very first direct detection of neutrino was called “Project Poltergeist” and was performed in Hanford (Washington, USA). The reactor was providing expected antineutrino flux of $10^{13} cm^{-2} s^{-1}$. According to Fermi theory, one would expect around a hundred of inverse beta-decays per hour in a ton of hydrogen-containing substance. Since the reaction of inverse beta-decay on hydrogen results in appearance of a neutron and a positron, it was possible to detect antineutrino reaction by electron-positron annihilation gammas.

The detector used in this experiment appeared to be a 300 l scintillator tank,

observed by two groups of 45 Photomultipliers (PMTs), divided for coincidence detection. The proton target used was based on Cadmium propionate ($C_3H_5CdO_2$). At the very first attempt was detected a difference in event flux between reactor on and off of 0.4 ± 0.2 events per minute, while the expected value was around 0.2 ev/min. Such result was later explained by different sources of backgrounds such as cosmic rates and underground tests in Los-Alamos and were not satisfactory for the sake of claiming antineutrino detection.

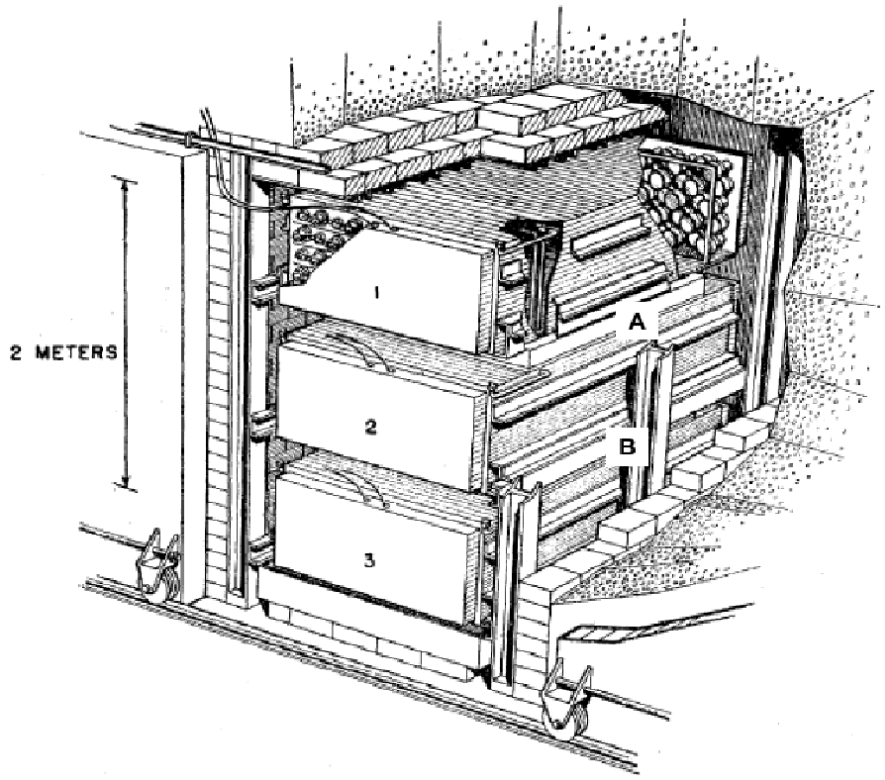

Figure 1.1: The antineutrino detector construction drawing. A,B - proton targets used for delayed neutron detection. 1,2,3 - liquid scintillator detectors connected to anticoincidence scheme and used for recombination gamma detection.

Thus, the antineutrino detection required to improve the existing setup [14]. The new setup was using a proton target, represented by two tanks filled with water solution of cadmium chloride. Annihilation gamma-quanta were detected in the liquid scintillator, that was filled into 3 tanks of 1200 l, located on both sides of the proton targets and observed by 100 PMTs(1.1) The neutron capture would be observed with a delay of around 10 μs with corresponding series of gamma-lines. In this case on would expect a very significant reduction of the background due to usage of coincidence scheme that significantly decreased acceptance of background

events. In fact, only usage of such scheme allowed neutrino detection from a reactor, rather than from a nuclear explosion as it was proposed in case of non-observation of antineutrino in reactor experiment. Moreover, there was used a third detector for cosmic rays, that played a role of active shielding. The second series of experiment was performed on Savannah River reactor with location of the detector on 11 m distance from the reactor and 12 m underground in order to protect it from cosmic radiation. After 100 days of data-taking there were detected (3.0 ± 0.2) events per hour . Such a measurement was definitely a proof of the antineutrino existence taking into account a unique signature of an actual antineutrino detection.

Taking into account that the cross section, derived from the experiment appeared to be $\sigma_{exp} = 1200^{+700}_{-400} \times 10^{-46} cm^2$ (considering the main uncertainty source of reactor calibration), that is in a good agreement with the value of $\sigma_{th} = 500 \pm 100 \times 10^{-46} cm^2$ obtained by theoretical estimates. All these facts allow to claim this beautiful experiment as the very first direct neutrino detection. Since this experiment took 5 years, the date of neutrino discovery is 1956.

1.2.4 First neutrino discovery: Homestake chlorine experiment

By the end of 1960's the situation in neutrino experimental physics was the following: while the detection of antineutrino was very well established and it was demonstrated that neutrino from a reactor can't be detected that easily and antineutrino and neutrino do not perform the same inverse beta decay reactions predicted by Fermi theory. Thus the challenge of neutrino detection still existed, the problem of neutrino detection was still waiting for its solution since all the previous studies were relying on the mighty power of a nuclear reactor. A new neutrino source was needed.

It appears that the most powerful source on neutrino already exists for billions of years - it is our Sun. In all stars powered by nuclear fusion process, neutrinos are produced in two basic reaction chains, CNO - cycle, predicted by H. Bethe in 1938 and pp-chain, described by him a year later. These reactions were predicted to produce neutrinos in a quite broad energy range, from 0 to 16 MeV and even higher if one considers a very rare process of hep-neutrino production. These neutrinos appeared to be possible to detect.

The Homestake neutrino observatory is located in the Homestake gold mine at the depth of 1478 m being the deepest operating mine in US. Thus, the laboratory is covered by around 4200 m of water equivalent[3] rock passive shielding.

[3]water equivalent - thickness of a layer of water with the same surface matter density, thus it is larger than the real depth by factor of average rock density ratio to water density. This unit

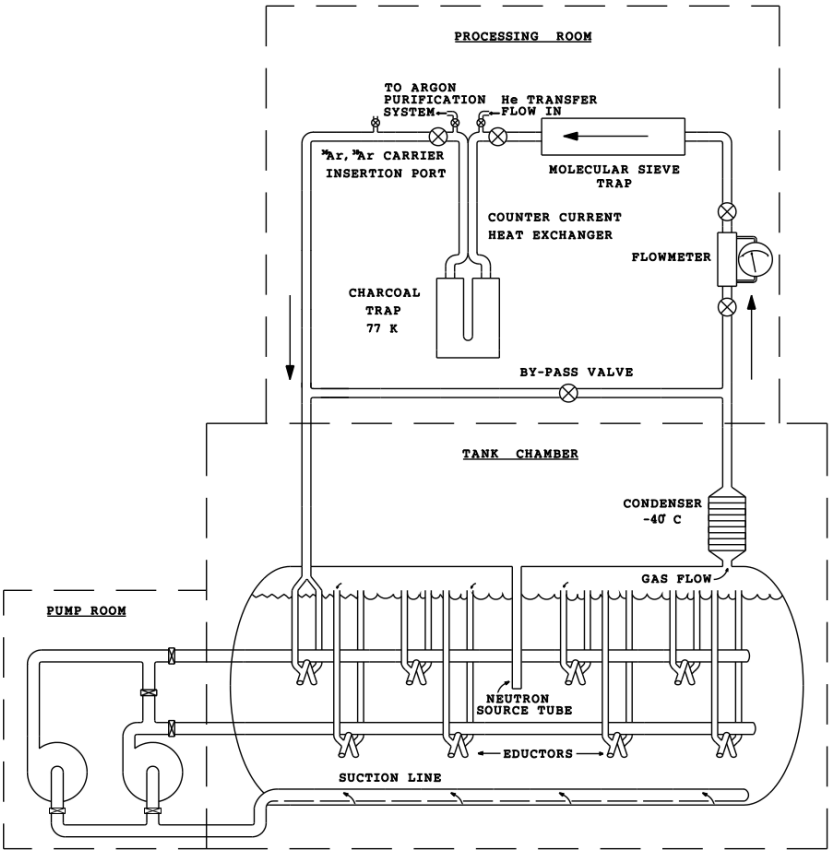

Figure 1.2: Principal scheme of Homestake Neutrino experiment

The experiment done in this observatory was performed by R. Davis, applying the same experimental technique that he already approved on a reactor a decade earlier, the one based on orginal idea of B.M. Pontekorvo [9]. Same time this study was strongly supported by J. Bachall, that was performing all computations from the theoretical side of this activity. The setup was including a single horizontal steel tank of 15 m long and 6 m in diameter giving the total volume of 615 tons of tetrachloroethylene (C_2Cl_4) (fig. 1.2). 95% of the detector was filled with the target material, while the remaining part contained pressurized He gas that was used for the extraction of neutrino interaction products. The detector was also provided with a tube for placing a calibration neutron source for extraction efficiency studies.

The detector construction was done with a very strong consideration of existence of argon in the atmosphere in quite large quantities, that lead to a necessity

is common for treating cosmic ray shielding in different underground laboratories

Decay Mode		Auger e^- [keV]	X-ray [keV]
K	81.5	2.823	0.0
L	8.9	0.270	0.0
K	2.7	0.202	2.621
K	5.5	0.201	2.622
M	0.9	0.018	0.0
K	0.5	0.007	2.816

Table 1.1: Principal radiations produced in the ^{37}Ar decay.

to guarantee high radiopurity of the constriction material and absence of possible leaks in all the piping structure. In any other case that would lead to a danger of very high non-neutrino production rate of ^{37}Ar that would lead to complete lack of success of the experiment as solar neutrino flux at the Earth is much smaller than the one produced by a reactor and statistical significance of all backgrounds grows dramatically.

Despite the size of the detector, the expected values of solar neutrino flux and cross section were giving quite small count rates of neutrino in this experiment. Moreover, since chlorine reaction threshold appears to be as high as 814 keV, it leads to acceptance of a very small part of solar neutrino spectrum, dominated by neutrinos from ^{8}B decay in the solar pp-chain. Thus the precision of extraction system and counting become crucial for observing neutrino events. The basic system of argon extraction remained the same as in the previous reactor experiment, so the volume was stripped with helium gas. Argon was extracted in the process of reverse osmosis into the gas phase with following passes through the trap system based on two traps with different temperatures allowing background separation and giving quite high efficiency of actual argon subtraction.

The lower temperature trap was cleaned from active gases by exposing to titanium powder in direct contact at the temperature of 900 °C and separation of other rare gases by gas chromatography. Than the trap was desorbed at 200 °C in a helium flow with a following collection by a smaller charcoal tram that was consequently desorbed into another step of purification, using a Toepler pump and following all steps of exposing to titanium and chromatographical separation from heavier noble gases and again collected on a nitrogen-cooled charcoal trap. Than it was transported from into a proportional counter for the sake of counting the number of radioactive argon atoms in the sample. Taking into account that argon life time is 37 days, it was necessary to perform the counting on the scale of once per week. One should take into account that neutrino count rate was giving the number of events less than one per week, so it was very important

to have a signature of actual argon decay, that could be distinguished by auger electrons or K-lines, see table 1.1. In order to avoid external background affection, the proportional counter was used inside a NaI scintillation detector working in anticoincidence scheme as an active shielding. Pulse-shape discrimination for electrons was also used. The proportional counter was periodically calibrated with ^{55}Fe source X-rays. Starting from some moment, the counting facility was moved underground next to the detector.

The total background for argon production included cosmic rays as well as internal activity in the detector construction and target material as well as (α,n) reactions. The total background was estimated as 0.07 events/day in the whole target mass. As a final result, the experiment gave the value of $0.478 \pm 30 \pm 0.029$ counts/day in the whole data-taking period 1970-1990 that corresponds to the value of $2.56 \pm 0.16 \pm 0.016$ SNU[4]. This observation brings us to the actual problem of solar neutrinos, neutrino oscillations and all the peculiar properties of this amazing particle. But in any case it was the very first experiment that succeeded to detect a neutrino directly and to perform it using the Sun as a source.

The importance of this experiment could hardly be overestimated as it had demonstrated that neutrino exists and it is a particle that has a lot of interesting features that were not expected to be, establishing the actual solar neutrino problem that still is not completely resolved. This experiment was awarded a Nobel prize in 2002.

[4]SNU - events per target atom per second, standard unit on radiochemical neutrino detectors

Chapter 2

Brief review of neutrino properties

2.1 Neutrino sources

Since the neutrino was detected in 1956 (speaking more precisely, that were antineutrinos from a reactor), it is interesting to understand the possible sources of neutrino that could be used for neutrino properties study. Moreover, as soon as neutrino properties are more or less established, neutrinos become a tool for studying its sources. Neutrinos have a unique feature, coming from the same source as its detection complexity: since neutrino is very weakly attenuated in matter, a neutrino beam detection automatically points out properties of the source without much role of propagational effects.

The most commonly mentioned sources of neutrinos are:

- antineutrinos from reactors
- neutrinos and antineutrinos from artificial radiochemical sources
- accelerator neutrino beams
- antineutrinos from the Earth created in beta-decay of daughter nuclei within natural radioactivity chains
- neutrinos from fusion reaction
- reactions powering stars, namely PP-chain and CNO cycle
- neutrinos from supernova explosions
- neutrinos from high-energy processes in cosmic ray accelerators

- atmospheric neutrinos, produced in the atmosphere by interactions of cosmic rays

Of course, one could imagine many more sources of neutrino, including such exotic ones as nuclear and thermonuclear explosions, relic neutrinos etc., but the mentioned ones are the most studied and are the most interesting for us in historical perspective.

2.1.1 Artificial neutrino sources

reactor antineutrino Reactor antineutrino is historically the first particle detected directly. A nuclear reactor is a very powerful source of radioactivity and its usage for the neutrino studies looks more than reasonable. Most of modern reactors use ^{235}U as fuel and work in the thermal part of neutron spectrum. Although the actual enrichment of the fuel $^{235}U/^{238}U$ ratio is relatively small (some reactors work even on natural uranium with this ratio of 720×10^{-5}) the fuel compound that actually produces most of the energy is still the lighter uranium[1] . Of course one could mention thorium reactor cycle or fast neutron reactors and even scientific reactors on intermediate spectrum, but exotic reactor types are not of much interest for neutrino studies. A thermal reactor produces energy in the process of fission of heavy nuclides and the average proton-to-neutron ratio is conserved in fission products. Taking into account A-dependence of A/Z ratio for stable nuclides (see fig. 2.1), one would immediately expect the nucleons to be beta-unstable due to proton deficit. Such beta-instability would practically always lead to presence of β^- decay, rather than β^+, that means generation of antineutrino. Taking into account that all existing reactors are based on fission and the A/Z dependence is monotone, one would expect the same tendency for‘ any reactors, although the mass distributions depend strongly on the neutron spectrum used in the reactor due to shell effects in a nucleus. In fact a significant paert of heat is produced in a reactor not due to kinetic energy of the fission products, but by later beta-dacays. Thus a reactor creates a massive neutrino flux of order of $10^{20}s^{-1}$ per gigawatt of thermal power that allows to have reliable neutrino detection. Moreover, as an artificial source, it allows us to study neutrino propagation on different distances from some meters up to hundreds of kilometers. Reactor antineutrino oscillations were studied with various experiments [15, 16, 17].

radiochemical sources The problem of a reactor is that its neutrino flux and spectrum are not known very precisely, as well as the spectrum can not be modified much. Moreover, it is a quite sophisticated, bulk and expensive construction.

[1] In industrial reactors branching ratio of fissions of ^{235}U, ^{239}Pu, ^{238}U and ^{241}Pu is respectively $0.59 : 0.28 : 0.08 : 0.05$

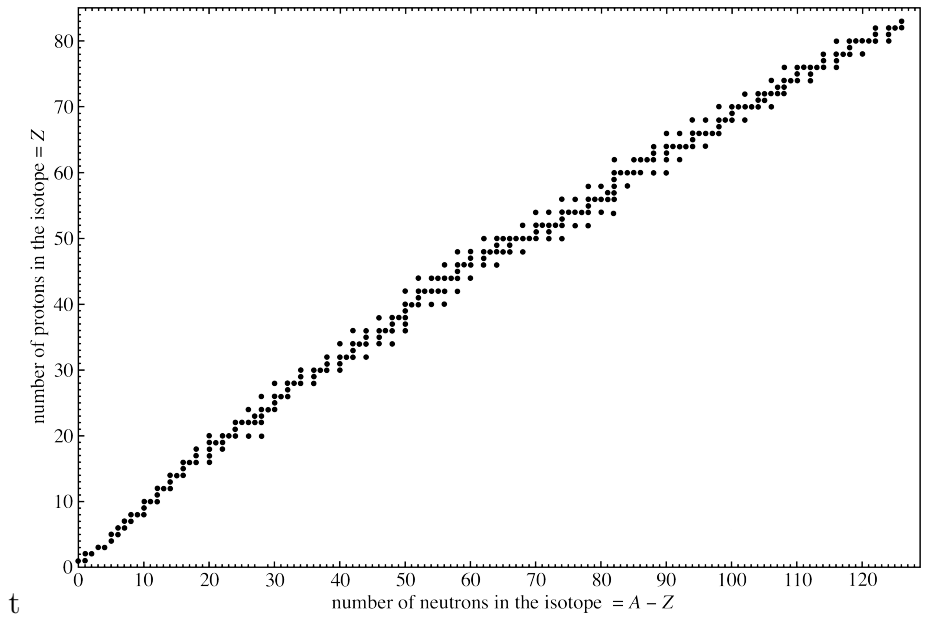

t

Figure 2.1: Atomic masses and charges of stable isotopes. Note the increase of neutron fraction with mass

.

Thus, in some cases one could use neutrino radiochemical sources. Such sources contain beta-decaying isotopes and the tiny interaction rate of neutrino automatically means massive radioactivity inside the source, of order of some MCi. They could be produced with chemically separated nuclides, that would mean that a source would have neutrino or antineutrino spectrum that could be measured through beta-spectrum with application of conservation laws. Moreover, such sources allow us to have monoenergetic neutrino lines form electron capture sources and are not limited with antineutrinos only like reactors. One could irradiate some isotope with neutrons and get a source with proton deficit, emitting actual neutrinos and positrons. Thus radiochemical sources could provide much more flexibility, still being artificial sources with all reactor advantages apart from the total flux, that is of course, lower, but could be still more than enough for reliable measurements. Such sources could be used for calibration of various neutrino experiments [18]. Radiochemical sources could be also used for sterile neutrino searches, e.g. in Borexino-SOX experiment it is planned to use sources of ^{144}Pr (extracted from used nuclear fuel) and possibly ^{51}Cr (produced by neutron irradiation) [19].

accelerator neutrino beams Both of the previous neutrino sources have one feature in common: they produce (anti-)neutrino in the same reaction in which it

was discovered - beta-decay. Such reaction is of course very important physical process, e.g., in astrophysics or in cosmology, but it is not the only process, that could be related with this particle and it can not provide the total picture of neutrino physics, since it covers only a very narrow energy range between some keV and some tens of MeV. The most popular way of creating neutrino beams of relatively high energy is based on usage of accelerators, e.g. synchrotrons, and producing neutrinos in weak decay of short-lived particles produced by the accelerator beam, e.g. pions and muons. Such neutrinos could be more or less focused by focusing the primary beam of charged particles and could be quite useful for the study of high-energy neutrino properties [20, 21].

2.1.2 Neutrinos form stars

Among all natural sources of neutrino one of the most important one is production in stars. Moreover, historically such neutrinos were the first to be detected in Homestake neutrino observatory. Stars are providing most of the late nucleosynthesis in the universe, from hydrogen to iron and further in supernova explosions. During this process they produce various types of neutrinos that could be studied as a particle and the same time serve as a tool for studying stars. The most important and easy to study for us is the closest star, the Sun, that is located in close proximity to our planet and appears to be the most powerful natural neutrino source at the Earth.

The original idea of the heat source powering stars was simply the gravitational force that would produce heat during compression of matter inside a star. Such mechanism could be an appropriate explanation of the star power, but there is a contradiction: life of the Sun is way longer than what could be provided with such algorithm [22]. Life of the sun could be estimated from radiogenic properties of substances of the Earth that show age exceeding a billion of years. One of the most curious examples is the natural nuclear reactor in Africa [23], that could have worked only with concentration of ^{235}U substantially exceeding the current one and corresponding to hundreds of millions years ago. So the Sun as well as all other stars should have a source of power different from just gravitation and much more powerful one.

CNO-cycle The first example of such energy source was proposed by H. Bethe in 1938. Practically, presence of large amount of hydrogen in the Sun was well-known from solar light spectrum that was missing absorption lines of hydrogen. Bethe proposed the reaction that was called the CNO-cycle [24]. This reaction was based on consequent merging of a hydrogen nucleus to ^{12}C up to oxygen resulting in helium production. Within this main reaction, so-called CNO-I, two neutrinos

are produced:

$$
\begin{aligned}
{}^{12}_{6}C + p &\rightarrow {}^{13}_{7}N + \gamma(1.95MeV) \\
{}^{13}_{7}N &\rightarrow {}^{13}_{6}C + e^{+} + \nu_e(1.20MeV) \\
{}^{13}_{6}O + p &\rightarrow {}^{14}_{7}N + \gamma(7.54MeV) \\
{}^{14}_{7}N + p &\rightarrow {}^{15}_{8}O + \gamma(7.35MeV) \\
{}^{15}_{8}O &\rightarrow {}^{15}_{7}N + e^{+} + \nu_e(1.73MeV) \\
{}^{15}_{7}N + p &\rightarrow {}^{12}_{6}C + \alpha(4.96MeV)
\end{aligned}
$$

One should consider also that there is a small probability of having electron capture instead of beta-decay that would lead to monoenergetic neutrino lines of 2.22 MeV and 2.75 MeV respectively. Another branch of this reaction is CNO-II that undergoes with branching of 0.04% in the Sun:

$$
\begin{aligned}
{}^{15}_{7}N + p &\rightarrow {}^{16}_{8}O + \gamma(12.12MeV) \\
{}^{16}_{8}O + p &\rightarrow {}^{17}_{9}F + \gamma(0.60MeV) \\
{}^{17}_{9}F &\rightarrow {}^{17}_{8}O + e^{+} + \nu_e(2.76MeV) \\
{}^{17}_{8}O + p &\rightarrow {}^{14}_{7}N + \alpha(1.19MeV) \\
{}^{14}_{7}N + p &\rightarrow {}^{15}_{8}O + \gamma(7.35MeV) \\
{}^{15}_{8}O &\rightarrow {}^{15}_{7}N + e^{+} + \nu_e(2.75MeV)
\end{aligned}
$$

There are also other branches that would gain importance in case of heavy stars [25], but in the current status of experimental physics they have no importance since the only star from which neutrinos could be observed in the Sun. Such reactions could undergo only at very high temperatures that would allow the Coulomb barrier crossing. Crossing it by energy that is definitely not possible at star internal temperature, thus crossing of the coulomb barrier is due to quantum tunneling that means that the reaction would be strongly dependent on the temperature inside the star. In the Sun, for example, CNO cycle can not provide the thermal power observed, but such reaction should in principle undergo, although is was never evidenced directly. Such reaction evidence is one of the most challenging problems of neutrino physics since it strongly depends on the solar composition, especially on the so-called "metallicity" that stands for contamination of heavy [2] elements in the star. But still, it appears that this is not the root of solar energy. However, it is should be the main energy source for stars, that are heavier than our Sun [25] and should be the main source of helium production in the universe.

pp-chain CNO cycle appeared not to be the main source of stellar neutrinos in case of light stars and surely not for the closest one to the Earth - the Sun. The

[2] heavier that helium

Sun produces much more heat than what could be expected from CNO-reaction and there should be present another source of power that would give all the heat the Sun actually produces. Such reaction was proposed by H.Bethe right after the CNO reaction and is the well known pp-chain [26]. The pp-chain is in general a reaction that extracts energy from merging four protons into a helium nucleus with extraction of 26.4 MeV of energy. This reaction chain should occur more easily than the CNO cycle due to smaller charges of participant nuclei and thus lower Coulomb barriers in the reaction. The pp-chain is also usually divided into three branches organized by intensity and thus importance of the corresponding reaction in the fusion energy production. Namely, pp-I cycle contains the following reactions:

$$\begin{aligned} p + p \rightarrow {}^{2}_{1}H + \gamma + \nu_e(0.42MeV) \\ p + {}^{2}_{1}H \rightarrow {}^{3}_{2}He + \gamma(5.49MeV) \\ {}^{3}_{2}He + {}^{3}_{2}He \rightarrow {}^{4}_{2}He + 2p \end{aligned}$$

This is the main reaction, powering the Sun and providing us with neutrino flux of $6.06 \times 10^{10} cm^{-2} s^{-1}$.[3] With existing nuclei one gets the other parts of pp chain. Among them, pp-II:

$$\begin{aligned} {}^{3}_{2}He + {}^{4}_{2}He \rightarrow {}^{7}_{4}Be + \gamma(0.478MeV) {}^{7}_{4}Be + e^- \rightarrow {}^{7}_{3}Li + \nu_e(0.862MeV) \\ {}^{7}_{3}Li + p \rightarrow 2{}^{4}_{2}He \end{aligned}$$

One should take into account that beryllium is produced in excited state with neutrino energy of 384 keV in around 10% of cases. pp-III originates from the same berillium with capture of a proton instead of electron with branching of 0.12 % in the Sun:

$$\begin{aligned} {}^{7}_{4}Be + p \rightarrow {}^{8}_{4}B + \gamma \\ {}^{8}_{4}B \rightarrow 2{}^{4}_{2}He + e^+ + \nu_e(15MeV) \end{aligned}$$

This reaction produces neutrinos with quite high energies that could be detected more easily due to cross section energy dependence and is historically very important. The same time, there is even more energetic neutrino, although produced with really tiny branching (pp -IV, so-called hep neutrino):

$${}^{3}_{2}He + p \rightarrow {}^{4}_{2}He + e^+ + \nu_e(18.8MeV)$$

Apart from the standard pp-I chain in 0.24 % of cases deutron is produced with another reaction:

$$p + e^- + p \rightarrow {}^{1}_{2}H + \nu_e(1.44MeV)$$

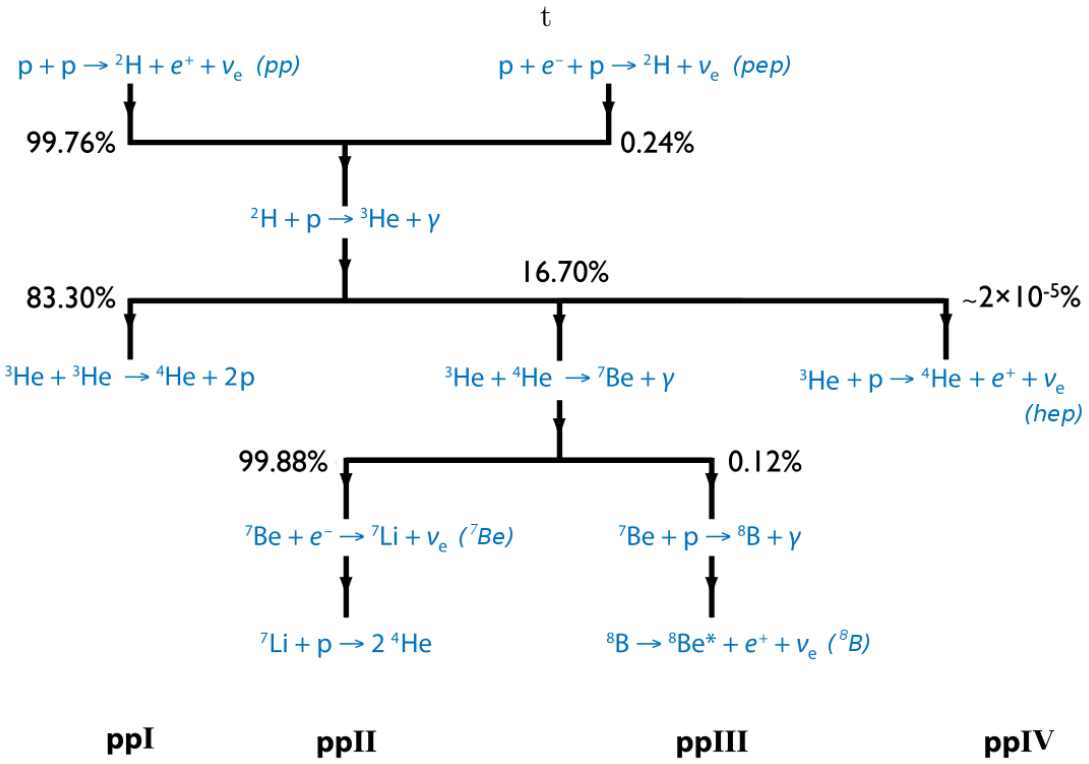

Figure 2.2: scheme illustrating pp-chain reactions in a star.

.

This reaction is called pep. Together with two beryllium lines they are the only monoenergetic neutrino lines in the pp-chain. The scheme of pp-chain is illustrated in fig. 2.2

neutrinos from the Sun The two processes described above should in principle undergo in any star, but the main interest for us in the current state of neutrino physics are the neutrinos coming from the closest star, the Sun, since all the others are quite challenging to detect. In this case we are limited on certain mass and type of the star and, thus, the branching ratios among the reactions. Since all the reactions undergo through Coulomb barrier, the probabilities depend upon temperature, so the energy distribution in the Sun as well as upon the concentration of corresponding nuclei. Consequently, the branching ratios also have this dependence and different reactions change intensity within the solar core that makes affection on matter oscillation effects mentioned below. The total picture of solar neutrino spectrum is represented on fig. 2.3. The solar neutrino spectrum consists of several components with different energies:

- pp-neutrino. Neutrino of pp-I part of the chain, has very low energy, beta-spectrum has endpoint of just 420 keV. Very challenging for experimental detection, especially spectrometric

- neutrinos from ^7Be. Two monoenergetic lines for which the ratio is defined strictly since the branching ratio could be measured on beryllium itself. Very important for oscillation studies due to the fact of being monoenergetic. High-energy line corresponding to ground-state daughter of the reaction has the energy of 864 keV thus it is achievable only for a limited number of experimental techniques

- pep neutrino. One more monoenergetic line with the same importance as beryllium line, but with much smaller amplitude. It is still quite challenging to perform detection of these neutrinos for most experiments.

- CNO neutrinos. Several continious spectra with different amplitudes that belong to the same cycle, thus with fixed amplitude ratio (all reactions apart from CNO-I could be neglected in solar case, at least at the current state of experimental physics).Since they belong to an absolutely different reaction, they are very important for solar models construction, but the same time are very challenging to detect in all current experiments due to correlation with background events.

[3]according to standard solar model, which is in agreement with all existing measurements up to now

t

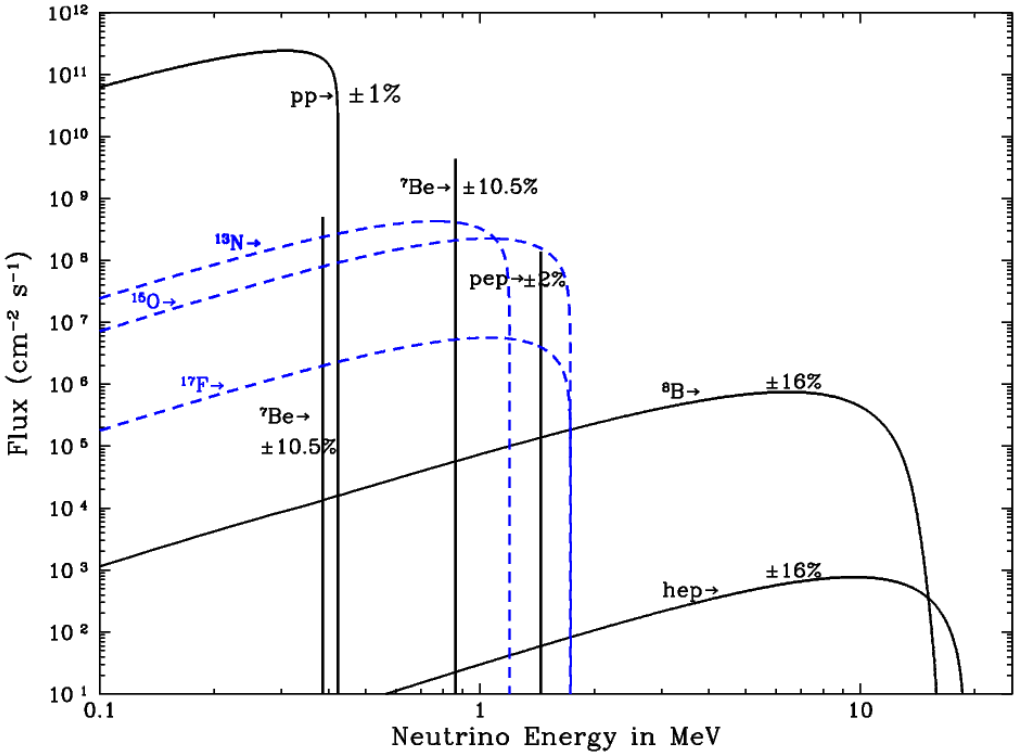

Figure 2.3: Nseutrino spectrum expected from the Sun

.

- neutrinos from ^{8}B. A continuous spectrum with high-energy endpoint of 15 MeV. Could be detected by all solar neutrino experiments with different lower energy threshold. The flux is quite low and thus making precision measurements is quite challenging. Production is strongly related with beryllium neutrino production.

- hep neutrino. Very high energy endpoint is combined with extremely low amplitude. Measurement of these neutrino is a great challenge even for the largest detectors. Theoretically could be detected by every detector, but with unachievable data-taking time, thus remain undetected until now.

2.1.3 Other sources of neutrinos

supernova neutrinos Another source of neutrinos that could be detected on the Earth is a supernovae explosion. Such events are expected to happen approximately once in 30 years within our galaxy creating massive bursts of neutrinos. In this case we discuss only core-collapse supernovae, rather than other types or classical novae that produce energy within so-called hot CNO cycle, in which a proton is merged before decay of beta-decaying participants of the loop. In a core-collapse supernova one gets matter with very large density and temperature resulting in massive neutrino production with neutrino energies of 10-15 MeV within few seconds(order of 10^{58} per event). Such neutrinos were already detected in 1987 by Kamiokande II, a water Ĉerenkov detector that detected 11 events within 13 seconds that could be associated to SN1978A supernova [27]. Such source of neutrinos could give a lot of useful information, e.g. neutrino mass from the delay with respect to the light flash observed, but this is a very rare event and detection of such neutrinos is a great luck. Such neutrino source is a motivation for all neutrino detectors to make their duty cycle as high as possible, even if it would be unlikely to detect it in close future. Another possibility strongly related with supernova neutrinos are gamma-ray bursts(GRBs), that could be described in some models as hypernova explosions. One could expect to have neutrino bursts in correlations with them, but at present there is no experimental evidence of any neutrino fluence of these mysterious cosmic objects.

high-energy cosmic neutrinos High-energy cosmic neutrinos are another neutrino source studied. In principle, every cosmic accelerator, e.g. supernovae reminants, are supposed to be a source of neutrino fluxes. Such sources have a lot of varieties and neutrino could be a contribute to multimesenger astrophysics, but at the moment it is too early to speak about neutrino astronomy. There are some Ĉerenkov detectors that are supposed to detect high-energy charged secondary particles of neutrino interaction, some of them even have some events detected,

e.g. IceCube ice Ĉerenkov experiment [28], but neutrino registration is counted as tens of neutrinos which could hardly evidence anything about astrophysical objects. At the same time, these fluxes are significantly smaller than atmospheric or accelerator neutrino fluxes that could be currently produced and thus make no practical interest for neutrino studies purposed to study the particle properties.

atmospheric neutrinos Atmospheric neutrinos are another quite powerful source that could be used for neutrino oscillation studies. These neutrinos are produced in the atmosphere by hadronic showers products created by original protons that are coming from outside the atmosphere and are known as cosmic rays.[4]. Energy of these neutrinos is quite high and reaches GeV scale and even higher. These neutrinos were used as one of the first demonstrations of neutrino oscillations that was derived from their zenith angle dependence[29].

geoneutrino Geoneutrino [30] is one of the applications of neutrino physics to the the physics of our planet. Inside the crust, and, probably, the mantle, one could expect some contamination of uranium and thorium that would obviously decay into natural radioactivity chains, in which several antineutrinos are emitted. Detection of these antineutrinos could bring light to the internal structure of the Earth. The possible impact of geoneutrino studies on the physics of neutrino itself is negligible since much higher fluxes could be obtained with nuclear reactors, so this is one more place where neutrinos play the role of a powerful messenger due to their low cross section of interaction with matter.

2.2 Neutrino interaction with matter

Neutrino direct detection is a primary goal for many experimental activities. They are a the door to the study of interesting phenomena including physics of neutrino itself as well as different objects on the earth and on the sky. Thus, one should consider the neutrino interaction with matter as a tool of neutrino detection. Here we will list the reactions that are currently used in this branch of research.

Historically, inverse beta-decay was the very first proposal of neutrino detection already in the end of the first half of XX century. It is still broadly used in various experiments. The cross section for a proton could be computed with Fermi theory much above the reaction threshold coming from energy conservation as [31]

$$\sigma_0(E_\nu) = \frac{G_f \cos^2\theta_c}{\pi}(1+3a^2)E_{e^+}p_{e^+} \approx 0.952 \times 10^{-43} cm^2 MeV^{-1} E_{e^+}p_{e^+}, \quad (2.1)$$

[4]cosmic rays also contain heavier nuclei, protons make up around 90 % of the flux

where G_f is the Fermi constant, θ_c is Cabibo angle and a = 1.26 is the axial coupling constant. The case of a complex nucleus involves corresponding form-factors that can be related with measurements of corresponding beta-spectra; close to the threshold one should consider also the threshold effects.

This reaction has some energy threshold depending on the nucleus used as well as energy dependence in the cross-section that limits abilities of experiments using this reaction to the high-energy part of the spectra. Still, in case of antineutrino such reaction could have a quite complex signature that could benefit in practically zero-background detection, that is of extreme importance in case of such weakly interacting particle.

Another reaction that could allow neutrino detection is elastic scattering on nuclei and on electrons. The reaction makes the greatest scientific interest is the second one since nuclear recoil has extremely low energy and therefore is difficult to detect. In case of electron a relatively energetic neutrino could pass to it nearly the total original energy in case of face-to-face collision, but still elastic scattering produces detector response which is strongly continuous for monoenergetic neutrino. This fact complicates the detection of monoenergetic lines and low-energy parts of continuous neutrino spectra. The differential cross section has the following form [32]:

$$\frac{d\sigma}{dt} = \frac{2G_f m_0}{\pi}\left(g_L^2(T)[1+\frac{\alpha}{\pi}f_-(z)]\right) + \\ + \frac{2G_f m_0}{\pi}\left(g_R^2(T)(1-z^2)[1+\frac{\alpha}{\pi}f_+(z)] - g_L(T)g_R(T)[1+\frac{\alpha}{\pi}f_{+-}(z)]\right), \quad (2.2)$$

where m_0 is electron mass, T - kinetic energy of recoil electron, q - incident neutrino energy, z = T/q. For electron neutrino one has

$$g_L^{(\nu_e,e)} = \rho_{NC}^{(\nu,l)}[0.5 - \widehat{k}^{(\nu_e,e)}(T)\sin^2(\theta_W(m_Z))] - 1, \quad (2.3)$$

$$g_R^{(\nu_e,e)} = -\rho_{NC}^{(\nu,l)}\widehat{k}^{(\nu_e,e)}(T)\sin^2(\theta_W(m_Z)), \quad (2.4)$$

$$\rho_{NC}^{(\nu,l)} = 1.0126 \pm 0.0016, \quad (2.5)$$

$$\widehat{k}^{(\nu_e,e)}(T) = 0.9791 + 0.0097I(T) \pm 0.0025, \quad (2.6)$$

$$I(T) = \frac{1}{6}\left(\frac{1}{3} + (3-x^2)[\frac{1}{2}x\ ln\left(\frac{x+1}{x-1}\right) - 1]\right), x = \sqrt{1+2m_0/T} \quad (2.7)$$

For other types of neutrinos

$$g_L^{(\nu_e,\mu)} = \rho_{NC}^{(\nu,l)}[0.5 - \widehat{k}^{(\nu_m u,e)}(T)\sin^2(\theta_W(m_Z))], \quad (2.8)$$

$$g_R^{(\nu_e,\mu)} = -\rho_{NC}^{(\nu,l)}\widehat{k}^{(\nu_m u,e)}(T)\sin^2(\theta_W(m_Z)), \quad (2.9)$$

$$\widehat{k}^{(\nu_m u,e)} = 0.9970 - 0.00037I(T) \pm 0.0025 \quad (2.10)$$

In these formulae radiative corrections to neutrino-electron interaction are also accounted for. The corresponding expressions are:

$$f_-(z) = \left[\frac{E}{l}\ln\left(\frac{E+l}{m_0}\right) - 1\right]\left[2\ln\left(1-z-\frac{m_0}{E+l}\right) - \ln(1-z) - \frac{1}{2}\ln z - \frac{5}{12}\right] + \frac{1}{2}[L(z) - L(\beta)] - \frac{1}{2}\ln^2(1-z) - \left(\frac{11}{12}+\frac{z}{2}\right)\ln(1-z) + z\left[\ln z + \frac{1}{2}\ln\left(\frac{2q}{m_0}\right)\right] - \left(\frac{31}{18}+\frac{1}{12}\ln z\right)\beta - \frac{11}{12}z + \frac{z^2}{24}, \quad (2.11)$$

$$(1-z^2)f_+(z) = \left[\frac{E}{l}\ln\left(\frac{E+l}{m_0}\right)\right]\times \times\left((1-z^2)\left[2\ln\left(1-z-\frac{m_0}{E+l}\right) - \ln(1-z) - \frac{\ln z}{2} - \frac{2}{3}\right] - \frac{z^2\ln z + 1 - z}{2}\right) - \frac{(1-z)^2}{2}(\ln^2(1-z) + \beta[L(1-z) - \ln z\ln(1-z)]) + \ln(1-z)\left[\frac{z^2}{2}lnz + \frac{1-z}{3}\left(2z-\frac{1}{2}\right)\right] - \frac{z^2}{2}L(1-z) - \frac{z(1-2z)}{3}\ln z - \frac{z(1-z)}{6} - \frac{\beta}{12}\left[\ln z + (1-z)\left(\frac{115-109z}{6}\right)\right], \quad (2.12)$$

$$f_{+-}(z) = \left[\frac{E}{L}\ln\left(\frac{E+l}{m_0}\right)\right]2\ln\left(1-z-\frac{m_0}{E+l}\right) \quad (2.13)$$

One should recall increase of the cross-section with energy that allows better detection of high-energy spectral part even for comparatively small fluxes . This reaction is used in most current real-time neutrino detectors. An example of electron recoil curve could be found on fig. 2.4.

2.3 Neutrino oscillations

Among all phenomena concerning neutrino one of the most important one is neutrino oscillations [33], [34], that is an explanation of different experimental phenomena observed at the moment. We start discussing briefly the theoretical framework of neutrino oscillations. We will focus at first on two-neutrino oscillations because of their experimental importance and then we will give the more general result for three families oscillations. Later, we will discuss neutrino oscillations in matter according to MSW theory. The reference for this section is [31].

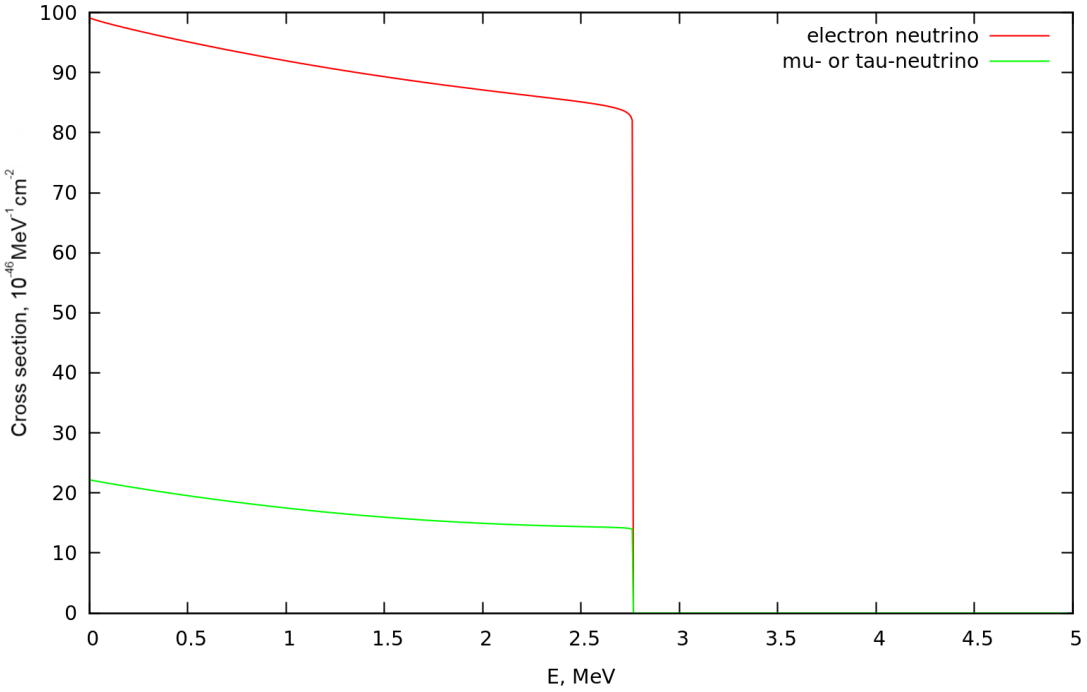

Figure 2.4: Neutrino-electron elastic scattering differential cross section for a monoenergetic neutrino with energy of 3 MeV, computed according to [32]

.

2.3.1 Oscillations in vacuum

Neutrino oscillations are a quantum mechanical consequence of the existence of nonzero neutrino masses, neutrino (lepton) mixing and of the relatively small splitting between the neutrino masses. The neutrino mixing and oscillation phenomena are analogous to the $K^0 - \bar{K}^0$ and $B^0 - \bar{B}^0$ mixing and oscillations in the hadronic sector [35].

In all the cases of practical interest, neutrino fluxes are weak in the sense that multi-particle Fermi-Dirac effects can be neglected. This means that without any loss of generality, one-particle non relativistic quantum mechanics is the right framework to describe neutrino oscillations. The procedure one should follow to derive the neutrino oscillations formulas consists of:

- building a neutrino wave-packet taking into account the dynamics of the specific process that produces it;
- studying the wave-packet evolution (the lighter mass eigenstate moves faster than the heavier one so that at some point the two wave-packets no longer overlap, destroying oscillations);

- computing the observable to be measured taking into account what the detector is actually doing (oscillations are a quantum interference effect and the necessary coherence is destroyed if the neutrino mass is measured with enough precision to distinguish which one of the neutrino mass eigenvalues has been detected).

If we focus on a stationary neutrino flux or on experiments which only measure time-averaged observables, it is possible to avoid using the wave-packet formalism in favor of a more straightforward derivation. In this condition, in fact, a neutrino wave is fully described by its energy spectrum. Thus, it is possible to describe oscillations in terms of plane waves. The basic observation behind this statement is that the most generic neutrino state is a superposition of Hamiltonian eigenstates whose interference terms $\sim e^{i(E-E')\cdot t}$ average to zero when computing any physical observable. It is possible to prove this statement both in the case in which the state is pure and in the case in which the state is described by a density matrix.

This simplifying condition is valid in all realistic experiments: if an experiment can measure the time of neutrino detection with $\Delta t \sim ns$, it is not sensible to interference among neutrinos with $\Delta E \gg \frac{1}{\Delta t} \sim 10^{-6}\,\mathrm{eV}$, which is much smaller than any realistic energy resolution.

Deviations from the oscillation probabilities that we are about to derive are negligible even when considering a pulsed neutrino beam or a short supernova neutrino burst.

2.3.2 Two neutrino oscillations

Let us suppose that we deal with just two different kinds of neutrinos, ν_e and ν_μ[5]. These states are dynamical and do not coincide with the free Hamiltonian eigenstates but of course the former ones can be projected on the latter ones and therefore it is possible to write

$$\begin{pmatrix} \nu_l \\ \nu_{l'} \end{pmatrix} = \begin{pmatrix} \cos\theta & \sin\theta \\ -\sin\theta & \cos\theta \end{pmatrix} \begin{pmatrix} \nu_1 \\ \nu_2 \end{pmatrix}, \tag{2.14}$$

where ν_1 and ν_2 are the mass eigenstates and the 2×2 mixing matrix is unitary and described by just one mixing angle, θ. We assume that at the production region, $x \approx 0$, ν_e are produced with energy E. Since ν_1 and ν_2 have different masses, the initial ν_e becomes some other mixture of ν_1 and ν_2 or, equivalently of ν_μ and ν_e.

Since we are interested in the stationary condition, we can neglect the time dependence in the propagation. If for the initial state the equation $|\nu(x=0)\rangle =$

[5]The definition of electron/muon/tau neutrinos is the following: electron/muon/tau neutrino is the neutral particle which is produced together with an electron/muon/tau in a weak charged current interaction.

$|\nu_e\rangle = \cos\theta\,|\nu_1\rangle + \sin\theta\,|\nu_2\rangle$ holds, at a generic position x we have

$$|\nu(x)\rangle = e^{ip_1 x}\cos\theta\,|\nu_1\rangle + e^{ip_2 x}\sin\theta\,|\nu_2\rangle \tag{2.15}$$

where p_1 and p_2 are the mass eigenstates momenta, since we do not care about the time dependence. The amplitude for the transition $\nu_e \to \nu_\mu$ is $A_{e\mu} = \langle\nu_\mu|\nu(x)\rangle$ where $|\nu_\mu\rangle = -\sin\theta\,|\nu_1\rangle + \cos\theta\,|\nu_2\rangle$ as can be easily read from Eq. 2.14. So we have

$$\begin{aligned} A_{e\mu} &= \left\langle(-\sin\theta\,|\nu_1\rangle + \cos\theta\,|\nu_2\rangle)\,|\,\left(e^{ip_1 x}\cos\theta\,|\nu_1\rangle + e^{ip_2 x}\sin\theta\,|\nu_2\rangle\right)\right\rangle = \\ &= -\sin\theta\cos\theta e^{ip_1 x} + \sin\theta\cos\theta e^{ip_2 x} \end{aligned} \tag{2.16}$$

The probability of transition from ν_e to ν_μ is the square of the amplitude:

$$\begin{aligned} P_{\nu_e\to\nu_\mu} = |A_{e\mu}|^2 &= \sin^2\theta\cos^2\theta\left(1+1-2\mathrm{Re}(e^{ip_1 x}e^{ip_2 x})\right) = \\ &= 2\sin^2\theta\cos^2\theta\left(1-\mathrm{Re}(e^{i(p_1-p_2)x})\right) = \\ &= 2\sin^2\theta\cos^2\theta\left(1-\cos(p_1-p_2)x\right) = \\ &= \sin^2 2\theta\sin^2\frac{p_1-p_2}{2}x = \\ &\simeq \sin^2 2\theta\sin^2\frac{\Delta m^2_{12}x}{4E} \end{aligned} \tag{2.17}$$

where $\Delta m^2_{12} \equiv m^2_2 - m^2_1$ and the ultrarelativistic approximation was used. In fact since $m_\nu < 1\,\mathrm{eV}$ and $E_\nu \sim \mathrm{MeV}$ and so $E_\nu \gg m_\nu$ in all experimental applications, it is possible to write

$$p = \sqrt{E^2 - m^2} = E\sqrt{1-\frac{m^2}{E^2}} \simeq E\left(1-\frac{m^2}{2E^2}\right) \tag{2.18}$$

neglecting higher orders than $\frac{m^2}{E^2}$. For this reason we have

$$p_1 - p_2 = \sqrt{E^2 - m^2_1} - \sqrt{E^2 - m^2_2} \simeq \frac{m^2_2 - m^2_1}{2E} \equiv \frac{\Delta m^2_{12}}{2E} \tag{2.19}$$

Therefore the probability of ν_μ appearance at the detection region $x \approx L$ is

$$P_{\nu_e\to\nu_\mu} = \sin^2 2\theta\sin^2\frac{\Delta m^2_{12}L}{4E} \tag{2.20}$$

As it can be seen from this equation, neutrinos must have different masses in order for oscillations to occur. In addition to that, this formula is symmetric for $\theta \to \frac{\pi}{2} - \theta$ and so by the two neutrino oscillations it is impossible to discriminate whether $\theta > \frac{\pi}{4}$ or $\theta < \frac{\pi}{4}$. Of course, oscillation effects are maximal for $\theta = \frac{\pi}{4}$.

Since neutrinos cannot decay, the survival and appearance probability have to sum up to 1:

$$P_{\nu_e \to \nu_e} + P_{\nu_e \to \nu_\mu} = 1 \tag{2.21}$$

A convenient numerical relation is found restoring $\hbar$ and c factors in Eq. 2.20. In fact we can define the oscillation phase φ as following:

$$P_{\nu_e \to \nu_\mu} = \sin^2 2\theta \sin^2 \varphi \tag{2.22}$$

$$\varphi = \frac{\Delta m^2_{12} L}{4E} \tag{2.23}$$

Since φ has to be dimensionless, the right way to put back $\hbar$ and c factors is

$$\varphi = \frac{\Delta m^2_{12} c^4 L}{4E\hbar c} \tag{2.24}$$

By inserting the constant values we get

$$\varphi = 1.267 \frac{\Delta m^2_{12}}{\mathrm{eV}^2} \frac{L}{\mathrm{km}} \frac{\mathrm{GeV}}{E} \tag{2.25}$$

which is very useful and of easy and practical application. From this expression it is straightforward to notice that oscillations are suppressed by the Lorentz time-dilatation factor m/E as well as it happens in decays. From Eq. 2.25 it is also possible to obtain an expression for the oscillation wavelength:

$$\begin{aligned} &\sin \varphi = \sin kL = \sin \frac{2\pi}{\lambda} L \\ &\to \lambda = \frac{2\pi L}{\varphi} = \frac{8\pi E}{\Delta m^2_{12}} = 2.48\,\mathrm{km} \frac{E}{\mathrm{GeV}} \frac{\mathrm{eV}^2}{\Delta m^2_{12}} \end{aligned} \tag{2.26}$$

There are some interesting different regimes of these formulae that are useful when facing a realistic setup where the neutrino beam is not monochromatic, and the energy resolution of the detector is not perfect. In this case it is needed to average the oscillation probability around some energy range ΔE. Furthermore, the production and detection regions are not points: one needs to average around some path-length range ΔL, too. If $\varphi \ll 1$, the oscillation probability is very small, up to the point that there is no oscillation at all. On the contrary, if $\varphi \gg 1$, the sine squared averages to $1/2$ and the oscillation probability becomes constant and independent from the energy and the distance between the production and detection points. In this case the appearance and survival probabilities become:

$$P_{\nu_e \to \nu_\mu} = \frac{1}{2} \sin^2 2\theta, \quad P_{\nu_e \to \nu_e} = 1 - \frac{1}{2} \sin^2 2\theta \tag{2.27}$$

2.3.3 Three-neutrino oscillations

In the case of more than two types of neutrinos, the formalism is the same as the one used for the simpler case of two families. In the case of three families it is possible to write

$$|\nu_l\rangle = \sum_{j=1}^{3} U_{lj}^* |\nu_j\rangle \tag{2.28}$$

where $l = e, \mu, \tau$ and U is the neutrino mixing matrix (Pontecorvo-Maki-Nakagawa-Sakata matrix or PMNS matrix, [36]). If the number of leptonic eigenstates is equal to the number of mass eigenstates, U is a unitary matrix, i.e. $UU^\dagger = U^\dagger U = 1$, because of the conservation of probability. There is also the possibility that the number of mass eigenstates is higher than the number of active neutrinos[6]: these states are the so-called "sterile neutrinos" because they are chargeless for any known interaction in the SM. In this thesis we will assume that sterile neutrinos do not exist.

Of course this kind of formalism for the description of neutrino oscillations can be easily adapted to the most general case of n families, simply adding dimensions to the PMNS matrix U. Since U is unitary, it can be shown that the number of free parameters needed to describe it consists of $n(n-1)/2$ angles and $(n-1)(n-2)/2$ physical phases in the case of Dirac neutrino fields or $n(n-1)/2$ phases in the case of Majorana neutrino fields [37]. In the case of 3 families the usual parametrization of U is the following:

$$\begin{aligned} U = &\begin{pmatrix} 1 & 0 & 0 \\ 0 & \cos\theta_{23} & \sin\theta_{23} \\ 0 & -\sin\theta_{23} & \cos\theta_{23} \end{pmatrix} \cdot \begin{pmatrix} \cos\theta_{13} & 0 & \sin\theta_{13}e^{-i\delta} \\ 0 & 1 & 0 \\ -\sin\theta_{13}e^{i\delta} & 0 & \cos\theta_{13} \end{pmatrix} \cdot \\ &\begin{pmatrix} \cos\theta_{12} & \sin\theta_{12} & 0 \\ -\sin\theta_{12} & \cos\theta_{12} & 0 \\ 0 & 0 & 1 \end{pmatrix} \cdot \begin{pmatrix} e^{i\phi_1/2} & 0 & 0 \\ 0 & e^{i\phi_2/2} & 0 \\ 0 & 0 & 1 \end{pmatrix} \end{aligned} \tag{2.29}$$

where δ e $\phi_{1,2}$ are respectively the Dirac and Majorana phases.
By following straightforwardly the steps done in the previous section, it is possibile to derive the expression for the probability of oscillation also in this case. Just for the sake of completeness we write here the expression for the vacuum oscillation probability $l \to l'$ with $l \neq l'$:

$$P(\nu_l \to \nu_{l'}) = \sum_j |U_{l'j}|^2 |U_{lj}|^2 + 2\sum_{j>k} |U_{l'j}U_{lj}^* U_{lk} U_{l'k}^*| \cos(\frac{\Delta m_{jk}^2}{2p} L - \varphi_{l'l;jk}) \tag{2.30}$$

where $l, l' = e, \mu, \tau$ and $\varphi_{l'l;jk} = \arg(U_{l'j}U_{lj}^* U_{lk} U_{l'k}^*)$.

[6] With "active neutrinos" we mean the neutrinos that weakly interact.

2.3.4 MSW theory

The MSW (Mikheyev-Smirnov-Wolfenstein, [38, 39, 40, 41]) effect is the effect of transformation of one neutrino species (flavor) into another one in a medium with varying density. The Hamiltonian of the neutrino system in matter, H_m, differs from the Hamiltonian in vacuum, H_0: $H_m = H_0 + H_{matt}$ where H_{matt} describes the interaction of neutrinos with the particles of matter. However, the cross section for the interaction of a neutrino with an energy $\sim$ MeV with the Earth is very low. The probability of such a reaction is of the order of 10^{-12}. Still, the presence of matter can significantly affect neutrino propagation.

This phenomenon has a well known optical analogue. A transparent medium negligibly absorbs light, but still significantly reduces its speed according to its refraction index. Since matter is composed by electrons (rather than by muons and taus), electron neutrinos interact differently than muon or tau neutrinos. This gives rise to a flavor-dependent refraction index. Forward scattering of neutrinos interferes with free neutrino propagation, giving rise to refraction and so changing the description of neutrino oscillations.

Since weak neutral current interactions of neutrinos on quarks and electrons are the same for all flavors, they do not give contribution to transitions between active neutrinos. The interesting effect is due to $\nu_e\, e$ scattering mediated by the W boson that is described at low energy by the effective Hamiltonian

$$H_{eff} = \frac{4G_F}{\sqrt{2}} \left(\bar{e}\gamma_\mu P_L \nu_e\right) \left(\bar{\nu}_e \gamma^\mu P_L e\right) = \frac{4G_F}{\sqrt{2}} \left(\bar{\nu}_e \gamma_\mu P_L \nu_e\right) \left(\bar{e}\gamma^\mu P_L e\right) \tag{2.31}$$

where the Fierz identity and the fact that fermion operators anticommute were used. Since we are studying the effect of electrons in matter on neutrinos that propagate at a speed really close to the speed of light, we can assume that electrons are at rest. This condition describes well both what happens in the Earth and in the Sun. If electrons are at rest, just the piece with $\mu = 0$ survives and so

$$\begin{aligned} &\left\langle \bar{e}\gamma_\mu \frac{1-\gamma_5}{2} e \right\rangle = \frac{N_e(x)}{2} (1,0,0,0)_\mu \\ &\Rightarrow \langle H_{eff} \rangle = \sqrt{2} G_F N_e(x) \left(\bar{\nu}_e \gamma_0 P_L \nu_e\right) \end{aligned} \tag{2.32}$$

This shows explicitly that just electron neutrinos are involved in this kind of interaction. In the basis of flavour eigenstates, i.e.

$$\psi = \begin{pmatrix} \nu_e \\ \nu_\mu \\ \nu_\tau \end{pmatrix} \tag{2.33}$$

the matter Hamiltonian is

$$H_{matt,\nu} = \sqrt{2} G_F N_e(x) \begin{pmatrix} 1 & 0 & 0 \\ 0 & 0 & 0 \\ 0 & 0 & 0 \end{pmatrix} \tag{2.34}$$

where G_F is the Fermi coupling constant and N_e is the density of electrons in matter. It can be shown that in the case of antineutrinos just a sign changes $H_{matt,\bar{\nu}} = -H_{matt,\nu}$.

The potential $V = \sqrt{2} G_F N_e$ does not produce oscillations at all, it just changes the ν_e phase. "Matter oscillations" are different from vacuum oscillations because of this difference in the ν_e phase. In order for this effect to occur it is needed that the vacuum Hamiltonian is of the same order of the matter potential. If we define $K \equiv \frac{\Delta m^2}{2E}$ (this is the term which matters in vacuum oscillations) it is required that $V/K \sim 1$ to observe matter effects. A practical expression of this ratio, used in solar neutrinos physics, is the following:

$$\frac{V}{K} = \frac{\sqrt{2} G_F N_e}{\frac{\Delta m^2}{2E}} = \frac{\rho Y_e}{100\,\text{moles/cm}^3} \frac{\Delta m^2_{12}}{\Delta m^2} \frac{E}{5\,\text{MeV}} \tag{2.35}$$

where ρ is the density of the matter and Y_e is the fraction of electrons per atoms ($Y_e = \frac{Z}{A}$ for neutral matter). Useful numbers are the following: $\rho \sim 12\,\text{g/cm}^3$ in the centre of the Earth while $\rho \sim 150\,\text{g/cm}^3$ in the center of the Sun. If $V/K \ll 1$ matter effects are negligible, while the more you increase the energy, the more matter counts.

Let us study in more detail what happens when only two families of neutrinos give contribution to this effect. This is the typical condition that occurs while studying neutrino oscillations inside the Sun.

In this case and in the base of flavor eigenstates, the vacuum Hamiltonian can be written as

$$H_0 = R \begin{pmatrix} \frac{m_1^2}{2E} & 0 \\ 0 & \frac{m_2^2}{2E} \end{pmatrix} R^t, \quad R = \begin{pmatrix} \cos\theta & \sin\theta \\ -\sin\theta & \cos\theta \end{pmatrix} \tag{2.36}$$

It is possible to modify the way to write down the Hamiltonian as following

$$\begin{pmatrix} m_1^2 & 0 \\ 0 & m_2^2 \end{pmatrix} = \begin{pmatrix} \frac{m_1^2 - m_2^2}{2} & 0 \\ 0 & \frac{m_2^2 - m_1^2}{2} \end{pmatrix} + \frac{m_1^2 + m_2^2}{2} \begin{pmatrix} 1 & 0 \\ 0 & 1 \end{pmatrix} \sim \begin{pmatrix} \frac{m_1^2 - m_2^2}{2} & 0 \\ 0 & \frac{m_2^2 - m_1^2}{2} \end{pmatrix} \tag{2.37}$$

just because a rigid shift in all energies is not physically relevant. This means that for H_0 we have

$$H_0 = \begin{pmatrix} \cos\theta & \sin\theta \\ -\sin\theta & \cos\theta \end{pmatrix} \begin{pmatrix} -\frac{k}{2} & 0 \\ 0 & \frac{k}{2} \end{pmatrix} \begin{pmatrix} \cos\theta & -\sin\theta \\ \sin\theta & \cos\theta \end{pmatrix} = \frac{k}{2} \begin{pmatrix} -\cos 2\theta & \sin 2\theta \\ \sin 2\theta & \cos 2\theta \end{pmatrix} \tag{2.38}$$

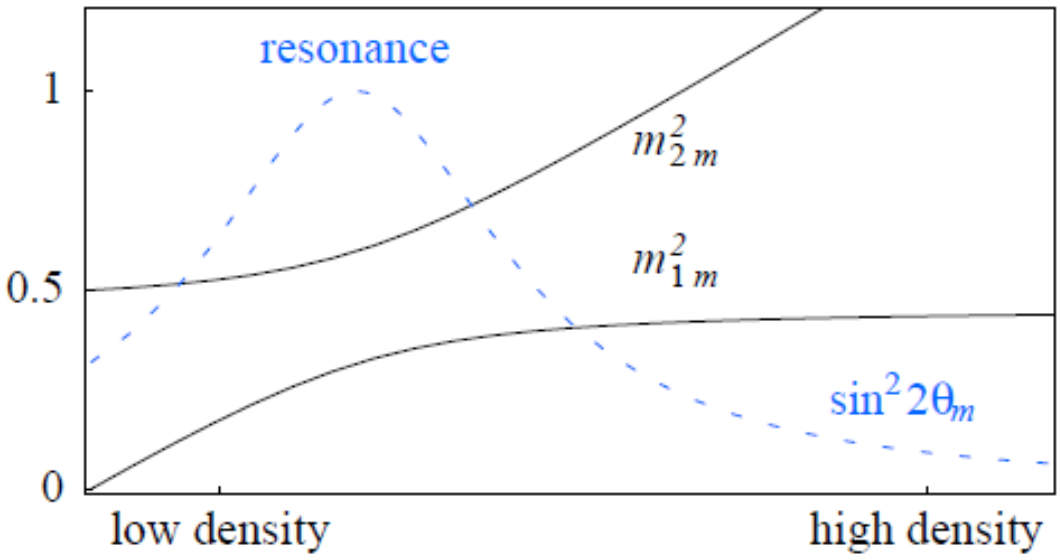

Figure 2.5: Effective masses and mixing angle in matter for two neutrino flavors as a function of the density for $\theta = 0.3$, $\Delta m^2 = 0.5\,\mathrm{eV}^2$ [31].

.

where we have defined $k \equiv \frac{m_2^2 - m_1^2}{2}$.
Recalling the form of the matter Hamiltonian from Eq. 2.34, we have

$$H_{matt} = \begin{pmatrix} V & 0 \\ 0 & 0 \end{pmatrix} \tag{2.39}$$

where $V = \sqrt{2} G_F N_e$. As we did in Eq. 2.37, we can subtract the trace from H_{matt} and so we can get

$$H_{matt} \sim \begin{pmatrix} \frac{V}{2} & 0 \\ 0 & -\frac{V}{2} \end{pmatrix} \tag{2.40}$$

The full Hamiltonian H is the sum of the vacuum and the matter terms, i.e. $H = H_0 + H_{matt}$:

$$H \equiv \frac{k_M}{2} \begin{pmatrix} -\cos 2\theta_M & \sin 2\theta_M \\ \sin 2\theta_M & \cos 2\theta_M \end{pmatrix}, \quad \text{where} \quad \begin{Bmatrix} k \sin 2\theta \equiv k_M \sin 2\theta_M \\ k \cos 2\theta \equiv k_M \cos 2\theta_M \end{Bmatrix} \tag{2.41}$$

By these definitions, the Hamiltonian in presence of matter has the form as the one in vacuum. The only difference is in the presence of two effective parameters,

k_M and θ_M, that can be derived easily from the previous equation:

$$k_M = \pm\sqrt{(k\sin 2\theta)^2 + (k\cos 2\theta - V)^2}$$
$$\tan 2\theta_M = \frac{\sin 2\theta}{\cos 2\theta - \frac{V}{k}} \tag{2.42}$$

The last equation shows that we can find some values of the energy so that $\tan 2\theta_M = +\infty \Rightarrow \theta_M = \frac{\pi}{4}$. This is the so called condition of "resonance": even if the vacuum mixing angle θ is very small, for some neutrino energies and when neutrinos propagate in the matter, the *effective mixing* can be larger, and even maximal, i.e. $\theta_M \sim \frac{\pi}{4}$. The behavior of the parameters in Eq. 2.42 is sketched in Fig. 2.5. As an additional comment, instead of defining the parameter k_M, one usually defines the "effective masses" simply by $k_M = \frac{\Delta m^2_M}{2E}$.

2.3.5 Application of MSW theory to solar neutrinos

In order to study solar and supernova neutrinos it useful to develop an approximation for the oscillation probabilities for neutrinos produced in the core of the star (where matter effects are important), that escape into the vacuum (where matter effects are negligible). At certailn energies matter effects are important. Here, we discuss the case of two neutrino generations in the Sun.

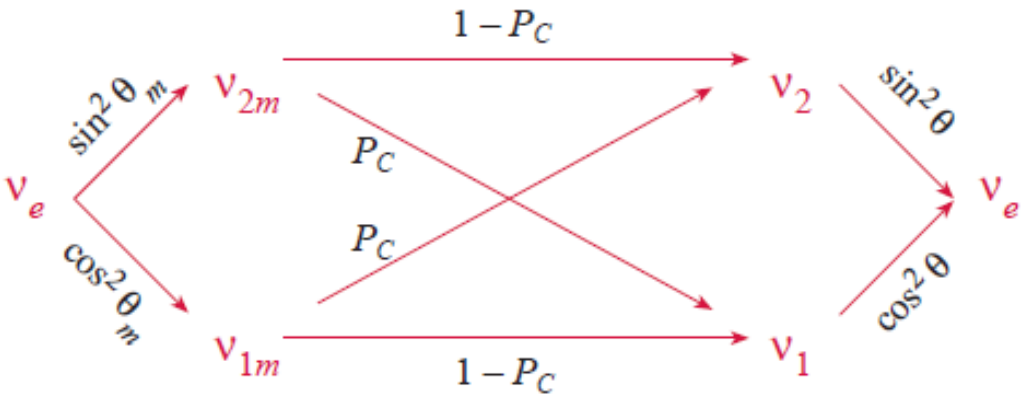

Figure 2.6: Propagation of a neutrino from the Sun to the Earth [31].

ν_e are produced in the inner part of the Sun ($r \sim 0$). Since inside the Sun the relation $|\nu_e\rangle = \cos\theta_M |\nu_{1M}\rangle + \sin\theta_M |\nu_{2M}\rangle$ holds, the probabilities of ν_e being $\nu_{1M}(r = 0)$ or $\nu_{2M}(r = 0)$ are $\cos^2\theta_M$ and $\sin^2\theta_M$ respectively. When there is resonance, i.e. matter effects are dominant, $\sin^2\theta_M = 1$ and so $|\nu_e\rangle \approx |\nu_{2M}\rangle$.

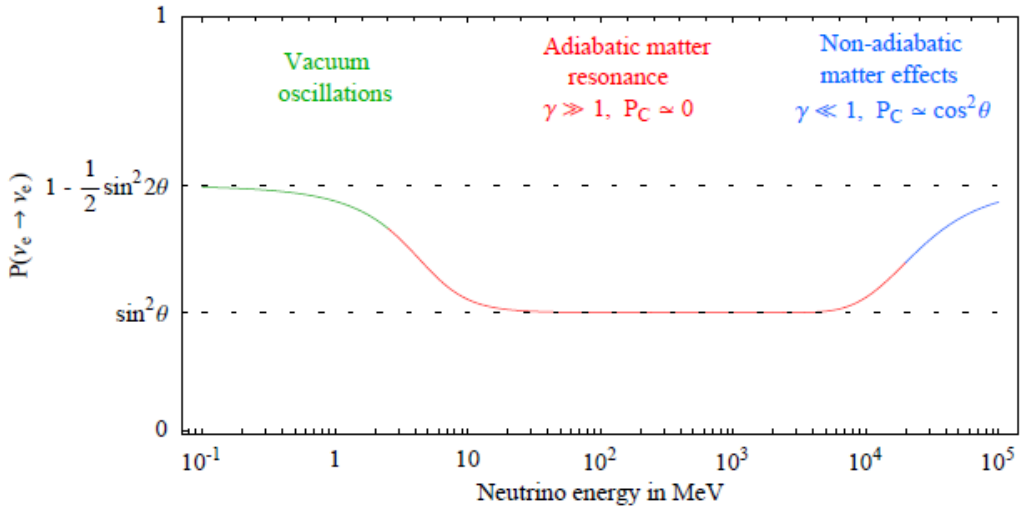

Figure 2.7: Behavior of $P(\nu_e \to \nu_e)$, first presented in [39], that illustrates the limiting regimes of Eq. 2.43(absorption is neglected). At lower energies matter effects are negligible. At intermediate energies matter effects are dominant and adiabatic. At higher energies the MSW resonance is no longer adiabatic. The numerical example corresponds to solar oscillations. γ is the so called "adiabaticity parameter" that measures how much adiabatic the process is. For further details, see [31].

It can be seen that the neutrino oscillation wavelength λ is much smaller than the solar radius: in this case phases average out so that it is possible to combine directly probabilities instead of amplitudes. In addition to that, the "adiabatic approximation" is valid in this situation. This means that the solar density changes very "slowly" and that each neutrino mass eigenstate stays the same. In the limit in which the density is constant this is fully true of course, but when density variations become "fast", it is possible to observe some level-crossings between the two mass eigenstates[7]. We will call the probability of mass-flipping P_C [42] but we are not going to derive an expression for it, since it is not strictly useful for generic understanding of the problem[8]. A more detailed discussion can be found in [31].

After the production in the core of the Sun and the propagation through it and to the Earth, neutrinos propagate in the atmosphere and eventually in the Earth before reaching the detector. This introduces very small modifications.

In Fig. 2.6, the situation briefly discussed is summarized. Electron neutrinos

[7]We are working in the base of the Hamiltonian eigenstates in the center of the Sun.
[8]moreover, P_C is very small in case of LMA solution prefered by experimental evidence

are produced and with certain probabilities ($\cos^2\theta_M$ and $\sin^2\theta_M$) they are one of the two Hamiltonian eigenstates in the point of production (i.e. the core of the Sun). Neutrinos then traverse different densities on their way through the Sun. This means that the eigenstates at the point of production are no more eigenstates of the Hamiltonian, because H depends on the density: it is possible that flips between the two initial eigenstates occur. Finally, neutrinos propagate in the vacuum and so the mixing angle is just θ. In any step of the process, oscillations are averaged because $L \gg \lambda$.

As a final result, combining all the probabilities of fig. 2.6, one gets [43]:

$$P(\nu_e \to \nu_e) = \frac{1}{2} + \left(\frac{1}{2} - P_C\right) \cos 2\theta \cos 2\theta_M \tag{2.43}$$

where, again, θ_M is the mixing angle at the production point. As a summary of this formula, it is very useful to take a look at Fig. 2.7, where electron neutrinos survival probability is plotted as a function of neutrino energy. As it was previously anticipated, where neutrino energy is sufficiently small matter effects are negligible, while increasing the energy, their contribution gets higher. The red part of the line shows the transition from vacuum to matter enhanced oscillations in condition of adiabaticity. This is what actually happens inside the Sun with typical solar neutrino energies. If the energy increases more, then non adiabatic effects get more relevant.

Chapter 3

Solar neutrino experiments

The first discovery of neutrino was performed in Homestake observatory and it was neutrino from the sun. All the further studies of neutrino properties could hardly be separated from solar neutrino experiments. And while the Sun is not studied well enough to predict neutrino production and propagation exactly such experiments study simultaneously the Sun as it is and neutrino properties as they are. Regretfully, in case of neutrino rather than antineutrino it's hardly possible to have a low-energy artificial source on distances corresponding to significant oscillation effects, thus solar neutrino physics is one of the main parts of neutrino physics as it is. Moreover, this is a great opportunity to study the Sun and to get better understanding on what to expect from generic stellar construction. The field of solar neutrinos includes a large number of different experiments and provides us with practically the full spectrum of possible neutrino detection techniques and is very interesting both in the sense of neutrino studies as well as in generic low-background physics. In this section we will review the most important solar experiments of the past and present.

3.1 Solar neutrino problem

The solar neutrino problem was established by Homestake neutrino observatory. It detected neutrino flux of 2.56 SNU while the theoretically predicted flux considering solar model was giving prediction of much higher flux, order of three times more. Despite all the measures that were taken to understand leakage of events from the experimental setup including calibrations of extraction and counting efficiencies, the result did not change much: the neutrino flux observed was still way too small with respect to the predicted one with very high statistical significance. That meant that there is something wrong with solar model or neutrino physics since the experiment was unlikely to produce such discrepancy itself due to ex-

perimental error. But what? Maybe solar model? Since the only flux measured was the flux of boron neutrinos it was quite possible that the sun is constructed differently and produces less neutrinos above experimental threshold: one needed to lower the threshold and to detect pp neutrino which are related with solar luminosity as it is and can not variate that much. Or there was still a possibility of some unknowns with neutrino itself, so it propagates in a way different from expectations. That created the theory oscillation and of matter effects and was another possibility of explaining neutrino deficit phenomenon. But in any case it had to be investigated in order to get an understanding of the reasons that we observe less neutrinos than we expect. Here the story of neutrino problem begins and starts it's slow movement to the solution that hopefully will appear sometime: it is still not understood completely even now.

3.2 Gallium experiments: SAGE and GALLEX

Some additional information on solar neutrino problem could be derived in case one cold lower experimental threshold. In fact, chlorine experiments have an intrinsic problem having energy threshold of 814 keV that automatically means that a significant amount of solar neutrinos are simply not registered due to their low energy. Same time one could try to perform an analogical experiment with lower threshold by changing the nuclei for inverse beta-decay neutrino registration.

In 1965 Kuzmin proposed a possibility of performing neutrino detection based on Gallium reaction[44]:

$$\nu_e + {}^{71}Ga \rightarrow {}^{71}Ge + e^- \tag{3.1}$$

Source	Flux (10^{10} cm^{-2} s^{-1})	Cl (SNU)	Ga (SNU)
pp	5.95 ($1.00^{+0.01}_{-0.01}$)	0.0	69.7
pep	1.6×10^{-2}($1.00^{+0.3}_{-0.3}$)	0.22	2.8
hep	9.3×10^{-7}	0.04	0.1
^{7}Be	4. 84 $\times 10^{-1}$($1.00^{+0.24}_{-0.24}$)	1.15	34.2
^{8}B	5.25×10^{-4} ($1.00^{+0.16}_{-0.16}$)	5.76	12.1
^{13}N	5.48×10^{-2} ($1.00^{+0.21}_{-0.17}$)	0.09	3.4
^{15}O	4.80×10^{-2} ($1.00^{+0.25}_{-0.19}$)	0.33	5.5
^{17}F	5.63×10^{-4} ($1.00^{+0.25}_{-0.25}$)	0.0	0.1
Total		$7.6^{+1.3}_{-1.1}$	128^{+9}_{-7}

Table 3.1: The solar neutrinos fluxes and neutrino capture rates in the Cl and Ga detectors under assumption of no propagational effects on neutrino flux [45, 46]

Such reaction would have energy threshold of 233.2 keV that means that it is able to be induced by all kinds of solar neutrino. In the table 3.1 one could see the improvements that are obtained by migrations from chlorine to gallium. An enormous amount of efforts were performed to create an active experiment using such reaction, namely the extraction algorithm becomes way more sophisticated with respect to chlorine experiment that means way more complicated chemistry. Nevertheless in the end of 80's - beginning of 90's two different experiments based on this reaction started data-taking.

3.2.1 GALLEX/GNO neutrino experiment

One of these two experiments is GALLEX/GNO that was built in national Gran Sasso Laboratory (LNGS) in Italy [47]. The detector target mass was represented with a 54 m^3 tank filled with 101 tons of gallium chloride solution in hydrochloric acid($GaCl_3 \cdot HCl$) that corresponds to total Gallium mass of 30.3 tons (fig. 3.1).

Periodicity of extraction was three weeks; each extraction cycle included germanium chloride extraction by nitrogen stripping since this substance is gaseous with consequent absorption in water. After some chemical procedures germane gas (GeH_4) was obtained and used for counting purposes.

Such detector should be operated under consideration of non-neutrino germanium production in (p,n) reaction that means that one needs to keep appropriate purification level as well as good cosmic ray shielding to prevent cosmogenic germanium production, that means corresponding neutron shielding reducing the fast neutron flux produced in the rock under muon affection. Acidity of the solution was kept for ensuring of germanium production in form of chloride that could be separated from basic target substances due to volatility. The overall extraction procedure efficiency was as high as 94.1 %; counting was performed in xenon environment with application of low-background proportional counters, distinguishing reaction of electron capture on germanium by characteristic gamma-rays.

The detector was operated since 1991 and finished operation in 2003, providing quite high statistics of gallium neutrino data.

Germanium extraction procedure As in every radiochemical experiment the most thin moment is related with the procedure of neutrino interaction product extraction from the bulk of detector target mass. Neutrino production is very small and counts single atoms per target mass of tons so efficiency of extraction procedure should be very high and separation ability of the approach should also be outstanding to concentrate all of final atoms in a small volume for counting purposes. In case of GALLEX/GNO the extraction procedure included the following steps:

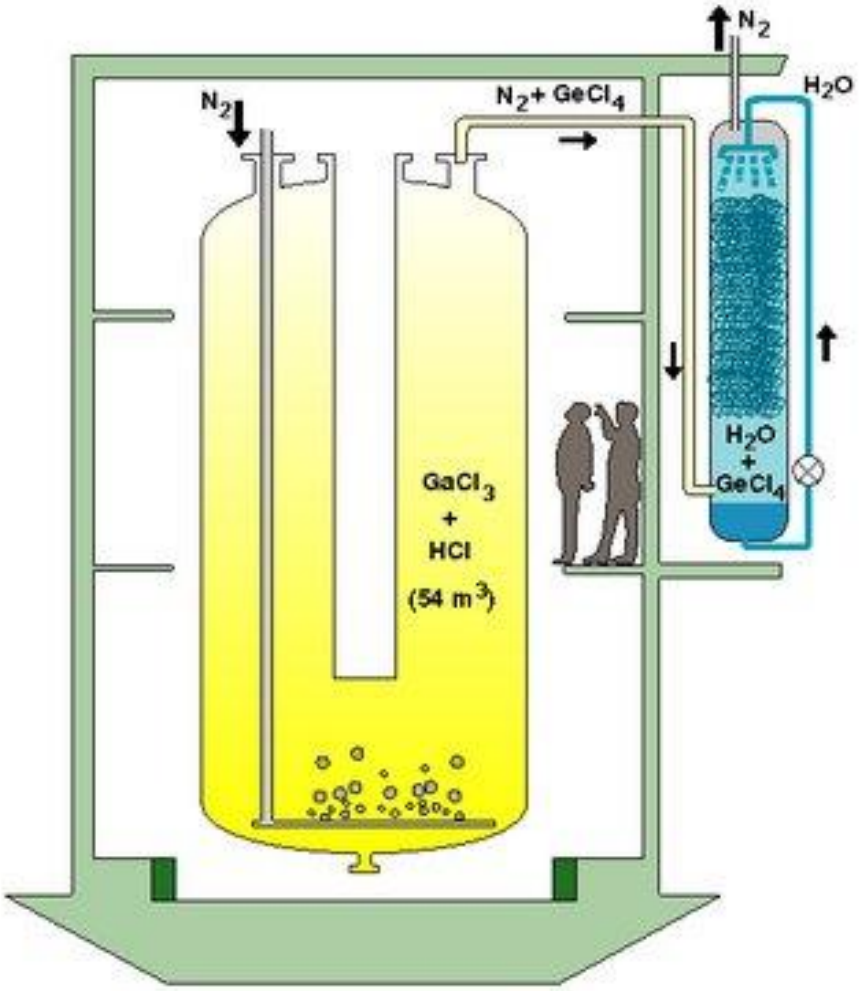

Figure 3.1: Principal scheme of GALLEX/GNO Neutrino experiment

- In the beginning of every run around 1 mg of stable germanium carrier was added to the target solution; during and after this addition the solution was stirred with nitrogen flux for 9 hours. Carryover stability was monitored with stable enriched isotopes of germanium, i.e. ^{72}Ge, ^{74}Ge, ^{76}Ge. The checks were performed between runs with mass-spectrometric approach, germanium concentrations were controlled through absorption atomic spectroscopy. On three-week basis the solution was stripped with 1900 m^3 of nitrogen within 20 hours with temperature of 20 °C Extraction efficiency typically stayed around 99%. Such number allowed performance of extraction efficiency correction

on the level of target gas stripping

- The volatile germanium tetrachloride was absorbed in water by scrubbing the outcome gas through three large absorber columns (3 m high, 30 cm in diameter)at 12°.

- The germanium tetrachloride gas was desorbed with consequent reabsorption in 50 mL of specially prepared tritium-free water. This sample was finally used in germane gas production for the consequent purification procedures precessing counting phase.

The procedure resulted in production of actual germane gas that was possible to use for the final analysis with the known and controlled extraction efficiency that was needed to perform the corresponding corrections in derivation of the number of neutrino events.

counting Counting of the obtained atoms number is also a quite sophisticated and crucial phase of the experiment. In order to optimize the counting efficiency, germane was mixed with xenon gas with proportion of 30/70. At this phase the extraction efficiency was controlled through the values of original and extracted non-radioactive carrier. A filled proportional counter was embedded in lead mold with preamplifier box that was mounted inside a Faraday cage. The typical delay between the beginning of extraction phase corresponded to the value of 14 hours, while germanium has the life time of 11.43 days so the loss of statistics throughout the extraction procedure was considerably small. Germanium electron capture could be distinguished by X-ray cascades of energy of 10.36 keV (K-line, the more intensive line) and 1.17 keV(L-line). As for calibration purposes were used xenon fluorescence X-rays with energies of 1.03 keV, 5.09 keV and 9.75 keV, that allowed to understand energy response and resolution of the proportional counters.

The obtained count rate of original GALLEX experiment in 1991 - 1997 gave the value of 71.3±7.2 SNU. The result of the following phase called GNO is demonstrated on fig. 3.2 and shows quite stable rate with the average value of 67.6 ± 5.1 SNU that is approximately twice smaller than the value expected from the solar model, so this experiment confirms solar neutrino problem also with much lower threshold; As the procedure of carrier-based calibration did not look very reliable, the detector was calibrated with ^{51}Cr neutrino source and had shown satisfactory result of neutrino detection with valid systematic uncertainty. Still, gallium in complex chemical form could be a source of doubts as well as the chemical procedure of germane production, so one could think of pure metallic germanium detector as a more clear alternative. And such detector actually existed.

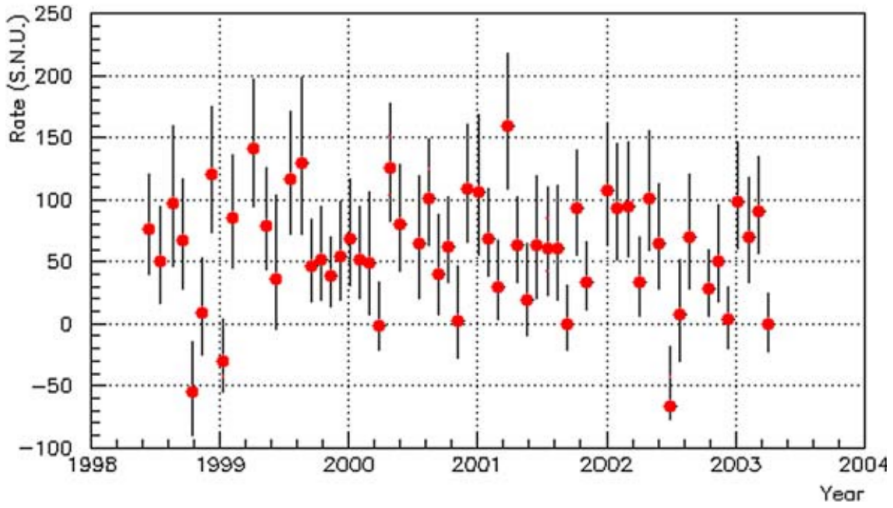

Figure 3.2: Count rate of GNO Neutrino experiment

3.2.2 SAGE

Soviet-American Gallium Experiment (SAGE) is another experiment based on inverse beta-decay on gallium [48]. The main difference with respect to GALLEX/GNO is usage of gallium in metallic form rather than in form of solution that means more simple chemistry application. Of course that means production of metallic gallium in appropriate amount that means very large cost and complexity of such experiment organization. But the situation was that soviet industry was unable to provide appropriate purity of gallium chloride and thus it was decided to perform the work with metallic gallium. Such decision it allowed to overcome purification issue since pure metallic gallium was less sensitive to radioactive admixtures. The possibility of efficient extraction germanium atoms from metallic gallium was already demonstrated by R. Davis and was confirmed within preliminary studies. In 1984 the group that performed GALLEX/GNO experiment was separated from the group that pursued metallic gallium experiment; that allowed to have two experiments using the same neutrino registration methods with absolutely different algorithms of extraction the increased reliability of combined solar neutrino results.

INR (Institute of Nuclear Research) Baksan Neutrino Observatory was organized in the north Caucasian mountains close to the Baksan river source at about 1700 m above ground level. The experimental tunnel with horizontal access was located inside the rock of Andirtchi mountain. Building of this laboratory was started in 1967 with the purpose of locating there three different radiochemical neutrino experiments based on inverse beta-decay of chlorine, lithium and gallium

and thus sensitive to different parts of solar neutrino spectrum. The laboratory has the passive shielding of 4700 meters of water equivalent (m.w.e.) with measured muon flux of $(3.03 \pm 0.10) \times 10^{-9} cm^{-2} s^{-1}$

An advantage of liquid metallic gallium usage is in much lower sensitivity to external radioactivity that was approximated to be less than 1 % with respect to neutrino germanium production for neutrino rate expected from Standard Solar Model even in case of no specific measures applied for external neutron flux reduction. Nevertheless, the laboratory used special low-background concrete that apart from the construction function provided significant reduction of neutron background since it was expected to obtain neutrino rate lower than expected as it happened in case of chlorine experiments.

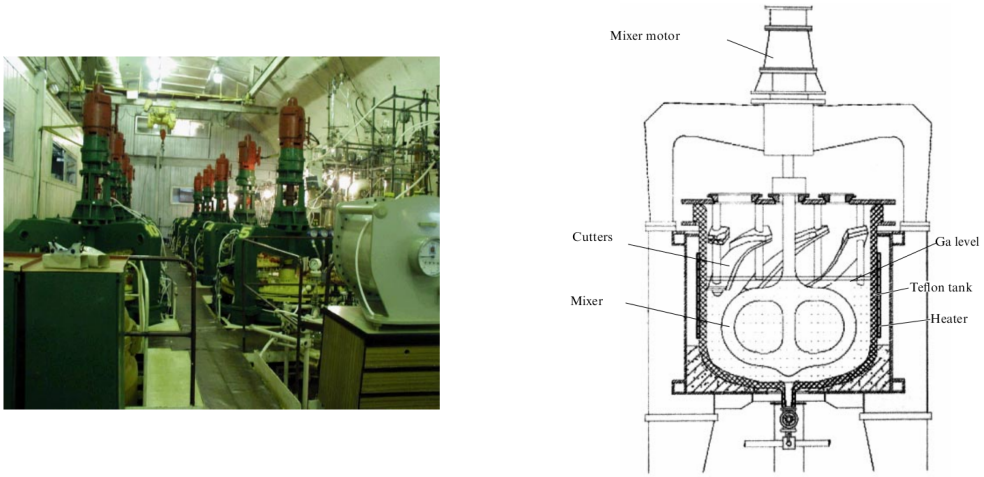

Figure 3.3: Picture and Principal scheme of SAGE chemical reactor.

The detector target was containing by 50 t of metallic gallium located in 7 chemical reactors(fig. 3.3). Every measurement was started from adding tablets of gallium alloy with stable germanium in known quantities for the purpose of extraction efficiency control. Germanium was uniformly distributed in the total gallium mass. Taking into account expected neutrino rate of 128 SNU and total mass of ^{71}Ga of 19.9 tons giving germanium production of 1.9 atoms per day together with germanium life time of 11.43 days one could establish single run exposure duration of 4-6 weeks until stabilization of Ga/Ge ratio in the target. After exposure cycle germanium atoms were extracted and counted with xenon-based proportional counters.

extraction procedure Extraction procedure was performed within chemical reactors, that were connected to each other with Teflon piping fitted with a fluid pump allowing to transport liquid gallium among them. A reactor had construction

of 2-ton Teflon barrel where mixture with chemical reagents was provided by a specially designed mixer with maximum velocity of 80 rpm. As for more efficient mixing the reactor was equipped with Teflon mixers located on the inner side of the upper cap. Extraction of germane gas was performed with vacuum pump. Extraction efficiency strongly dependent on the hydrogen peroxide concentration in a chemical reactor as well as of the volume of water phase that was defining efficiency of consequent concentration of germane needed for counting analysis performance. A method accounting all possible issues of the chemical process was developed and provided overall extraction efficiency of $95 \pm 3\%$ with residual of less than 1 % of gallium.

counting phase Counting phase of SAGE experiment was in a lot of sense analogous to the one used in GALLEX/GNO experiment where proportional counters were used to detect K- and L-captures of germanium atoms by corresponding X-ray cascades. Starting from 2001 the experiment uses YCT(Yants-Carbon-Thin) counters developed in INR specially for this experiment. These counters used thin carbon cathode on the inner layer of the quartz vessel rather solid cathodes in classical scheme. This allowed to exclude "dead" volume behind the cathode , decreasing counting efficiency uncertainty. Together with all other measures applied in these counters volume efficiency of counting reached the value of 96 % with uncertainty of only 1 % than allowed to increase intensities by 25% and 10 % in K- and L-peaks respectively. Impulses from the proportional counter were also selected by shape of the signal front edge that was steeper for expected X-rays with respect to background events. Counting was performed within 5-6 months inside NaI block connected as anticoincedence scheme for active shielding purpose . In order to reduce radon contamination around the counters the counting system was fluxed with evaporating nitrogen. The same time the facility had also a passive shield constructed of consequent layers of iron, lead copper and wolfram. All components of the system were constructed with usage of special low-radioactivity materials.

The counting system provided minimization of uncertainties that could appear within this phase together with maximization of counting efficiency giving the maximum achievable precision for this detector type.

results The detector was running for quite large temporal period. In the meanwhile it was calibrated with chromium source and the calibration gave satisfactory results on the detector neutrino detection reliability. The final results grouped by runs and years are represented on fig.3.4

The overall number gave $65.4 \pm 2.7 \pm 2.7$ SNU that is in a good agreement with the final GNO results and is a definite confirmation of solar neutrino problem

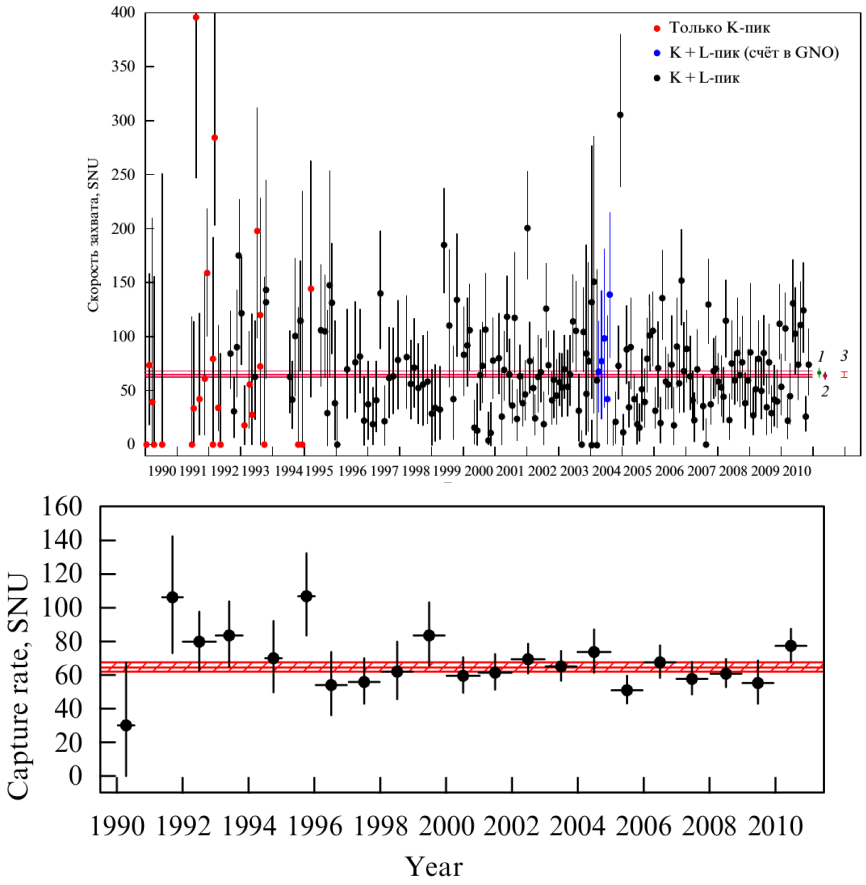

Figure 3.4: Results of SAGE detector binned by runs(upper) and years (lower). On upper plot blue points correspond to counts in GNO and red ones to SAGE accounting only K-line rather than both K- and L- lines.

as a physical phenomenon. Since gallium detectors detected most of the solar spectrum it was practically unbelievable that the root of the problem was lying in our understanding of the sun. So one could expect oscillational solution, but the last word in this problem was said by the next detector type - Ĉerenkov effect water detectors.

3.3 Ĉerenkov neutrino experiments: SNO and SuperKamiokande

All the detectors mentioned were based on radiochemical algorithm. This algorithm provides very good neutrino interaction signature, but two pieces of infor-

Particle	Energy threshold (MeV)
$e^{\pm}$	0.768
$\mu^{\pm}$	158.7
$\pi^{\pm}$	209.7

Table 3.2: Čerenkov threshold energy of various particles in water.

mation escape from these detectors: time and energy. Absence of temporal information prevents these detectors from observation of such important phenomena as temporal variations of neutrino related with distance to the sun and propagation through the Earth that could be detected in case of a real-time detector. Absence[1] of energetic information does not allow to distinguish different spectral components of solar neutrino spectrum and thus significantly limits the detector abilities; in fact these detectors just produce one integral number. So the way to overcome such limitations one should build a real-time spectrometer capable of neutrino detection, and such task is outstandingly difficult since neutrino interaction rate is tine with respect to possible backgrounds. Same the detector should be big, very big in order to be able to register significant number of neutrinos. One of the possibilities of a real-time detector is a water Ĉerenkov-based detector.

3.3.1 Physical principle

In a medium with an index of refraction n the light velocity is c/n. When a charged particle passes through the medium with a velocity larger than the phase speed of light, so called Čerenkov light is emitted [49]. This threshold velocity corresponds to a minimum energy; some examples of this threshold energy in the case of water ($n = 1.33$) are shown in Tab. 3.2.

Čerenkov light is emitted in a cone of half angle θ from the direction of the particle track, where θ is given by

$$\cos\theta = \frac{1}{n\beta}\,, \tag{3.2}$$

with $\beta = v/c$. In water, θ has a value of 42° for $\beta = 1$.

The spectrum of the Čerenkov light as a function of the wavelength λ is:

$$\frac{\mathrm{d}N}{\mathrm{d}\lambda} = \frac{2\pi\alpha x}{c}\left(1 - \frac{1}{n^2\beta^2}\right)\frac{1}{\lambda^2}\,, \tag{3.3}$$

where α is the fine structure constant and x is the length of the charged particle trajectory. A charged particle emits about 390 photons per centimeter of path

[1] threshold of the reaction actually gives some information of neutrino energy, especially in case of several reactions combination

length in the water in the wavelength region approximately 300-700 nm, where the photomultipliers are sensitive.

The event vertex and direction of the charged particles are reconstructed using the hit PMT locations and times that on practice results in Time-Of-Flight (TOF) likelihood analysis, while the energy could be estimated by the number of registered PMT hits or charge. Thus such detectors could have sensitivity to directionality, time and energy of an event and the only practical disadvantage is inability to work at low energies close to Ĉerenkov Threshold.

3.3.2 Sudbury neutrino observatory

The first examples of large water Ĉerenkov detectors existed before appearance of the Sudbury neutrino observatory, by this detector is probably among the most important in the history of solar neutrino physics. The detector was located at 2 km underground in INCO's Creighton Mine in Canada on the depth of 2 km or 5900 m.w.e. that made this laboratory the deepest in the world until recent construction of PandaX laboratory in China. SNO was built for the sake of studying neutrinos from ^{8}B with different reactions on heavy water.

Radiochemical experiments detected less neutrinos than expected by factor of 2 in the total energy range and by factor 3 at high energies. These experiments had sensitivity to electron neutrino only and as neutrino oscillations became the most reasonable explanation of this observation it became a great interest to check out the channels that were hidden from the radiochemical experiments with an appearance experiment on non-electron neutrinos. SNO was designed mostly to perform this check and thus to be sensitive to all neutrino flavors.

SNO detector has construction of an acrylic sphere with radius of 6 m filled with a kiloton of ultrapure heavy water. The sphere was surrounded by stainless steel geodesic support structure fitted with 9438 inward-looking and 91 outward-looking 20cm PMTs(photomultipliers). The whole construction was located in an underground cavity (fig. 3.5), filled with 7 tons of ultrapure light water. The radioactive background treatment was quite careful ind included careful selection of construction materials by the criterion of low level of radioactive impurities. Also the detector was equipped with a purification system providing purification of water inside the acrylic vessel as well as the outer volume that served as a shield for external activity coming from the rock and support structure. The purification system succeeded to reduce natural radioactivity in the heavy water target to the levels of $4.5 \times 10^{-14} g/g$ for uranium and $7.7 \times 10^{-15} g/g$ for thorium that reduced the number of neutrons that could mimic neutrino signal in the detector to the level below one event per day. Large depth provided the detector with reduction of muon rate to the level of 70 muons/day.

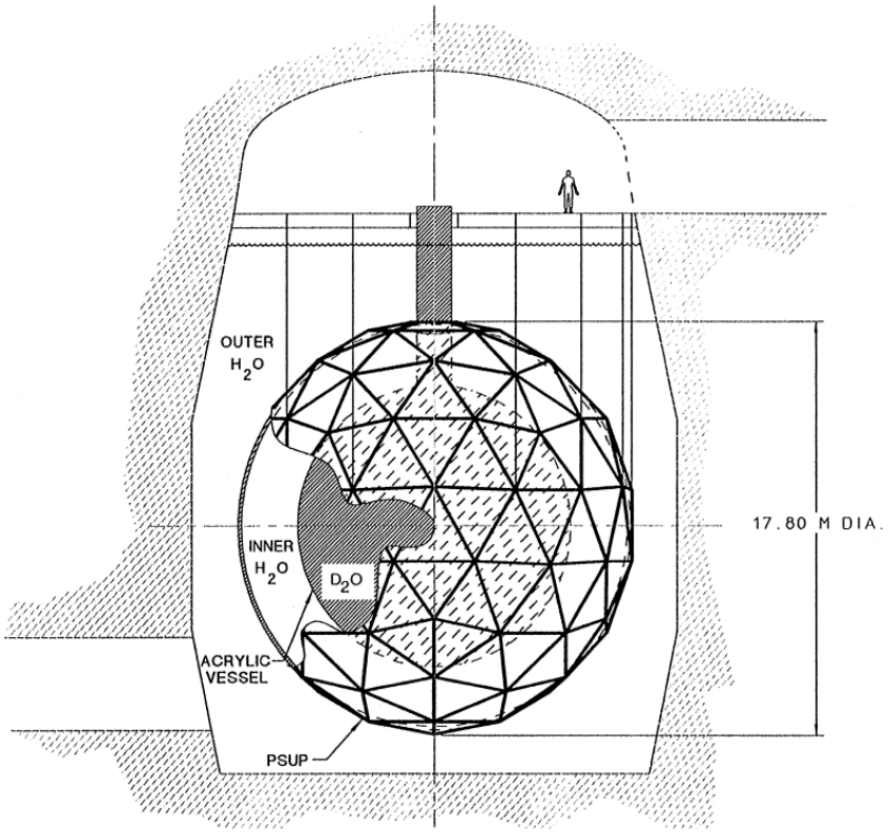

Figure 3.5: Principal scheme of SNO neutrino detector

Stability of the detector conditions was ensured by routine calibrations including:

- optical calibrations with nitrogen laser optically connected to an isotropic scattering ball that allowed monitoring of optical conditions nonuniformity as well actual conditions of the PMTs including quantum efficiencies and electronic channel gains.

- gamma-ray calibrations with ^{16}N(6.13 MeV), accelerator-produced gammas from reaction $^3H(p,\gamma)^4He$ (19.8 MeV) that included usage of miniature particle accelerator and with ^{24}Na gamma source(1.4 MeV, 2.8 MeV)

- electron calibrations with ^{8}Li source producing beta-spectrum with endpoint of 13 MeV

- neutron calibrations with ^{252}Cf sources

Neutrino detection was performed through the following reactions:

$$\begin{aligned} \nu_e + d &\rightarrow 2p + e^-(CC) \\ \nu_x + d &\rightarrow p + n + \nu_x(NC) \\ \nu_e + e^- &\rightarrow \nu_x + e^-(ES) \end{aligned} \tag{3.4}$$

The reactions corresponding to elastic scattering(ES), neutral(NC) and charged (CC) current thus allowed to separate different flavors of neutrino. The charged current reaction with the threshold of 1.44 MeV was possible to perform only by electron neutrino interaction and was detected by moving electron that was getting most of the reaction energy due to smallest mass providing significant information on the original neutrino spectrum. This reaction was distinguished by 42° half-angle cone with reconstruction of event vertex and direction through Time-Of-Flight analysis.

The neutral current reaction with the threshold of 2.22 MeV was detected through the free neutron that was thermalized and captured inside the detector. The capture resulted in one or several gammas producing multiple Compton electrons that were detected by Ĉerenkov radiation.Importance of this channel meant that one needed high efficiency of radiative neutron capture.

The elastic scattering reaction is mostly sensitive to electron neutrinos since inclusion of charged current interactions increases the cross section approximately by factor of 6. This reaction was also detected by Ĉerenkov radiation of a single electron, thus could have been distinguished from charged current reaction due to directionality and (less) spectral shape since recoil electron is not gaining the total amount of neutrino energy and momentum.

Such organization of the detector data analysis allowed to test neutrino fluxes of all flavors, providing a practical test of oscillation hypothesis based on migration of solar neutrinos to the channels invisible for radiochemical experiments due to oscillation process.

Experimental results The experiment was operated in three phases with different operating conditions that were changed for the sake of improvement of charged/neutral current neutrino separation

SNO I covering 306.4 live days, operated from November 1999 through May 2001 with pure heavy water. The NC channel neutrons are captured by deuterium, producing a 6.25 MeV ray; since the neutron capture efficiency of deuterium is low (14.4%), was not possible directly differentiate CC, ES and NC interactions. In fact, the separation was done only selecting a certain kinetic energy threshold

($T \geq$5 MeV) for particles inside the fiducial volume ($R \leq$550 cm). The flux of ^{8}B neutrinos (in units of 10^6 cm^{-2}s^{-1}) measured in this phase, assuming the standard spectrum shape without any propagational deformation, is [50]:

$$\phi_{\rm CC} = 1.76^{+0.06}_{-0.05}({\rm stat})^{+0.09}_{-0.09}({\rm syst})\,,$$
$$\phi_{\rm ES} = 2.39^{+0.24}_{-0.23}({\rm stat})^{+0.12}_{-0.12}({\rm syst})\,,$$
$$\phi_{\rm NC} = 5.09^{+0.44}_{-0.43}({\rm stat})^{+0.46}_{-0.43}({\rm syst})\,.$$

The 5.3 σ difference between the NC and CC fluxes provide an evidence for neutrino flavor transformation. In addition, the NC flux is in agreement with the Solar Standard Model prediction for ^{8}B: $\phi_{\rm SSM} = 5.05^{+1.01}_{-0.81} \times 10^6 {\rm cm}^{-2}{\rm s}^{-1}$.

SNO II covering 391.4 live days, operated from July 2001 through August 2003 with 1950 kg of purified NaCl dissolved in the heavy water [51]. The salt was added in order to improve the neutron detection efficiency to 39%, allowing a more easily NC and CC signal statistical separation. In fact the neutron capture cross-section of ^{35}Cl in NaCl was increased (44 mb versus 0.0005 mb due to the ^{2}H) and gamma rays produced are a cascade with 8.6 MeV energy, well above to the analysis's electron kinetic energy threshold ($T \geq$ 5.5 MeV). After the fiducialization the model-independent flux of ^{8}B neutrinos in the SNO detector results [52]:

$$\phi_{\rm CC} = 1.59^{+0.08}_{-0.07}({\rm stat})^{+0.06}_{-0.08}({\rm syst})\,,$$
$$\phi_{\rm ES} = 2.21^{+0.31}_{-0.26}({\rm stat})^{+0.10}_{-0.10}({\rm syst})\,,$$
$$\phi_{\rm NC} = 5.21^{+0.27}_{-0.27}({\rm stat})^{+0.38}_{-0.38}({\rm syst})\,,$$

and the ratio of the CC and NC reactions is $\phi_{\rm CC}/\phi_{\rm NC} = 0.306 \pm 0.026({\rm stat}) \pm 0.024({\rm syst})$, in agreement with the Solar Standard Model predictions and the hypothesis of flavor transformation. It is possible to derive the mixing parameters without any constrains on the ν_e from ^{8}B spectra: the best-fit point obtained by a global analysis combined with other solar and reactor neutrino results yields Δm^2_{12}=$7.1^{+1.2}_{-0.6} \times 10^{-5}$ eV^2 and $\theta_{12} = 32.5^{+2.4}_{-2.3}$ degrees, rejecting the maximal mixing at a level equivalent to 5.4 σ.

SNO III covering 385.17 live days, operated from November 2004 through November 2006 with an array of ^{3}He proportional counters [53]. After removing all NaI salt from the previous phase, the counters, composed by 36 strings that were deployed in the D_2O forming a lattice on a 1 m grid, were used for a direct counting of NC neutrons by ^{3}He(n,p)^{3}H reaction. The string were able to detect both proton and triton (764 keV total kinetic energy) between 191-764 keV energy,

allowing a direct separation of the NC and CC/ES signals. The efficiency was highly increased since the neutron capture cross section on ^{3}He is $\sigma_{^3\mathrm{He}} \approx 10^7 \times \sigma_{^2\mathrm{H}}$. Four additional strings filled with ^{4}He were insensitive to the neutron signals and were used to study backgrounds. After the fiducialization and fixing the energy threshold to 6.0 MeV, the more precise flux of ^{8}B neutrinos directly measured in the three different channels is [54]:

$$\begin{aligned}
\phi_{\mathrm{CC}} &= 1.67^{+0.05}_{-0.04}(\mathrm{stat})^{+0.07}_{-0.08}(\mathrm{syst})\,, \\
\phi_{\mathrm{ES}} &= 1.77^{+0.24}_{-0.21}(\mathrm{stat})^{+0.09}_{-0.10}(\mathrm{syst})\,, \\
\phi_{\mathrm{NC}} &= 5.54^{+0.33}_{-0.31}(\mathrm{stat})^{+0.36}_{-0.34}(\mathrm{syst})
\end{aligned}$$

and the ratio of the CC and NC reactions is $\phi_{\mathrm{CC}}/\phi_{\mathrm{NC}} = 0.301 \pm 0.033(\mathrm{total})$ that is in agreement with the previous measurements.

A combined analysis of all three SNO's phases [55] provides a total flux of solar neutrinos from ^{8}B results of $\phi_{\mathrm{SSM}} = (5.25 \pm 0.16(\mathrm{stat})^{+0.11}_{-0.13}(\mathrm{syst})) \times 10^6 \mathrm{cm}^{-2}\mathrm{s}^{-1}$, in agreement with the Solar Standard Model predictions (high metalicity case, HZ).

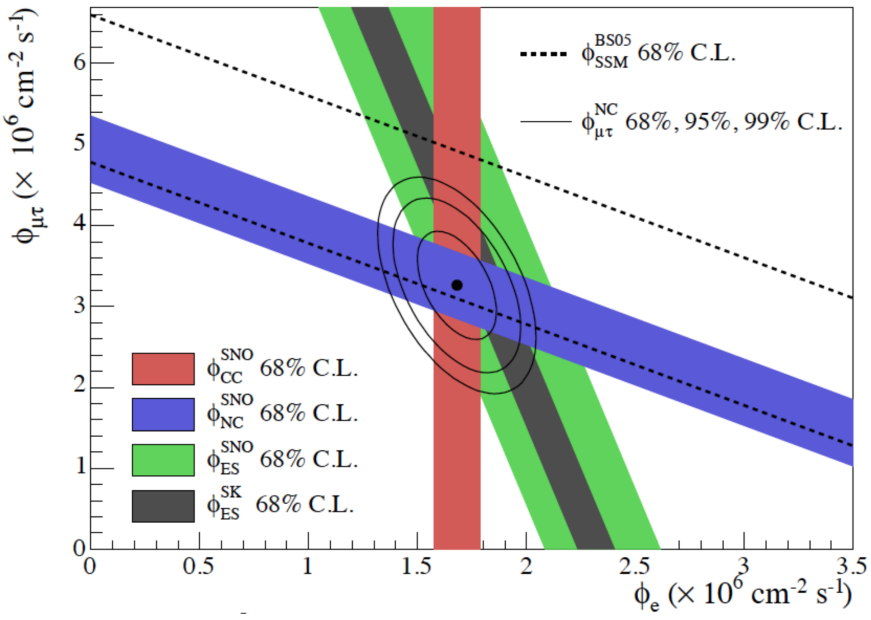

Figure 3.6: final result of SNO experiment on neutrino flux measurement through different currents. Dashed lines represents expected number of neutral current counts in case of no-oscillation scenario according to standard solar model.

The SNO experiment resulted in a strong proof of neutrino oscillations since it succeeded to observe appearance of non-electron flavors of solar neutrino. The only

serious discrepancy remained at this moment was the difference between disappearance of neutrino at different energies. Such behavior cold have been explained by neutrino matter oscillations within the Sun and thus conditions of matter resonance in oscillations of high-energy part of solar neutrino spectrum. In order to understand properly the properties of matter oscillations one should observe solar neutrino spectrum with a threshold that a water Ĉerenkov detector can not afford. But there is also another way is to increase precision of the spectral shape that was done by recent studies of SuperKamiokande detector, which is the largest neutrino detector ever built, even being built not for neutrino purposes.

3.3.3 SuperKamiokande

The SuperKamiokande detector is the successor of Kamiokande detector, that was built in Kamioka observatory of the Institute for Cosmic Ray Research, Japan, Tokyo for the purposed of proton decay search[56]. Despite it's inability to detect proton decay as it is it measured much less solar neutrinos that were considered a background in this rare process study than was expected from solar model and that lead to activities already related to neutrino study. The SuperKamiokande detector started it's operation in 1996 as a detector with 15 times increased mass and designed for the main purpose of proton decay search, but with neutrino program included in the studies. This detector has the total mass of 50 ktons, exceeding SNO by more than ten times and due to design oriented on higher energies was able to perform profound studies of atmospheric neutrinos confirming oscillation also for this neutrino energies. But we will take a closer look mostly on the solar neutrino studies performed by this detector.

detector construction SuperKamiokande is a large cylindrical water Ĉerenkov detector containing 50000 tons of ultrapure water, located 1000 m beneath the peak of mount Ikenoyama in Kamioka. The detector is optically divided into inner detector with mass of 32.5 kton surrounded by 2.5 m water shield, 2 m of which is the active veto outer detector; the structure dividing the detector contains an array of photomultipliers with 11146 ID (inner detector) and 1885 OD(outer detector) large PMTs.(fig. 3.7) Electronic part of such detector becomes complicated due to the large amount of channels and detector size that means relatively large rate of detector events, especially under consideration of relatively thin passive shielding of cosmic muons. Being equipped with classical essential front-end electronics the detector was fitted with an analogue "hitsum" trigger (a trigger counting number of hits within some temporal window with consequent comparison with an established threshold) that was replaced with a computer in the beginning of the last detector phase, phase IV that started in 2008 and actually brought the most valuable results on solar neutrino. Another important task in such massive detectors is

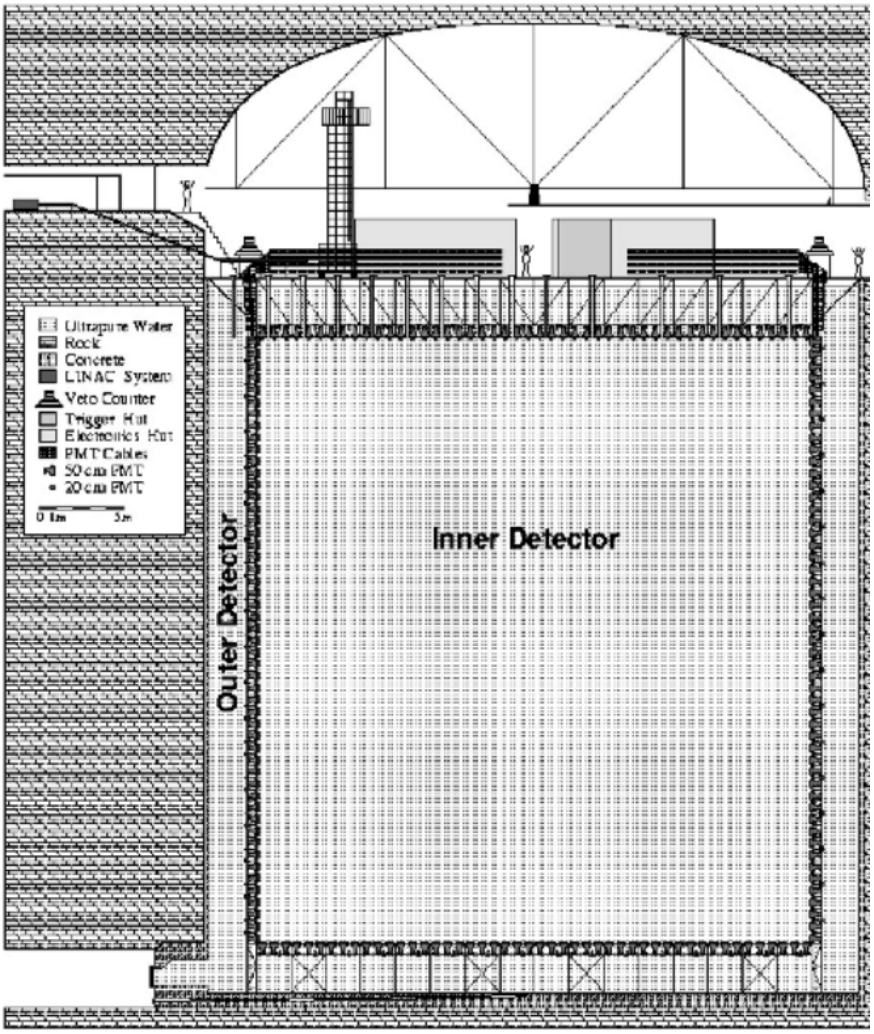

Figure 3.7: Principal scheme of SuperKamiokande detector

keeping stability of light attenuation together with small value of it since it is a very strong source of systematic uncertainty in energy reconstruction. In order to provide it there was installed a purification system continuously purifying and providing 60 tons of purified water per hour to the bottom of the detector. Only in 2010 it was found out that this system was also providing U/Th contamination convection within the detector volume that could mimic low-energy solar neutrino and thus the system was also fitted with a temperature control system keeping the temperature stability at the level of 10 centigrades and minimizing convection inside the detector and resulting in significant decrease of natural radioactivity in the central region of the detector.

event reconstruction Such complicated detector data analysis involves such activity as event reconstruction designed to reconstruct position, direction and energy of each event in the detector. Results of such reconstruction are very helpful in improvement of signal/background ratio due to selection of positions, directions and pulse-shape/light distribution shape discrimination. SuperKamiokande detector reconstructs position of the event vertex through likelihood-based TOF analysis which considers maximum likelihood approach with respect to temporal hit distribution obtained within gamma-calibrations done with Ni neutron capture gammas with known source position corrected by corresponding TOF delays. Directional analysis also considers maximum likelihood approach, where likelihood is constructed within comparison with monte-carlo simulation of Ĉerenkov process. In the last two phases the simulation was performed in an energy-dependent way with consequent consideration of energy dependence that improved precision of direction reconstruction. Energy is derived from the total number of PMT hits within the first 50 ns with consideration of light travel time by it's subtraction. Attenuation was measured with decays of cosmogenically induced isotopes under consideration of axial symmetry of Ĉerenkov light cone and is considered for compensation of light loss. Stability of water transparency is observed within 0.5 %. Also was introduced such parameter as "multiple scattering goodness" that was a likelihood-based parameter allowing to treat direction reconstruction reliability as well as to distinguish multiple scattering, e.g. for beta/gamma discrimination. The detector was calibrated linear accelerator monoenergetic electrons as well as with cosmogenic ^{16}N, that was used for cross-checks of accelerator electron energy. Accelerator energy was also controlled with a germanium detector outside the detector setup. Absorption position dependency was derived in calibration and used in energy scale position-dependent reconstruction; variation of absorption was reaching 60 % with respect to the mean value, so such accounting appeared to be mandatory.

results of the experiment The data obtained in the experiment were originally preselected with treatment by the value of $signal/\sqrt{background}$ that resulted in several limitations on data used in further analysis. One of the points was selection of fiducial volume in order to avoid PMT enclosures and convection regions with relatively high background; The final fiducial volume appeared to have 22.4 tons of water (fig. 3.8) and was reduced to 13.4 tons for the energy region below 5 MeV since this region was stronger affected by natural radioactivity contamination. External gamma-events were separated with application of distance and directionality cuts with respect to PMTs and support structure. Cosmogenic events were removed geometrically by vetoing muon tracks and muon stopping points with consequent reduction of signal efficiency of 20 %. Same time cosmogenically induced

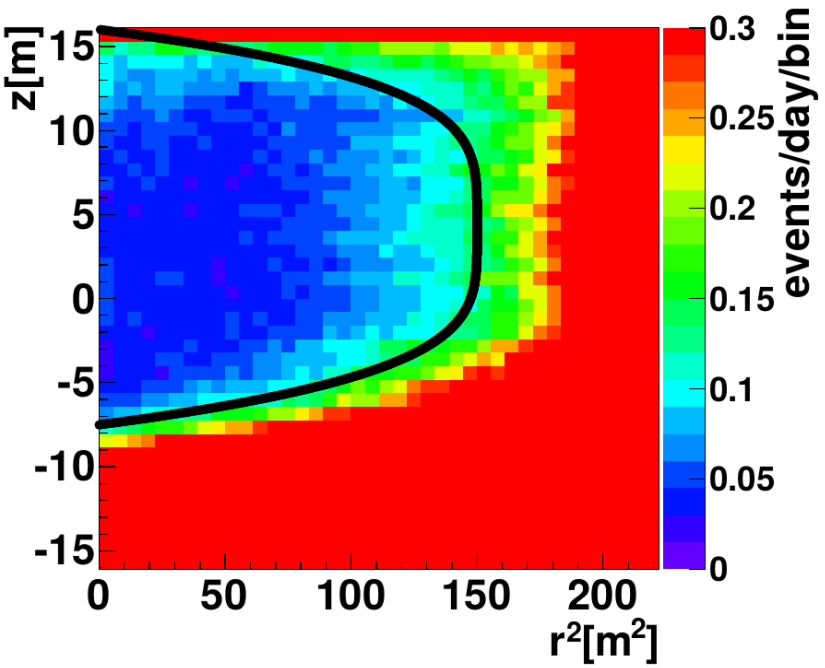

Figure 3.8: fiducial volume selection in SuperKamiokande detector for neutrino studies.

avalanche process regions were removed with geometrical cuts; An advantage of water detector is absence of long-lived cosmogenics allowing to set temporal veto as short as 30 s.

Solar neutrino spectrum was simulated with Monte-Carlo simulation in order to have a description of behavior of energy-to-light transformations as well as light propagation and electronics with the original spectrum taken from [57]. Counting of non-background events gave the total combined neutrino flux of $(2.345 \pm 0.016 \pm 0.036) \times 10^6 cm^{-2} s^{-1}$ under assumption of non-oscillation scenario with the lower energy threshold of 3.5 MeV. Such treatment of the neutrino flux within non-oscillation scenario is possible only with relatively high energy threshold with well-established matter resonance of electron neutrino survival probability where spectral shape is indistinguishable from non-oscillated spectrum and was proposed by SNO and SK in the first measurements. Same time nowadays it looks inconsistent since thresholds are lowering band precision is improving so it make s more sense to produce a neutrino spectrum (fig. 3.9) and compare it with the most probable MSW solution, Large Mixing Angle (LMA). Also was performed a fit with free MSW parameters, shown on fig. 3.10 in combination with day/night neutrino flux variation data that was also detected at certainty level exceeding

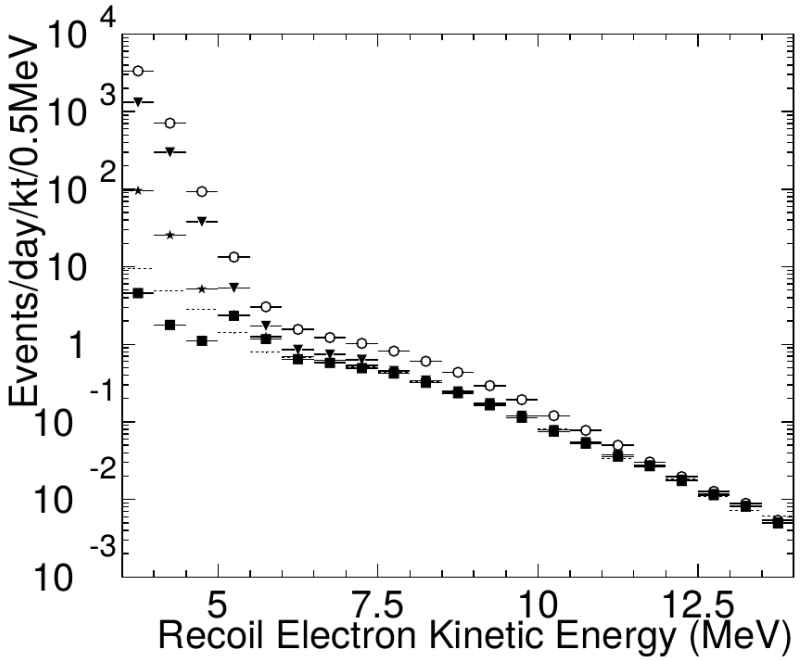

Figure 3.9: neutrino spectrum obtained by SuperKamiokande neutrino detector. Final spectrum of phase IV is represented by solid squares, phase III - by dashed lines. Other lines represent the spectrum on different levels of data selection

99.7 %. The result of the detector gives a good hints for MSW-LMA solution but still allows serious deviations in neutrino matter oscillations due to relatively high lower detection threshold not allowing to probe transition region more profoundly.

3.4 Scintillator experiments: KamLand and Borexino

Ĉerenkov neutrino detectors have a lot of advantages: water could be purified to very high level of radiopurity, oxygen and hydrogen don't have long-lived radioactive components, thus these detectors do not have intrinsic backgrounds, these detectors could be purified to a very high purity level, they have very small light attenuation of light, they are able to reconstruct particle directionality. But they have a very strong limitation which is intrinsic and unavoidable - Ĉerenkov light threshold of 768 keV for electron that sets lower energy threshold at values of around 3.5 MeV due to lack of light on lower energies. And the only way to

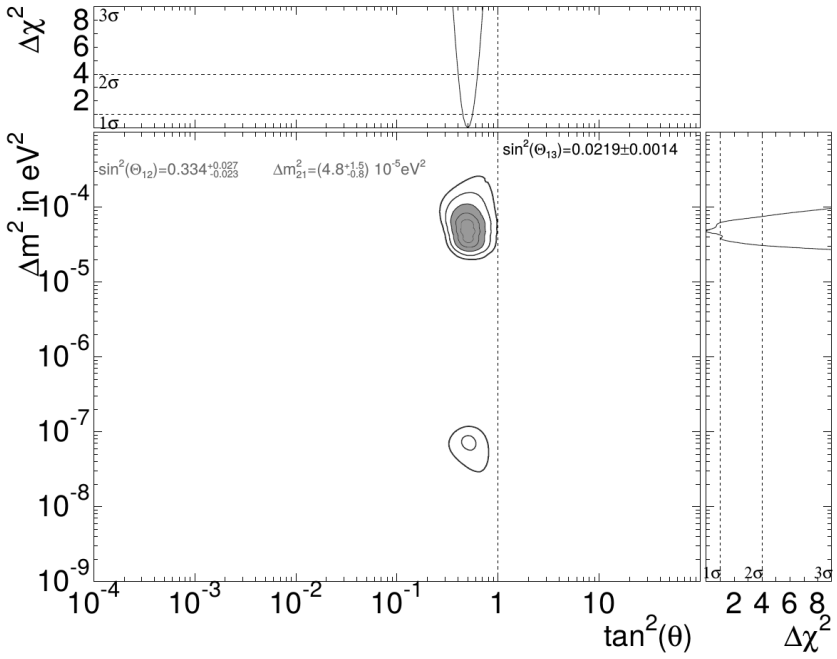

Figure 3.10: MSW theory parameter limits obtained by SuperKamiokande neutrino detector by spectral shape together with day/night variation.

overcome this limitation is to use calorimetric approach, so semiconductors, gas chambers, time-projection chambers, bolometers or scintillators. Among all these approaches the only one that could be created with size feasible for solar neutrino detection is liquid organic scintillator[2]. Thus we have the approach of liquid organic scintillators as a neutrino detector.

In order to be able to detect neutrinos of lower energies such as solar or reactor neutrinos in a real-time experiment, it was necessary to exploit a new experimental method. At the same time it was necessary to conserve the ability of repurification and building a relatively large volume detector. In order to meet these requirements liquid scintillator detectors were considered. This kind of detector have light yield of around 10000 photons/MeV, which is about two orders of magnitude larger than for Čerenkov detectors. Moreover, there is no physical lower limit on the energy of the detected particles. The lower threshold for detection is determined only by radioactive backgrounds and electronic noise.

The physical process underlying liquid scintillator detectors is the scintillation of organic liquids, i. e. the emission of optical photons as a result of electronic

[2]in principle, argon TPC detectors, especially with underground-depleted argon could be used for neutrino detection in future as they are reaching feasible masses, but there are no valid detectors up to the moment

excitation. Ionizing radiation can cause scintillation by primary ionization followed by energy distribution amongst the scintillator molecules. An important point for the detection of scintillation light is transparency of the scintillator itself to its own light. In organic scintillators, this can be achieved due to a difference in transition energies between excited and non-excited states, so that light is re-emitted at a larger wavelength than it was absorbed (so-called Stokes Shift). This makes the absorption of the re-emitted light energetically impossible. Another option is the addition of wavelength shifters which reemit absorbed light at longer wavelengths (lower energy), so that it is not energetic enough to have a strong absorption in the scintillator volume.

Liquid scintillators can be created in a large range of varieties. Additives to the scintillator allow to change various properties, e. g. the emission spectrum, light yield or the cross section for neutron capture. In low-background physics, purification techniques can be applied to the scintillator to remove radioactive impurities. Active background suppression can be employed in liquid scintillators, as well. At the same time it is possible to reach a rather large mass of detector fiducial volume. Energy resolution of liquid scintillator detectors is limited, e. g. compared to semiconductor detectors, bolometers or TPCs. Still, the possibility to obtain a larger mass allows this technique to be competitive.

3.4.1 KamLAND antineutrino detector

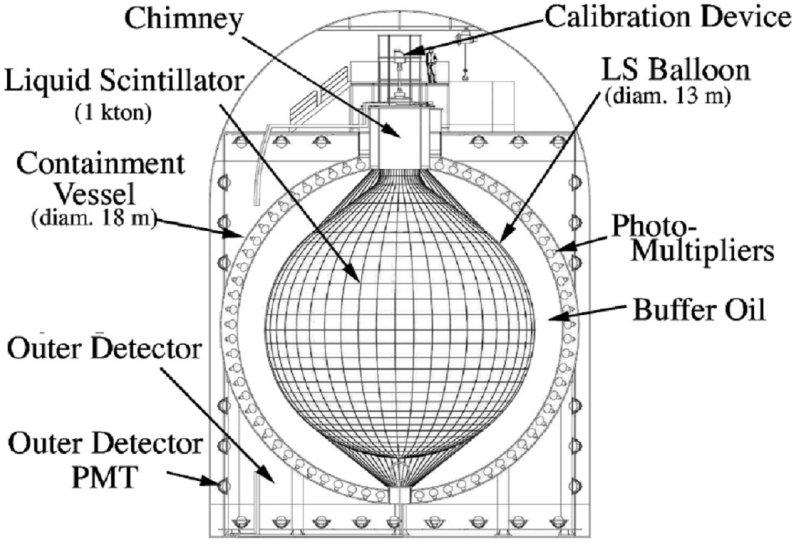

Figure 3.11: Principal scheme of KamLand antineutrino detector

KamLand neutrino detector was designed mostly for the purpose of reactor antineutrino study on baselines around 180 km and started data-taking in 2002. This detector was located in Kamioka laboratory and surrounded by several power nuclear reactors bringing parameters of antineutrino matter oscillations that are compatible with parameters obtained in solar experiments, e.g. SuperKamiokande. But once again our interest is directed to detection of solar neutrinos with this detector.

The detector consists of a plastic film balloon with diameter of 13 m containing liquid scintillator. The balloon is surrounded with 18 m stainless steel sphere, fitted with 1879 PMTs; the space between steel sphere and the balloon is filled with purified mineral oil and serves the purpose of shielding the scintillator from external radiation. The sphere itself is contained inside 3.2 kton cylinder filled with pure water and working as a Ĉerenkov outer detector (fig. 3.11).The detector appeared to have contamination levels of $883 \pm 20 \mu Bq$ of ^{85}Kr and $58/4 \pm 1.1 \mu Bq$ of ^{210}Pb, that made low energy neutrino studies quite sophisticated. After the purification these contents were reduced by six and four orders of magnitude respectively, being still relatively high.

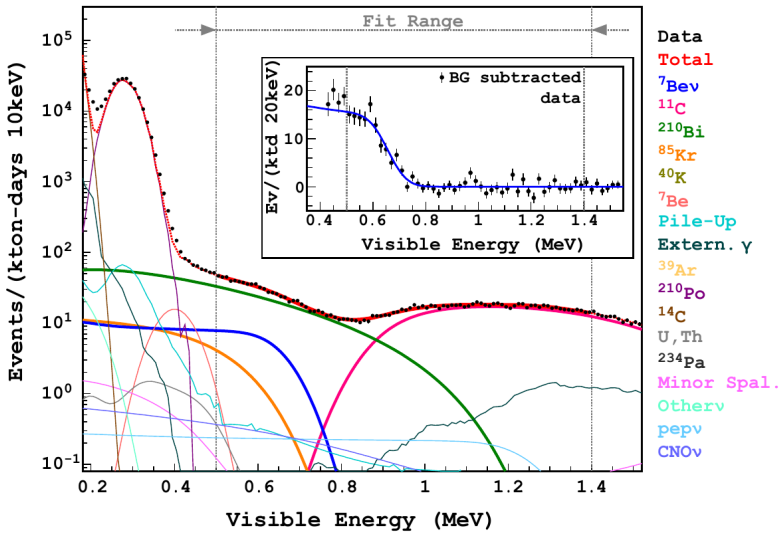

Figure 3.12: final spectrum of KamLand detector used for ^{7}Be neutrino measurement, collected only in the cleanest cubes of the detector fiducial volume.

Data selection was performed through performance of radial cut according to TOF position reconstruction, charge-based discrimination of cosmic muons with special treatment of high-charge muons as more probable cosmogenic background producers, as well as geometrical fast-coincidence analysis, removing events too

close in space and time in order to suppress fast coincidence chains, e.g. ^{214}Bi-^{214}Po. The event selection also included vertex-time-charge fit quality test for the sake of elimination of noise and pile-up events[3]. The detector was selected in cubes and short data-taking intervals in order to select the time-space part of the detector with the lowest background rate and thus to improve signal/noise ratio to background nonuniformity inside the detector. With all the measures it was succeeded to measure neutrinos from ^{7}Be as $582 \pm 94(kton * day)^{-1}$ that corresponds to $(5.82 \pm 1.02) \times 10^{9} cm^{-2} s^{-1}$ (the numbers correspond to 0.862 keV line only)[58]. The same time the detector succeeded to register neutrinos from ^{8}B, but the threshold of such detection was limited to 5 MeV due to thoron contamination and thus this measurement is worse than the one performed by SK both by means of threshold and precision, giving only $(2.7 \pm 0.4 \pm 0.1) \times 10^{6} cm^{-2} s^{-1}$ under assumption of non-oscillation scenario [59]. Beryllium neutrino result is also hardly a success since a more precise measurement was done several years earlier by another scintillation detector - BOREXINO. Still, KamLAND has the honor of being the first large liquid scintillator detector that started data-taking plus it has produced outstanding results in antineutrino detection part where high purity is not of primary importance.

[3]pile-up stands for two simultaneous scintillation flashes from two different events in the detector

Chapter 4

Borexino neutrino detector

4.1 Motivations for Borexino

The original concept of the Borexino detector was proposed in late 80's by R.S Radavan as a scintillator neutrino detector that would have been able to detect low-energy neutrinos covering energy range of gallium observatories, but with an ability to perform neutrino spectrometry. Special interest was directed to low-energy part of neutrino spectrum, below 1 MeV, opening possibilities for more profound studies of neutrino, including spectrum distortion related with non-standard neutrino interactions. The original name stands for Boron Experiment (BOREX) corresponding to a possibility of detection antineutrinos produced due to spin-flip in the solar matted in case neutrino is a Majorana particle with inverse beta-decay on proton producing neutron with consequent capture [61]. Such project required an outstanding level of radiopurity that was hardly believable to be achieved. In order to demonstrate existence of a technology in 1993 was built BOREXINO CTF(Counting Test Facility), a small prototype neutrino experiment, that demonstrated radioactivities of thorium below 1.7×10^{-16} g/g, radon at the level of $(1.9 \pm 0.4) \times 10^{-15}$ g/g and ^{40}K at the level of 45 ppm (treated with delayed coincidence and spectral analysis respectively) that was actually even below the levels that were expected. The CTF detector succeeded to perform several neutrino measurements itself [62] and demonstrated that a scintillator could be purified enough to perform low-energy solar neutrino spectroscopy. That meant the start of the actual Borexino neutrino detector program. One interesting point is that it was decided to refuse boron contamination and to concentrate on actual electron recoil spectroscopy as it is due to larger cross section, so boron remained only in the name of the experiment, but is not related to the actual experimental apparatus.

4.2 Borexino detector construction

The leitmotiv of the whole Borexino project is purity. Radiopurity was and is the main advantage of this experiment and the only property that allows it to measure solar neutrino spectrum with comparatively high precision.

The detector design is based on a concept of graded shielding, so radiopurity level is increasing from outside and inside the detector. The main housing of the detector is a cylinder with hemispheric top ending and has diameter of 18 and height of 15.7 m and is made of stainless steel. Inside is located a stainless steel sphere made fixed by stainless support structure with diameter of 6.75 m and thickness of 8 mm. The space between the outer barrel and stainless steel sphere is filled with ultrapure water and is equipped with 300 8-inch PMTs that serve the purpose of Ĉerenkov muon veto and is called outer detector (OD). On the inner side of the stainless steel sphere (SSS) are located 2209 8-inch PMTs of the inner detector (ID) and the volume is filled with pseudocumene (C_9 H_{12}). Within the inner detector there are located two transparent spherical nylon vessels with refractive index close to refractive index of pseudocumene with radii of 5.5 m (radon barrier) and 4.25 m (inner vessel) located concentrically with stainless steel sphere.(see fig.4.1) The scintillator volume inside the inner vessel has admixture of PPO that works for the purpose of creating Stokes shift. Scintillator outside the inner vessel was originally planned to have no admixture but was finally filled with DMP that quenches light production decreasing affection of high-energy cosmic muons on the data-taking procedure. The detector is equipped with different kinds of service machinery allowing various service operations, such as

- temperature sensor system
- laser PMT calibration system
- piping for inner and outer detector filling and purification
- calibration system that could be inserted from above and move a source around the detector inner vessel
- CCD system for an additional positioning possibility
- pit inside SSS with external access for external gamma-source calibrations
- pit under the detector with a railway designed for the sake of neutrino source calibration
- purification plants, storage vessels and other external equipment

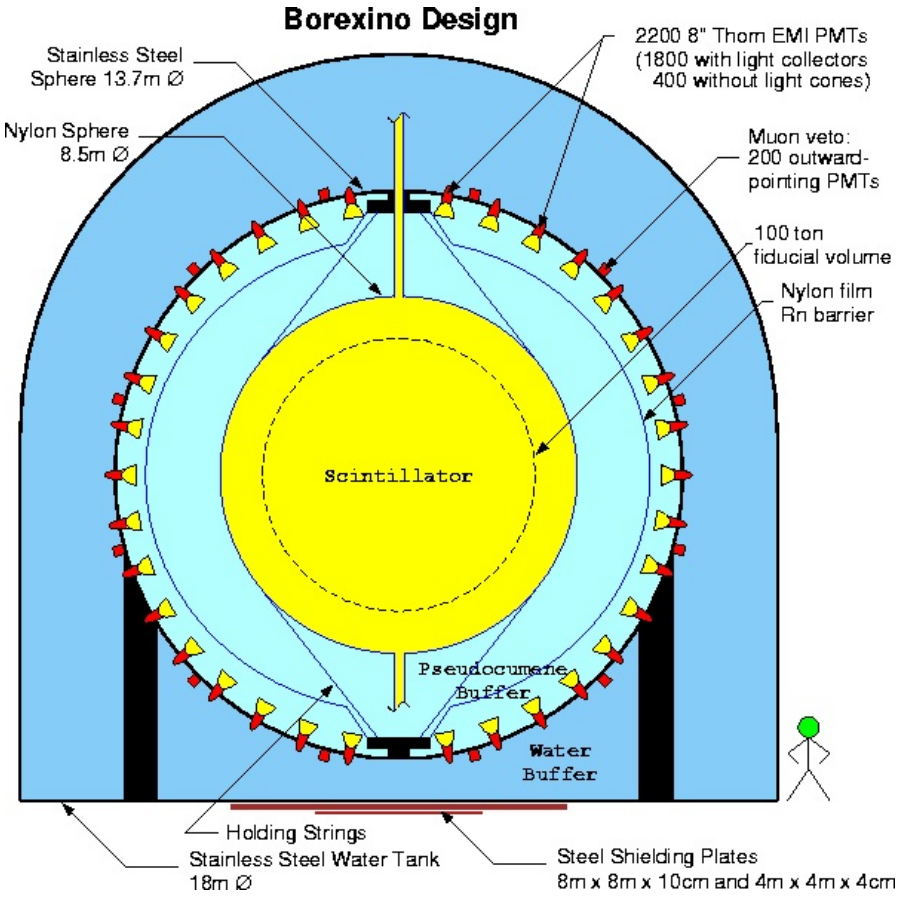

Figure 4.1: Principal scheme of Borexino neutrino detector

4.2.1 Construction materials

Construction of the detector was performed according to a design project containing radioactivity level requirements that are tabulated in 4.2.1. Such approach means careful selection of materials combined with various test of construction material samples. Cosmogenically produced ^{14}C (endpoint of 144 keV) is a quite important background at low energies reaching 400 keV due to pile-up events and effects of detector resolution. Its level was minimized due to careful selection of old petroleum with $^{14}C/^{12}C$ ratio of 10^{-18} that is a million times lower than a typical ratio for naturally occurring carbon; The level could be easily measured since it is one of the main backgrounds in any organic material that practically blocks any activity below 150 keV setting the lower energy threshold.

Vessel production was another issue of the detector crucial for any further activities. No factory nylon was able to fulfill the radiopurity requirments of the project, thus the nylon film was taken with the minimum thickness achievable

The design radiopurities of the major BOREXINO detector components.

Components	^{238}U (g/g)	^{232}Th (g/g)	^{nat}K (g/g)	other
Stainless steel tank wall	$1{\cdot}10^{-8}$	$1{\cdot}10^{-8}$	$1{\cdot}10^{-5}$	
Water buffer	$1{\cdot}10^{-10}$	$1{\cdot}10^{-10}$	$1{\cdot}10^{-7}$	
Water CTF shield	$1{\cdot}10^{-13}$	$2{\cdot}10^{-13}$	$2{\cdot}10^{-10}$	^{222}Rn – 1 μBq/kg
Stainless Steel Sphere	$2{\cdot}10^{-10}$	$1{\cdot}10^{-10}$	$3{\cdot}10^{-7}$	
PMTs	$3{\cdot}10^{-8}$	$1{\cdot}10^{-8}$	$2{\cdot}10^{-5}$	
PC buffer	$1{\cdot}10^{-15}$	$1{\cdot}10^{-15}$	$5{\cdot}10^{-12}$	
Nylon film for inner vessel	$5{\cdot}10^{-12}$	$2{\cdot}10^{-11}$	$1{\cdot}10^{-8}$	^{226}Ra – 12 μBq/kg
Scintillator	$1{\cdot}10^{-16}$	$1{\cdot}10^{-16}$	$1{\cdot}10^{-14}$	^{14}C/^{12}C – $1{\cdot}10^{-18}$
N_2 for scintillator sparging				^{222}Rn – 1 μBq/m^3

Table 4.1: Radioactivity levels design requirements of various constructions of Borexino detector

that required special design due to requirements of mechanical durability and the production of the film was organized in the underground facility clean room with careful selection of basic materials giving unique radiopurity level of materials.

Construction structures appear to be another serious demand in the detector construction. Radioactivity levels were measured within three different laboratories on material samples in order to provide radiopurity level required. Compiled results of the material studies are demonstrated on 4.2.1

Radon levels were treated with special low-background emanation setup, transporting radon to charcoal trap with helium flux where it was absorbed and then measured in order to control the low-radioactivity level.

Another important part pf the detector was nitrogen, used for stripping in purification plant that finally allowed the unique radiopurity level of the detector. That meant minimization of radon content in the nitrogen itself so it meant usage of special pure nitrogen in the system.

Apart from germanium, other approaches were used in admixture level determination, e.g. plasma spectrometry [63]. All the measures were taken for providing higher possible radiopurity level inside the inner vessel and reaching really unique level of radiopurity. Such careful detector construction was nevertheless not enough for neutrino studies as it was, so the detector design considered minimization of solid materials inside the scintillator volume and gradual decrease of radioactivity to the lowest level in the actual fiducial volume in the detector. The only part of the detector that was unavoidably undermining the efforts were the PMTs that were factory-made and contained very large (compared to the rest of detector construction materials) contamination of natural radioactivity. The only way to work this out was the selection of less radioactive PMTs; still they be-

	^{226}Ra (mBq/kg)	^{238}U (g/g)	^{228}Th (mBq/kg)	^{232}Th (g/g)	^{40}K (mBq/kg)	^{nat}K (g/g)	^{60}Co (mBq/kg)
PMT inner parts							
Ceramic plates for dynodes structure	170± 50	(1.4±0.4) 10^{-8}	310±60	(8±1) 10^{-8}	960±450	(3±1) 10^{-5}	< 40
Dynodes	< 280	< 2.3 10^{-8}	450±163	(1.1±0.4) 10^{-7}	< 240	< 7.6 10^{-6}	< 290
Aluminum for dynodes structure	1190±100	(9.6±0.8) 10^{-8}	980±80	(2.4±0.2) 10^{-7}	2800±600	(9±2) 10^{-5}	< 80
Metallic comp. for dynodes structure	< 62	< 5 10^{-9}	< 20	< 5 10^{-9}	< 340	< 1.1 10^{-5}	< 12
Glass							
Sand for glass manufacturing	40±3	(3.2±0.3) 10^{-9}	<3.1	< 7.6 10^{-10}	< 25	< 8.1 10^{-7}	< 1.6
ETL low radiation glass	820±230	(6.6±1.9) 10^{-8}	130±12	(3.2±0.3) 10^{-8}	500 ±120	(1.6±0.4) 10^{-5}	
Base glass	520±90	(4.2±0.7) 10^{-8}	410±90	(1±0.2) 10^{-7}	226000±6200	(7.3±0.2) 10^{-3}	
PMT ancillary parts							
Mu-metal	57±20	(5±2) 10^{-9}	< 27	< 6.6 10^{-9}	< 180	< 5.8 10^{-6}	< 9
Phenolic resin coated sample	86±12	(7±1) 10^{-9}	610±203	(1.5±0.5) 10^{-8}	< 400	< 1.3 10^{-5}	< 10
Voltage divider printed circuit board	170±60	(1.4±0.5) 10^{-8}	80±40	(1.9±1.0) 10^{-8}	770±360	(2.5±1.2) 10^{-5}	
Complete voltage divider	680±30	(5.5±0.3) 10^{-8}	320±20	(7.9±0.6) 10^{-8}	3200±320	(1.0±0.1) 10^{-4}	< 15
Master Bond EP45HT for PMT sealing	< 40	< 3 10^{-9}	< 24	< 6 10^{-9}	< 310	< 1 10^{-5}	< 11
Cable and connectors							
Complete RG213 Suhner cable	22±6	(1.8±0.5) 10^{-9}	< 20	< 5 10^{-9}	< 140	< 5 10^{-6}	
Complete Jupiter connector	56±15	(4.5±1.2) 10^{-9}	2.4±1.2	(6±3) 10^{-9}	< 300	< 1 10^{-5}	< 20
Neoprene connector boot	1400±400	(1.1±0.3) 10^{-7}	1300±300	(3.1±0.7) 10^{-8}	1600±250	(5.1±0.8) 10^{-5}	< 18
Jupiter connector O-rings	1400±340	(1.1±0.3) 10^{-7}	1200±370	(2.9±0.9) 10^{-7}	7900±300	(2.5±1.1) 10^{-4}	
Optical fiber							
Teflon for optical fibers coating	28±4	(2.3±0.3) 10^{-9}	< 6	< 1.4 10^{-9}	< 60	< 2 10^{-6}	< 2.4
Kevlar	430±80	(3.5±0.6) 10^{-8}	< 140	< 3.4 10^{-8}	< 870	< 2.8 10^{-5}	< 68
EPO-TEK 353ND resin	< 47	< 4 10^{-9}	< 24	< 6 10^{-9}	< 320	< 1 10^{-5}	< 17
Stainless steel samples							
AISI304L for SSS	4.6±0.9	(3.7±0.7) 10^{-10}	11.4±1.1	(2.8±0.3) 10^{-9}	< 14	< 4.5 10^{-7}	6±1
Piping steel	< 14	< 1.1 10^{-9}	< 10	< 2.5 10^{-9}	< 34	< 1.1 10^{-6}	14±4
Steel for flanges	6.2±1.2	(5±1) 10^{-10}	6.5±1.6	(1.6±0.4) 10^{-9}	< 13	< 4.2 10^{-7}	14±1
Steel for storage vessel	17±3	(1.4±0.2) 10^{-9}	3.8±2.6	(9.3±6.4) 10^{-10}	< 19	< 6 10^{-7}	12±2
Steel TK3B for storage vessel	5±1	(4±1) 10^{-10}	5±2	(1.2±0.5) 10^{-9}	4±2	(1.3±0.6) 10^{-7}	46±3
Steel foil for Rn emanation test	0.6±0.2	(5±2) 10^{-11}	0.2±0.1	(5±3) 10^{-11}	1.8±0.6	(6±2) 10^{-8}	18±1
Miscellaneous							
Nylon Curbell 5, 6" rod for caps CTF	< 0.6	< 0.5 10^{-11}	< 0.5	< 1.2 10^{-10}	< 3	< 1 10^{-7}	< 0.2
Nylon 2.5" Pipe for IV connection	< 1.2	< 9.3 10^{-11}	< 0.9	< 2.2 10^{-10}	< 18	< 6 10^{-7}	< 0.4
Nylon fishing line, monofilament.	< 1.1	9 10^{-11}	< 0.6	< 1.5 10^{-10}	4.8±2.5	(1.6±0.8) 10^{-7}	< 0.4
Tensylon rope for IV	< 0.3	< 2.4 10^{-11}	< 0.3	< 7 10^{-11}	15±2	(4.7±0.5) 10^{-7}	< 0.1
SilicaGel 60 for purification column	100±50	(8±4) 10^{-9}	< 160	< 4 10^{-8}	< 600	< 2 10^{-5}	< 90
Charcoal for radon adsorption	< 300	< 2 10^{-8}	< 500	< 1 10^{-7}	< 2000	< 6 10^{-5}	< 100

Table 4.2: Radioactivity levels of various constructions of Borexino detector tested on material samples with HPGe detectors

come the main radioactivity source in the detector, bringing the most of external gamma-background in the spectrum.

4.2.2 Liquid handling

Liquid handling is one of the most important parts of the detector operation organization since it deals with internal backgrounds that are intrinsically indistinguishable from neutrino-induced signal. The list of internal backgrounds in the fluid starts from ^{14}C that was suppressed by selection of old oil and can't be modified since carbon enters chemical structure of the scintillation itself. All the other backgrounds are admixtures and include noble gases (radioactive krypton, argon

and radon) as well as ^{40}K, Uranium and thorium chains, long-lived ^{210}Pb with its daughters, especially ^{210}Po that could be chemically binded to the scintillator chemical structure creating metal-organic composition and other impurities that could shadow neutrino electron recoil spectrum measurement.

filling the detector Purification of the scintillator used in the detector operation should be done with intermediate purification since the detector is to be filled with the purest scintillator possible [64]. Before filling the scintillator all surfaces that could be in contact with fluids were carefully cleaned, filled with nitrogen and sealed until active operation. Before filling the detector, vessels were inflated with high-purity synthetic air with reduced contamination of noble gas impurities; the synthetic air was mixed with sulfur fluoride in order to perform a check on possible leakages. After performing this check, the air was replaced with specially-developed nitrogen delivered in liquid form and evaporated inside the detector. The next step of filling the detector included filling with high-purity deionized water, stripped with nitrogen before filling the detector. Water was then displaced from all three volumes with purified scintillator and buffer solutions. The scintillator was delivered by a special tanker developed for this purpose and used only for pseudocumene transport. Purification included redistillation of the scintillator, nitrogen stripping with low-background nitrogen and humidified to 70% RH with ultrapure water. The prepared scintillator was mixed in-line with corresponding admixture (PPO/DMP) and brought into the detector. The scheme of detector filling is demonstrated on fig. 4.2

repurification system of the detector Since Borexino detector is designed for long operation duration it can't be just filled once since temperature and pressure conditions vary with time and relative pressure should be kept within specific limit with some excess from inside in order to keep shape of inner vessels. Pressure differentials are adjusted by setting appropriate levels in standpipes on top of each volume. Each standpipe goes to the liquid hear tank located in the clean room on the top of the detector. Adjustment is performed trough additional hydrostatic pressure tuning, while all tanks are connected to a common nitrogen blanket providing equal pressure in each tank. The pressure gradients are limited to the value of 5 cm of water volume by construction of inner vessels and that means specific care in pressure operation.

There are several ways of operating vessel and buffer repurification. Repurification system is represented with a continuous loop(fig. 4.3) that considers possibilities of nitrogen stripping as well as water extraction and distillation. This system is also planned to be equipped with a system providing partial distillation or rectification in future. A full campaign of water extraction campaign was

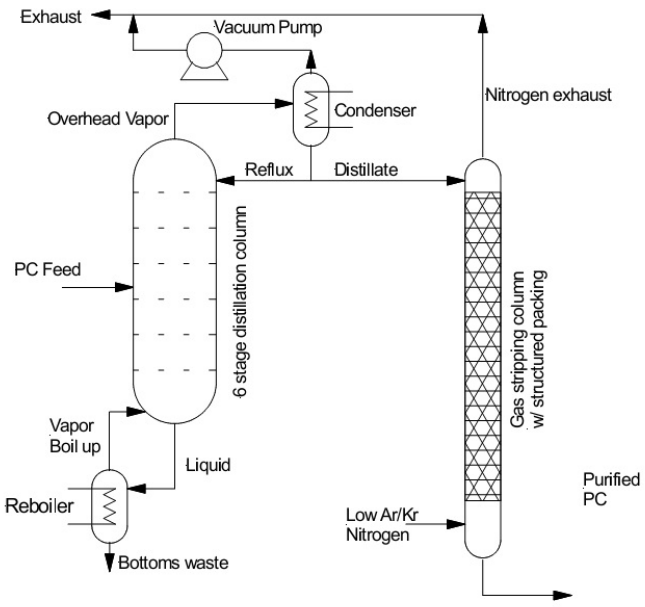

Figure 4.2: Principal scheme of Borexino detector scintillator preparation system

performed in 2010 and resulted in outstanding improvements, such as

- radon level in inner 3.5 m sphere decreased by factor of 60 giving around 200 events in 4 years
- thorium level decreased to the level below observational abilities corresponding to 12 events at 95% C.L. in 4 years
- ^{210}Pb(detected by decay of ^{210}Bi) decreased to the level of around 20 counts/day/100 t decreasing by more than factor of 2 with demonstration of even better suppression possibility
- ^{85}Kr level decreased to the level limited by 5 counts/day/100 t at 95 % C.L.

The only background that was not reduced is ^{210}Po that is probably chemically binding to the scintillator and could be removed either electrochemically, either with partial distillation or rectification. This is more about the matter of future of the detector. Apart from lead and polonium (polonium is mentioned separately due to absence of equilibrium and relatively long half-life of 138 days) there are practically no significant internal non-cosmogenic backgrounds in the detector spectrum and that is a great victory of detector purification. That makes the detector a unique piece of medium with the lowest radioactivity level on our planet.

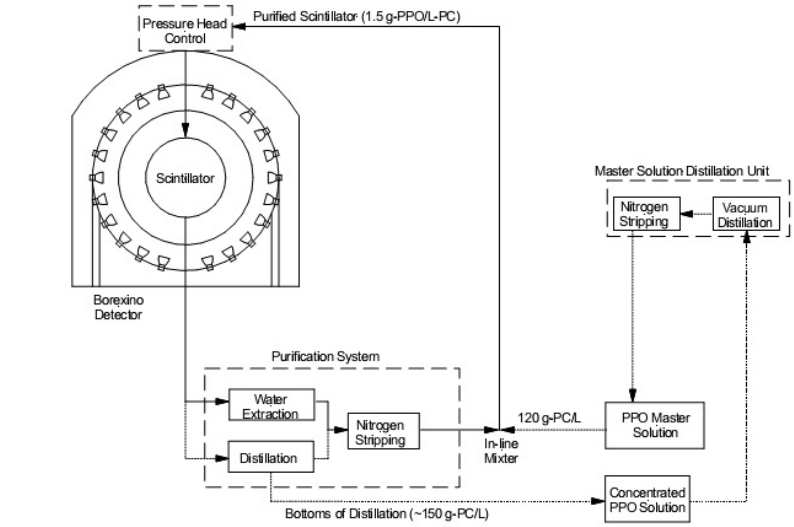

Figure 4.3: Principal scheme of Borexino detector repurification system

4.2.3 Borexino electronics construction

Having 2209 PMTs located uniformly over the SSS the detector obtains plenty of information about each scintillation flash in the detector considering temporal and amplitude information from such a large number of channels. That makes the total detector electronics quite sophisticated structure that has to be gathering and systematizing scintillation signal into digital form.

Each PMT is equipped with single-output voltage supply with increased voltage gradient between two first pairs of dynodes with resistance of dynode step of 1 $M\Omega$, minimizing charge losses in voltage divider itself. The system provides derived (by CR chain) signal with almost perfect pole-0 compensation providing practically monopolar signal in the output, that is passed to the front-end. High voltage could be regulated in range of 1100-2000 kV allowing application of voltage finetuning for channel properties equalization.

The front-end electronics considers shaping and integration of the signal and provides two signals, inverted amplified raw PMT signal and shaped integrated signal that could be used for temporal and amplitude analysis respectively. Each channel is replicated 8 times on each front-end board that gives 160 channels in 20 boards per VME-standard crate. Each board has a single control block. The timing signal is analyzed by a programmable dual-threshold discriminator (timing-amplitude threshold levels are applied decreasing effect of amplitude effects on temporal information). Dead time of this discriminator is of order of 140 ns that means that in case of two hits in the channel happen, they are treated as a single

hit with cumulative charge. Each hit registration starts a couple of 30-ns pulses with 80 ns separation that is used as primary level trigger. Temporal information is obtained by 20 MHz clock 16-bit counter (Gray counter) and digitized amplitude of saw-shaped (triangular) signal synchronized with the clock by 8-bit ADC. The amplitude data is integrated by a gateless integrator and considered within 80 ns from hit time by digitizing "base" and "peak" with 8-bit digitizer. Integrator resets automatically after each pulse ant thus does not have any dead time at all and the charge is reconstructed as

$$Q = G(V(t_0 + 80ns) - V_{off}) - (V(t_0) - V_{off}),$$

where G is the integrator gain of 129mV/pC and V_{off} is DC offset intentionally added in order to maintain signal polarity.

The detector is equipped with a classical "hitsum" trigger with a specific threshold of number of PMTs fired within a temporal gate of 48-99 ns (in data taking the values were set to 60/99 ns with 25/20 PMTs fired in different periods data taking). At each edge of intrinsic clock each crate counts the number of channels exceeding threshold occurred in three previous clock cycle, where the clock is establishing the time window of the trigger. The digital numbers are provided and summed up in order to decide triggering. As an addition, there are some other service triggers, such as synchronized with laser calibration system of the detector, pulser trigger designed to test front-end electronics and random trigger with frequency of 2 Hz done for dark current control. A special trigger with 100 times longer DAQ gate(1.6 ms vs 16 μS) is used after each muon event, recognized by OD (With typical threshold value of 6 PMTs fired).

The data are recorded in binary form considering overall hit temporal and amplitude information with granular basis of a trigger gate for all trigger types, related to ID and OD signals as well as service trigger and is recorded on HDD storage as well as on magnetic tape backup system. Practically, data analysis is performed starting from this binary files . Each run correspondes to 21600 s of data taking in case it was not stopped due to some external reasons; granularity of data allows to apply validation procedure on run basis allowing to exclude runs with inappropriate data quality.

4.2.4 Detector calibration

Between two data-taking phases the detector was calibrated with radioactive sources [65] in order to check all approaches applied in data analysis and for the sake of better understanding the detector response. The calibration campaign is involving several steps of calibration:

- external gamma-calibration with thorium source. This operation allowed to cross check simulations and modeling of gamma-propagation as well as energetic data for external gamma

- Radon source calibration that was used for establishing position reconstruction as well as for alpha-response of the detector

- Energetic calibration. This point is very important and includes a lot of sources supposed to cover the spectrum. Am-Be neutron source covered with steel gave several gamma-lines related with neutron capture on different nuclei providing energies up to 9 MeV. The same time the detector was calibrated with beta-decaying sources allowing to understand the detector response for the most interesting interacting particle such as an electron

The calibrations were performed with a large variety of positions within inner sphere of 3 m allowing to understand positional reconstruction. Positions were controlled through optical CCD cameras, which provided modest reconstruction precision. As for the purpose of position reconstruction uncertainty studies were performed some measurements with source located on vertical axis fixed by a precisely measured rod, that allowed to estimate uncertainty of vertical coordinate reconstruction, which could be assumed for other axis, which have actually less probability to have a shift since temperature and pressure gradients as well as nonuniformity of active PMT distribution are oriented mostly along Z-axis.

Calibration data are widely used for all studies related with detector simulation and data analysis techniques, such as position and energy reconstruction, data selection, pulse-shape discrimination etc.

4.3 Borexino generic data processing

4.3.1 Routine calibrations

Since the detector is a large volume of liquid it could have transparency nonuniformities that would be also time-dependent. Large number of channels and PMTs involves a necessity to control all the properties of data acquisition system as well as optical properties of the fluid.

Electronic calibrations are performed by setting a pulse to the test inputs of front-end electronics together with a pulse going onto the BTB(Borexino Trigger Board) that triggers an event window with all channels getting same signal and allowing to perform calibrations of channel basis. Optical calibration is also quite important. As for this purpose was developed a system including The following parts(fig. 4.4):

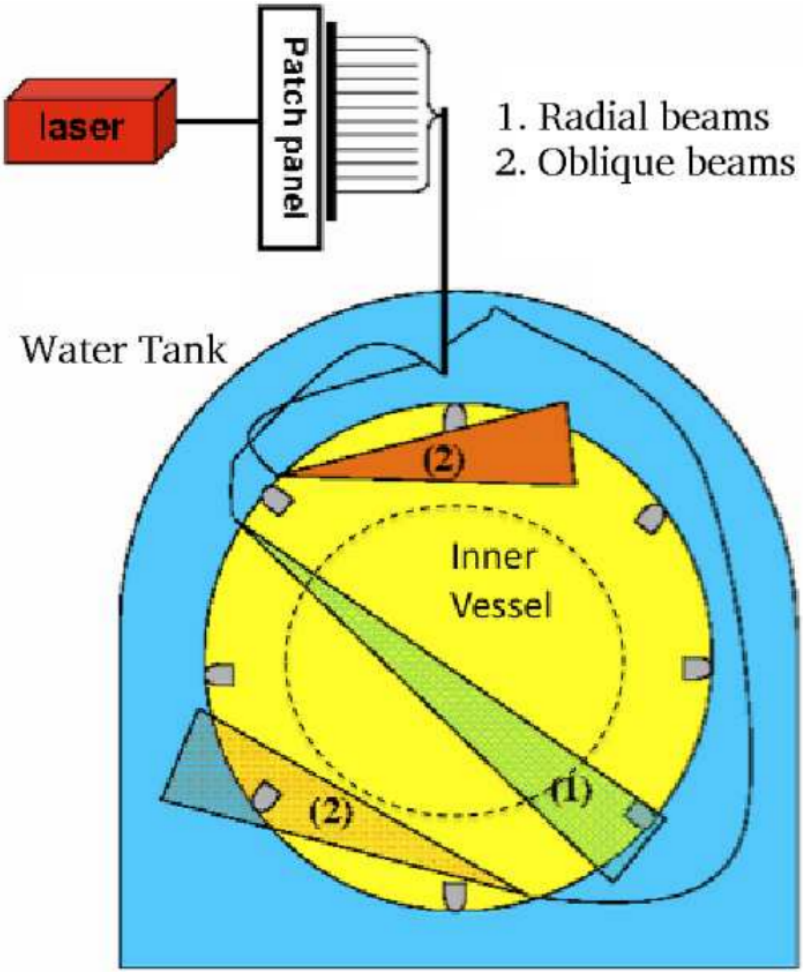

Figure 4.4: Scheme of laser calibration system used for routine detector calibration

- Two lasers, a semiconductor diode laser with wavelength of 394 nm as well as a solid state laser with wavelength of 355 nm

- 31 fibers entering SSS at 31 different position and working by single fiber at a time collecting light coming from a single point on a sphere

- feedthroughs of two types: one crossing the whole sphere by the diameter and another providing light non entering inner vessel with active scintillator. Light crossing distance is varied in range between 2.5 and 7.88 m. Due to collimation of the system it is possible to separate light coming from reemission in the scintillator from the direct laser light

The system allows to calibrate the gains separately from optical properties and from the scintillator together with PMT intrinsic gains and to equalize data-taking channels on software level, allowing to reconstruct charge in terms of photoelectrons with channel-dependent calibrations on run basis.

Speaking about software level of data processing, when we have obtained the channel calibrations together with hit timing we are going into the direction of such fundamental software object as "decoded hit". The only point remaining is so-called "decoded time" that is supposed to consider also time-of-flight correction of hits timing for which one needs to know the event position.

Since the detector works on a specific DAQ gate corresponding to a single triggering and reaching 1.6 ms in the special case of aftermuon DAQ window, our "event" does not correspond to a single scintillation flash, but to a single triggering. An alternative name is "cluster" that corresponds to a cluster of hits exceeding some limit - but already decoded hits, so ones obtained after Gray crossing compensation. In this case the detector has a purely software level threshold of clusterization algorithm. All the further analysis is hold on cluster basis rather then just events, event number remains only for data granulation purpose. One should consider that an event could have no clusters, e.g. in case of random trigger.

Position reconstruction

Position reconstruction is a fundamental step in data analysis since it allows to get the physical scintillation shape after time-of-flight correction as well as to separate cleaner inner regions, perform geometrical coincidence analysis, treat the data quality and a lot more. Reconstruction is done on cluster basis where cluster is expected to be a single scintillation flash (in some cases it is not so, e.g. in pile-up clusters). Position reconstruction approach is based on maximization of likelihood of the hit temporal distribution to expected one after compensation by time of flight to each PMT from reconstructed point, namely,

$$L(x,y,z) = \sum_{all\ hits\ within\ cluster} -\log(A_{expected}(\delta_t(x,y,z), Q_{hit})), \qquad (4.1)$$

Where $\delta t(x,y,z)$ is light propagation time from point (x,y,z) to the PMT position. Such minimization is multiparameter and sometimes underset since the are a lot of effects that could potentially worsen the reconstruction, such as

- reflections that result in a delay different from expected for straight flight path, accounted in the model
- pile-ups with low-light buffer events; despite light quencher decreases the light by factor of ten, some photons coming from ^{14}C decay electrons or ex-

ternal gammas interaction in the buffer could still reach PMTs in correlation with analyzed scintillation cluster with relatively high probability

- Radioactivity in glass. Since PMT glass is one of the main U/Th sources the activity is enough to make affection through direct interaction with photocathode; that create an avalanche of electrons that produce very high charge in the PMT. Such hits are expected with mean value of around 1 per cluster and could affect reconstruction of low-light clusters

- variations in charge. Different charges of hits should be treated differently (since hit separation is at least 80 ns it corresponds to two photons within this time and one should simply take temporal distributions for n photons arriving, see fig. 4.5)

- phase speed of light in the fluid is different from c and one should account for some empirically derived effective refractive index.

- dark rate pile-ups could affect low-light clusters reconstruction as well

All these factors make reconstruction quite a sophisticated thing to do. Nevertheless, there are ways to struggle this. Presence of unphysical minima leads us to importance of minimization starting point, that means development of less precise, but more reliable algorithm. A role of such algorithm could be played by charge baricentration, so simple averaging of PMT positions(positions of centers of photocathodes for instance) weighted by collected charge in the cluster. Such approach gives resolution of around 1 m for an average cluster but the same time it is a very reliable approach.

In order to decrease effects of pile-ups, including buffer events and dark hits one should consider limitation of the cluster part duration in the likelihood computation; the same time usage of the very first part of the cluster would decrease affection of reflections since all reflected photons are delayed more by several nanoseconds. The same time taking too few first hits leads to decrease of precision by statistical algorithms that leads to usage of specific tuning of the part of the cluster used by the reconstruction algorithm. Technically, it is done by making expected signal PDFs (probability distribution functions) limited in duration and is tuned for reliable reconstruction on energies above 400 keV typical for neutrino from ^{7}Be recoil electrons.

Tuning of expected PDFs is quite important since we have quite long time reconstruction reset time of 80 ns in which charge is just integrated and probability of having charge exceeding one per channel is quite high. Tuning was done with usage of laser and electron source for channel charges up to 10; same time high charges on low light are unphysical and induced by radioactivity in PMT glass,

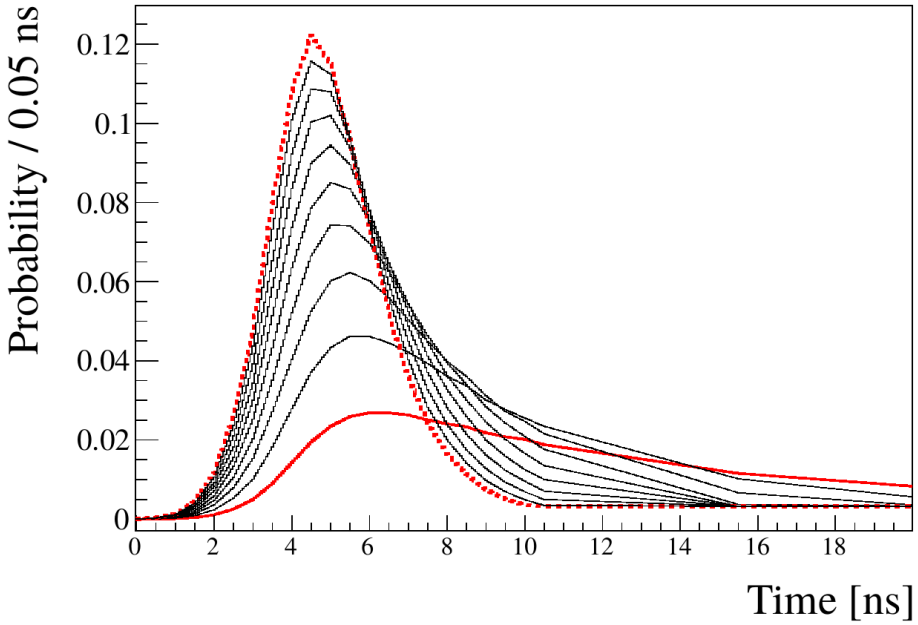

Figure 4.5: Expected scintillation shape PDFs for different charge values on PMTs; The PDF used is selected if registered charge is smaller or equal to the PDF charge and exceeds the PDF for lower charge. The expected charges change from 1 p.e. (solid red line) to 10 p.e.(dashed red line) with step of 1 p.e.

but at the moment there is no cut on charge in reconstruction; still, this is a problem in case of low-energy events (fig. 4.6). The PDFs are tuned for electron events (gamma-scintillation is quite similar since gammas still produce electrons by Compton scattering and photoelectric process, just with larger space distribution) and thus since scintillation of alpha-particles is longer, the algorithm could be expected to be less reliable. Nevertheless, since the front edge is more important in minimization, the algorithm works with alphas as well, and it was demonstrated in calibration campaign where source position was known. The same approach gave the value of effective refractive index of 1.68 used in the analysis; in fact PDFs should be dependent, e.g. on cluster charge due to different probabilities of having second photoelectron in 80 ns, but this dependency is also neglected.

Technically speaking, position reconstruction algorithm is implemented in software reconstruction framework right after clusterization algorithm and is intrinsic in events reconstruction algorithm since it allows to get so-called "reconstructed" hit times corrected for time-of-flight for photons producing photoelectrons under assumption of straight flight path. So in the very end we have hit clusters with

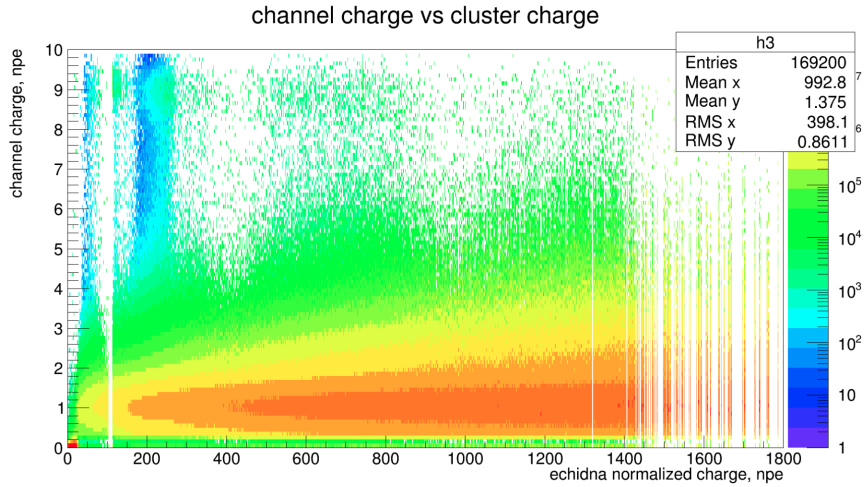

Figure 4.6: hit charge distribution in respect to the total charge collected in a cluster which is roughly proportional to cluster energy, normalized to flat energy distribution. One could observe some hits with charge of around 9 p.e. corresponding to activity in glass, while the main trend has mean charge roughly proportional to total cluster charge.

hits containing charge in photoelectrons (that should be related with physical number of channel photoelectrons, at least effectively) and times of the real photon production(although with some spread coming from reconstruction algorithm)

The algorithm of position reconstruction is quite far from perfection and has a lot of room for improvement (PDFs for particle types, charge dependency, high-charge cut and so on), but at the moment it is already very good. It provides typical resolution of 20 cm or less in energy range of interest with indistinguishable systematic shift (tab. 4.3).

4.3.2 Energy reconstruction

Energy reconstruction is the next step in analysis of data, at least logically, since it is possible to perform most of the studies using energy estimators such as nmpts (number of PMTs fired within cluster duration), nhits (number of hits within cluster duration) or charge (integral charge of all hits within cluster duration). Here one should consider physics of detector energy deposit, where energy is released through processes of scintillation (with consequent wavelength shift) and Ĉerenkov radiation (also with consequent wavelength shift). Scintillation should also account quenching effect, which important at low energies. Also different particles produce different amount of light in scintillation, so alphas produce approximately 14 times less light then betas and gammas. The light produced in this processes is collected

CCD x	DAQ x	CDD y	DAQ y	CCD z	DAQ z
26,8	26	8,6	7,9	101,2	96
7,8	7,1	-9	-7,9	0,8	-3,8
10,3	9,6	-10,9	-12	-98,6	-101,2
136,6	134,1	15,5	14,4	-171,8	-172,6
-60,7	-59,3	91,7	90,8	-179,7	-181,1
-60,7	-59,3	91,7	90,8	-179,7	-181,1
-75,7	-76,1	-192,6	-193,3	-129,8	-133,1
-120,8	-121,7	-316,4	-316,8	40,4	35,8
350,5	349,2	2,1	1	52,8	49,9
-89,1	-87,9	199,8	198,8	-122,4	-126,2
-151,8	-151,2	310,1	309,1	53,4	50
10	10,3	8,6	7,2	-198,5	-200
-129,9	-125,3	276,7	276	-123,2	-126,5
312	312,1	-3,1	-3,4	-120,3	-122,8

Table 4.3: Examples of position of radon source reconstructed by CCD cameras and TOF position reconstruction of DAQ data. Values agree within precision of CCD system, where uncertainty is fully systematic

by PMT system and it can't be done with the same probability in such large detector: light is attenuated in the scintillator and buffer, reflected etc. Nonuniformity of light collection is produced by a list of effects:

- PPO concentration, as well as chemical purity of scintillator, which affect light yield in the scintillation process: time- and spatial-dependent effects
- Temperature non-uniformity and temporal instability, which affects light yield due to its temperature dependence: time- and spatial-dependent effect
- Light attenuation lengths non-uniformity and temporal instability due to non-uniformities and temporal instability of PPO and DMP concentration, affecting light collection in the detector: time- and spatial-dependent effects
- Reflective and refractive properties of materials used inside the detector, affecting light collection: time- and(possibly) spatial-dependent effects
- PMT distribution temporal changes, affecting overall light collection: time- and spatial-dependent effect
- Intrinsic PMT quantum efficiency changes: time- and spatial-dependent effect (if present and significant)

- Electronic channels condition: time- and spatial-dependent effect
- Light quenching in scintillation: spatially and temporally stable effect
- Other effects, affecting relation of particle energy and electronics response

Independent accounting on all these effects, which are unknown would be a nightmare, so the only way out of this situation is going empirical way. For such action were developed so-called "effective quantum efficiencies", that are practically relative probabilities of having a hit in a channel per some specific standard scintillation and deserve a separate discussion that could be found below. These values could be used as a weight of a channel in the final energy variable derivation. Since a standard event is taking place in the center of the detector, one could make assumption that open angle to a PMT would be close to actual probability of photon arrival to this PMT, so assume equality of "effective" and geometrical solid angles. Under this assumption one gets "effective solid" angle from reconstructed event position by relating it to the geometrical solid angle from the detector center, such as

$$\Omega_{eff} = \Omega_{eff(center)} \times \frac{\Omega_{event}}{\Omega_{center}} \tag{4.2}$$

, where $\Omega_{eff(center)}$ is effective quantum efficiency of the PMT, Ω_{event} and Ω_{center} are simply geometrical angles (computed under assumption of large distance to PMT, $R \gg r_{PMT}$). The PMT could be given a weight of Ω_{eff} within the intrinsic procedure of energy estimator normalization, considering actual number of valid channels used in data taking at the moment of the cluster scintillation, so for energy estimator Q is

$$Q_{norm} = Q * \frac{2000}{\sum_{valid\ channels} \Omega_{eff\ i}} \tag{4.3}$$

Such normalization algorithm was implemented in a weighted way with weights considering effective quantum efficiencies and geometrical solid angles independently as well as in unweighted way; the last approach was used in all published analysis and is valid only within relatively small fiducial volumes where light collection is acceptably uniform. The distribution of corrected response for monoenergetic events simulated by monte-carlo could be found on fig. 4.7

Another point is related with conversion from light to actual energy. It is an independent operation since all the other correction consider only conversion from energy estimator variable into actual amount of light. First point is the Ĉerenkov radiation contribution decreasing the light yield for energies above 165 keV. As for

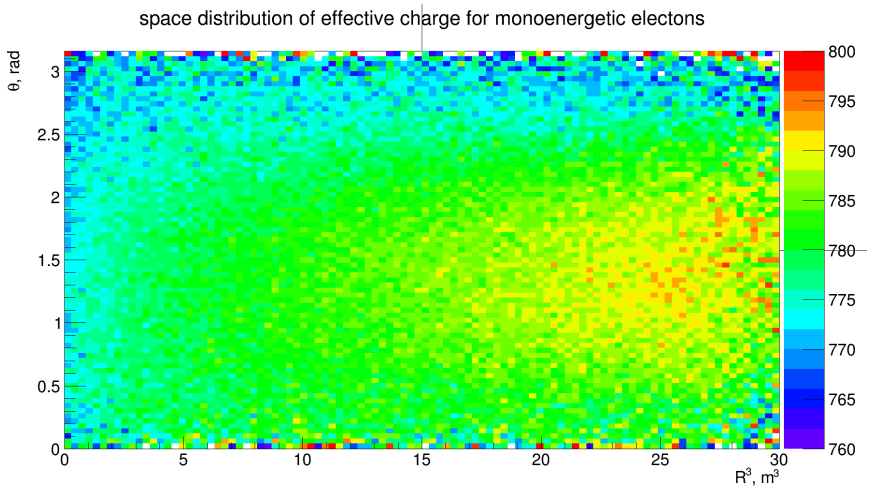

Figure 4.7: Peak positions for geometrically corrected normalized charge for monoenergetic events of 1460 keV within data taking phase II in monte-carlo simulation. One should consider precision of this simulation light amplitude reconstruction itself of order 1 %, comparable with maximal variation on the plot

the purpose of its consideration one uses an empirical interpolation of calibration data done with a function of the following type:

$$x = log(1 + \frac{E}{E_{min}})$$

$$\delta N_{PE} = (C_1 + C_2 x + C_3 x^2 + C_4 x^3) \times (1 + C_5 E),$$

where C_i are some fitted constant, E_{min} is the Ĉerenkov effect lower threshold and E in actual electron energy. This model was approved to describe the effect of light loss due to this effect with precision exceeding other uncertainties sources and was widely used in all previous analyses.

Consideration of quenching could be done with analytical description of Birks formula with $k_b = 0.0154$ and is important only at very low energies, so will affect only studies involving pp-neutrinos and ^{14}C.

4.3.3 Event shape variables

Understanding of the signal nature and quality is a quite important point in data analysis. That means that one needs some treatment of compatibility of detected signal with physical scintillation. A typical way of doing it is pulse-shape discrimination(PSD), that could be done with decoded hit times and amplitudes in a cluster. But the same time having multiple variables allows us to have another

treatment that we will call "event shape". In fact, a physical scintillation and consequent reemission create photons with uniform distribution coming from a small region of the detector sensitive volume. Sphericity of the detector allows to perform statistical checks of sphericity of light distribution in a cluster. There is a number of approaches:

- computation of spherical harmonics coefficients for fired PMTs positions. Obviously, for a physical event all coefficients apart from Y_{00} should be distributed around 0 and all problematic events could be separated. It appears that coefficient Y_{10} is the best option in data quality treatment
- likelihood to uniform distribution in different variables, e.g. polar angle
- full likelihood related with free light amount computed by the following way:

$$L(E,\vec{x}) = \prod_{i}^{n_{hit}}(1-e^{-E\mu_i}) \times \prod_{j}^{n_{not\ hit}}(e^{-E\mu_j})$$

  (producing over enabled channels), where

$$\mu_i(E,\vec{x}) = \eta\frac{\Omega(d,\theta)exp(-d/\Lambda)\times QE}{\Omega(d_{center,\vec{0}})exp(-d_{center}/\Lambda)},$$

  where Ω is the solid angle, computed analytically and Λ is attenuation length (attenuation is actually computed in IV and buffer independently. Such approach gives good likelihood treatment as well as best fit energy, ratio of which to simple energy estimators such as charge is one of the best data quality parameters.

- uniformity of hit distribution over crates and boards. Boards are connected the way that channel number increases with azimuthal angle in a monotone way, so intrinsically nonuniformly allowing to perform search for board correlation

These treatments allow to detect most of nonphysical clusters and even allow to discriminate some classes of events, e.g. likelihood energy treatment allows to discriminate pile-ups, although relatively weakly (fig. 4.8). Still, temporal treatment of most of events is usually a more powerful approach,e.g. for alpha/beta and electron/positron discrimination.

4.3.4 Alpha/Beta discrimination

Alpha/beta discrimination is another possibility to decrease background since signal of interest is totally electron. Luckily, discrimination of these signal types

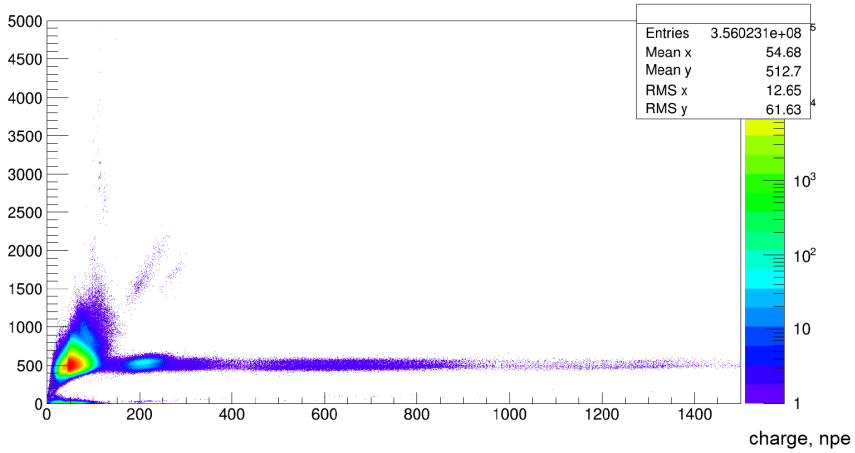

Figure 4.8: Ratio of maximum-likelihood energy and normalized charge within phase II of data-taking. One could observe pile-up of ^{14}C-^{14}C located at charges below npe above the general beta-event trend and shaped as a triangle as well as some badly shaped events at around 200 npe

could be done since alpha scintillation has longer duration (fig. 4.9). In this case one could think of discrimination method using the difference of pulse shapes. The easiest way to do it is usage of tail-to-total ratios that meas simply ratio between number of hits in some last part of a cluster (e.g. with reconstructed time of more than 50 ns with respect to cluster start) in respect to total number of hits. Another simple possibility is to go through temporal quantiles that give the time corresponding to some first fraction of hits, e.g. time corresponding to the last hit of first 20 % of hits in a cluster. Such approach discriminate alphas, but they don't have enough resolution power, especially in case of low light.

Another possibility is to use Gatti filter [66] which considers a value computed as

$$G = \sum P_i S_i, \tag{4.4}$$

where S_i is binned signal temporal distribution and weights are given as

$$P_i = \frac{\overline{\alpha_i} - \overline{\beta_i}}{\overline{\alpha_i} + \overline{\beta_i}}, \tag{4.5}$$

where $\overline{\alpha_i}$ and $\overline{\beta_i}$ are normalized PDFs of alpha- and beta- signals. Such value has the advantage of being normally distributed around two values and allows to apply the approach of binned statistical subtraction, but still does not allow to cut out alpha events since discriminative power is relatively low.

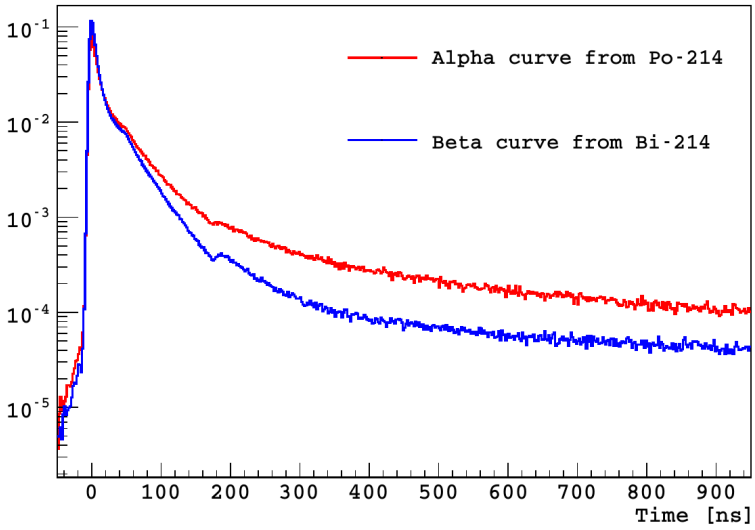

Figure 4.9: difference in scintillation shapes of alpha- and beta-events selected with ^{214}Bi-^{214}Po delayed coincidence. Alpha scintillation has a visible longer duration.

But let's come back to quantiles and tail-to-totals. They are quite good discrimination parameters themselves, so why not to combine them? There are plenty of discrimination algorithms that could find the best variable computed on their basis. One of them which is used in Borexino is Multi-Layer Perceptron (MLP), exploiting neural network trained on some samples of alpha-and beta-events using quantiles or tail-to-total ratios as input parameters for the treatment. The best choice appears to be quantiles that provide discrimination with efficiency exceeding 99 % even at relatively low energy.

The source of PDFs for discrimination training is the only one - we have delayed coincidence analysis of ^{214}Bi - ^{214}Po events that are beta and alpha decays respectively. In the process of water extraction in purification the detector was full of radon allowing to make up samples of 15000 events of both kind that allow to train discrimination variables.

Cutting data always considers new bases introduced into the dataset. So if dataset is cut, it requires appropriate statistical treatment in the further analysis. The most reliable variable in this case is MLP-derived parameter that has exponential energy dependence, that could be demonstrated for both alpha- and beta-events in monte-carlo simulation and on source data for beta-events. All other approaches bring much more complication into analysis, although statistical subtraction (with quite sophisticated application algorithm) was used in analysis

of Phase I data.

4.3.5 Electron/Positron discrimination

Another way to reduce background or to improve understanding of the data composition is pulse-shape electron/positron discrimination. Positrons are caused by inverse beta-decay of antineutrino, or, in most of cases, are emitted from cosmogenically produced radioactive nuclides through beta-decay. For instance, positron causes scintillation in a different way than an electron due to inclusion of recombination process. In a significant number of cases electron-positron pair creates orthopositronium and this fact changes scintillation time creating a component delayed by life time of orthopositronium (fig. 4.10). Moreover, recombination creates

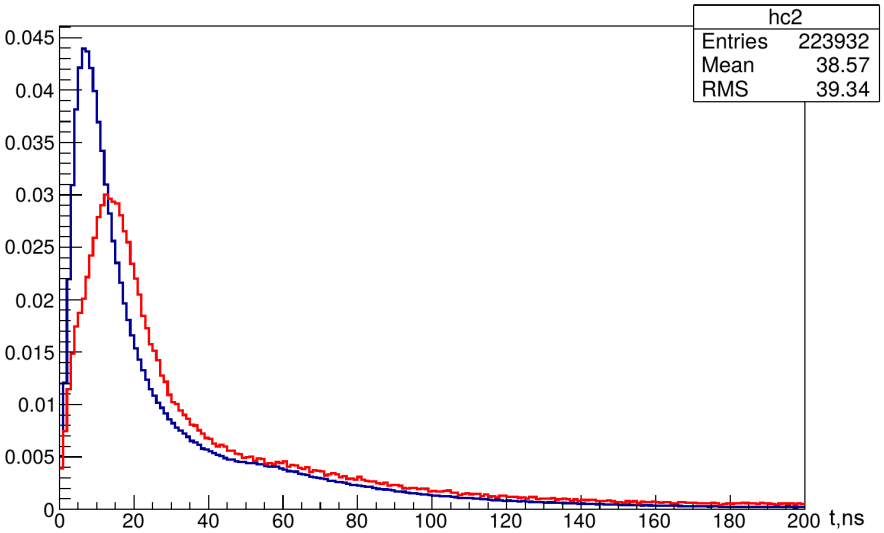

Figure 4.10: Pulse shape difference for electron and positron samples that could be used for pulse-shape discrimination of positrons in case of orthopositron formation

a couple of gammas (all other cases with higher number of gammas are much less probable and could be neglected) and thus has quite different geometrical pattern. Discrimination could be done by a set of parameters, such as

- position reconstruction likelihood
- cluster rise time
- cluster mean time
- quantiles or tail-to-total ratios

Among all of them, likelihood of position reconstruction could has the main discrimination power. Still, other parameters could be combined with some classification algorithm and trained on samples of electrons (same as the one used for alpha/beta discrimination) and positrons (^{11}C sample produced by specific setting of TFC veto system described below). In any case discrimination ability should be studied thus the sample is divided into two subsets for training and testing and it is more statistically profitable to use not BDT(Boosted Decision Tree, classification algorithm used for the purpose in Phase I analysis), but to use simple position reconstruction likelihood value at the minimum normalized by number of PMTs fired per cluster. Discrimination power of BDT/likelihood parameters is still very low, so it could be used only for estimation of fraction of positron events in the data, e.g. per energy bin of the spectrum.

4.3.6 Generic data quality treatments

Having all the power of information of event shape, pulse shape, charge and timing it is possible to develop a system that could treat data by generic quality. There are the approaches of selection of data that are considered "good":

- trigger type. One takes neutrino trigger only, thus non-service trigger in anticoincedence with OD
- clusterization. Non-clusterized data are not analyzed
- difference between triggering time and first cluster start time. This is criterion of triggering reliability since clustering is software based and thus absolutely stable.
- Crate uniformity. Correlations of level above 75% of hits on 1 crate (of 13 active) are excluded from analysis
- spherical harmonics coefficient Y_{10}. It is cut by some empirical curve. Very unrealizable approach that is refused in all low-energy analysis. Plus this coefficients have non-accounted time dependence in both mean value and variance. Used in Phase I analysis.
- Number of peaks in a cluster, derived by standard features of ROOT environment, should be one. Removes close coincidences together with electronic problems.
- "q/qrec". Ratio of charge and reconstructed energy, where energy is reconstructed from number of PMTs fired by likelihood approach, but in severely

simplified case (flash in the center, absolute transparency and PMT uniformity, fixed probability of having a second hit, thus computable analytically). Quite simple but still effective approach.

- fraction of hits with no charge. If more than half, such event is removed

Most of these approach remove very few events and are not harmful for the final result just by statistical reasons. Same time these approaches could be used for removing some runs from the final dataset.

An independent, but still effective treatment is ratio of charge and likelihood-reconstructed energy(by full algorithm). It allows to remove some runs with lower data quality and has very good discriminative power of any problems in data-taking. Removing of such runs improves goodness-of-fit for the final solar analysis, but this is the only indirect evidence of its usability simply because data are quite good on their own. This could be also demonstrated with compatibility in respect to temporal Poisson statistics which is quite satisfactory unless decaying ^{210}Po present in the data sample.

4.3.7 Muons in Borexino

All the analysis steps described above are considering inner detector only. The same time we have muon flux of order of 4300 muons per day inside SSS inner volume and they are a danger themselves together with induced cosmogenic nuclides. Discrimination of these muons is a quite specific task that considers both inner and outer detectors. The steps of discrimination are:

- coincidence of ID and OD detector
- presence of muon cluster in OD independently of ID
- pulse-shape discrimination by cluster mean time or peak time since muon is a long track producing long-term scintillation, much longer than point-like scintillation
- non-decoding of more than 95% of hits, mostly it is about electronic noise; such events are not clusterized
- overlapping with service interrupt of the trigger (although it is hardly about muons)
- Cluster start time in respect to trigger reference located far away from the typical position - discrimination is due to different rising edge of a muon

Such definition gives very high muon discrimination efficiency that could be treated by position reconstruction likelihood(since muon is not point-like) and trough CNGS beam [67].

Muons are removed from the spectrum as well as every event within 300 ms after each muon crossing SSS due to electronic instability. More profound vetoing of muons is done for cosmogenic purposes depending on the specific analysis needs.

Muons are tracked by OD Ĉerenkov light as well as by TOF or baricentration algorithms in around 50 % of cases [67], but in case of crossing inner vessel the number is much better. That also allows some approaches for cosmogenic activity vetoing.

4.3.8 Fast coincidence chains tagging

The detector despite being purified up to a very high level still contains natural radioactivity that could be discriminated by fast chain tagging. Such tagging becomes possible in case there is a chain with two consequent reactions within short period of time (so the intermediate nucleus has relatively sort lifetime). In the detector it is possible to tag ^{238}U or radon[1], ^{232}Th or thoron and ^{85}Kr. In case of radon it is coincidence of ^{214}Bi - ^{214}Po, where polonium lives 236 μs, in case of thoron it is ^{212}Bi - ^{212}Po with polonium live time of 300 ns and in case of krypton it is beta decay followed gamma-decay with width of 1.5μs. In all cases the chains are fast so the probability of accidental coincidence is low. Together with temporal treatments one uses geometrical one, but one should consider not only systematic, but also statistical shift between the events that results in limiting distance to 1-2 m since resolution of position reconstruction depends on energy. Energy is also limited within some windows.

Bi-Po coincidence has another advantage of having an alpha decay that could be discriminated with existing techniques, decreasing accidental coincidence probability. Tagging efficiency is around 89.1 % and is limited with mostly position reconstruction issues.

^{212}Bi - ^{212}Po has very short-lived polonium that produces high-energy long-range alpha particle and thus it is mostly limited by time reconstruction efficiency to the level of 25 %.

Krypton discrimination has a different problem. Lifetime is perfect and there are no problems related to timing, being still very short for having very few accidental coincidences. But this channel has branching of only 0.4 % and energy of prompt beta is very small, endpoint of the spectrum is 176 keV. In total only around 1 of 1000 decays of krypton could be tagged making this analysis quite unprecise since the prompt energy simply doesn't cause triggering. Still, krypton

[1] fast chain is located after the emanation phase

discrimination is very important for low-energy neutrino analysis.

4.4 Effective quantum efficiencies

It is widely known that different Photomultipliers appear to be different in the sense of light detection efficiency, even in case they represent the same model and materials. This effect is caused by different intrinsic properties of PMT photocathodes, and it is possible to judge it through such value as quantum efficiency, which could be defined as probability of a photoelectrons exit from photocathode in case of a photon arrival to it. This parameter also depend on photon properties, especially wavelength.

In case of Borexino experiment we have constant spectrum of light produced in an event, so in our case it is possible to understand quantum efficiency as average quantum efficiency over light reemission spectrum of PPO. This intrinsic quantum efficiencies are taken into account since the very beginning of data analysis.

The effective quantum efficiencies are more specific parameters, that could be introduced in case of liquid scintillator setup such as Borexino. This parameter has a definition, which differs from one for quantum efficiency of a PMT, and it appears to be probability of hit signal detection in case of an event, observed by a PMT, normalized to solid angle of observation and number of photons in this event.

Such definition of quantum efficiency appear to include several points of physical background:

- Light propagation from the source. Either solid angle on current PMT is out of scope, some local effects of absorption and reflection could affect the final number
- Electronic channel properties. Level of electronic noise together with correspondingly tuned gain and threshold could affect the probability of detecting a hit in the channel
- Intrinsic quantum efficiency of the photocathode. It is still the major factor affecting the probability of hit registration

Equality of intrinsic and effective numbers could be reached the following way: as we normalize to solid angle in case of no absorption/reflection we have 100% probability of photon appearance on photocathode, as well as any photoelectron would reach first dynode causing a signal, which will be detected in case of neglectable dark current, noise etc.

Although in the first approximation effective quantum efficiency is equal to the intrinsic one, its difference could bring sufficient nonuniformities in light collection.

As understanding of light collection is urgent for every light-channel detection, even small deviations in light collection have very high importance, as deviations in light collection introduce systematic error to energy reconstruction.

4.4.1 Mechanism of obtaining effective quantum efficiencies

According to the definition given, in order to obtain effective quantum efficiencies for the detector, one needs a source observed equally by each PMT, or at least by a sufficiently large group of PMTs, in which an average value of intrinsic QE could be considered independent from group selection. As Borexino detector is spherical with all PMTs aligned with sphere radius, a light source located in the center of the detector will be observed equally by each PMT.

An important point is that some PMTs (in fact, most of them) are equipped with light concentrators, which are increasing effective solid angle of source observation. So the PMTs with and without light concentrators should be judged as two separate classes. We would consider this classes to have equal mean quantum efficiencies as the PMT constructions are equal, while both classes have enough statistical significance for such assumption. But for some purposes, e.g. energy reconstruction, one could need concentrator effect to be accounted inside these numbers thus these numbers will be treated as a single group as well, so we will have two sets of numbers.

As the number of photons produced in the central region of the detector depends on event energy, one should choose a source, which would be distributed uniformly in the central region in order to fix amplitude spectrum coming to the PMTs. Such source should also have high statistical significance in order to derive effective quantum efficiencies without too high statistical error. Under such conditions we are left with only one possible source, which is ^{14}C with some radial cut for central region establishment.

Having a light source, located in the detector central region , which is observed equally by each PMT, it is possible to consider effective quantum efficiency to be proportional to hit count rate of the corresponding PMT. Making such consideration we assume that average event rate of ^{14}C remains constant in time in case the lifetime of different PMTs is different; such assumption could be reasonable according to the data we observe.

The absolute value of effective QE makes no interest as energy calibration of the detector is performed by peak positions and affects only the scale in dimensionless numbers it could be reasonable not to derive the absolute values from data, but to establish some normalization to a reasonable number, e.g. normalize to coincide average values of measured QE and effective QE.

4.4.2 Software implementation of effective quantum efficiency obtaining

In order to obtain the values for effective quantum efficiencies were performed the following operations:

- ^{14}C source cuts from standard Borexino raw rootfiles with radial cut of a sphere with diameter of 1.3 m located in the center
- establishment of channel lifetimes during run periods in order to compute hit rates
- Binding software to create output effective QE libraries in format of database output used in all Borexino applications
- a module for attachment of produced libraries to MC simulation

In order to cut ^{14}C events there was performed trigger cut, cutting out non-neutrino-like events (trigger type=1), as well as energy rage cut in "nhits" variable, were selected only "single-cluster" events (events which are not followed by others within 2 ms time window) and radial cut, cutting out a sphere of 1 m radius in the center of detector. Data from water-extraction periods was not used as well.

Subtraction of dark hits was performed using random trigger (tt64) events by computing the average rate of such event hits in detector channels; the number of dark hits in total amount of hits is proportional to the sum of time windows length for events of interest, so, taking into account that time windows of tt1 and tt64 are the same, the number of dark hits per channel should be renormalized to the ratio of events of interest and tt64 events:

$$N_{dark\ hits\ in\ ROI}[channel] = N_{total\ dark\ hits}[channel] \times \frac{N_{events\ of\ interest}}{N_{events\ of\ random\ trigger}}$$

In order to obtain channel lifetime were performed several sessions of Borexino database reading, withdrawing information on channels disabled during runs, including last valid event on the channel and run durations. As for channels disabled after start of run data-taking, the lifetime was computed as difference between GPS time (in seconds) of the last valid event for the channel and GPS time of the first valid event in the run. The typical result of such operation is illustrated on fig. 4.11

In order to perform electronic channel condition control during withdrawal of hit rate the data was withdrawn using "charge" variable, with filling charge histograms for each channel during each period. The typical charge distribution is illustrated of fig. 4.12 . The control was performed by shape of the distribution (visually for channels returning numbers significantly different from average) and by mean value ($\pm 15\%$) of average value (automatically).

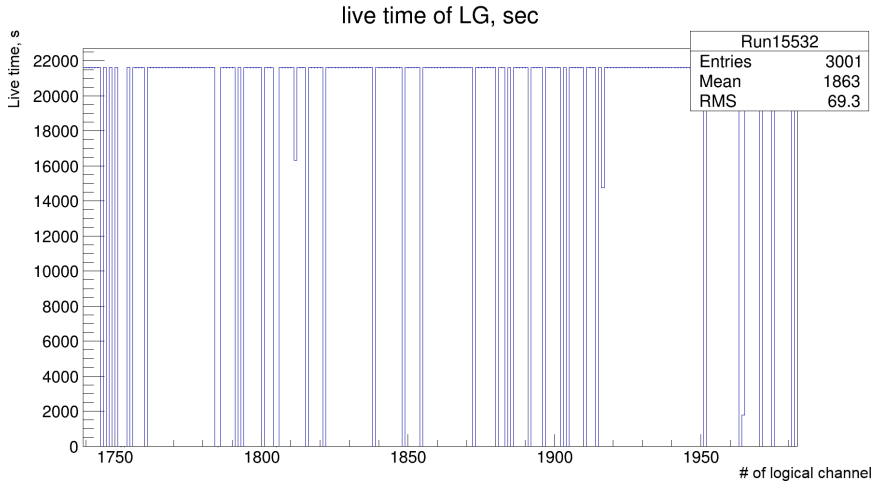

Figure 4.11: An example of channel lifetime distribution in a run

4.4.3 Discussion on the values

Having all this data it is relatively easy to obtain hit rates for each PMT, one should just consider two separate classes of PMTs with and without concentrators and changes in mapping between logical channels of electronics and numbers of physical positions of PMTs (so-called "holes"). Such information was withdrawn from database. If the mapping was changed during considered period of data withdrawal, such data was not taken into account; live time was computed individually for each channel and temporal period using pre-computed libraries of channel live time.

As the effects of light propagation as well as electronic channel parameters could change with time, one should compute effective QE for some considerable temporal periods during the whole detector history. In order to verify that the effects of changing of fluidodynamical properties of the detector, it is possible to take a look at geometrically united groups of PMTs, ordered by ϕ and θ angles. Such plots demonstrate, e.g. quite strong anticorrelation for groups, opposite in phi angle, that could be observed in fig. 4.13

Such temporal behavior of effective QE gives us a strong hint that there is some fluidodynamical movement effect on light collection in the detector and this numbers allow us to take it into account, e.g. significantly improving monte-carlo simulation of light collection.

Speaking of overall effects in effective QE, one could sum up its most important features:

- Distribution of effective QE is quite similar to the distribution of real measured QE, as the intrinsic QE is still the major factor for this number(see

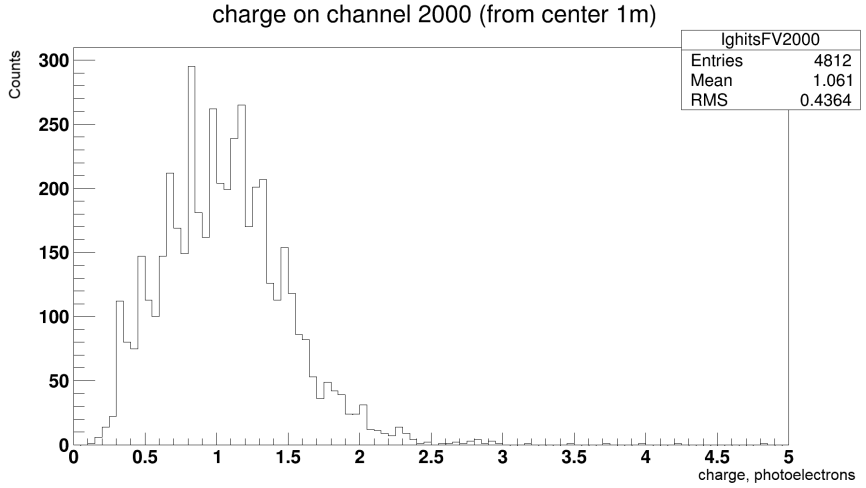

Figure 4.12: An example of channel charge distribution for ^{14}C events.

fig. 4.14)

- If one studies the temporal behavior, it appears to be systematic and shows anticorrelation for opposite zones
- Introduction of such numbers into MC simulation fits nonunifomities in light collection between simulated and real data

So, it is possible to conclude that usage of such numbers could be considered an improvement in detector simulation, coming from taking into account some effects, which are intrinsically unmeasurable but play an important role in the detector response.

4.5 Cosmogenic veto system. Three-fold Coincidence

One of the most important backgrounds in the region of interest for solar neutrino search is ^{11}C, a cosmogenic isotope, produced by spallation of stable ^{12}C induced by a muon[2]:

$$^{12}C(\mu, n + \mu)^{11}C$$

this isotope appears to be a beta-plus decayer and decays into Boron with half-life of 20.39 minutes:

$$^{11}C \rightarrow^{11} B + e^{+}$$

[2]there are other channels of this isotope production, such as (p,d) reaction, but they take place mostly in avalanche process and thus we neglect it for single-site production

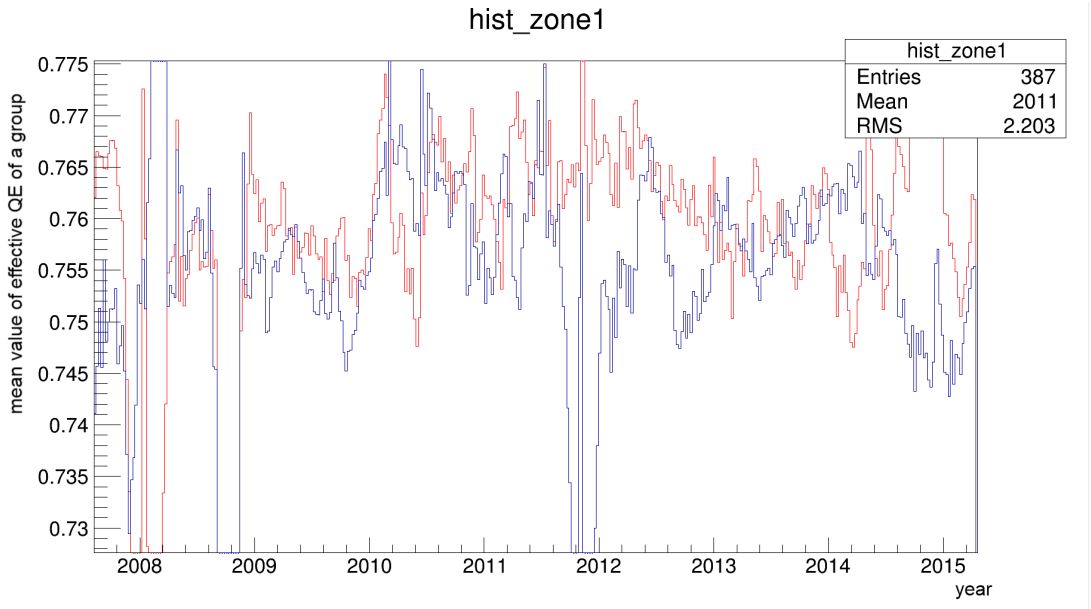

Figure 4.13: temporal dependence of mean effective QE for groups PMTs, located in $\pi/5$ sectors opposite in ϕ

The endpoint energy of the decay spectrum is located at 0.96 MeV, but in Borexino the reconstructed energy includes also two gamma-quanta of positron annihilation and thus one observes the beta-spectrum moved by 1022 keV in respect to 0. So the spectrum of ^{11}C is located exactly at the energies of pep-neutrinos as well as neutrinos emitted in CNO cycle, and this fact makes it a great interest for investigation.

Abilities of PSD discriminations are quite limited, moreover, PSD as pulse shape could have an energy dependence, which would seriously limit its abilities due to the fact that ^{11}C has continuous spectrum. Here we'll review how it is done in Borexino solar analysis in LNGS implementation, currently used in the analysis, although there are two other implementations, following the same idea with some modifications in details.

4.5.1 Three-Fold Coincidence: physics background

In principle, ^{11}C decays could be subtracted by putting a veto on the region of its atoms location, that could be found from measurement of properties of other products of the reaction of spallation: muon and neutron. As the only source of this background is muon flux, one could consider the most simple possibility of detection of this nuclide: simply to put a cylindrical veto on the muon track with radius, that could be understood from the tracking precision. Theoretically

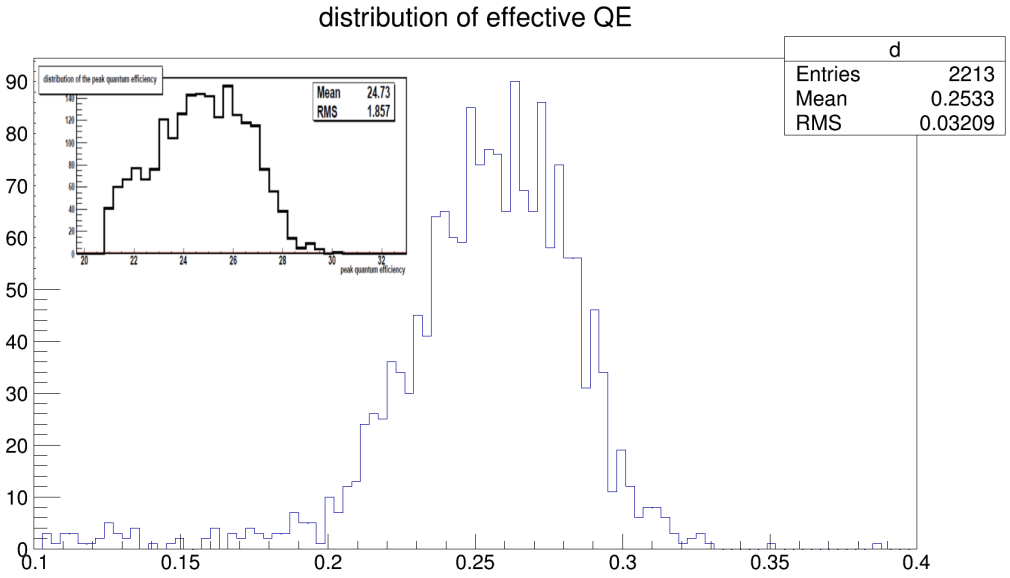

Figure 4.14: Effective quantum efficiency distribution vs measured quantum efficiency distribution. In the upper left corner os demonstrated the distribution of real quantum efficiencies measured in PMT test in units of percent

speaking, such approach would give ^{11}C subtraction efficiency close to 100% for single-site production, but there is a problem: in Borexino the efficiency of muon tracking (algorithm "muon_internal_large", combination of all possible muon discrimination algorithms) is around 50%, so it will not give the desired background suppression even taking into account that as for muons producing ^{11}C (distinguished by presence of neutron capture right after) this number is higher and reaches around 70 %.

Under this circumstances one has to take control of spallation-produced neutrons as well. These neutrons could be distinguished by process of gamma-decay of excited state of ^{2}H, produced by neutron capture (the capture on ^{12}C has a negligibly small branching ratio). As this gamma-line produces a narrow peak with energy of 2.22 MeV, that would be an easy task, but there is a special feature of clusters right after muon: as muon deposits a very high energy (several hundred MeV) inside inner detector, it overflows electronic channels to so-called condition of "empty boards" (number of DAQ boards, saturated by signal induced by muon-related light deposit and remaining saturated at the moment of trigger signal of aftermuon event, which is corresponding to closure of this event time window and distinguished by presence of no signal from the boards), partially blinding the detector. Thus energy reconstruction of such events is ambiguous and imprecise(see

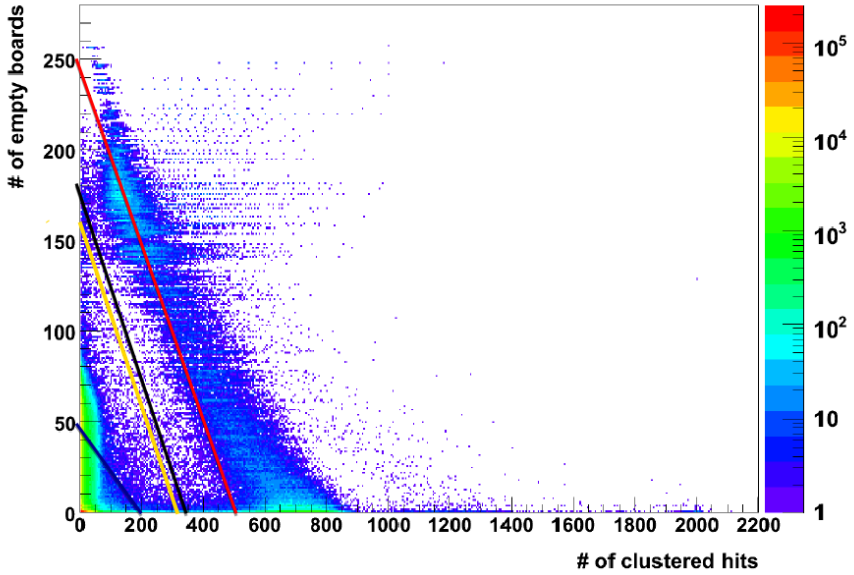

Figure 4.15: Number of empty boards vs number of PMT fired. One could distinguish declined stripe (mostly neutrons) and low-energy bulb (^{14}C). Lines represent various neutron definitions, yellow line is the definition used in the analysis (all events above the line are considered neutrons)

fig. 4.15), even without considering charge collected by PMT electronics and relying only on number of hits. Under this circumstances the only way to act is to take into account that most of events right after muon are neutrons and ^{14}C in accidental coincidence and thus to neglect presence of any other events after muon. Under such assumptions it is possible to develop some definition of neutron, which would reliably select most of neutron events with a minimal fraction of ^{14}C contamination. As from fig. 4.15, it is possible to expect such definition to have a shape of

$$N_{hits} > P_2 - P_1 \times N_{empty\_boards}$$

It is possible to tune the parameters of such model according to TFC efficiency, where live time subtraction would increase in case of hardening of the definition while the ^{11}C discrimination would improve; The optimal value would be defined from optimal balance of live time and ^{11}C discrimination.

Another problem caused by the same reason is position reconstruction of neutron events. The position reconstruction in Borexino is based on PDF likelihood of the events in detector, tuned for electron events, obtained in calibration campaign. This algorithm works quite well for beta- and gamma-events under normal opera-

tion conditions and only in statistical sense (so only in the sense of mean value for statistically significant number of events), but in case of large number of empty boards and absence of charge information (as electronic system is mostly saturated by the previous muon charge) the derived pulse shapes are severely distorted casing the fit not to converge(in around 5% cases) or at least to loose precision by several times (from 0.2 m to around 1.3 m); moreover the position reconstruction algorithm is unreliable in some cases (large fraction of reflections, activity in the glass of PMTs, causing excessive electronic emission from photocathode etc.), so the position reconstruction is expected not to work always reliably on events basis even apart from muon saturation effects. This causes a necessity of having a proper treatment of position reconstruction quality, that could be performed on event basis. It is possible to check a lot of possibilities for position reconstruction treatment (e.g number of empty boards, so level of hit detection saturation, mean value of charge per hit, so level of charge measurement saturation, convergence of position reconstruction algorithm, asymmetry of position reconstruction likelihood function, value of this likelihood at minimum, position reconstruction error derived from corresponding Hessian matrix computed with full second derivatives or with independent left and right ones etc.), but the only criterion for such treatment is the following: if it is an increase the veto size for events selected by some criterion will improve the TFC performance, such criterion has good correlation with position reconstruction precision. Among all possibilities available in data of cycle18 it appears to be possible to use effectively only two value of position reconstruction likelihood (negative logarithmic likelihood in fact), normalized by number of PMTs used for position reconstruction (so fired for the reconstructed events as the current algorithm uses all light emitted by event). Parameters of veto in dependence of these parameters could be also derived according to TFC performance. The only limitation that was introduced is that there are only three values of neutron veto radius and, correspondingly, two thresholds of likelihood value, while lack convergence corresponds to less strict threshold, so the veto radius depends on position reconstruction normalized likelihood value as a sum of two Heaviside functions.

A useful tool that could improve the efficiency of neutron detection is external neutron reference: Analogue sum or Flash-ADC system (first one replaced by the second in 2010) , which could detect a neutron without being distorted by the effect of "empty boards". Analogue sum system also was synchronized with trigger time and thus gave cluster-by-cluster agreement with laben data while FADC has a separated trigger system and provides agreement only on event (triggered DAQ window) basis. This systems have neutron detection efficiency at the level close to 100%. But one should take into account that FADC system didn't show very high reliability due to summing a lot of PMTs per channel and thus the data of

FADC system contain quite high amount of noise most of the time and thus are usable only for a small fraction of time; moreover, standard Borexino electronics has already very high performance of neutron detection and the main trouble of TFC remains in position reconstruction quality.

4.5.2 Three-Fold Coincidence: program implementation

Taking into account all physics, underlying the TFC filtering, one could consider the a logical chain of veto production, that would provide reasonable ratio of live time loss together with best possible ^{11}C suppression performance.

In the lngs_c11_c18 filter the veto is established the following way (assigned parameter values are changeable up to some extent according to performance requested):

- beginning of a run: we should put a total veto in the beginning of a run due to the fact that we know nothing about ^{11}C production before the run started. We put 1 hour in the very beginning of data array processed and for the rest we put the veto dynamically: $3600 * (1 - \exp(-dt[s] * \frac{1}{600}) + 600)$ s
- Veto initiated by muon events:
- number of empty boards exceeding 160: full detector 2h veto (one of possible avalanche process criteria, detector saturation by massive light production)
- number of muon daughters with energy exceeding 100 n.p.e. exceeds 42: full detector 2h veto (another criterion of avalanche process, neutron burst in the detector)
- The first inner detector cluster starts after more than $2\mu s$ after muon outer detector cluster start: possibly the inner detector was completely blind due to some saturation, veto is applied on the muon track since nothing better is available
- In case a neutron is detected by Analogue sum system: spherical veto on neutron position. If the total dark rate on channels fired is below 40 hits in the cluster window - additional spherical veto on position orthogonal projection of the neutron position to the track, if above - additional cylindrical veto on the muon track
- in case of FADC reference reporting more neutrons than standard electronics: treat all muon daughters (events after muon within 1.6 ms) as LABEN-detected neutrons, putting corresponding veto on positions/projections; Veto part disabled for final analysis due to low efficiency

- in case of a neutron detected by LABEN (or considered so due to FADC reference if enabled): do the same as for neutrons detected by analogue sum, but do not put projection veto if analogue sum reference is present
- use only neutron veto with reduced temporal duration (up to 2 live times) and radius (up to 1 m) for low-noise single-cluster events in order to establish enhanced ^{11}C sample, used in further analysis including MC simulation verification and pulse-shape discrimination algorithms

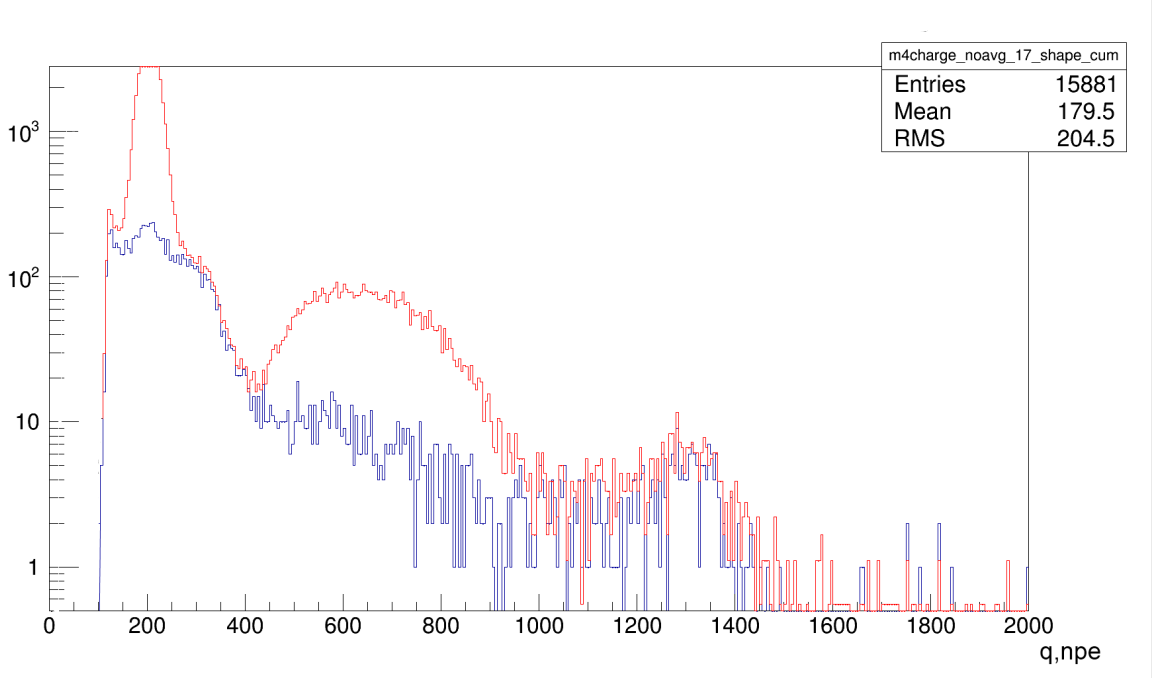

Figure 4.16: TFC result for Borexino Phase II
Spectra in charge variable m4_charge_noavg_corrected (cluster charge with correction for some electronic effects, usually very small) with and without TFC filtering and MLP alpha-subtraction normalized to the same exposure. Low-energy part of the spectra removed for computational purposes; TFC-subtracted spectra are affected by cut on MLP alpha/beta discriminator.

Regarding the numbers of this veto (veto radii, veto durations, thresholds, neutron and muon definition), it is possible to tune this numbers according to the performance but typical time would lie between one and three hours, while the radii of track veto and especially neutron veto request more serious consideration. Parameter tuning gives 0.8 m as a good value for track veto radius and it cuts

out negligibly small exposition, but due to not so high tracking efficiency what is really important is the neutron veto radius and the corresponding thresholds of position reconstruction treatment.

The current values for these parameters are the following:

- neutron definition: $N_{normalized\ hits} > 310 - 2 \times N_{empty\_boards}$
- neutron veto radius used for enhanced sample: 1.0 m
- neutron veto radii: 1.1 m, 1.5 m, 2.4 m
- Track veto radius: 0.8 m
- neutron/track/full blackout veto duration: 7200 s
- Thresholds for neutron veto selection for normalized likelihood of position reconstruction: 4.55, 4.85 (below lower one - minimal radius, above higher - maximum radius)

As every veto applied on detector, TFC is subtracting some exposition from data. In this case it is important to understand the amount of exposition subtracted. There are two standard possibilities: ^{210}Po peak fitting and toy Mote-Carlo. The Po peak method is based on assumption that Po amount in original and TFC-subtracted approach are same. Toy MC relies on playing fake event positions according to uniform distribution in some volume equal or larger than fiducial volume used in analysis with constant rate (2Hz is used in current code) and computing numbers of these fake events in FV independently of veto and outside it; the ratio of these numbers will indicate the ratio between expositions of initial and TFC-subtracted spectra.

4.5.3 Other approaches in TFC veto

There are other possibilities to improve TFC veto system, namely

- use likelihood approach, so computing likelihood of event being ^{11}C according to the parent composition with some expected radial and temporal distributions, where temporal distribution is obviously an exponential decay and radial is to include properties of position reconstruction. Such approach could in principle increase flexibility of TFC veto, but much more it increases tuning complexity making the veto extremely different to setup. Thus, at the moment the algorithm implemented (Mainz code) has no advantages in efficiency

- Position reconstruction is definitely a keystone, but it is not the only point. "empty boards" parameter also has different meaning in different times, thus it is possible to follow expected values and resolution making threshold time-dependent. It was implemented in another code, Milan one and shows some improvement in efficiency. Still, improvements are not dramatic.

All the approaches could be mixed, but it would not benefit much in respect to existing state. TFC is limited just by position reconstruction uncertainly rather than by anything else and this makes it practically impossible to improvable; All algorithms show very close results and follow practically the same curve of efficiency vs surviving exposure.

4.5.4 Three-Fold Coincidence: efficiency treatment

The algorithm described above was implemented in order to process Borexino data of phase I and phase II. The result of this subtraction is presented on fig. 4.16 for phase II data. It appears that it is very difficult to treat the result properly as the surviving fraction of ^{11}C is small in respect to the amount of other backgrounds in the region.

Estimate of the efficiency is possible with usage of PSD approach, as in this case its efficiency could be understood from enhanced sample, allowing us to compute overall amount of ^{11}C remaining by a simple proportion; taking into account small statistics of PSD - selected events it could be important to understand systematic uncertainty and non-physical event acceptance of such estimates. Thus this approach can't give any serious precision of TFC efficiency estimate.

TFC efficiency also could be estimated by usage of the fact that^{11}C decays with lifetime of around 1761 s while other spectral components appear to be uncorrelated with muon events[3]. If one could define a set of events with times $\{T_i \mid T_{i+1} \geq T_i\}$ which contains all parents of ^{11}C, it could be possible to measure the rate of non-cosmogenic and cosmogenic components.

Let's define exposure as

$$E = \int\limits_{live\ time} M(t)dt$$

Correspondingly, one could write

$$E = \int_0^\infty \frac{dE}{d\tau} d\tau$$

[3]apart from fast cosmogenics,which are a negligible contribution in the region

where to $\tau = (t - T_i | T_i \leq t \leq T_{i+1})$. As our knowledge of temporal dependence (exponential decay with known decay time or stable flux) corresponds to rate of this events per unit of exposure, The number of events with known rate $R(\tau)$ could be written as

$$N = \int_0^\infty R(\tau) \frac{dE}{d\tau} d\tau$$

So in order to understand the number of events of each kind one needs to find the differential exposure. If one has some events with constant rate and $\tau = t + C_i$, where C is a constant, if $\frac{\partial R}{\partial t} = 0$ then $\frac{\partial R}{\partial \tau} = 0$ as well since delay to last muon depend only on time and nothing else. In this case the previous expression will look like

$$N = \int_0^\infty R \frac{dE}{d\tau} d\tau = R \times \int_0^\infty \frac{dE}{d\tau} d\tau$$

If one simulates toy Monte-Carlo events with constant rate and plots their spectrum, that would give

$$\frac{dN_{const}}{d\tau} = R \frac{dE}{d\tau}$$

,so this is a way of numerical calculation of the differential exposition respect to τ. In this case it is possible to the spectral fit of real events with respect to τ with a function

$$F(\tau) = \frac{dN_{const}}{d\tau} * \sum_{all\ \ species} R_j(\tau)$$

, where $R_j(\tau)$ are constant or exponential functions. The ratios of rates will appear to be proportional to integrals like

$$N_j = \int_0^\infty R_j(\tau) \frac{dE}{d\tau} d\tau$$

, where all functions are known up to a constant factor and could be normalized according to the total number of events as $\sum_j N_j = N_{total}$. As soon as the decay times of all components are known and could be fixed the errors on the derived numbers of events will be proportional to the errors of fit coefficients. The results of such computation could be seen on fig. 4.17

As soon as one has a technique of fitting the temporal dependence, the only problem is to find the set of times $\{T_i \mid \ T_{i+1} \geq T_i\}$. The requirements for such set are tho contradictory ones:

- the set should include ^{11}C parents with minimum leakage that would bring systematic error to the analysis
- the set should not include too much non-parent events as the typical τ should not be much smaller then ^{11}C lifetime

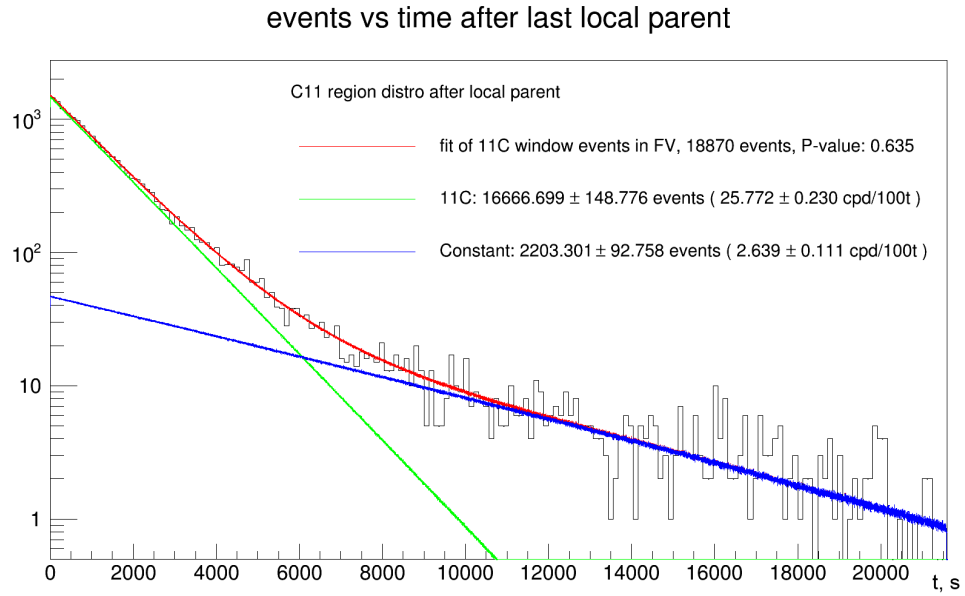

Figure 4.17: temporal fit of ^{11}C region
Fit of Phase II data in 11C region vs time from the last parent TFC veto covering the point of corresponding event.

The possible solution of this problem is usage of TFC with stricter tuning taking the starting time of last veto that, covering the position of ^{11}C candidate, for which τ is computed. The geometrical nature will thus require geometrical uniformity for toy Monte-Carlo calculation of differential exposition as τ will become positional-dependent. This could provide parent leakage of less than 1 %, still leaving the possibility to disentangle constant background from ^{11}C (see fig. 4.17). Nevertheless, it is much more precise than all other possible approaches and TFC precision efficiency is seen to be exceeding 93% if one takes constant component derived with consideration of systematic shift into higher values due to parent leakage.

4.6 Monte-carlo simulations

Every modern experiment in particle physics relies on monte-carlo simulation since not every king of physics could be studied independently in real calibration. Monte-carlo simulation of a scintillator-based detector could never be easy, but it is still very important since there are plenty of processes that could not be accounted otherwise. The Borexino detector analysis framework includes monte-carlo simulation done with maximum available precision allowing to reconstruct even quite

nontrivial parameters such as pulse-shape discriminators.

The simulation software is based on Geant 4 framework that is based on concept of using all processes user-definable, although modern packages of this software usually include quite a lot of different interaction libraries. In case of a scintillator it is intrinsically important since properties of detector target are significantly dependent on the real detector operation conditions.

Particle simulation on energies of order of 1 MeV considers mostly electromagnetic processes and thus it could be done without much unknowns. The only specific part is the Ĉerenkov light production since refractive index has some spectral dependence that should be accounted according to external measurements.

Scintillation process is modeled according to the measurements of the scintillator spectrum and quenching as well as temporal light distribution with a single parameter of light yield scaling the whole photon spectrum produced. Light absorption and reemission are also simulated with measured spectra and single scaling parameters, being made as close as possible to physical detector. The same approach is used in case of all materials used in the detector, although reflective properties of all materials are parametric since all available information is once again spectral; reflective properties of non-polished surfaces also consider some empirical "ground surface" reflective model.

Construction of the detector in monte-carlo is practically full and includes everything that is located inside the detector (fig. 4.18) The only specific part of geometry that deserves specific attention is the vessel, which, having quite low affection on light propagation, still plays a significant role in light distribution since it separates media with different optical properties. The vessel deformation is considered on weekly basis according to the studies done by fitting ^{210}Bi events on the vessel with a function that involves a Gaussian in respect to radius, and describes the vessel with Lagrangian polynomials in therms of polar angle under assumption of cylindrical symmetry, that is quite expected due to such symmetry of the detector as well as of gravitational force affecting it and could be demonstrated by fitting a ring on the equator of the detector.

In order to account for detector nonuniformities one uses effective quantum efficiencies for the PMTs, in this case the value normalized to the same mean for sets of PMTs with and without light guides independently since light guides are simulated inside monte-carlo model itself. This allows to reach very high precision of light collection reconstruction all over the detector (fig. 4.19).

Having a very large number of parameters inside the monte-carlo model it is very important to tune them all together in order to reproduce the physical processes close to the way they are taking place inside the detector. The task of tuning is quite sophisticated and involves a scheme, bringing parameters into the place (fig. 4.20), applied on calibration data on various source in various positions.

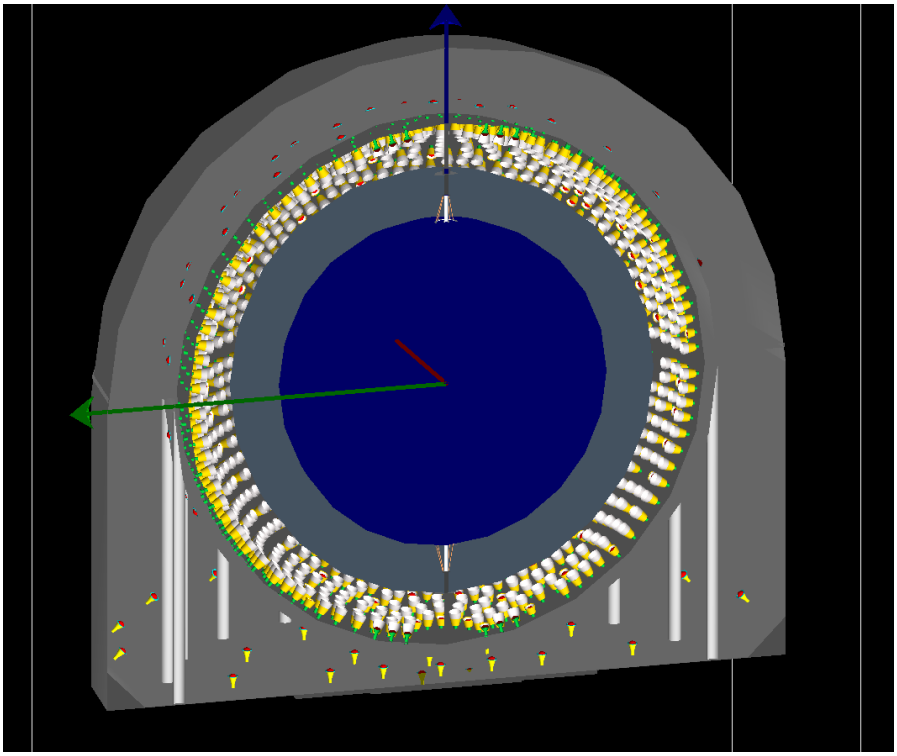

Figure 4.18: 3D render of Geometry used in the MC simulation of the detector, part of the detector is not visualized to show internal part.

It is worth mentioning that all parameters, even attenuation lengths fall nearby their measured values in close proximity so Mote-carlo tuning brings the simulation software to good compatibility with real data. Input particles in monte-carlo simulation could belong to all varieties of backgrounds in the detector. One specific part belongs to external gamma-background. Since external activity is very large, it is practically impossible to simulate it as it is so the simulation was separated into two parts, where first was simulated only propagation of gamma-quanta with importance biasing (increasing importance factor from outside to inside in layers with propagation between layers involving splitting a particle into several of destroying a particle with corresponding probability), and second originated from previously derived energy deposits and simulated light only in region of interest. Such approach allowed optimization of the simulation making it possible to simulate real statistics in 5 years with reasonable computational complexity.

The monte-carlo simulation framework is broadly used in all kinds of analysis, studies and developments of pulse-shape discrimination, event shape discrimination, production of spectra, studying detector response etc. and everywhere it shows satisfactory agreement with all kind of data allowing to have any kind of

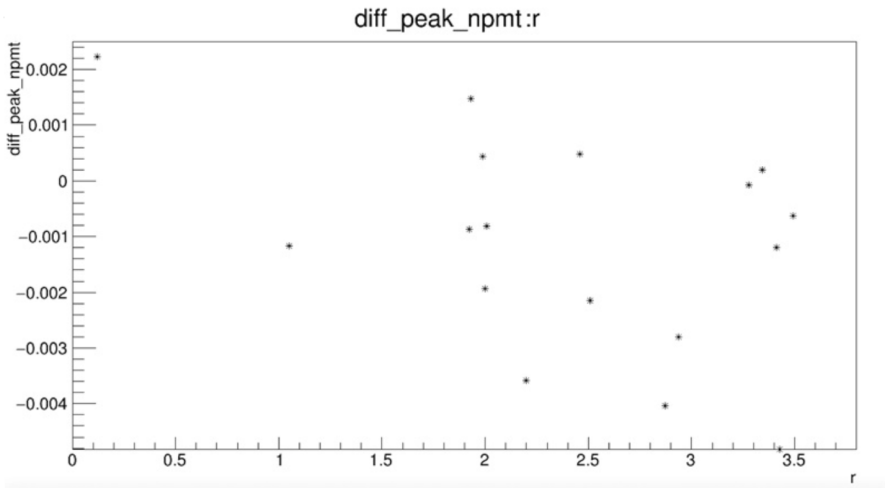

Figure 4.19: Light collection reproduction of MC simulation checked on various monoenergetic gamma-sources in units ($\frac{Q_{mc}-Q_{center}}{Q_{center}}$) in respect to distance to the center of the detector, demonstrating that reconstructed light collection lies within 1% of its real value

event inside the detector with consideration of all physical processes. For this purpose it also includes simulation of detector electronics, merging data with physical dark rate(channel-dependently) and producing binary file fully compatible with the generic data analysis framework, containing also some additional information that could be known only in case of monte-carlo simulation. That allows simple simultaneous analysis of real and monte-carlo data and increases efficiency of monte-carlo implication.

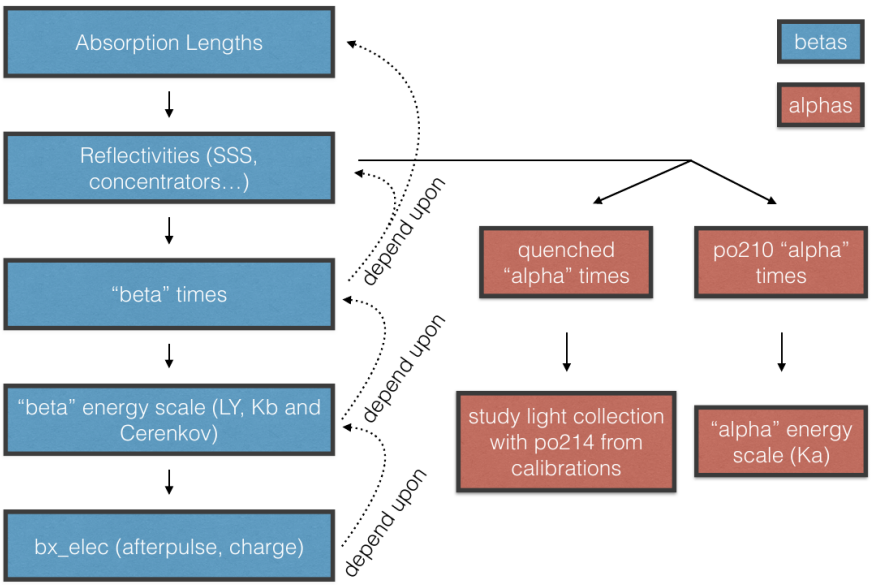

Figure 4.20: Graphical scheme of monte-carlo simulation tuning operations, showing consequence of parameter tuning for reproduction of physical calibration data

Chapter 5

Borexino phase II preliminary analysis of low-energy solar neutrino spectrum

5.1 Analysis approach

Generally speaking, Borexino is a calorimeter with some energy resolution so it produces an energy spectrum of events with some additional information on geometrical distribution, coincidences, pulse shapes etc. The purpose of analysis effort is identification of all spectral components for the sake of extracting information on neutrino fluxes that are present in the spectrum. Complexity of analysis is due to the large number of components of the spectrum. The basis of analysis of low-energy part of the spectrum (below 2 MeV) is in maximum likelihood fit with spectral components input into the fit in convolution with some detector energy response function. Since there are a lot of them, one has to involve complications of the fit with various approaches, such as pull terms or simultaneous fitting of a number of histograms in order to introduce additional information coming from independent studies of backgrounds in the detector. Such approach becomes possible only in case spectra are known, that means some assumptions on neutrino spectra, at least for continuous components, Luckily, only pp-neutrino and CNO neutrino have continuous spectra, while matter oscillations do not affect pp-spectrum due to low energy and CNO is simply very difficult to extract from the spectrum so minor differences in the shape are still not crucial. All the other components have known energy spectra since they belong to background composition.

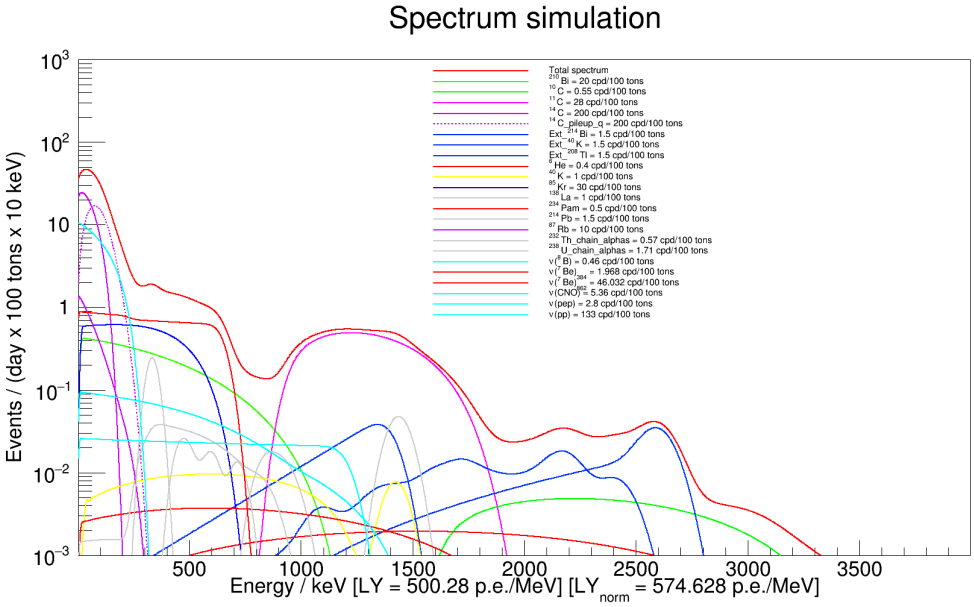

Figure 5.1: Simulated spectrum of the detector below 3.5 MeV. Simulation considers detector response in the beginning of Phase II, rates of components are expressed in units of counts/day/100t. Some natural activity components are set to Phase I values. The aim of this plot is to show principal spectrum composition and it has nothing to do with real experimental data.

5.1.1 Borexino spectrum below 3 MeV

The expected spectrum of Borexino is shown at fig. 5.1. It includes four statistically significant neutrino electron recoil components, that include pp-neutrino, ^{7}Be neutrino (2 lines of 384 keV and 862 keV), pep-neutrino and CNO neutrino. The same time in the spectrum there are several kinds of background.

Natural and long-lived cosmogenic internal radioactivity is represented by ^{14}C, ^{210}Bi, ^{85}Kr, ^{210}Po, ^{40}K. Polonium and bismuth are respectively daughter and parent nuclei, but in the detector they are out of balance due to different chemical properties; Bismuth itself is relatively short-lived and is originated from ^{210}Pb, but energy of this decay is very low and thus totally shadowed by ^{14}C. Still , bismuth lives too long for fast coincidence discrimination. The same time ^{14}C has rate high enough to produce pile-ups with all the spectrum, where statistically significant ones are only pile-up with ^{14}C itself and ^{210}Po. Pile-up is the major problem in pp neutrino studies.

Another background is cosmogenic and is represented by two carbons, ^{10}C and ^{11}C as well as by ^{6}He; other cosmogenic backgrounds are not statistically significant in low energy region and play their major role only at higher energies. The most

important of them is ^{11}C which lives quite long and could be treated specially with TFC veto system. These backgrounds play a very important role in studies related to pep and CNO neutrinos.

The last piece of the puzzle are external backgrounds that are mostly represented with ^{214}Bi, ^{208}Tl and ^{40}K. These backgrounds originate from sources which are several orders of magnitude stronger than every internal background, around 10 kBq, and are strongly suppressed by attenuation in the buffer. They could be treated through strong radial dependence, thus they could be even extracted from the spectrum if needed. Still, they are quite a problem in low energy region studies. The same gammas also intensively scintillate in the buffer and, being below trigger threshold, strongly pile-up with the spectrum creating another component.

Such a complex spectrum is a very difficult task to deal with, since there are a lot of different correlations that would lead to a very sophisticated likelihood profile in the minimization procedure with a large number of unphysical minima and large statistical uncertainties on most of the amplitudes. The most remarkable correlations are:

- ^{210}Bi and CNO neutrino. Extremely strong, there is nearly degeneration on the detector statistics
- pile-ups and pp neutrino. Also extremely strong, even stronger than in case of bismuth and CNO neutrino
- cross-correlation of ^{210}Bi, ^{85}Kr, ^{210}Po and ^{7}Be neutrino recoil electrons together with detector resolution. It could strongly affect measurements of ^{7}Be neutrino and should be taken with care in analysis
- pep- and CNO-neutrino. Another quite strong correlation caused by lack of resolution power

All these correlations make an idea of simple energy spectral fit a real nightmare. They have to be broken, otherwise no neutrino flux measurements are possible, at least up to a valuable precision level.

5.1.2 Generic approach of spectral fitting

The spectral analysis performed is based on likelihood maximization fitting. Generally speaking, the likelihood function used for fitting is simply binned Poisson likelihood, that could be written as

$$L = \prod_{bins} \frac{\lambda^x exp(-\lambda)}{\Gamma(x+1)},$$

where x is the number of counts in the bin and λ is the number of counts expected from the model. There are two approaches for model development. One of them is usage of monte-carlo framework for components simulation with consequent passing of monte-carlo data through the standard data-selection chain. Another way is going through analytical approach, in which components are modeled the following way: one considers backgrounds to have some spectral shape

$$P_i(E) = \int P_{i0}(E) \times F_{resp}(E - E_0) dE_0,$$

where $P_{i0}(E)$ is the spectrum of i-th spectral component and $F_{resp}(E - E_0)$ is the detector energy response function, modeling the actual detector response for a delta-function of energy E_0. The expected number of counts in a bin is computed by multiplication of the response function value at the center of the bin and the corresponding bin width, so under assumption that the spectrum is not changing significantly within a bin.

The actual function used in minimization is constructed as the sum of negative logarithmical likelihood and, if necessary, some additional terms:

$$-ln(L) = \sum_{bins} \lambda + ln(\Gamma(x+1)) - x \times ln(\lambda) + \Lambda_{add} \tag{5.1}$$

In case of unstatistical error in the bin, e.g. after statistical subtraction operations or in case of low monte-carlo statistics giving larger statistical error coming from model used one uses the Poisson likelihood scaling as

$$\theta = \sqrt{\frac{\delta x^2}{x}}$$

$$-ln(L_i) = ln(\theta) + \frac{\lambda}{\theta} + ln(\Gamma(\frac{x}{\theta} + 1)) - \frac{x}{\theta} \times ln(\frac{\lambda}{\theta}) \tag{5.2}$$

In this case the width of the likelihood distribution becomes the same as requested by the bin error, while the likelihood shape remains Poisson in order to maintain a possibility to treat low bin statistics correctly.

In order to input additional information,e.g. external and uniform backgrounds or amplitudes of some components derived independently, one could consider additional pull terms, creating additional minima related to the input values. E.g. , the uniform background part could be fixed as a pull term related to an integral of uniform background in some range, namely

$$V = \int_{E_{min}}^{E_{max}} \sum_{uniform} P_i(E) de \tag{5.3}$$

$$\Delta(-ln(L)) = \frac{(V - V_{expected})^2}{2\delta_V^2} + \frac{1}{2} log(2\pi\delta_V^2) \tag{5.4}$$

In case of absolutely flat basic likelihood, the error on integral V will be obviously δV, so the information about the expected value and the error is included into fit; One should understand that such expression is correct only in case of high statistics in V and assumes parabolic profile in the negative logarithmic likelihood function for estimation of this value from the radial distribution. In case of low statistics one should migrate to scaled Poisson distribution instead of Gaussian pull term.

Since TFC creates a veto system, it divides the detector into two parts, inside and outside the veto, enhanced and subtracted spectra. They could be fitted complementarily, that means that the likelihoods are multiplied and minimized together. Such approach allows to conserve statistics while using all advantages of TFC; all non-cosmogenic components apart from ^{210}Po, which is nonuniform in space and time, will remain the same in both spectra and thus will conserve statistics.

Another possibility is using not a pull term, that means adding some synthetic likelihood, but the real likelihood function of an independent approach measurement, e.g. for radial distribution fitted with monte-carlo simulated external and internal components. This is also a complementary fit and it is a more fair approach especially in case the independent measurement is not very precise. This approach is internally called "'multivariate fit"', but it is not a real multivariate in fact.

Overall, the negative logarithmical likelihood used looks the following way:

$$\theta_i = \sqrt{\frac{\delta x_i^2}{x_i}}$$

$$\begin{aligned} -ln(L_i) = &\sum_i \left(ln(\theta_i) + \frac{\lambda_{enhanced\ i}}{\theta} + ln(\Gamma(\frac{x_{enhanced\ i}}{\theta_i} + 1)) - \frac{x_{enhanced\ i}}{\theta_i} \times ln(\frac{\lambda_{enhanced\ i}}{\theta_i}) \right) \\ &+ \sum_i \left(ln(\theta_i) + \frac{\lambda_{subtracted\ i}}{\theta_i} + ln(\Gamma(\frac{x_{subtracted\ i}}{\theta_i} + 1)) - \frac{x_{subtracted\ i}}{\theta_i} \times ln(\frac{\lambda_{subtracted\ i}}{\theta_i}) \right) \\ &+ \sum_{additional\ histograms} \left[\sum_i \left(\frac{\lambda_{k\ i}}{\theta_i} + ln(\Gamma(\frac{x_{k\ i}}{\theta_i} + 1)) - \frac{x_{k\ i}}{\theta_i} \times ln(\frac{\lambda_{k\ i}}{\theta_i}) + ln(\theta_i) \right) \right] \\ &+ \sum_{pull\ terms} \left(\frac{(V_i - V_{expected\ i})^2}{2\delta_{V_i}^2} + \frac{1}{2} log(2\pi\delta_{V_i}^2) \right), \end{aligned} \tag{5.5}$$

where k runs over additional histograms and i is bin number on corresponding histogram. This likelihood should be filled with all possible information that could be derived from the data in order to break correlations and finally perform measurement of neutrino fluxes.

5.1.3 Data selection

The low-energy part of the spectrum should be prepared by data selection. Data selection was performed according to standard scheme with refusal of all shape cuts that were used only for run selection. Total exposure time appeared to be 1157.4 days including the dataset from 11 December 2011 up to 10 April 2016, finished by trigger system upgrade with prolongation only for special purposes, e.g polonium evolution studies.

In addition to quality cuts there was done removal of all muons with usage of all definitions excluding discrimination by excess of non-decoded hits within 0.3 s after the previous muon. The same time a veto of 0.3 s was applied after each muon together with 10 s cut after each muon suspicious for avalanche process (with the same definition of such muons as in TFC algorithm) in order to exclude aftermuon electronic features together with fast cosmogenic backgrounds. Fast chains are also removed with a criterion of coincidence within 2 ms and 1.5 m.

In order to proceed, the detector sensitive volume was fiducialized into 3 different fiducial volumes:

- "be7"[1] fiducial volume, $R < 3m$ and $|Z| < 1.67m$, 75.5 tons
- "pep" fiducial volume, $R < 2.8m$ and $-1.8 < Z < 2.2m$, 71.3 tons
- "conic cut fiducial volume" $R < 3m$ with cutting out all events located in cones with full angle of 90deg and originating in points (0,0,-2) and (0,0,2), so $|Z| - 2 < R_{xy}$., 99.3 tons

Cutting out the poles is important since light collection nonuniformity is stronger there due to light shadowing by vessel endcups. It appears, that there is no need of specific nonuniformity correction in first two volumes, while in the largest one it is needed. The volumes are separated enough from the vessel not to account for reconstruction of scintillation flashes on the vessel inside the fiducial volume even despite the vessel deformation, so fiducial volumes are defined as rigid spheres. Further enlargement in not useful due to significant increase of external background components.

[1] although the volumes are named according to some neutrino spectrum components these are just names; all components are fitted in every fiducial volume

5.2 Complex moments in the analysis

Complexity of solar neutrino spectral analysis is originating from internal correlations of the spectral components and thus it makes the likelihood function quite nontrivial. In this section we will review the approaches used of inputting additional non-spectral information to the fit bringing it to stable convergence to a single set of values of all backgrounds.

5.2.1 Pile-up events treatment approach

Pile-up spectrum is very strongly correlated with pp neutrinos. That means that understanding of pile-up shape and amplitude with enough precision is crucial for measurement of this neutrino flux. Thus establishment of spectral shape and amplitude of this background becomes a crucial point in pp neutrino detection.

There are two possible approaches of pile-up treatment, i.e. treatment of pile-up as a solid thing of pile-up of non-triggering signal with triggering one independently on the nature and division into components and detailed analysis. The first approach could be realized by convolving expected spectral PDFs with non-triggering signal of the detector, that could be obtained either from random trigger gates, either from normal trigger gates outside clusters. Both approaches bring in some risk: random trigger data contains poor statistics, while in normal trigger one unavoidably takes signal in correlation with triggering data, just right after a triggering hit cluster. The stability of the last approach could be tested by moving the window of hits, mixed out with normal data, but still such approach, which is called "'synthetic pile-up"' [68] is valid and, moreover, brings inside the amplitude of the signal automatically, although with some systematic uncertainty.

Another approach is based on various pile-up components, such as

- ^{14}C - ^{14}C
- ^{14}C - ^{210}Po
- External backgrounds in buffer - ^{14}C
- External backgrounds in buffer - ^{210}Po

This is obviously not the full list of pile-ups, but only these ones have statistical significance. Extraction of such events from data with pulse-shape or event-shape discrimination uniformly in energy is impossible due to lack of resolution power in existing approaches. Thus samples of each pile-up type can't be derived from data and the only approach is to use monte-carlo simulations and to try to fit random trigger data with this technique (fig. 5.2 or by fitting "'synthetic pile-up"' with monte-carlo data selected by the same criteria (fig. 5.3). The same

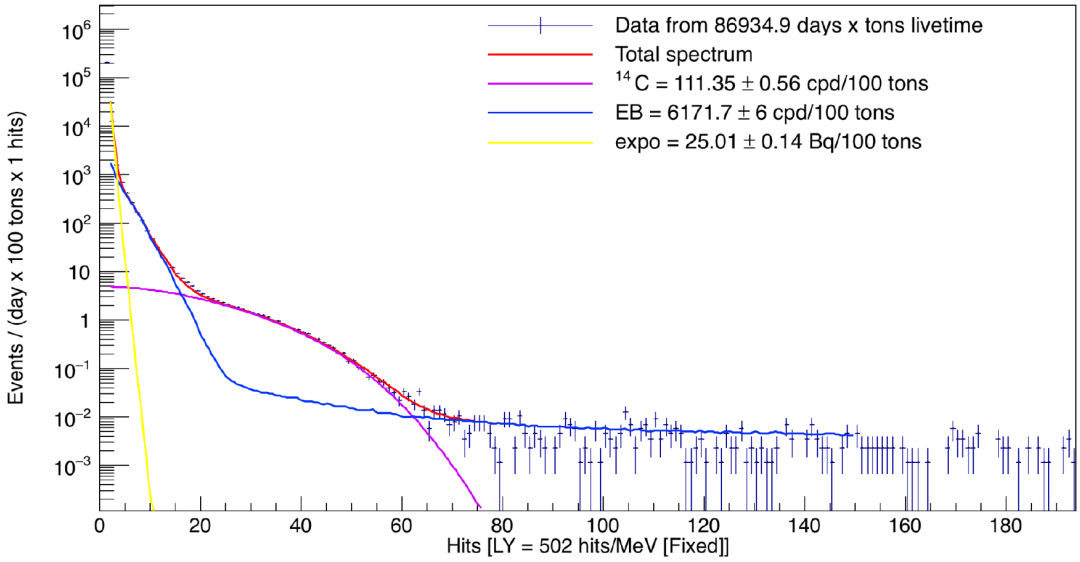

Figure 5.2: Fit of random trigger content devoted to discriminate various pile-up components

time we face the problem with amplitude of each component. Especially since the trigger threshold is close, triggering efficiency gets significantly below 100 % at the energies reviewed. In this case one could do the following: bound ^{14}C - ^{14}C component with some measurement of ^{14}C rate and put a pull term of pile-up integral in some range, e.g. 100-120 nhits, fixing ratios of backgrounds according to expectations from random trigger fit. In this case it is possible to resolve the correlation ant the only piece of the puzzle is ^{14}C rate.

Measurement of ^{14}C rate could be done by spectral fitting, but proximity of trigger threshold makes us input the unknown trigger efficiency curve. The solution is in usage of non-triggering clusters for the purpose since the threshold of them is coming from clusterization only(fig. 5.4). In this case it is possible to perform a fit and establish a rate of around 400 Bq/kt with acceptable precision although the statistics of non-triggering cluster is much lower.

5.2.2 Krypton problem

Another serious problem is cross-correlation of ^{210}Bi, ^{85}Kr, ^{210}Po and ^{7}Be neutrino recoil electrons together with the detector resolution. Cross-correlation of these fluxes is a severe problem for precision measurements of beryllium neutrino flux and could be weakened by applying some efforts on fluxes of krypton and polonium as well as by profound studies of detector response.

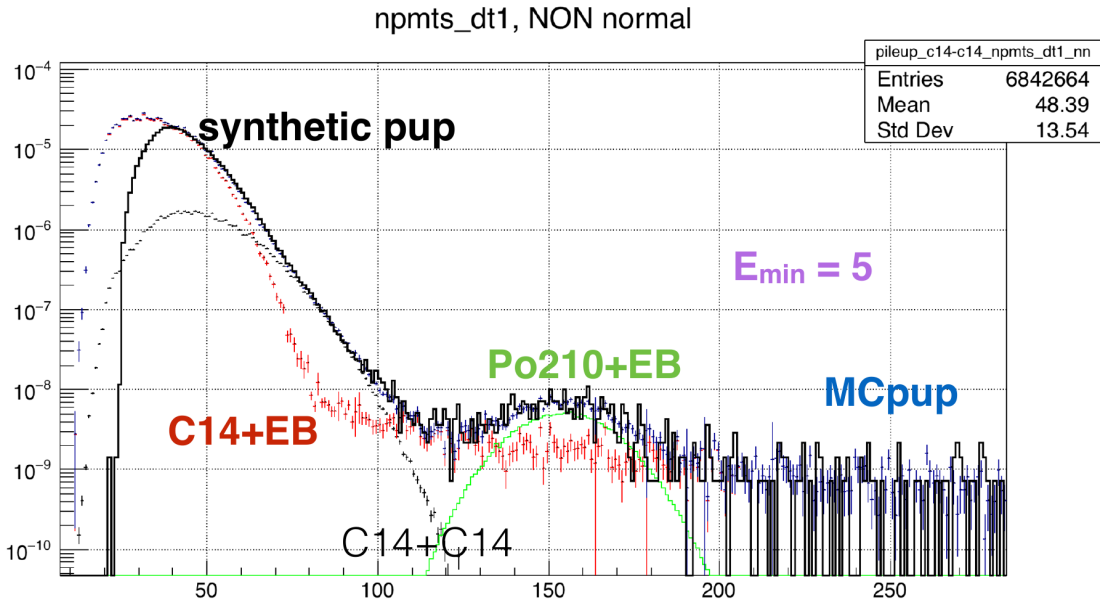

Figure 5.3: Fit of "'synthetic pileup"' devoted to discriminate various pile-up components. Threshold for piling up hits from the window with the data cluster is 5 hits.

One of the way of proceeding deals with krypton. It could be measured, although with relatively low precision with delayed coincidence scheme by a rare decay mode of $\beta + \gamma$. Here the problem is in very low energy of beta-event which is quite often below trigger threshold. The situation is that in Phase II of data taking it is not possible to detect krypton by this scheme and it is possible only to establish a limit of 4.9 cpd/100t at 95% c.l. Moreover, no krypton was detected in the detector after purification campaign by scintillator studies, so presence of this spectral component is not really expected. The same time, being included in the model composition, it could be reconstructed at quite high rates due to internal correlations and it can't be excluded by default since limit on its rate is quite weak. That makes quite strong problem that could be resolved by application of other correlation-breaking methods such as alpha-subtraction, but not in a very reliable way. There is one way of establishment of a better limit on this component. One could expect a noble gas with long live time to be uniform in volume. In this case, using coincidence data far away from the vessel with fiducial volume of approximately 200 t (so keeping away from accidental coincidences with bismuth of the vessel that could mimic delayed gamma), one could double the limit(fig. 5.5). That could make us more confident in absence of krypton more and thus to expect it not to be present accounting on it only as a systematic uncertainty source. Still, the fit could be done with a pull term on this flux bringing it to zero

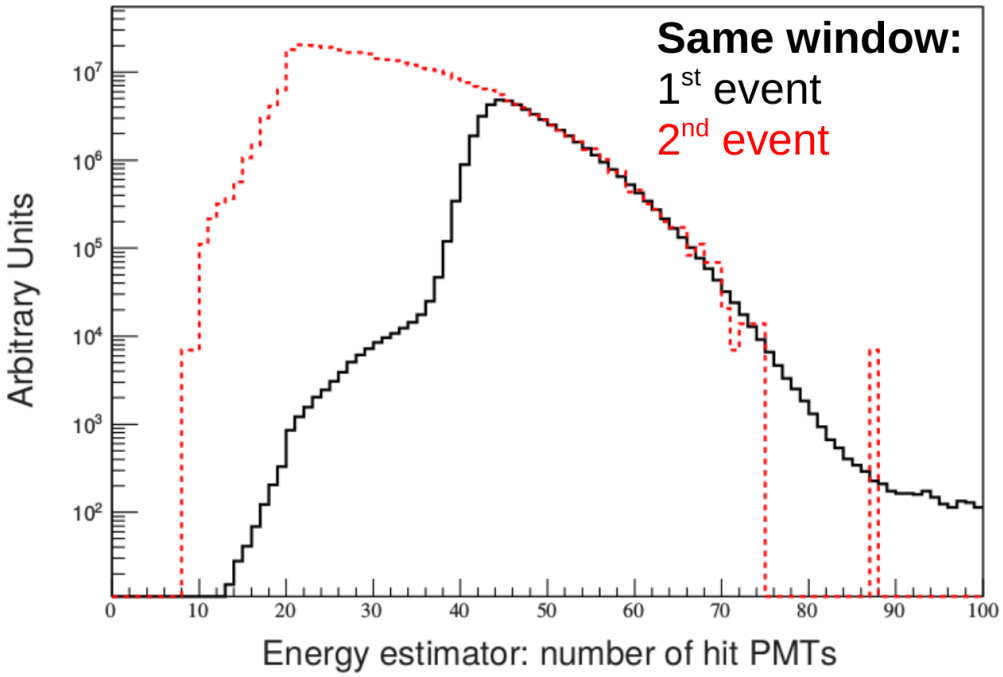

Figure 5.4: Comparison of data from 1-st and second cluster in the gate demonstrating possibility of deriving ^{14}C rate due to low clusterization threshold.

according to our expectations; such pull term should of course have uncertainty value corresponding to 68 % c.l. as arranged in the likelihood organization.

5.2.3 The story of ^{210}Po and ^{210}Bi

Another dangerous source of uncertainty is correlation between ^{210}Bi and CNO neutrino flux, practically prohibiting any attempt to register CNO neutrino. This correlation could be broken only through measurement of one of the components, the same way as with pileup and pp neutrino correlation. That means that one has to establish spectral shape of ^{210}Bi as well as amplitude of thus component inside fiducial volume. Since spectral shape is a measurable value, the main trouble is in establishment of amplitude. one should consider decay chain that brings bismuth decays inside the spectrum:

$$^{210}Pb \rightarrow e^- + \mu_e + ^{210}Bi \rightarrow e^- + e^- + 2\nu_e + ^{210}Po$$

Polonium is alpha-decayer and could be discriminated through pulse-shape approaches with efficiency of 99.4 % and its amplitude (that could be easily understood as it is a monoenergetic peak with a specific pulse shape) should be the

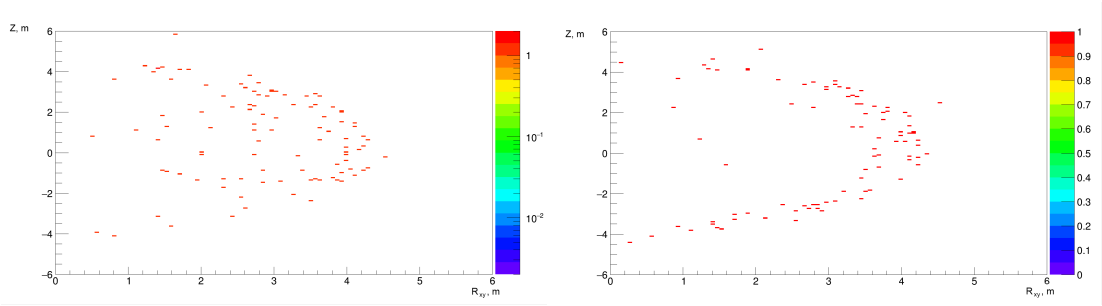

Figure 5.5: Krypton space distribution in data-taking phases I(left) and II(right). Event at around 4 m correspond to accidental coincidence of ^{14}C in the scintillator and ^{210}Bi on the nylon vessel. It is possible to notice good compatibility of this distribution with the uniform one in case of prominent separation from the vessel.

same as in case of bismuth. But polonium decays with half-life of 138 days and has different chemical properties in respect to bismuth and after purification these components are strongly out of equilibrium, resulting in having order of 50 times more polonium than bismuth. Polonium could bind to the scintillator chemically and thus be transported within the scintillator volume, including transportation from vessel endcups that has quite high internal concentration of this activity (and it is undetectable due to tiny tracklength of alpha inside nylon). It could be released from outside the fiducial volume in unknown amounts and quantities, still decaying inside fiducial volume, so we have polonium event rate density inside fiducial volume of

$$\frac{dR_{Po}}{dV}(t) = \frac{1}{\tau}\frac{dN(t)}{dV} \times + \frac{1}{\tau}\int_0^t \frac{d}{dV}A(t) + C, \tag{5.6}$$

where C is bismuth contamination and A(t) is an unknown flux that bringing polonium inside the fiducial volume from external sources. The only hope to get the bismuth rate is to find to nullify this term, at least locally and to perform an exponential fit of polonium decay to extract term C responsible for bismuth content. And this is a very serious challenge since one has to

- create detector conditions in which support term $A(t)$ nullifies at least locally in some volume
- find locality in the detector where one could neglect support term (exactly neglect, not limit from above: it could be both positive and negative, so the flux of polonium could be both incoming and outcoming) and demonstrate viability of such selection
- find a way to use local knowledge of Bismuth concentration for the whole fiducial volume and demonstrate its viability

Speaking about the first point of a puzzle, one should consider the following: the temperature in Hall C, where the detector is located is variated with time, following the year temperature trend since the tunnel is connected with ventilation system of the automobile tunnel, making the temperature conditions of the detector unstable: the detector is mounted on the rock with quite stable temperature. Temperature of the air is always higher, so the detector is constantly affected by a thermal gradient that is blocking movement over vertical axis, while in horizontal plane it is mixed out with quite high fluid velocity of order of 10 m/day. Still, the source of polonium works only over vertical axis, so such gradient is just making polonium distribution cylindrically symmetrical due to mixing (symmetry of the detector works against radial movement as well according to fluidodynamical simulations, performed by finite element approach (FOAM) in Boussinesq approximation). But every decrease of local thermal gradient immediately results in vertical mixing bringing polonium inside the fiducial volume. Construction of the detector also softens the situation since water layer of the outer detector works as a low-pass thermal filter, but the affection of temperature variation is still quite strong. In order to decrease the mixing was performed thermal insulation of the detector, that resulted in constant growth of thermal gradient through a significant part of Phase II of data-taking(fig. 5.6), as well as a system of active temperature control on the top of the detector, that allows to prolong the period of gradient growth in it will be needed in future.

Now let's move to the next subject, technology of polonium constant term extraction. Polonium could be separated by MLP discrimination parameter with efficiency known from the parameter studies as well as spectral fits and equal to 99.4 % on corresponding energy with negligible acceptance of beta-events. That means that we can track polonium inside the detector, dividing the fiducial volume into cubes and tracking polonium. It could be done under assumption of importance of only z-movement due to full mixing in horizontal plane. The idea is to find a clean bubble, where support term is nullified. Obviously one should have a minimum of polonium concentration is minimal, and since there is no production of polonium inside fiducial volume we would expect it to be the clean bubble searched since excessive transport outside some volume (negative support term) is hardly possible as it needs outgouing flux with concentration exceeding concentration inside the volume itself. Search for a minimum is proposed to be done with Unbiased Minimum Finder (UMF). This algorithm works through a weighted likelihood function of

$$L = \prod_i P(x_i|\mu)^{\omega_i} \tag{5.7}$$

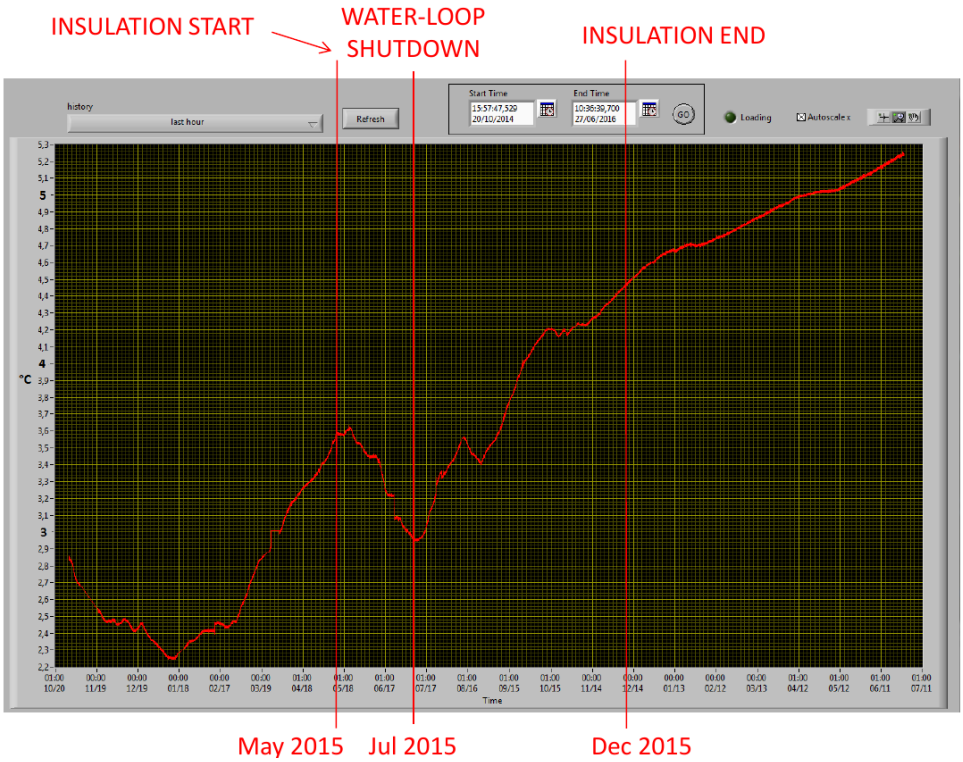

Figure 5.6: Temporal evolution of thermal gradient inside the detector. It is possible to notice that for quite a long time the evolution shows monotone growth, that is very positive in the sense of convective motion reduction.

, where weights are defined as scaled Poisson with scaling parameter s:

$$\omega_i = \frac{\frac{\mu}{s}\frac{n}{s}e^{-\frac{\mu}{s}}}{\Gamma(\frac{n}{s}+1)} \tag{5.8}$$

Applying Minimum Variance Unbiased estimator principle on centered distribution of variable θ,

$$E[\tilde{\theta}-\theta] = V_{ar}[\theta] + \delta^2_{bias},$$

One tries to minimize variance and thus bias (under assumption that all biases present work only in the direction of variance increase), finding scaling factor for likelihood corresponding to UME. With such approach one searches for the region (bubble) with minimal polonium value and the unbiased value in this bubble. Such operation is done on small temporal periods in order to be able to fit temporal distribution recovering the constant term of polonium content (with consideration of lead decay with live time of 32.3 years). The bubble movement is illustrated on fig. 5.7. The temporal distribution was fit for derivation of bismuth content

(fig. 5.8, giving the final value; Statistical agreement of the fit and stability of last part where exponential is dominated by constant term confirms the hypothesis of nullifying support term on the bubble, while precision achieved allows to break the CNO-bismuth correlation in the spectral fit. Still, this approach contains quite a number of assumptions that could bring some systematic uncertainty on the final value that be quite significant.

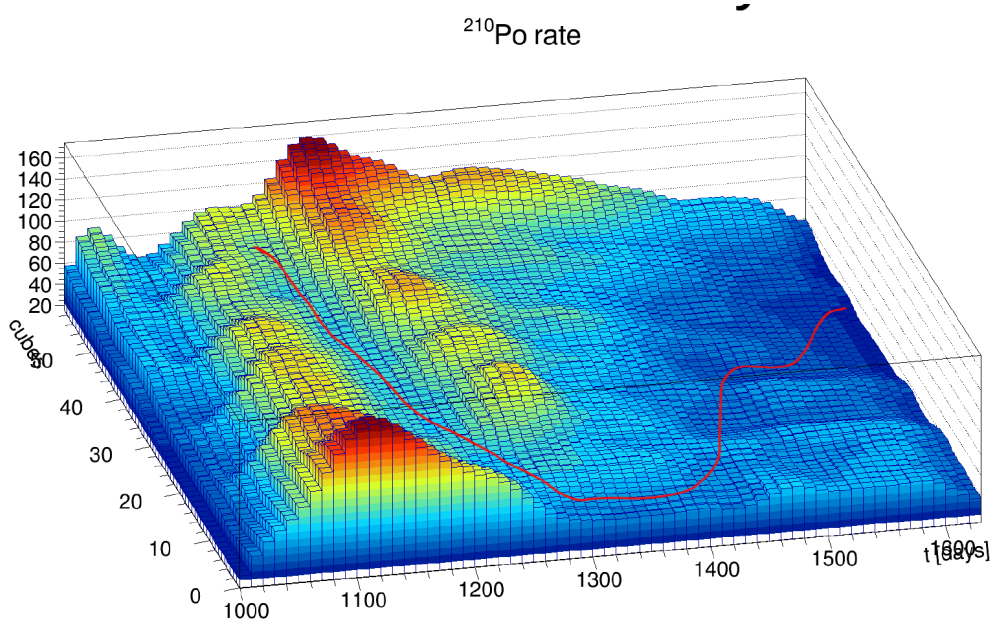

Figure 5.7: Trajectory of lowest concentration of polonium(clean bubble movement) in the detector evolution; Cube number increases in a monotone way with Z coordinate

The only point remaining is bismuth content, that could be checked by simple counting analysis to be uniform(since one could find an energy region, where bismuth is the only significant non-neutrino component, while neutrinos interact uniformly over the detector due to low cross section that can not sensibly reduce their flux). Satisfactory uniformity of lead in the fiducial volume is one of the most solid properties of the detector, allowing to measure bismuth content only per some limited region and generalize it for the whole fiducial volume. Now all tasks established are more or less satisfied and it is possible to apply a pull term for bismuth content in the fit likelihood.

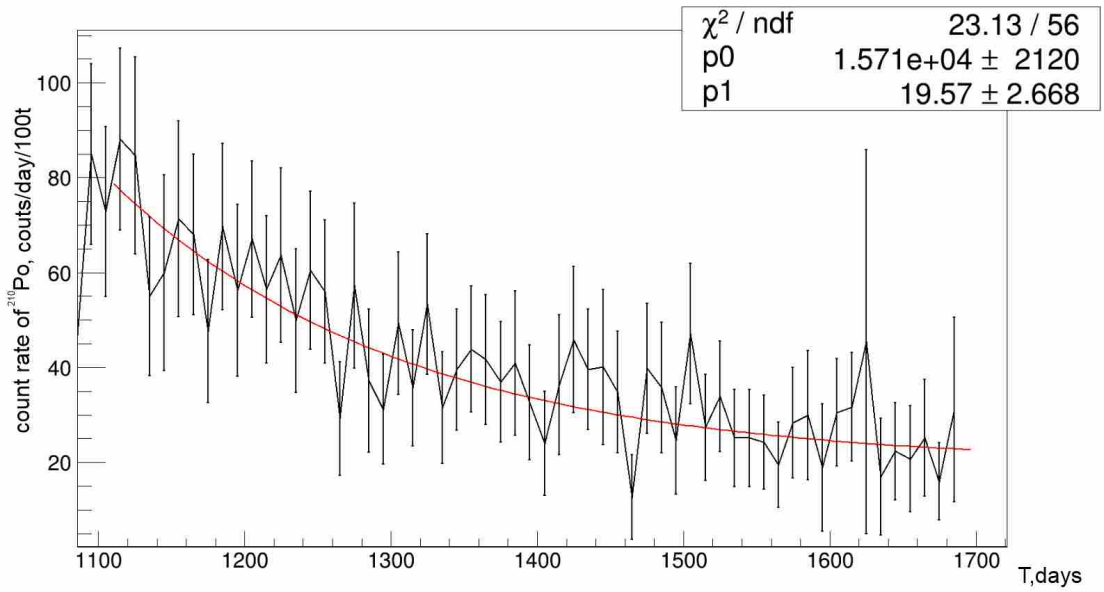

Figure 5.8: Temporal fit of Polonium content in the clean bubble, found by unbiased minimum finder.

5.2.4 Full MLP-subtracted fit

Another powerful tool of correlation braking is alpha-subtraction. But since it is a pulse-shape algorithm and hit statistics is limited, such approach is automatically energy-dependent. Energy-dependence is to be studied and applied in the fitting procedure. Such studies could be performed on pure beta samples, taken from calibration data as well as for all types of events in mote-carlo simulation. The results of the studies are presented on fig. 5.9. Since the detector conditions change (number of active PMTs decreases), it is hardly possible to believe in conservation of parameters, but exponential trends could be expected for beta-events and we will assume the same trend for alphas (confirmed by monte-carlo studies), but the parameters of the function are quite impossible to expect to be conserved. The way out is to try to describe the spectra distortion with exponential functions for alpha- and beta-events with some parametrization. One should also consider, that

- variables with fixed window clusterization could correlate with MLP through intrinsic MLP parameters at large times and thus will not have exponential dependence - they can not be used in alpha-subtracted fits
- pileup events will have dependence different from alpha- and beta-scintillation. MLP subtraction should be applied only outside regions, where pileup has any statistical significance

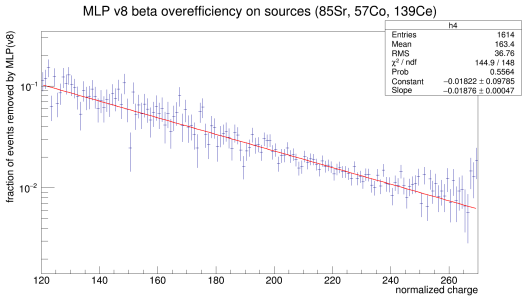

MLP charge dependence, calibration

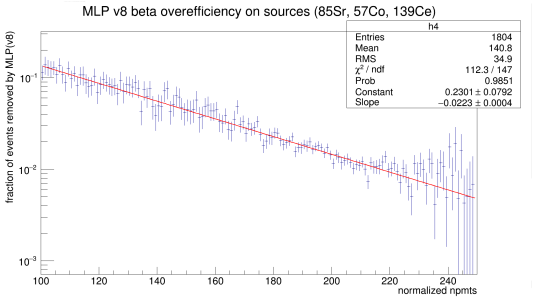

MLP npmts dependence, calibration

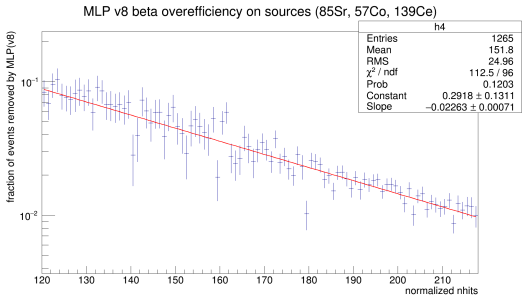

MLP nhits dependence, calibration

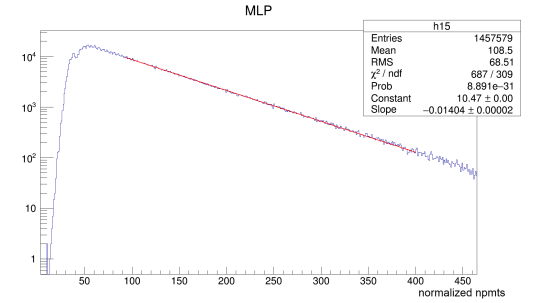

MLP npmts dependence, MC

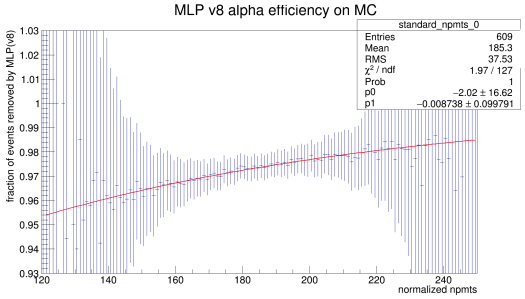

MLP nmpts dependence,
alpha-particle, MC

Figure 5.9: Energy dependence of MLP parameter (fraction of events removed by the discriminator), studied on calibration data and monte-carlo simulation, all plots are showing dependence for beta-events apart from the lowest one; In all cases it is possible to see good statistical agreement with single exponential function description in the region of interest that could be seen from goodness-of fit

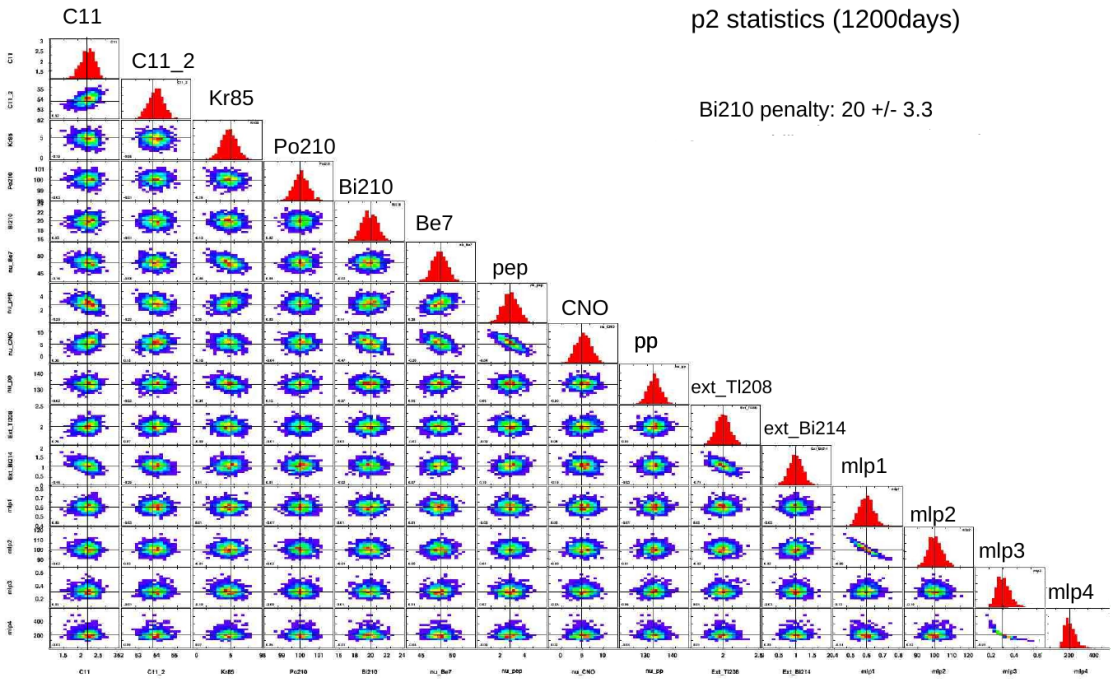

Figure 5.10: Correlation plot for MLP fitting approach test with toy Monte Carlo. Each point is shown on every correlation pattern is a result of a single realization fit. Vertical lines correspond to injected values of Toy MC. This plot demonstrates an ability of the fit procedure to reconstruct injected values of all parameters, including MLP corrections (a_β = mlp1,a_α = mlp3, b_α = mlp4, b_β = mlp2).

Taking all this into account, one divides data into two parts which are containing alpha-events (by MLP criterion) in polonium region and containing all events outside polonium region and beta-events outside the region, expecting spectrum distortion in the polonium region as

$$\begin{aligned} F(E) &= F_\beta + F_\alpha \\ F_\beta &= \left(F_\beta \times (1 - a_\beta exp(-E/b_\beta))\right)_{sub} + \left(F_\beta \times a_\beta exp(-E/b_\beta)\right)_{comp} \\ F_\alpha &= \left(F_\beta \times a_\alpha exp(-E/b_\alpha)\right)_{sub} + \left(F_\alpha \times (1 - a_{beta} exp(-E/b_\alpha))\right)_{comp}, \end{aligned} \quad (5.9)$$

where a,b are free model parameters and lower indexes of brackets divide PDFs into alpha- and beta - ones. Thus, finally instead of fitting a spectrum with total PDF F(E), we divide the spectrum into alpha and beta parts, fitting them with PDFs inside polonium region:

$$\tilde{F}_\beta = \left(F_\beta \times (1 - a_\beta exp(-E/b_\beta))\right) + F_\beta \times a_\alpha exp(-E/b_\alpha)$$

$$\tilde{F}_\alpha \quad = \quad (F_\beta) \quad \times \quad a_\beta exp(-E/b_\beta \quad + \quad F_\alpha \quad \times \quad (1 \quad - \quad a_\beta exp(-E/b_\alpha)) \quad (5.10)$$

The same time we will nullify $\tilde{F}_\alpha$ outside it, making $\tilde{F}_\alpha = F(E)$ outside polonium region, where we will define this region with some rigid bounds, e.g. 120-320 in nhits variable. Here the lower bound is the most important since it pileup should be statistically insignificant in respect to other components inside this region, but the region should cover as much polonium, as possible. Since we will have an additional histogram, dividing each spectrum into alpha- and beta-components, we automatically expand the total likelihood to

$$\begin{aligned}
-ln(L_i) = &\sum_i \left(ln(\theta_i) + \frac{\lambda_{enhanced\ \beta\ i}}{\theta_i} + ln(\Gamma(\frac{x_{enhanced\ \beta\ i}}{\theta_i} + 1)) - \frac{x_{enhanced\ \beta\ i}}{\theta_i} \times ln(\frac{\lambda_{enhanced\ \beta\ i}}{\theta_i}) \right) \\
&+ \sum_i \left(ln(\theta_i) + \frac{\lambda_{enhanced\ \alpha\ i}}{\theta_i} + ln(\Gamma(\frac{x_{enhanced\ \alpha\ i}}{\theta_i} + 1)) - \frac{x_{enhanced\ \alpha\ i}}{\theta_i} \times ln(\frac{\lambda_{enhanced\ \alpha\ i}}{\theta_i}) \right) \\
&+ \sum_i \left(ln(\theta_i) + \frac{\lambda_{subtracted\ \beta\ i}}{\theta_i} + ln(\Gamma(\frac{x_{subtracted\ \beta\ i}}{\theta_i} + 1)) - \frac{x_{subtracted\ \beta\ i}}{\theta_i} \times ln(\frac{\lambda_{subtracted\ \beta\ i}}{\theta_i}) \right) \\
&+ \sum_i \left(ln(\theta_i) + \frac{\lambda_{subtracted\ \alpha\ i}}{\theta_i} + ln(\Gamma(\frac{x_{subtracted\ \alpha\ i}}{\theta_i} + 1)) - \frac{x_{subtracted\ \alpha\ i}}{\theta_i} \times ln(\frac{\lambda_{subtracted\ \alpha\ i}}{\theta_i}) \right) \\
&+ \sum_{additional\ histograms} \left[\sum_i \left(\frac{\lambda_{k\ i}}{\theta_i} + ln(\Gamma(\frac{x_{k\ i}}{\theta_i} + 1)) - \frac{x_{k\ i}}{\theta_i} \times ln(\frac{\lambda_{k\ i}}{\theta_i}) + ln(\theta_i) \right) \right] \\
&+ \sum_{pull\ terms} \left(\frac{(V_i - V_{expected\ i})^2}{2\delta^2_{V_i}} + \frac{1}{2} log(2\pi\delta^2_{V_i}) \right),
\end{aligned} \quad (5.11)$$

where likelihood of alpha-part is computed only in intersection of polonium range and fit range, while beta-likelihood is computed in the whole fit range and without distortion outside polonium region. That means that we are now fitting four energy spectra with some additives in order to get the final result with quite sophisticated likelihood function, that allows to describe spectrum distortion and take advantage of both pulse-shape discrimination and TFC veto together with inputting additional information on pile-up and other measured background components.

The remaining issue is reliability of reconstruction of MLP corrections $a_{\alpha,\beta}, b_{\alpha,\beta}$ that are input into the likelihood as additional free parameters, sophisticating the likelihood function, although some additional information is input due to multiplication of the number of spectra participating in the analysis. This could be performed with fitting of synthetic data, sampled according to some modelled PDFs, so testing the procedure in a way decoupled from other effects. The result of such studies is demonstrated on fig. 5.10 and shows good reconstruction of MLP corrections, that were introduced in the spectrum manually with known injected values.

5.2.5 About goodness of fit

Since Borexino is a low-background detector and even these low-background data are divided into several parts, usage of classical χ^2 approach for minimization and goodness-of-fit treatment is not viable. Usually it becomes necessary to switch from χ^2 to Poisson likelihood mode when mean value of the distribution goes below 20, so at the level of 20 events per bin, and in case of our data, especially in case of TFC-subtracted spectrum the condition for χ^2 usage is not satisfied in most of cases. That stands for switching to entirely Poisson mode, forgetting about all χ^2-related values, such as ratio of χ^2 to number of degrees of freedom as goodness-of-fit estimator. We will use so-called p-value that will have the following meaning: it is the probability of having present or larger than minimized likelihood value in case of statistical distribution of data in respect to the model corresponding to best fit point. The most simple way is to sample histograms according to the best fit according to the model obtained in the fit and derive likelihood distribution corresponding to the model obtained in the fit (practically, it is an analogue of χ^2 distribution, but obtained for generic likelihood function with monte-carlo approach). Having this distribution F(L), it is quite easy to derive p-value as

$$p = \frac{1}{\int_0^\infty F(L)dL} \int_{L_{data}}^{\infty} F(L)dL \times 100\% \tag{5.12}$$

Obviously, perfect p-value is 50%, while 0% and 100% are both limit cases of infinite and null likelihood, both equally unacceptable. In principle acceptable p-values are to be established and we are going to use range $[10\%; 90\%]$, so we believe that the dataset could be inside more probable 80% of possible statistical distribution if the data is in agreement with the model. In fact, it is quite weak limit on acceptable p-value, the usual one in used in χ^2approach, dobled square root of number of degrees of freedom, corresponds to central 68%.

Another point related with goodness-of-fit is normalization effect. For instance, every variable used for energy estimation has to be normalized due to compensate the effects of detector evolution, but it appears that it creates a jitter in spectral data shape, for instance, if we normalize values of hits or PMTs fired (integer variable) from 0 to 1500 with a value of e.g. 1600/2000, we will have some bins with no content at all since rounding will fill bins before and after it. The solution is very simple: one could derive relative probability for filling a bin. It is done the following way: for all backgrounds constant in time we use distribution of live PMTs in each event; then we simulate a flat distribution of events with number of events proportional to number of events in a bin of this distribution and sum them up, simulating evolution of the detector, creating a distribution of relative probabilities of bin filling that we use to correct model PDFs. Analogically but independently we work with polonium since its rate decreases with time; distri-

butions of relative probabilities should be computed inside and outside TFC veto due to temporal nonuniformity of the veto and, possibly, some background components. In case of normalization using effective QE and(or) geometrical correction, it should be accounted in the normalization factor distribution. In case of charge the variable is not integer, but has integer nature(the number of photoelectrons) and thus still has such effect, although reduced. In this case it is possible to apply different dithering techniques, considering some small artificial jitter of value used for spectrum histogram filling, usually the addition has width of 1/2 photoelectron or is dependent on number of live PMTs. Such approach is not precise, but in case of charge a precise approach is possible only after potentially dangerous operation of rounding. In case of monte-carlo PDFs usage, the PDFs are coming from simulation of the real detector and thus spectral bins are reweighed with filling probability computed from simulation normalization factor distribution on PDF formation stage, making them smooth (fig. 5.11), removing goodness-of fit problems coming from the model. The smoothed model is fixed with data-derived bin filling relative probabilities within likelihood computation during minimization procedure.

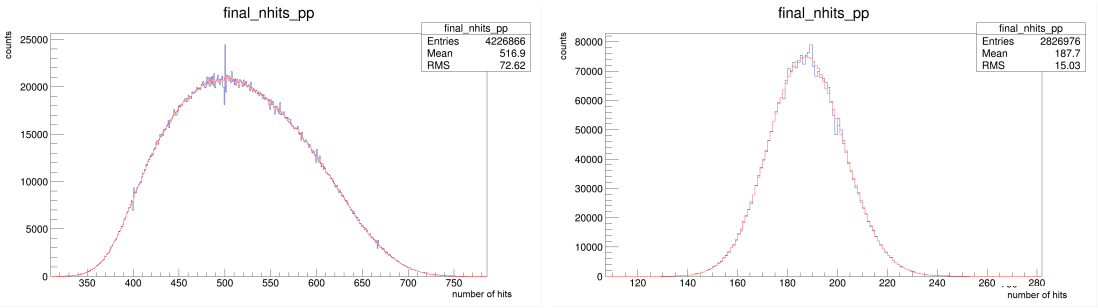

^{11}C, before and after PDF correction ^{210}Po, before and after PDF correction

Figure 5.11: Examples of monte-carlo PDFs correction by reweighing with relative bin fill probabilities for normalization effects compensation

5.3 Preliminary results

Here we will list the results obtained in the real data spectra fitting. The list of fits should include

- two PDF models: analytical approach(with some response function, e.g. [69]) and monte-carlo simulated
- three fiducial volumes: "'pep"', "'be7"', "'conic cut"'

- three different energy estimators, nhits, npmts, charge
- various ranges, including and excluding pp region
- usage of TFC and (or) MLP spectrum division with complementary fitting

Large amount of combinations of these fits allows to perform cross-checks and keep result stability. The combinations are limited by impossibility of low-energy part fitting in charge since effects of activity in PMT glass are not compensated and distort the spectrum severely; the variable accounting for problems with charge variable was created but was not produced for technical reasons.

The most simple fit is illustrated on fig. 5.12 and includes analytical fit of a single energy spectrum in npmt variable (with fixed cluster duration of 230 ns) with content convolved with contamination of first 230 ns of random trigger to account for various pile-ups. Such fit Has all correlations applied and overparametrizes the dataset, but it still converges to reproducible values due to appropriate choice of initial point close to physical minimum. Fluxed of pep- and CNO-neutrinos are fixed to MSW-LMA + HZ model since the fit is not sensitive to them. χ^2 treatment is valid for this energy region. Fig. 5.13 demonstrates the fit of simple energy spectrum with monte-carlo PDFs in nhits energy estimator with slightly extended energy range in three fiducial volumes. In this case the monte-carlo pile-up is used with appropriate penalty term and the fit is performed in all three fiducial volume; Full-scale p-value is now unavoidable since the spectrum partially includes low-content bins. Fluxes of neutrino are compatible in all fiducial volumes as well as in respect to previously mentioned fit.

Now we go in the direction of complicating the system: radial dependencies are used, ^{11}C treatment with normalized position reconstruction likelihood as well and we now work with complementary fit of two energy spectra according to TFC(fig. 5.14). The fiducial volume is pep and bismuth pull term is applied. Let's switch to charge. Charge reproduction in monte-carlo is not very good, so we work with analytical response, generalized gamma-function[69]. The same time we don't add ^{11}C and radial histograms into the likelihood scheme since in analytical approach with iteration-based convolution with response function it becomes technically impossible. The result in be7 fiducial volume with reduced dataset (exclusion of 2012, when polonium rate was the highest and bismuth content was nonuniform)is demonstrated at fig. 5.15.

Now let's consider also alpha/beta pulse-shape discrimination. Application of the fitting technique is done in two combinations of variable and fiducial volumes and is demonstrated of fig. 5.16. Bismuth pull term is applied as well in case of TFC application. Finally, the most full fit is demonstrated on fig. 5.17. It considers simultaneous discrimination of CNO- an pep-neutrino and gives us a

measurement of pep neutrino flux as well as some evidence of CNO neutrino at the levels of

- pep: 2.65 ± 0.7 cpd/100t that stands for $(1.31 \pm 0.35) \times 10^9\ cm^{-2}s^{-1}$ under assumption of MSW-LMA or $(8.6 \pm 2.3) \times 10^8\ cm^{-2}s^{-1}$ under assumption of no-oscillation scenario (MC multivariate fit in pep FV)
- CNO: 5.3 ± 1.8 cpd/100t that stands for $(5.2 \pm 1.8) \times 10^8\ cm^{-2}s^{-1}$ under assumption of MSW-LMA (analytical fit in charge in pep FV, MLP-subtracted, reduced dataset)
- ^{7}Be: 48.5 ± 1.16 cpd/100t that stands for $(4.94 \pm 0.12) \times 10^9\ cm^{-2}s^{-1}$ under assumption of MSW-LMA or $(3.148 \pm 0.075) \times 10^9\ cm^{-2}s^{-1}$ under assumption of no-oscillation scenario (analytical fit in charge in pep FV, MLP-subtracted, reduced dataset)
- pp: 137.7 ± 9.5 cpd/100t that stands for $(6.32 \pm 0.44) \times 10^{10}\ cm^{-2}s^{-1}$ under assumption of MSW-LMA or $(4.00 \pm 2.76) \times 10^{10}\ cm^{-2}s^{-1}$ under assumption of no-oscillation scenario (MC fit in conic-cut FV, spectrum only, MC pileup treatment)

Speaking about likelihood profiles and thus significance of fluxes in respect to null hypothesis, they could be derived only in case of monte-carlo fit (fig. 5.18) due to technical complexity, but in analytical approach they were demonstrated at leas to be symmetric with MINOS error treatment algorithm (varying parameter, minimizing with its fixed value and other parameters free and getting likelihood profile, but using also optimized algorithm for getting to desired likelihood excess in respect to minimum instead of full profiling) to be symmetric and thus is very likely to be similar.

5.4 Systematic uncertainty sources

Having a good statistical scheme of the fit is still to be related with the physics of the detector. For instance, in some scheme the fit is not allowing variations of some undefined variables and functions, e.g. monte-carlo PDFs include detector response, while its modeling is intrinsically imprecise. Some variables could be also railed to physical bound in minimization and thus not accounted in error estimations. Moreover, there are some detector properties that are affecting scaling of overall signal, e.g. exposure estimation. All these are sources of systematic and unconsidered statistical uncertainties. This uncertainties sources include

- exposure definition (fiducial volume and live time, full spectrum scaling)

- fixing ^{8}B neutrino flux - unconsidered statistical uncertainty
- ^{85}Kr content - rails to 0 and thus needs statistical treatment; Due to low importance in the fit should be variated according to coincidence-based estimate, at 68 % C.L level as all errors are treated this way
- internal ^{40}K rate - similar to krypton case, but without independent estimate
- in case of monte-carlo fit - detector response in terms of resolution and energy scale. Could be treated by convolution with a gaussian of variable width, providing resolution variation in positive direction (negative is intrinsically impossible) and by spectrum scaling

Among all these uncertainty sources the really systematic one (for current analysis scheme) is exposure estimation, so it is crucial to understanding of the final result; all the other sources are statistical, but need a modified fitting operation for estimation since fixing some parameters is simplifying the fit and is positive in physical minimum search, but is the same time a bias source that should be resolved after the minimum is found.

Speaking about exposure uncertainty, we have every reason to neglect time estimation uncertainty in respect to fiducial volume mass, since charge is collected by a scheme with zero dead time, rate of the detector is very low and the only source of uncertainty is GPS time of the system, giving less than 0.1 % overall [70]. Fiducial volume estimation uncertainty is one of the largest; it is related with biases in position reconstruction. These biases are small, but nevertheless not excluded; estimation was done in [71] by getting uncertainty on Z axis through specific calibration with fixed-length rods giving very high precision of position definition with consequent generalization of this uncertainty to XY plane; Still, this uncertainty is of order of 1% that is dominated by statistics in all cases.

One should take into account that in case of MINOS technique usage, variation of all non-fixed parameters is performed even in case of rails and thus it is not important to have anything railed in the scheme; Inclusion of pull terms automatically inserts independent knowledge into the likelihood. Independent variation is needed only in case of fixed parameters in the fit.

In phase I analysis systematic estimates included so-called "'fit method"' uncertainty source. The physical source of this uncertainty was related with resolution of response function used and is accounted in statistical scheme of the fit; Variations not allowed statistically evidence convergence to unphysical minima and should be ruled out by comparisons of goodness-of-fit as well as profiling at larger ΔL values that could give minima separation visualization. Luckily, in our case central values are in statistical agreement that evidences convergence to the same, most likely physical, minimum in all fit implementations.

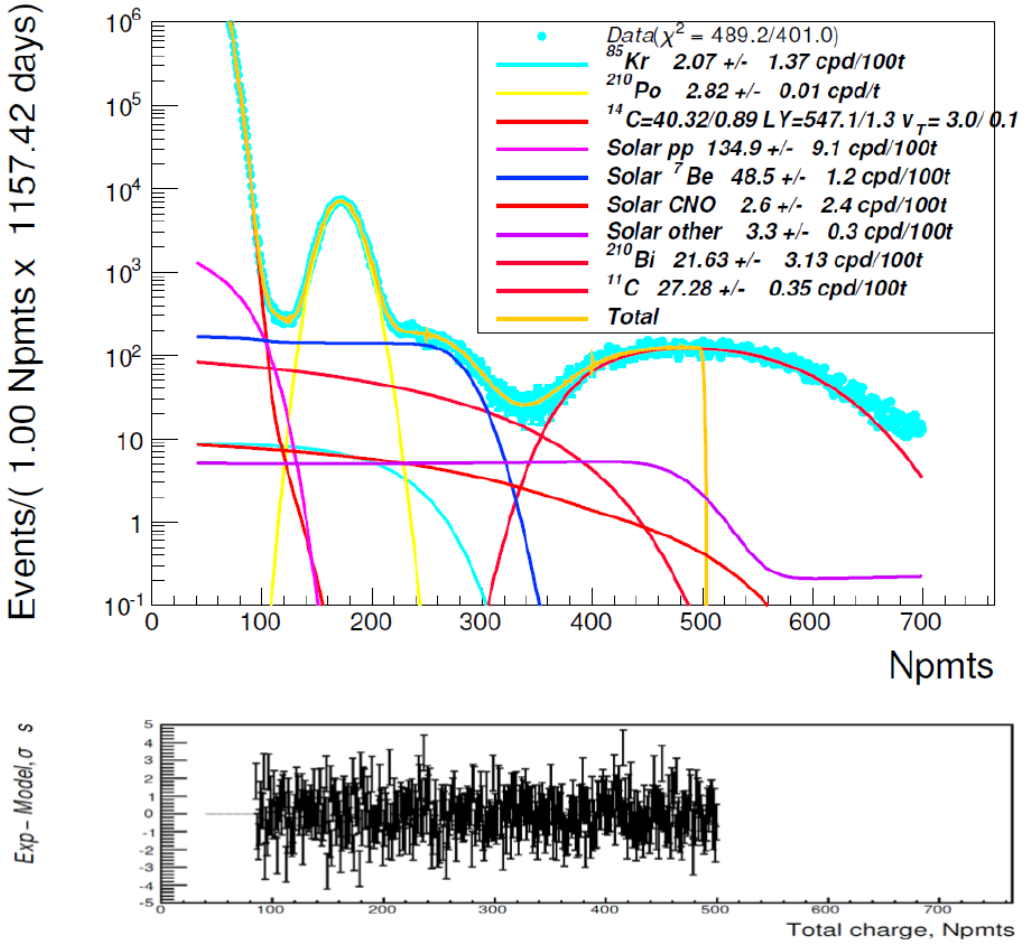

Figure 5.12: Example of Phase II data fit in units of number of PMTs hit within 230 ns fixed window; Pile-up is estimated through convolution with random trigger content.

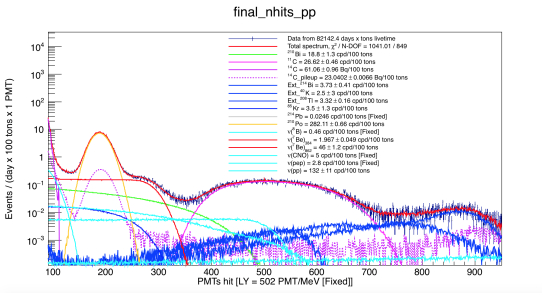

Fit in pep FV

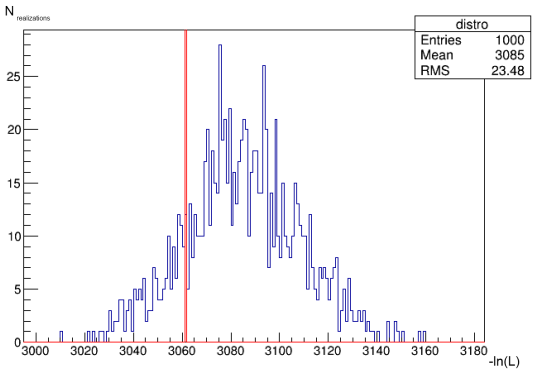

GoF treatment in pep FV

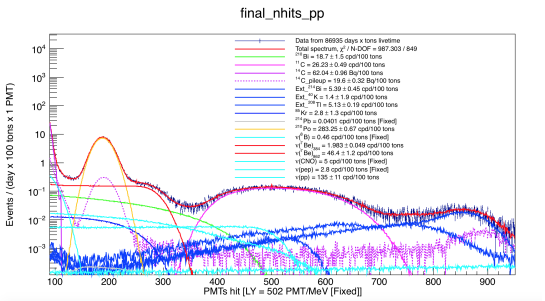

Fit in be7 FV

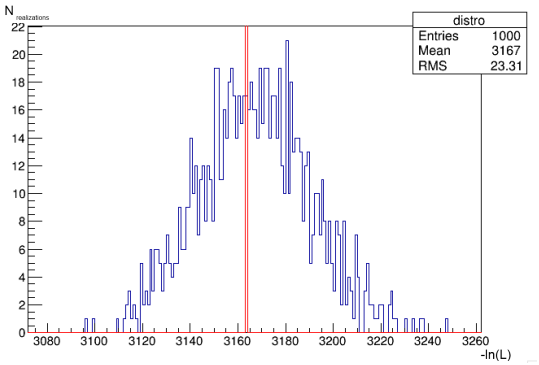

GoF treatment in be7 FV

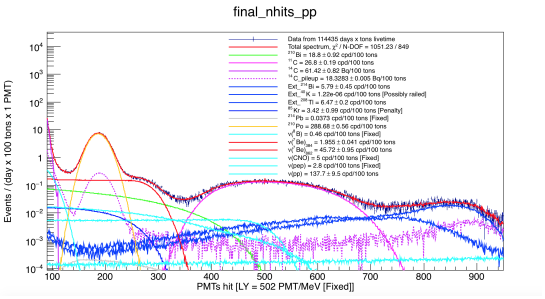

Fit in CC FV

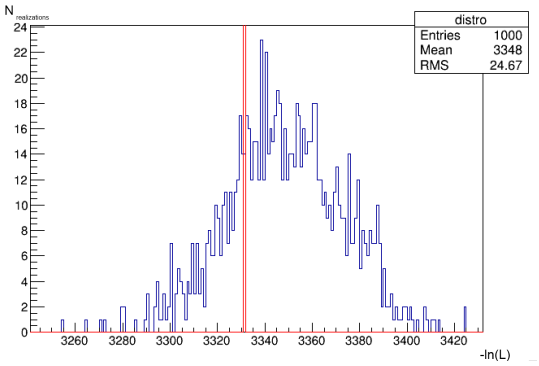

GoF treatment in CC FV

Figure 5.13: Fit examples with monte-carlo PDFs in three fiducial volumes; Pictures on the right show likelihood distributions sampled according to best fit functions and the actual dataset likelihood value.

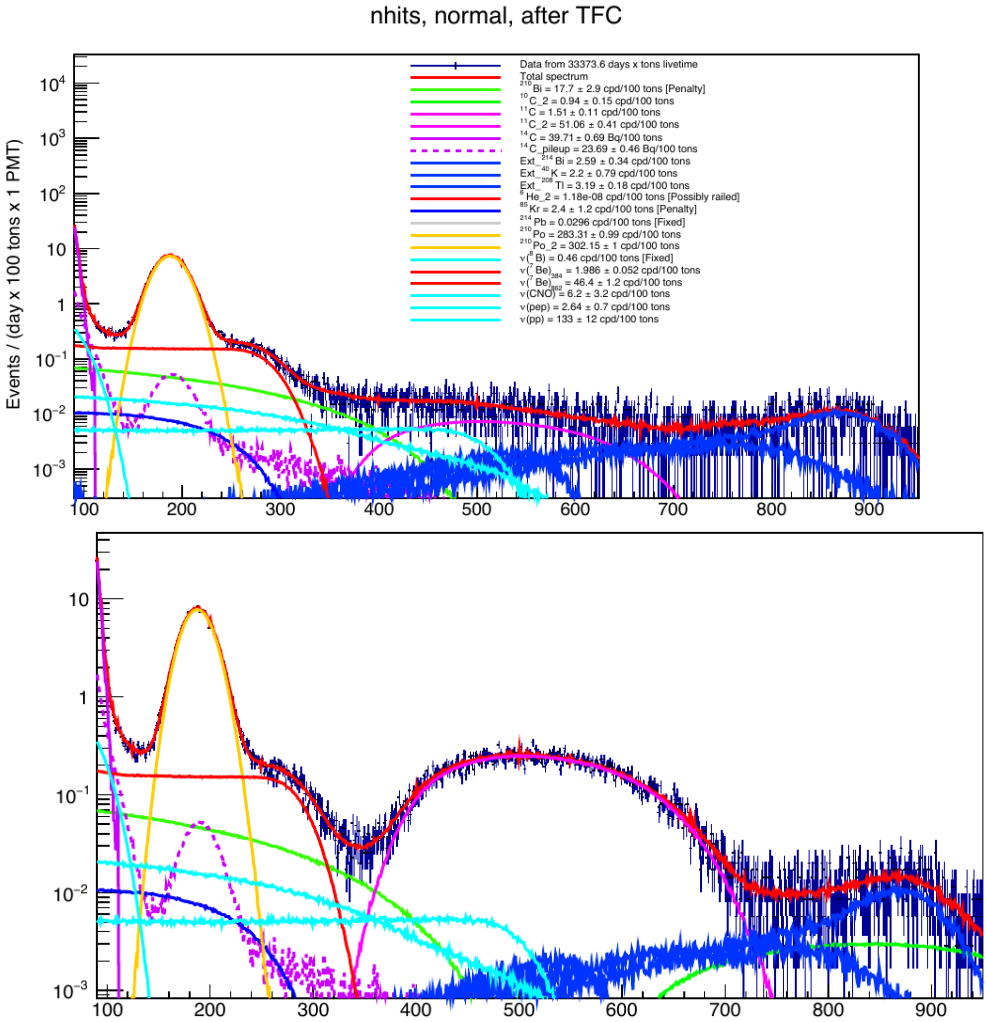

Figure 5.14: Example of fit of Phase II data with MC PDFs with full complementary set (radial dependence and electron/positron discrimination)

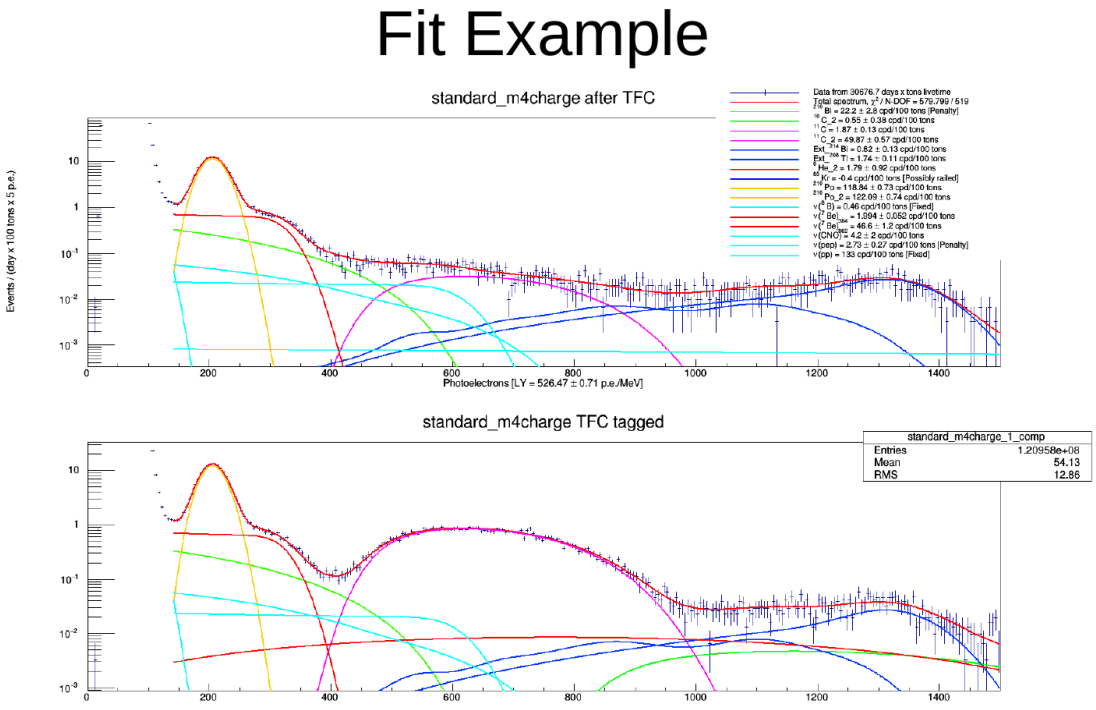

Figure 5.15: Example of fit of Phase II data in charge with analytical PDFs with bismuth and pep bounds (according to UMF measurement and former pp results, pep flux bounded with 10 %)

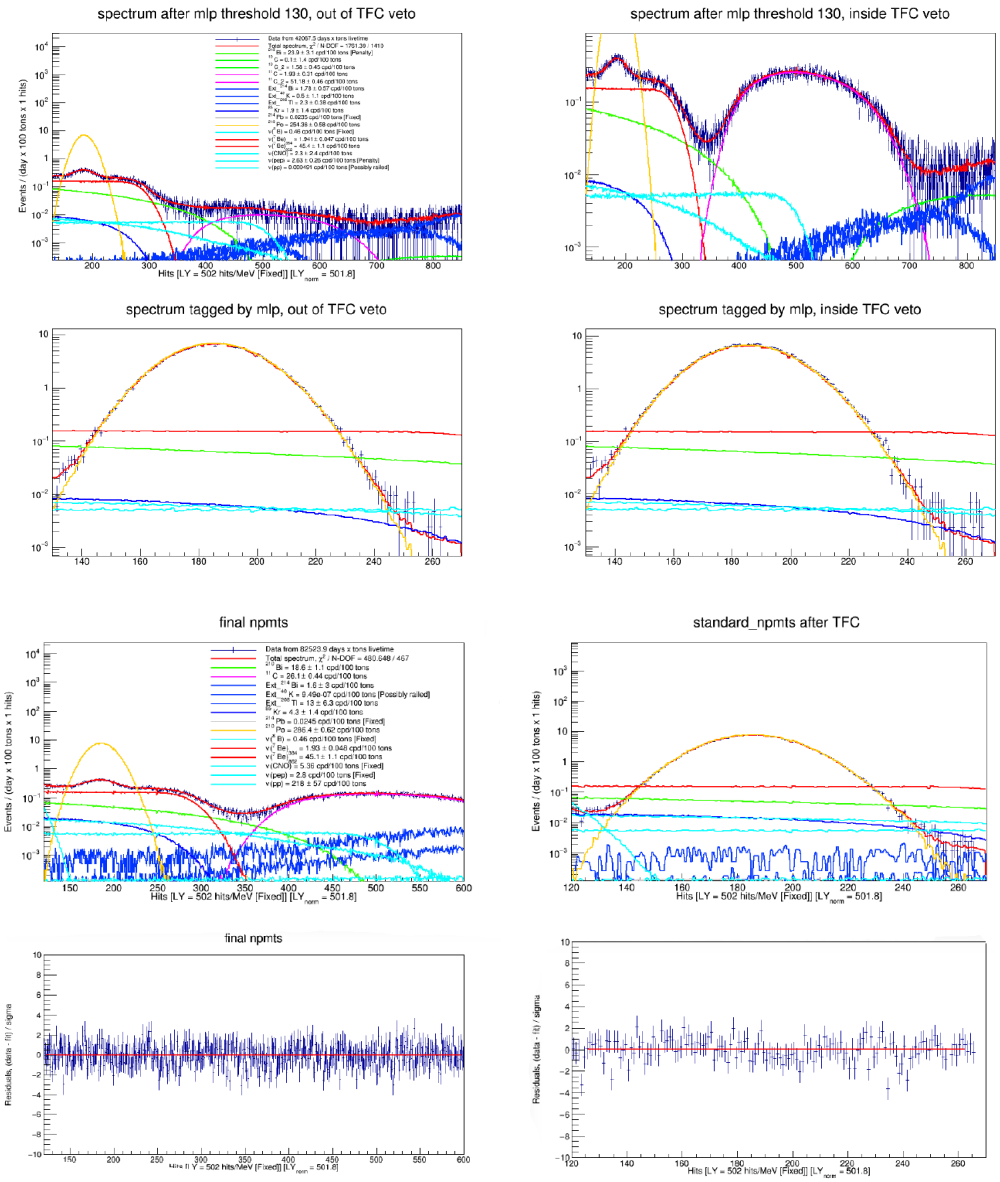

Figure 5.16: Example of fit of Phase II data with MC PDFs in nhits energy estimator(upper) and analytical PDFs in npmts energy estimator(lower) in be7 and pep fiducial volumes respectively in full MLP scheme with pull term on pep neutrino. Lower plots demonstrate residuals of the fit normalized to standard deviation in corresponding bins.

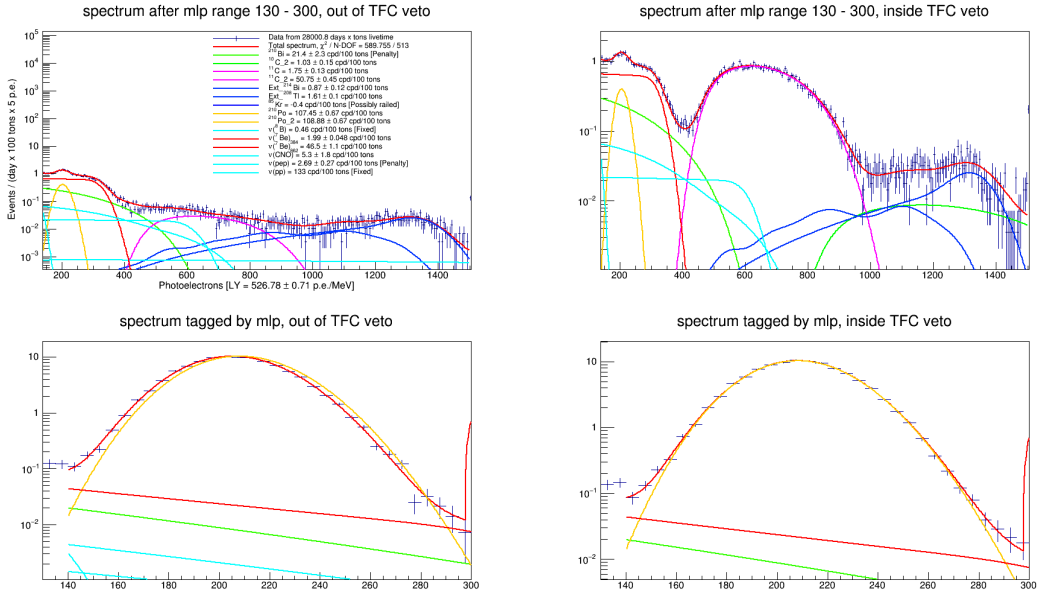

Figure 5.17: Example of fit of Phase II data in charge with analytical PDFs with bismuth and pep bounds (according to UMF measurement and former pp results, pep flux bounded with 10 %), with MLP histogram division in range 130 - 300 n.p.e.

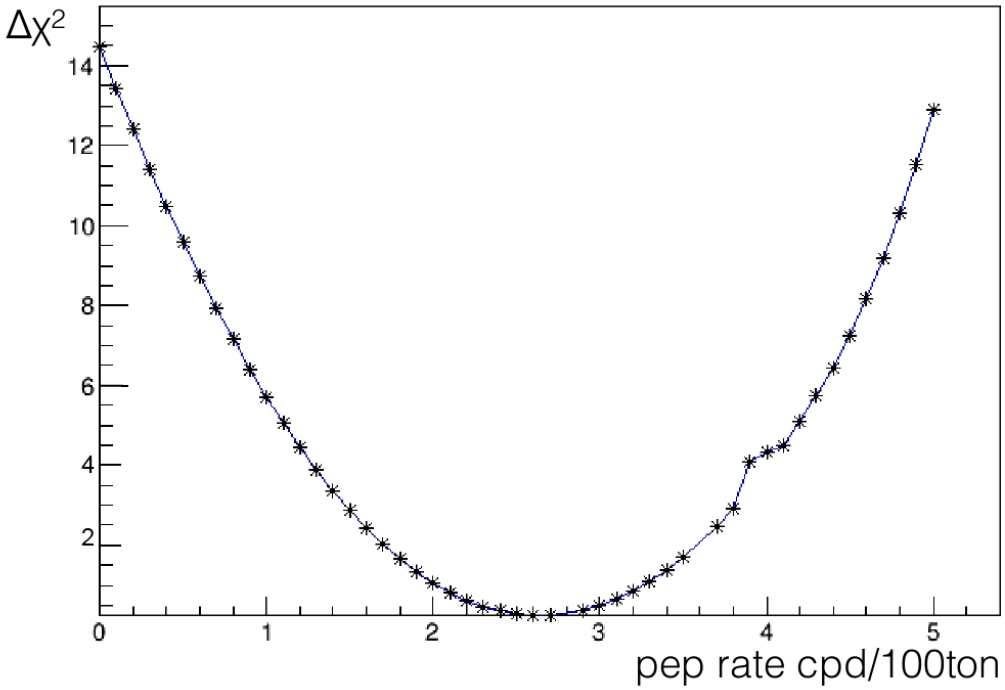

Figure 5.18: pep component likelihood profile for monte-carlo PDF full complementary set fit.

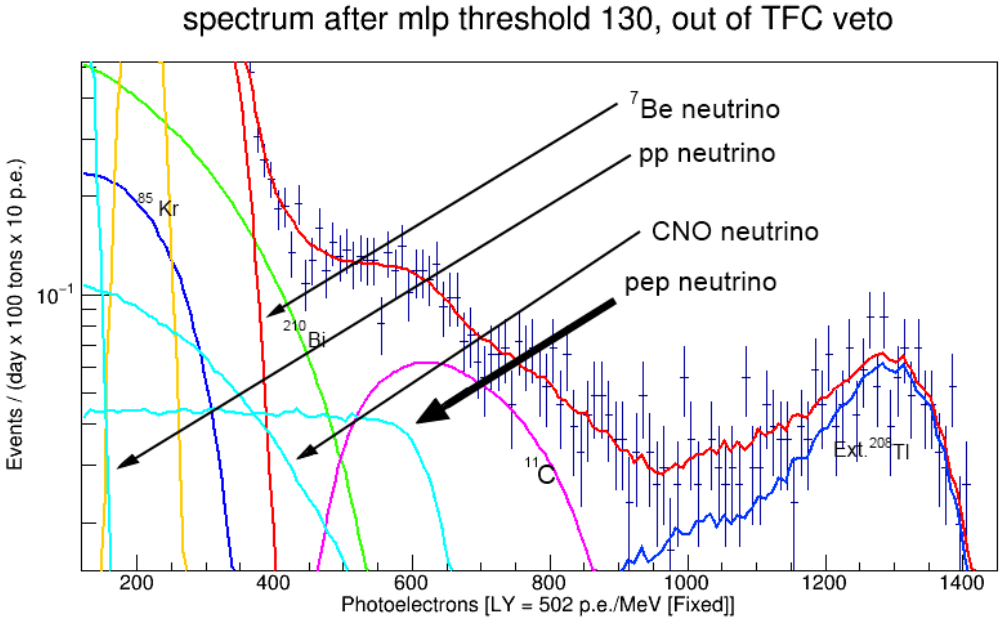

Figure 5.19: pep neutrino recoil electron shoulder with binning optimal for visualization

Chapter 6

Spectral analysis ^{8}B neutrino recoil electrons

6.1 Background composition

All the background composition reviewed in the previous section was devoted to low-energy part of the spectrum. Here we will review background composition at higher energies, reaching the detector saturation threshold of about 15 - 20 MeV[1]. As for the analysis systematization the backgrounds could be divided into three main groups:

- Internal backgrounds originating from natural radioactivity inside the detector fiducial volume
- External gamma rays, originating from natural radioactivity outside the detector fiducial volume
- Backgrounds induced by (α, n) reactions in the buffer and inside metal construction elements
- cosmogenic radioactivity inside the fiducial volume of the detector

Speaking of the Borexino spectrum at energies exceeding 1.7 MeV (as long as below ^{8}B neutrino electron recoil spectrum is naturally covered by other neutrino species), we expect to have the natural radioactive chains broken at the level of emanation at the first group, namely the ^{235}U and ^{232}Th chains are broken at the level of corresponding Radon isotopes, ^{222}Rn and ^{220}Rn [2]. Although in the

[1] nonlinearity of response due to saturation starts around 15 MeV, but the detector could be still used at higher energies in case of saturation effects consideration

[2] this radon has the historical name of thoron and thus will be named this way in order to distinguish it form radon

purification of the detector the levels of these activities were significantly decreased, these nuclides could be observed by a search for $^{212}Po -^{212} Bi$ and $^{214}Po -^{214} Bi$ delayed coincidences and appear in the spectrum below 3.5 MeV with the decays of ^{208}Tl and ^{214}Bi. These nuclides produce fully-contained $\beta + \gamma$ spectra with multiple realizations, see fig. 6.1,6.2

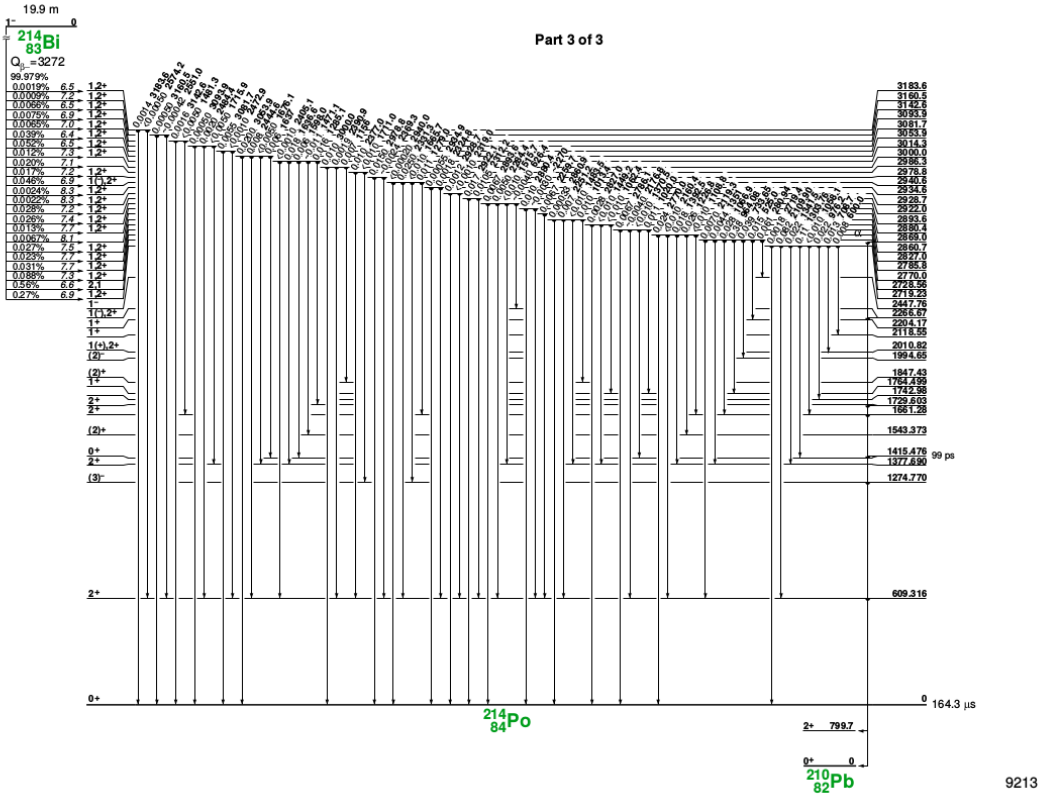

Figure 6.1: decay scheme of ^{214}Bi

The external background considers the decays of ^{208}Tl and ^{214}Bi, mostly concentrated in the glass of photomultipliers, where the concentration of these nuclides of the natural radioactive chain reaches level of several kBq. This activity is strongly suppressed by the detector buffer, but due to high activity still has quite high statistical significance in the region of 2-3 MeV.

Backgrounds induced by (α, n) reaction in the buffer and inside construction materials could play their own role due to neutron capture inside fiducial volume and especially within stainless steel constructions such as the main detector spherical housing and support structure. Radiative neutron capture inside the fiducial volume contributes with internal gamma-source of deuterium line of 2.21 MeV as

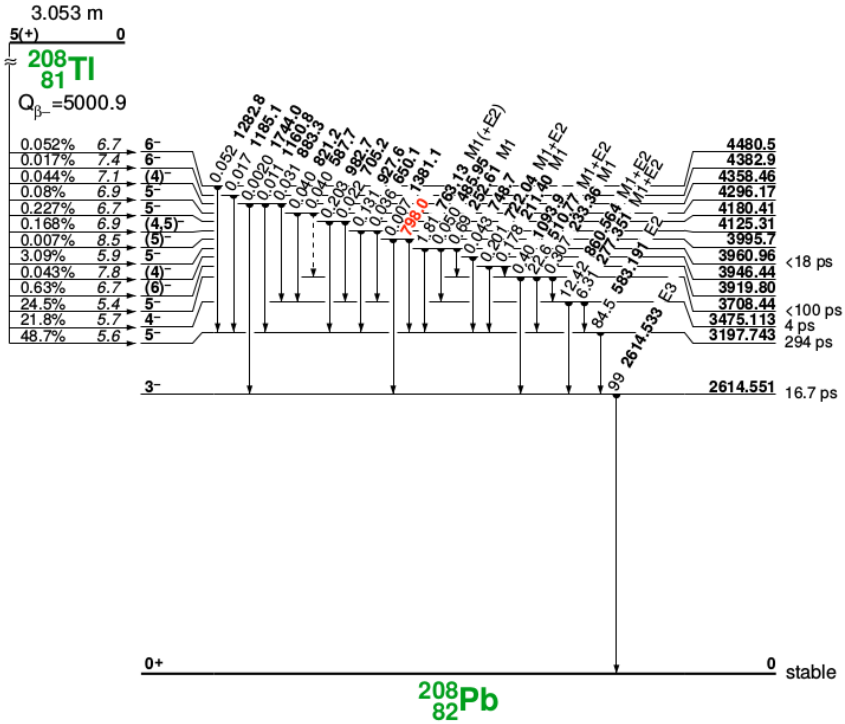

Figure 6.2: decay scheme of ^{208}Tl

well as with more energetic neutron capture lines, although with much smaller probabilities. Radiative capture in steel results in external gammas with high energies which despite their low rate have quite high penetrative abilities and could have some statistical significance in the region of interest.

The cosmogenic background in the high-energy region is the most rich by the number of components and could be represented with such nuclides as ^{12}B, ^{8}He, ^{9}C, ^{9}Li, ^{8}B, ^{6}He, ^{6}Li, ^{10}C and ^{11}C, produced by the muon flux penetrating the detector and performing the production by single-site reactions as well as in avalanche process. Among this list one could distinguish two isotopes of carbon, that are beta-plus decayers and have relatively low-energy endpoints together with ^{6}He, while all the others have high beta-transition energy and produce continuous spectra with the shape close to the spectrum of ^{8}B neutrinos. These nuclides could be grouped by their live time the following way:

- ^{12}B, $\tau = 0.031$ s
- ^{8}He, ^{9}C, ^{9}Li, 0.17 s $\leq \tau \leq$ 0.26 s

- ^{8}B, ^{6}He, ^{6}Li, 1.11 s $\leq \tau \leq$ 1.21 s
- ^{11}Be, τ = 19.9 s
- ^{10}C, τ = 27.8 s
- ^{11}C, τ = 1763 s

^{11}C has the transition energy of 1982 keV (and this is the total maximum energy release due to the fact that all possible β^{+} decays will be fully contained in the detector due to its size) and relatively long lifetime, it appears to be the natural threshold for ^{8}B neutrino measurement by an organic liquid scintillator detector as it is produced by relatively easy-going process and has high rate together with comparatively long lifetime, while all other backgrounds could and should be maximally suppressed in the data-preparation phase. Going to lower energies is possible only in case of decreasing cosmogenic background passively, thus going deeper underground.

6.2 Data preparation

Considering the importance of the neutrino electron recoil data at lowest achievable energy, we would aim to perform a measurement with the spectral sensitivity to the neutrino spectrum as low as 2 MeV, the endpoint of cosmogenic ^{11}C spectrum, putting the maximum effort to suppress all non-neutrino components.

The dataset used for the analysis includes the Phase II of Borexino experiment, namely

- 18 Dec 2011 - 11Oct 2015, 1170.471 days of live time

Such selection of the dataset is done due to very efficient purification campaign, performed between detector phases that significantly suppressed the internal natural radioactivity. Radon daughters by factor of 30 and thoron daughters up to below the detector sensitivity to corresponding coincidences. Since these backgrounds severely affect ^{8}B neutrino recoil electron spectrum in the low-energy region, especially below 3 MeV, reduction the dataset to phase II becomes unavoidable; since the detector sensitivity above 5 MeV is much below the one of Ĉerenkov effect detectors it does not make much sense to increase statistics in this region despite the possible precision improvement. The increased statistics was used for service purposes only, e.g. establishment of cosmogenic backgrounds and include also Phase I statistics (may 2007 - Dec 2009).

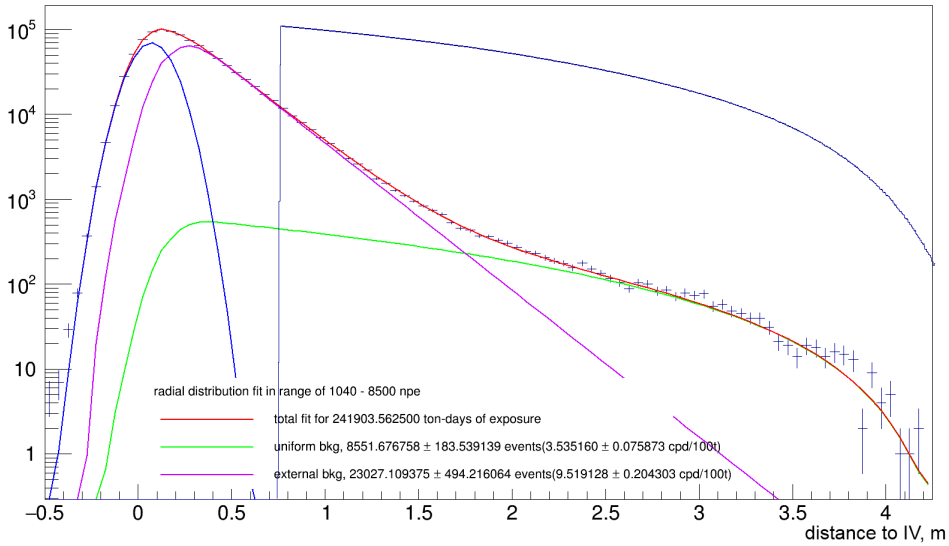

Figure 6.3: radial distributions fit in terms of distance to the inner vessel. Green line represents internal background, violet - external gamma-radiation and blue - vessel contamination. The dark blue line is proportional to dV/dD_{vessel} inside fiducial volume and is superimposed in order to demonstrate absence of vessel component within selected fiducial volume

6.2.1 Fiducial volume definition

Definition of fiducial volume should be done under consideration of natural radioactivity present on the inner nylon vessel that should be possibly avoided. On the other hand one has the purpose of the volume maximization in order to achieve the maximum sensitivity to the signal searched. Taking into account that the vessel is quite strongly deformed within the Phase II of data taking and such deformation appears to be time-dependent, the only solution would be to define the fiducial volume by limiting the minimum distance to the vessel in order to guarantee absence of vessel events reconstructed inside fiducial volume. Such possibility was given to the analysis by so-called Dynamic Fiducial Volume.

Dynamic fiducial volume is based on fitting ^{210}Bi decay events positions on the nylon vessel (data are selected at energies above 300 hits, on ^{7}Be shoulder and are located mostly on the vessel; lead contamination of the vessel is at leas 20 times higher than the whole inner volume). The fit was performed under assumption of cylindrical symmetry of the vessel and with interpolation in (θ, R) coordinates as Lagrangian polynomial (see fig. 6.4) with additional consideration of PPO

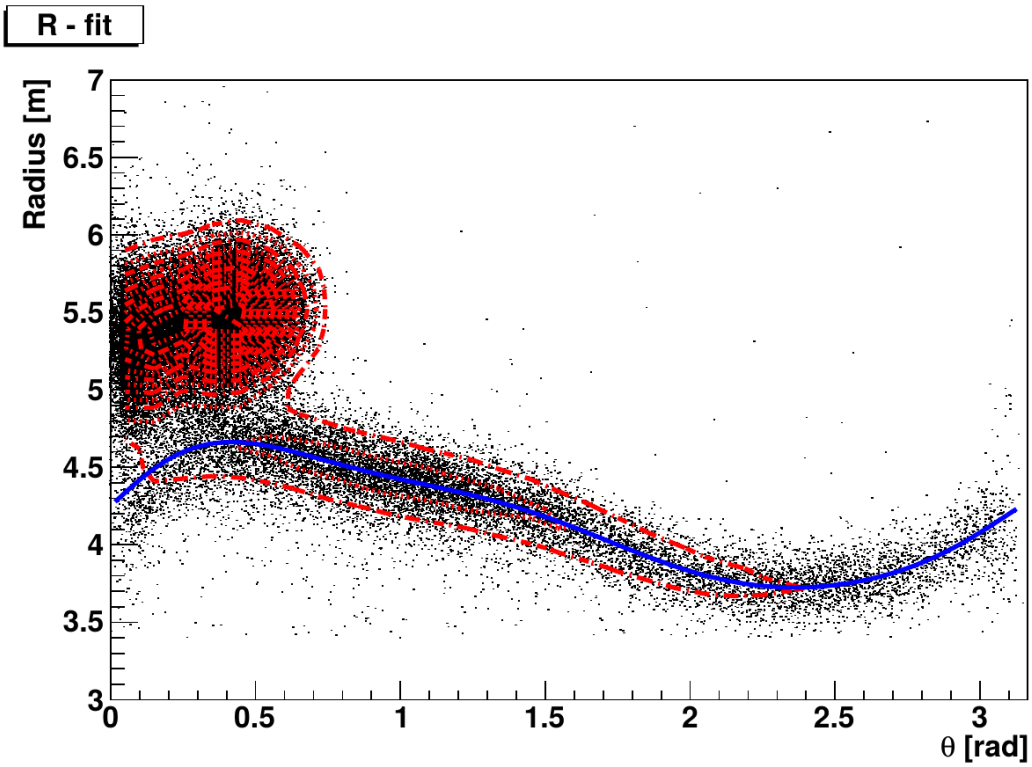

Figure 6.4: example of vessel shape fit in (θ, R) coordinates. One could observe the peak related with PPO leak at low θ values

leak into the buffer. The fiducial volume is defined through minimum distance to the vessel (by "rolling circle" approach). The approach shows reliable vessel reconstruction in agreement with CCD data (available in calibration campaign) and with conservation of inner vessel volume.

Estimation of the position reconstruction resolution and thus the minimal allowed distance between the vessel and reconstructed event position could be defined by fitting data radial distribution within the energy range of interest in units of distance to the vessel along radius. In order to perform such fit one could make the following assumptions:

- position reconstruction nearby the vessel has approximately gaussian shape, so affection of reflections and dark currents from different sources could be neglected at these relatively high energies

- external backgrounds could be described by exponential attenuation function convolved with a gaussian of position reconstruction at least in close

proximity to the vessel

Such assumptions can't be physically correct for the whole range of events since the external component originates at solid structure of the detector construction, while the radial variable is related to the deformed vessel, thus the functions used for non-vessel components play only the descriptive role. I this case one could perform such fit and establish the fiducial volume limitations, see fig. 6.3.

Taking into account obtained limit, the fiducial volume which is also supposed to avoid light collection shadowing induced by vessel support system, namely vessel endcups could be constructed in the following way:

- Minimal distance to the vessel is set to 0.75 m
- Regions close to endcups are cut out as $|Z| < \frac{d_0}{cos^4(\theta)}$ with d_0 values of 2.4 m in the northern hemisphere and 2.2 m in southern hemisphere, where Z is the vertical coordinate and θ is the plane angle of polar coordinate system

Such fiducial volume has the average mass of 145 tons and appears to be the largest fiducial volume in which one could apply relatively simple detector response approximations and neglect any vessel contamination contribution above 2 MeV.

6.2.2 Data quality treatment

The generic quality of the dataset used in the analysis is quite important since the imperfection of the dataset is a possible source of a systematic uncertainty . The standard procedure of data validation during the process of data-taking was applied before any other operation of the data analysis in order to establish an appropriate dataset. In addition to the standard data validation there were applied the following criteria of the data selection, selected among standard approaches by the criterion of absence of high-energy spectrum part distortion:

- neutrino trigger data only (triggering in inner detector standalone)
- only events with singular clusterization (only single scintillation flash)
- only beta-like events (according to the scintillation process, alpha-events are quenched in light by around 14 times and have a longer scintillation flash that could be distinguished by a variable produced by Multi-layer percerptron classification algorithm (MLP), that uses ten tail-to-total ratios with different time thresholds as inputs)
- Mach-4 crate faction not exceeding 0.75 (removal of events too correlated on a single rack of data-acquisition system)

- inner sphere with radius of 1 m in the center of the detector is removed due to the fact that in the stochastic nature of electronic noise the time-of-flight position reconstruction would have a tendency to reconstruct such events in the center of the detector, especially in case of high-statistics noise bursts that would affect the high-energy spectral region

This data selection scheme is supposed to provide the spectrum of beta and gamma physical scintillation flashes with a statistically negligible fraction of events of any other type.

6.2.3 Cosmogenic background measurement and suppression

The cosmogenic background has the most significant influence on the high-energy region and appears to be the most complex. The Borexino detector is equipped with outer detector that uses the Ĉerenkov radiation detection principle and is used as a muon veto; moreover, there are algorithms of inner detector muon discrimination that provide the muon detection efficiency exceeding 99.9 % [67].

As soon as the cosmogenic backgrounds are correlated with muons, which could be distinguished with very high efficiency, it is possible to use it to estimate the cosmic background rate by the decay time of the corresponding components. The mathematical background of this algorithm is the following:

If one could define a set of events with times $\{T_i \mid \ T_{i+1} \geq T_i\}$ which contains all parents of cosmogenic backgrounds, it could be possible to measure the rate of non-cosmogenic and cosmogenic components.

Let's define exposure as

$$E = \int\limits_{live\ time} M(t)dt \tag{6.1}$$

As soon as this value is time-dependent , one could non-trivially write

$$E = \int_0^\infty \frac{dE}{d\tau} d\tau, \tag{6.2}$$

where to $\tau = (t - T_i | T_i \leq t \leq T_{i+1})$. As our knowledge of temporal dependence in respect to the parent event (exponential decay with known decay time or stable flux) corresponds to rate of this events per unit of exposure $\frac{dE}{d\tau}$, The number of events with some rate $R(\tau)$ could be written as

$$N = \int_0^\infty R(\tau) \frac{dE}{d\tau} d\tau \tag{6.3}$$

So in order to understand the number of events of each kind one needs to find the differential exposure. If one has some events with constant rate, such as $t_i = t_0 + C \times i$, as $\frac{\partial R}{\partial t} = 0$ then every temporal derivative would be zero, $\frac{\partial R}{\partial \tau} = 0$ as well since τ depends only on time. In this case the previous expression looks like

$$N = \int_0^\infty R \frac{dE}{d\tau} d\tau = R \times \int_0^\infty \frac{dE}{d\tau} d\tau \tag{6.4}$$

If one simulates toy Monte-Carlo events with constant rate the distribution of such events in respect to τ would be

$$\frac{dN_{const}}{d\tau} = R \frac{dE}{d\tau} \tag{6.5}$$

, so this is a way of numerical calculation of the differential exposure respect to τ. In this case it is possible to perform the spectral fit of real events with respect to τ with a function

$$F(\tau) = \frac{dN_{const}}{d\tau} \times \sum_{all\ \ species} R_j(\tau), \tag{6.6}$$

where $R_j(\tau)$ are constant or exponential functions and the differential exposure is already computed numerically . The ratios of rates will appear to be proportional to integrals like

$$N_j = \int_0^\infty R_j(\tau) \frac{dE}{d\tau} d\tau, \tag{6.7}$$

where all functions are known up to a constant factor and could be normalized according to the total number of events as $\sum_j N_j = N_{total}$. As soon as the decay times of all components are known and could be fixed the relative errors on the derived numbers of events will be proportional to the relative errors of fit coefficients.

One more generalization of this approach could be done if one considers that the fiducial volume is time dependent and changes slowly in respect to the typical gap between two consequent events. In this case one could repeat the same derivation replacing all values by differential volume equivalents and requesting the toy monte-carlo events to be spatially uniform in order to consider the fiducial volume evolution.

Since such set of parents could be given by the system of muon discrimination[3] (the criterion of a muon is the standard muon-like definition, namely full muon

[3]unlike ^{11}C case, where parent set establishment was a keystone; Here non-Poisson statistics of parent set plays the major role instead

definition with exclusion of muons discriminated by excess of non-decoded hits appearing within 300 ms after the previous muon), one could perform a measurement of the actual cosmogenic background composition. Moreover, it is possible to perform a muon-related veto system in order to maximally suppress the cosmogenic components of the spectrum and to derive the actual suppression efficiency. Since the production is performed in two mechanisms, namely in avalanche process and as single-site production, one should consider the following system of veto:

- A short veto of 2 ms after each muon detected in order to prevent appearance of comogenically induced neutron capture events in the spectrum.
- A relatively long 20s veto after each muon creating an avalanche process, where the criteria of such muon are the following: more than 20 daughters with energy exceeding 200 keV (so not ^{14}C) or detector saturation by more than 2/3 ("empty boards" $>$ 160 or number of events with more than 100 normalized hits in the following neutron trigger window exceeding 20).
- Cylindrical veto on the muon track with the radius of 1.0 m in case the muon is tracked
- spherical veto on position of each neutron induced by muon and captured within the following 1.6 ms with the variable radius of the sphere depending on the quality treatment of neutron position reconstruction (complete analogue of spherical part of TFC veto). Duration of 120 s.
- 3.5s s veto after each muon crossing the inner detector in order to have a complete suppression of all short-lived cosmogenic components

One could consider the following point: since the cylindrical veto is applied only for single-site cosmogenic production, it should be equally efficient for all components, that could be observed in the table 6.1.

In this table the ^{11}Be rate is considered to be suppressed by the cylindrical veto equally in respect to all the other components (with consideration of ratio between live time and veto duration), which are measured by fitting the temporal distributions (see fig. 6.5)[4]. The spherical veto on muon-induced neutrons appears to be a very effective tool of ^{10}C suppression, but the same time it is correlated with other components of cosmogenic background. In the very end it is possible

[4]the fits shown are demonstrated in nonuniform binning with rescaling of bin content and show less reliable results than the fits used in analysis due to usage of χ^2 likelihood function. The fits used are done with Poisson likelihood and are not demonstrated as they are much less visual, the results are tabulated in table 1.

veto	^{12}B	^{11}Be	constant	$\tau \approx 1.16$ s
none	1.29 ± 0.024	0.04 ± 0.024	0.24 ± 0.024	0.61 ± 0.024
shower	0.79 ± 0.021	0.03 ± 0.021	0.26 ± 0.026	0.33 ± 0.02
Track veto	0.30 ± 0.013	0.02 ± 0.02	0.27 ± 0.027	0.10 ± 0.014
full geometrical	0.12 ± 0.008	0.02 ± 0.02	0.27 ± 0.013	0.02 ± 0.008
full	0	0.02 ± 0.02	0.27 ± 0.013	$\approx 10^{-3}$

Table 6.1: rates of cosmogenic components above 3.7 MeV in units of counts/day/100 t on various stages of cosmogenic veto application (inclusively from to bottom)

to make the full blackout as short as only 3.5 s reducing statistical significance of all short-lived cosmogenics up to negligible level. The veto system leaves in the spectrum only ^{11}Be, ^{10}C and ^{11}C that can not be removed completely due to their live time, reducing exposure only by 18%.

6.2.4 External background estimation and statistical subtraction

Another important background, especially in the region below 3.5 MeV appear to be the external gamma-background, namely the gamma-rays of natural ^{238}U and ^{232}Th chains coming mainly from the PMT glass. Although the detector is self-shielded by the buffer reaching the level of 2 m between the gamma source and fiducial volume, the activity is high enough to have a serious statistical significance inside the fiducial volume. Moreover, in case of the maximized fiducial volume used in this analysis even precise knowledge of the external gamma-fluxes won't save the sensitivity to ^{8}B neutrinos as their flux is insignificant in respect to the statistical fluctuation of external background signal.

The possibility to increase the sensitivity is in usage of the fact that the flux of external gammas is being attenuated during propagation inside the fiducial volume. The simplest model of such attenuation would be a simple exponential attenuation of the flux,

$$\Phi = \Phi_0 \times \exp(-d/d_0) \tag{6.8}$$

Taking into account spherical geometry of the detector, one gets

$$\Phi(r) = \Phi_0 \times r^2 \times \exp(-\frac{R_{det} - r}{d_0}) \tag{6.9}$$

In order to consider the non-sphericity and temporal evolution of fiducial volume one could apply a simple toy Monte-Carlo approach, simulating event uniformly

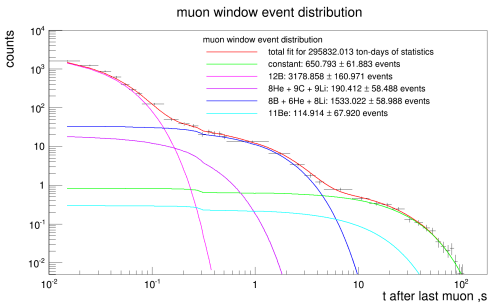

cosmogenic backgrounds temporal fit before veto application

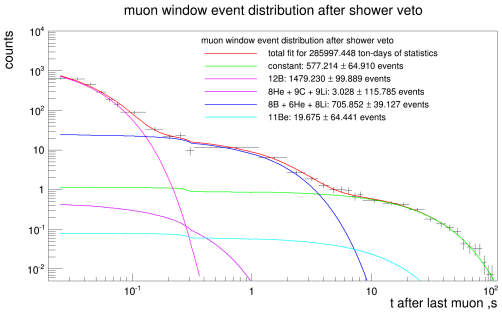

cosmogenic backgrounds temporal fit after shower veto application

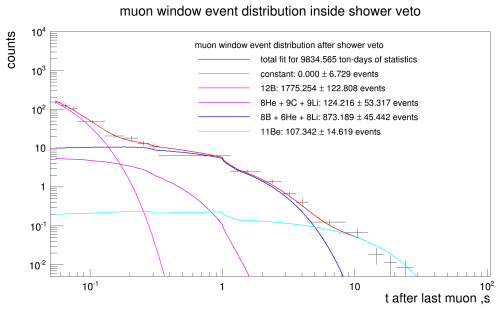

cosmogenic backgrounds temporal fit inside shower veto

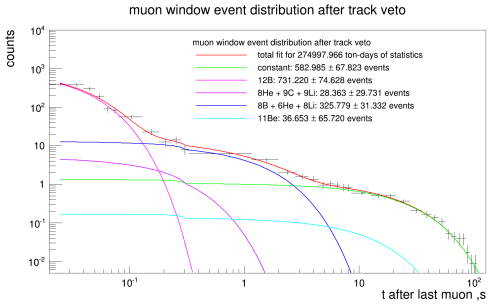

cosmogenic backgrounds temporal fit after track veto application

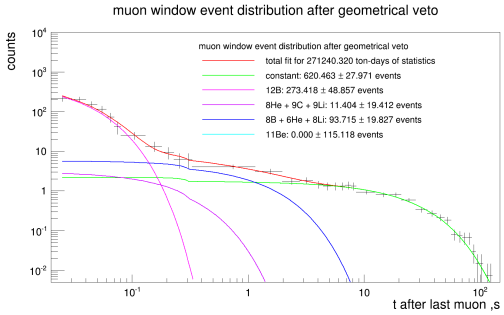

cosmogenic backgrounds temporal fit after geometrical veto application

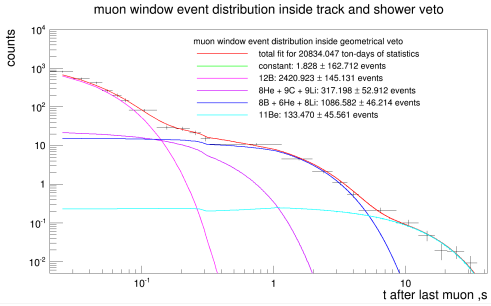

cosmogenic backgrounds temporal fit inside veto system

Figure 6.5: cosmogenic background temporal fits on different stages of veto system. The kink at 0.3s is related to an electronic effect increasing probability of fake pulse-shape muon discrimination shortly after a physical muon. Fits performed with nonuniform binning for demonstration purposes and could disagree with the ones used in analysis within statistical error

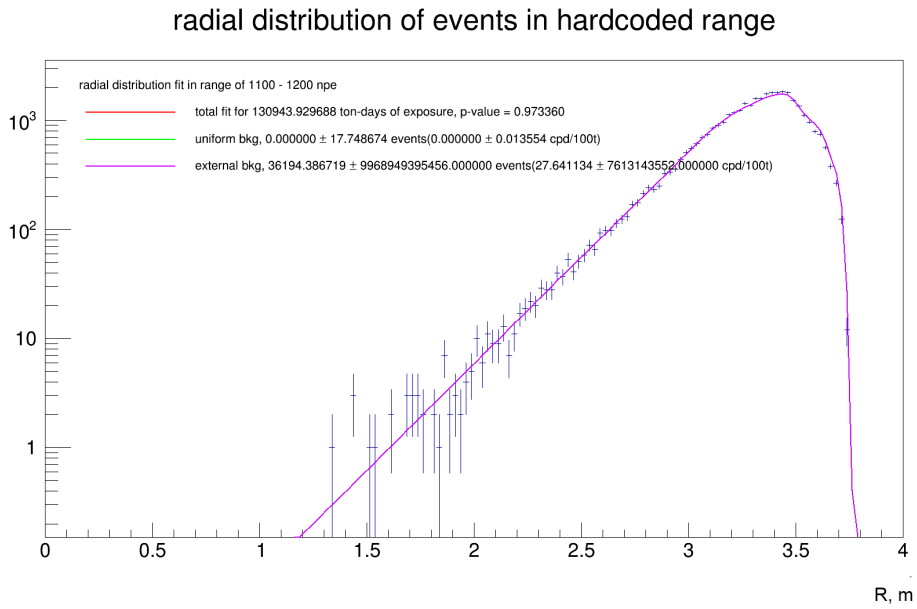

Figure 6.6: simple analytical model test on Monte-Carlo simulated external γ-rays of ^{214}Bi and ^{208}Tl in the range of 1100-1200 npe

in time and space and recording the radial distribution of such events as radial fiducial volume density u = u(r). In this case the count rates of events, uniformly distributed in fiducial volume and external background would have the following radial dependence:

$$N(r) = C_{uniform} * u(r) + C_{external} * \frac{u(r)}{R^2} \times \exp(-\frac{R_{det} - r}{d_0}) \tag{6.10}$$

One should consider that the parameter d_0 should be energy-dependent and thus this description is valid only in relatively narrow energy range in which one could neglect such dependence. This model could be compared with full Monte-Carlo simulation of external background and shows satisfactory agreement, as demonstrated on fig. 6.6. Fitting the real data distribution could give information on uniform background rate(fig. 6.7).

This Information could used for statistical subtraction of external backgrounds. The approach of statistical subtraction looks quite interesting as it would remove the effect of external backgrounds, although for the price of enlarged errors in the corresponding energy bins in a more visual way. In this case one should just put the bin value and error according to the radial distribution fit and consider them correctly in the likelihood value determination.

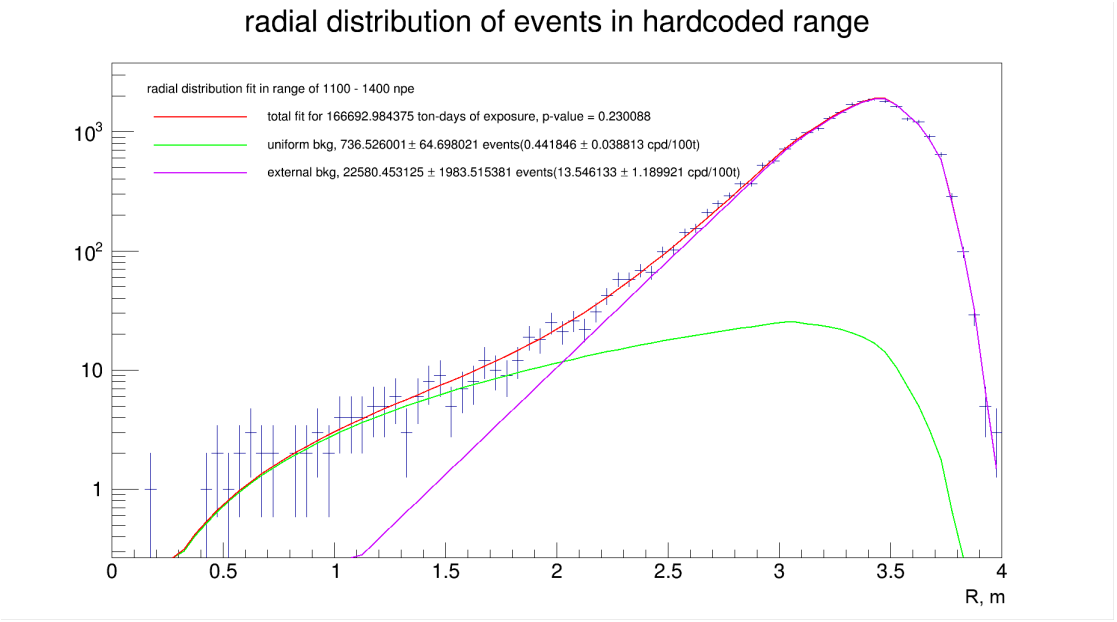

Figure 6.7: example of radial fit on data with a simple analytical model in the range of 1100-1400 npe

As long as the approach of statistical subtraction is more visual, we will try to develop scheme of it's application. It needs an automated procedure of radial dependency fitting also in case of seriously asymmetric statistics of external and internal background components, thus one needs a good way of initial parameter values establishment. The system used was the following:

- initial value of exponential slope is obtained by fitting monte-carlo simulation of external background in the corresponding energy range; one can't use this distribution as a fit function since the simulation including scintillation light is present only for Phase II period and within a sphere of R = 4 m, selected by energy baricenter of gamma interaction with matter. The attenuation is a good approximation of the real one and could be used as an initial value
- initial amplitudes of uniform and external components are taken from partial fit of real data radial distribution in ranges [0;2 m] and [2m; 4m] for uniform and external components correspondingly
- the fit is performed in the fill radius range with usage of these precomputed values with usage of negative logarithm of Poisson likelihood; the fit is bounded in order to avoid negative amplitude values

Application of such scheme shows reliable execution on the of Phase I, Phase II

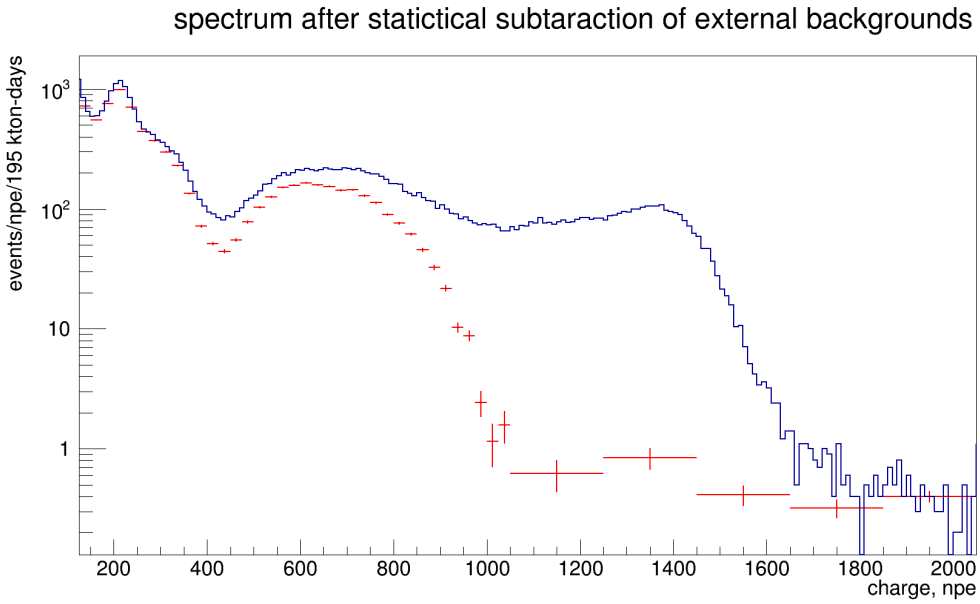

Figure 6.8: Spectra with and without statistical subtraction of external backgrounds in the range of 140 - 2000 npe for the full dataset. Bin-width of subtracted spectrum is selected according to bin statistics

and Phase I+Phase II datasets, giving for the full dataset mean goodness of fit of $< p >= 0.4$ and reproducing spectral shapes of internal components, see fig. 6.8.

6.2.5 Neutron-induced background sources

Neutron-induced backgrounds could be relatively important due to presence of capture peaks in the spectrum. Such neutrons could be originating from inverse beta-decay of proton caused by antineutrino flux from different sources, e.g. reactors, as well as by (n, α) reactions in all parts of the detector.

Neutron capture in the fiducial volume Since neutron capture in fiducial volume is dangerous for the lowest energies in the spectrum, one should perform the suppression with fast-coincidence scheme, where the prompt signal corresponds to neutron moderation or inverse beta-decay. Such scheme including a veto on each pair of events taking place within 1.5 m and 2 ms from each other was applied for each delayed event with energy above 1 MeV. In this case the only possibility to obtain a neutron capture appears to be a detection of a neutron, moderated inside the buffer to kinetic energy causing light emission below the trigger threshold. The limit on neutrons coming from the buffer was estimated in [72] and is small enough

to account it without consideration of the fraction of neutrons with undetectable prompt signal as long as one expects 0.85 neutrons from the buffer in the whole phase II of data taking at 90% CL independently of it's energy.

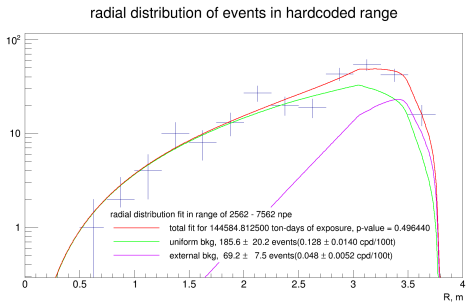

radial fit of events above 5 MeV outside veto system

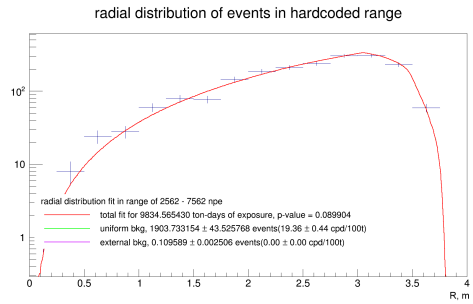

radial fit of events above 5 MeV inside shower veto

Figure 6.9: Radial fit of events above 5 MeV, showing presence of high-energy external component in agreement with expectations for neutron capture on steel. The same fit for events inside shower veto (strongly enhanced cosmogenic electrons) is shown to demonstrate absence of strong analysis bias.

(n, α) **reaction in the metal constructions** Another source of background is neutron capture on steel constructions of the detector. Since construction steel has quite high contamination of U/Th (see[63]) and the radiative capture produces relatively energetic photons, this background should play a statistically role in the background composition. Using the expected neutron yield, computed by SOURCES4A [73] software package together with a simplified monte-carlo simulation of relative capture probability on steel and considering attenuation according to [74], one gets the expected rate of order of 5×10^{-1} events/kton/day inside the fiducial volume. As long as such background is expected and, technically speaking, it is just another source of external gamma-background, one has to perform the radial fit in the energy range below 9 MeV in order to account for it's presence. The rate of such events is in agreement with rough estimate performed above, see fig.6.9

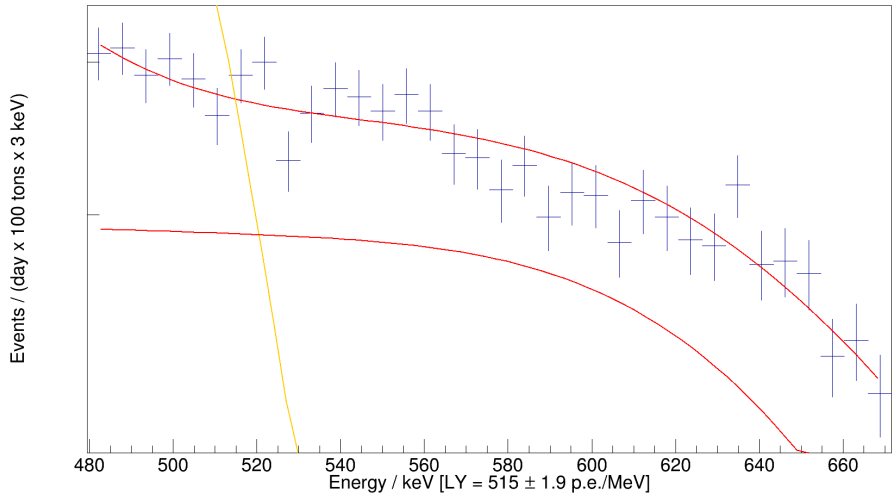

Figure 6.10: Energy response calibration fit of ^{7}Be neutrino electron recoil shoulder on Phase II statistics. This fit gave the values for response function parameters and overall detector calibrations used in further analysis. The fit also included fixed ^{210}Bi and ^{210}Po free in amplitude.

6.3 Final electron recoil spectrum derivation and subtraction

6.4 Statistical subtraction of backgrounds

As soon as the data selection produces the spectrum of uniformly distributed events inside fiducial volume, such spectrum still contains some background components which are to be accounted in order to extract the neutrino recoil electron spectrum. All these backgrounds have a spectral shape which is known up to the detector response, that could be understood through fitting the low-energy region spectrum, namely ^{7}Be neutrino electron recoil shoulder with an estimated detector response function with some free parameters. The response function used in this analysis is the so-called "generalized gamma-function", see [69]. The same fit would give a precise energy calibration of the spectrum, allowing to convert from effective photoelectrons to actual energy of beta-particle scintillation flash. The fit is illustrated at fig. 6.10.

Since the detector response is known, the background could be subtracted. The only source of uncertainty on all the background components is the statistical fluctuation of the total flux of corresponding background and the measurement precision of it's flux measurement. Statistical fluctuation of all spectral components are expected to be independent from each other, thus the variance of fluctuation of number of counts is expected to be

$$D_N = \sum_{species} D_i \tag{6.11}$$

for each energy bin of the spectrum. In this case one could express variance of ^{8}B neutrino recoil spectrum as

$$D_{(\nu,e)} = D_n - \sum_{bkg} D_i, \tag{6.12}$$

where i-th components correspond to the following set:

- residual ^{11}Be, according to the rate, measured by temporal fit with corresponding uncertainty
- ^{11}C, according to the rate measured by temporal decay fitting with corresponding uncertainty
- ^{208}Tl, according to the tagging system, with statistical uncertainty on tagged events
- ^{214}Bi, according to the tagging system, with statistical uncertainty on tagged events

One should also consider the limits on backgrounds below detector sensitivity, ^{10}C and radiative neutron capture peak, increasing uncertainties asymmetrically by the value corresponding to 68 % C.L. of the limit since all uncertainties used correspond to this level. The final output of such subtraction is demonstrated on fig. 6.11

6.4.1 Systematic uncertainties

Understanding of the background compositions would leave us with some extra uncertainty sources that should be also accounted. Among them are:

- uncertainties of detector calibration
- uncertainties of detector response

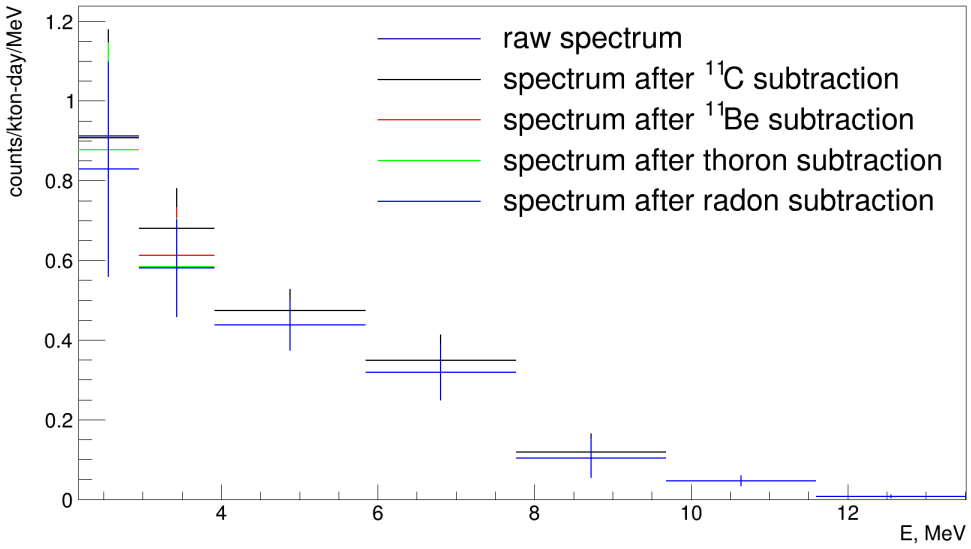

Figure 6.11: spectra on different stages of uniform background subtraction. Subtraction is performed consequently, so after radon daughters one expects it to contain only neutrino recoil electrons

- uncertainty of fiducial volume definition
- uncertainties of exposure definition

These effects could be estimated and propagated into final spectrum. First two groups of uncertainties will affect only the lowest energy bin as long as they would contribute into recoil electron flux only due to partial measurement of the spectrum. Overall calibration uncertainty is accounted as statistical in calibration fit, but since the further analysis is counting-based, it is to be propagated into the spectrum as systematic. Same operation should be done to energy response function parameter uncertainty in order to account for precision of broadening the resolution due to light collection nonuniformity.

Fiducial volume and exposure uncertainties affect normalization of the overall spectrum amplitude and originate from position reconstruction intrinsic biases and live time computation. Live time is computed with numerical precision of 10^{-4} with toy-Monte-Carlo approach used to account for geometrical veto system and such precision makes this uncertainty negligible respect to statistical fluctuations. The systematic uncertainty on fiducial volume definition was derived in [71] for a

source	value, events(2.15MeV threshold)	value, %(2.15MeV threshold)
detector response	10^{-2}	2.3×10^{-3}
detector calibration	10.2	2.34
fiducial volume	9.1	2.1
exposure	10^{-2}	2.3×10^{-3}
source	value, events(5MeV threshold)	value, %(5MeV threshold)
detector response	10^{-2}	5.7×10^{-3}
detector calibration	5.4	3.1
fiducial volume	3.7	2.1
exposure	10^{-2}	5.7×10^{-3}

Table 6.2: systematic uncertainties estimation

slightly smaller fiducial volume. Propagating the same linear bias to the fiducial volume used under assumption of bias change not more than factor of 2 within extra 50 cm of separation from the center that is compatible with stability of reconstructed deformed vessel volume temporal stability and compatibility with known physical value, one could expect this uncertainty not to exceed 1.5%. A more precise estimate of such uncertainty could be done by following count rate of ^{14}C taken from the second cluster in order to avoid trigger threshold effects, but such estimate is not need due to high statistical fluctuation of output spectrum and one could be limited with such conservative estimate. The tab.6.2 shows overall systematic uncertainty estimate of the measurement.

6.4.2 Towards neutrino fluxes

The spectrum obtained is supposed to include only neutrino recoil electron component since all sources of possible backgrounds are accounted. In this case one should consider a way to estimate properties of original neutrino spectrum. As long as the detector detects neutrino flux by two reactions of (ν_e, e) and (ν_x, e) scattering which have different differential cross sections including a difference in shape rather than just amplitude, a procedure of spectrum deconvolution becomes intrinsically impossible since the ratio of different types of neutrinos is unknown. Moreover, such deconvolution becomes impossible due to lower precision of recoil electron spectrum determination. In this case one could not derive the original neutrino spectrum without making any assumption on neutrino oscillation properties.

The most classical value for high-energy neutrino experiments is the neutrino flux under assumption of no-oscillation scenario. Such value remains feasible as

long as the electron neutrino survival probability remains flat within detected part of the spectrum and the effect of neutrino oscillation could be described by simple scaling the measured flux reversely proportional to actual survival probability inside matter resonance regime. Validity of such approach on measured spectrum could be checked by integrating the neutrino spectra above some thresholds and computing the neutrino flux under assumption that the neutrino spectrum corresponds to ^8B shape and contains only electron neutrino. In this case one could observe the following:

- above 2.17 MeV: $(2.6 \pm 0.3 \pm 0.1) \times 10^6 \frac{1}{cm^2 s}$
- above 5 MeV: $(2.4 \pm 0.3 \pm 0.1) \times 10^6 \frac{1}{cm^2 s}$

Same time, taking in to account low threshold of this measurement, one could compute fluxes under assumption of best fit MSW-LMA model:

- above 2.17 MeV: $(5.69 \pm 0.62 \pm 0.21) \times 10^6 \frac{1}{cm^2 s}$
- above 5 MeV: $(5.31 \pm 0.62 \pm 0.20) \times 10^6 \frac{1}{cm^2 s}$

In this case the fluxes are closer, although discrimination of vacuum-oscillation and LMA solution is still not achievable without inclusion of low-energy neutrino data that Borexino detector could provide. Taking into account ^{7}Be neutrino flux measurement from [75], that equals we could rule out vacuum-oscillation solution at 99.7 % c.l. basing on Borexino results only.

6.4.3 Fitting the final spectrum

The most common way of statistical compatibility check is maximum likelihood method that was applied to the final spectrum in order to check for statistical compatibility between it and the most common matter oscillation model, namely MSW-LMA. The parameters of the model taken were $\Delta m_{12} = 7.54 \times 10^{-5}$ and $tg^2(\theta_{12}) = 0.44$, two-neutrino approximation.

likelihood function construction Generally speaking, the likelihood function used for fitting is simply binned Poisson likelihood, that could be written as

$$L = \prod_{bins} \frac{\lambda^x exp(-\lambda)}{\Gamma(x+1)}, \tag{6.13}$$

where x is the number of counts in the bin and λ is the number of counts expected from the model. The model is the following: one considers neutrino recoil electron

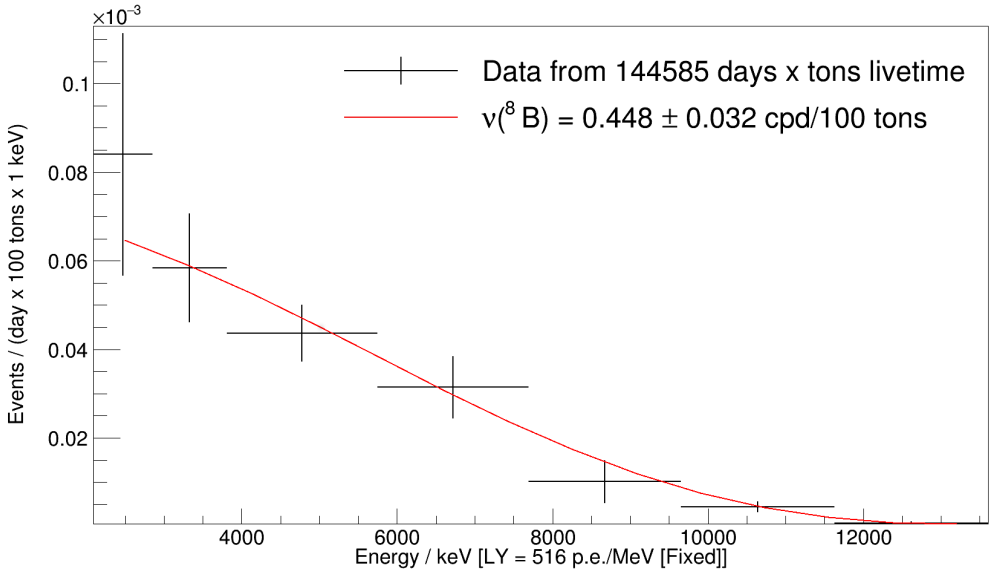

Figure 6.12: fit result on the final subtracted spectrum. It shows good statistical agreement to the model of MSW-LMA-HZ with the expected signal amplitude.

spectral shape

$$P_\nu(E) = \int P_0(E) \times F_{resp}(E - E_0) dE_0, \tag{6.14}$$

where $P_0(E)$ is the energy spectrum of recoil electrons and $F_{resp}(E - E_0)$ is the detector response function, modeling the actual detector response for a delta-function of energy E_0. The expected number of counts in a bin is considered by multiplication of the response function value at the center of the bin and the corresponding bin width, so under assumption that the spectrum is not changing significantly within a bin.

The actual function used in minimization is constructed as the sum of negative logarithmical likelihood and, if necessary, some additional terms:

$$-ln(L) = \sum_{bins} \lambda + ln(\Gamma(x+1)) - x \times ln(\lambda) + \Lambda_{add} \tag{6.15}$$

In case of unstatistical error in the bin after statistical subtraction of backgrounds one uses the Poisson likelihood scaling as

$$\theta = \sqrt{\frac{\delta x^2}{x}} \tag{6.16}$$

$$-ln(L_i) = ln(\theta) + \frac{\lambda}{\theta} + ln(\Gamma(\frac{x}{\theta} + 1)) - \frac{x}{\theta} \times ln(\frac{\lambda}{\theta}) \tag{6.17}$$

In this case the width of the likelihood distribution becomes the same as requested by the bin error, while the likelihood shape remains Poisson in order to maintain a possibility to treat low bin statistics correctly.

Data fit result The technique was applied to the final neutrino electron recoil spectrum in order to perform a statistical compatibility test with neutrino oscillation probability and to derive the total neutrino flux under assumption of the corresponding matter oscillation model. Such fit was performed under assumption of MSW-LMA model and neutrino electron scattering cross-section as [32] and is shown at fig. 6.12. The final number of counts corresponds to $(5.5 \pm 0.4) \times 10^6 \frac{1}{cm^2 s}$ under assumption of MSW-LMA.

Conclusion

In this thesis the study of total solar neutrino spectrum obtained by Borexino detector in phase II of data-taking was reviewed. Were obtained values of all solar neutrino fluxes apart from hep neutrino. The spectrum of ^{8}B neutrino recoil electrons was measured with the lowest visible energy threshold ever applied in analysis of this component and has spectral shape statistically compatible with MSW-LMA + HZ model and measured flux value of $(5.5\pm0.4)\times10^6\ cm^{-2}s^{-1}$ under assumption of this model. All the other fluxes were estimated in compatibility with the same model and among them was demonstrated statistical sensitivity to CNO neutrino flux with central value of $(5.2 \pm 1.8_{stat}) \times 10^8\ cm^{-2}s^{-1}$.

Phase II of Borexino detector shows that in case of low-energy neutrinos all fluxes are either dominated by systematic uncertainties, either are in strong correlation with essential backgrounds such, e.g. in case of ^{14}C and pp neutrino. That means that Borexino detector is already reaching limits on low-energy neutrino precision for organic liquid scintillator detectors and the future hope is on detectors with better resolution and lower backgrounds, such as detectors on ultrapure argon. The same time it could demonstrate that in case of detector enlargement liquid scintillator detectors could perform significantly improved studies of high-energy components such as neutrinos from ^{8}B and hep having relatively good resolution, large exposure, low background and lower analysis threshold close to natural limits related with presence of pep and CNO neutrino, allowing to study survival probability transition region.

Bibliography

[1] A.-H. Becquerel. "Sur la dispersion du rayonnement du radium dans un champ magnetique". In: *Comptes rendus de l'Academie des sciences* (130 1900), pp. 372–376.

[2] Professor Ernest Rutherford, M.A., B.Sc. and Professor Robert B. Owens, E.E. "II. Thorium and Uranium Radiation". In: *j-TRANS-R-SOC-CAN* 5.Section III (May 1899), pp. 9–12. ISSN: 0035-9122.

[3] C. D. Ellis and W. A. Wooster. "The continuous spectrum of β-rays". In: *Nature* 119 (1927), pp. 563–564.

[4] Wolfgang Pauli. *Letter to Tübingen conference participants*. Web document. Dec. 1930.

[5] E. Fermi. "An attempt of a theory of beta radiation." (In German). In: *Zeitschrift für Physik* 88 (3 1934), pp. 161–177. DOI: 10.1007/BF01351864.

[6] Barsukov O.A.. *Basics of nuclear physics. Nuclear technologies*. 2011.

[7] James S. Allen. "Experimental Evidence for the Existence of a Neutrino". In: *Phys. Rev.* 61 (11-12 June 1942), pp. 692–697. DOI: 10.1103/PhysRev.61.692.

[8] H. Bethe and R. Peierls. "The "Neutrino"". In: *j-NATURE* 133.3366 (Apr. 1934), pp. 532–532. ISSN: 0028-0836 (print), 1476-4687 (electronic). DOI: http://dx.doi.org/10.1038/133532a0.

[9] B. Pontecorvo. *Inverse β Process*. Chalk River Laboratory, PD-205. 1946.

[10] R. Davis. "Attempt to Detect the Antineutrinos from a Nuclear Reactor by the ^{37}Cl($\bar{\nu}$,e$^-$)^{37}A Reaction". In: *Phys. Rev.* 97 (3 1955), pp. 766–769. DOI: 10.1103/PhysRev.97.766.

[11] Enrico Fermi et al. *Work Carried Out by the Physics Division (experimental production of a chain reaction; exponential experiment with metal; effective temperature of the thermal neutrons)*. Report CP-387. inst-AEC:adr: inst-AEC, 1942, p. 1.

[12] S. Niese. "The discovery of organic solid and liquid scintillators by H. Kallmann and L. Herforth 50 years ago". In: *Journal of Radioanalytical and Nuclear Chemistry* 241.3 (1999), pp. 499–501. ISSN: 1588-2780. DOI: 10.1007/BF02347204.

[13] F. Reines and C. L. Cowan. "A Proposed Experiment to Detect the Free Neutrino". In: *Phys. Rev.* 90 (3 May 1953), pp. 492–493. DOI: 10.1103/PhysRev.90.492.2.

[14] F. Reines and C. L. Cowan. "The Neutrino". In: *Nature* 178 (Sept. 1956), pp. 446–449. DOI: 10.1038/178446a0.

[15] Andreas Piepke. "KamLAND: A reactor neutrino experiment testing the solar neutrino anomaly". In: *Nuclear Physics B - Proceedings Supplements* 91.1 (2001), pp. 99 –104. ISSN: 0920-5632. DOI: http://dx.doi.org/10.1016/S0920-5632(00)00928-2.

[16] A. Cabrera. "The Double Chooz Experiment". In: *Nuclear Physics B - Proceedings Supplements* 229 (2012), pp. 87 –91. ISSN: 0920-5632. DOI: http://dx.doi.org/10.1016/j.nuclphysbps.2012.09.014.

[17] F. P. An et al. "New Measurement of Antineutrino Oscillation with the Full Detector Configuration at Daya Bay". In: *Phys. Rev. Lett.* 115 (11 Sept. 2015), p. 111802. DOI: 10.1103/PhysRevLett.115.111802.

[18] V.N.Kornoukhov M.Cribier. *Toward the ultimate calibration of gallium detector with man-made neutrino source*. Institute for Nuclear Research RAS, 7-A, Pr-t 60th October Anniversary, Moscow, Russia.

[19] G. Bellini et al. "SOX: Short distance neutrino Oscillations with BoreXino". In: *JHEP* 08 (2013), p. 038. DOI: 10.1007/JHEP08(2013)038. arXiv: 1304.7721 [physics.ins-det].

[20] Kei Ieki. "Overview of the T2K Experiment". In: *Observation of $\nu_\mu \to \nu_e$ Oscillation in the T2K Experiment*. Tokyo: Springer Japan, 2016, pp. 19–34. ISBN: 978-4-431-55837-8. DOI: 10.1007/978-4-431-55837-8_2.

[21] M. Spinetti and A. Ereditato. "The Experimental Program with the CNGS Neutrino Beam". In: *Cosmic Radiations: From Astronomy to Particle Physics*. Ed. by Giorgio Giacomelli, Maurizio Spurio, and Jamal Eddine Derkaoui. Dordrecht: Springer Netherlands, 2001, pp. 167–172. ISBN: 978-94-010-0634-7. DOI: 10.1007/978-94-010-0634-7_16.

[22] By Sir William Thomson (Lord Kelvin). "On the Age of the Sun's Heat". In: *Macmillan's Magazine* 5 (1862).

[23] P. K. Kuroda. "On the Nuclear Physical Stability of the Uranium Minerals". In: *jcp* 25 (Oct. 1956), pp. 781–782. DOI: 10.1063/1.1743058.

[24] H. A. Bethe. "Energy Production in Stars". In: *Phys. Rev.* 55 (5 Mar. 1939), pp. 434–456. DOI: 10.1103/PhysRev.55.434.

[25] Georg Wolschin. "Thermonuclear Processes in Stars and Stellar Neutrinos". In: *Time, Quantum and Information*. Ed. by Lutz Castell and Otfried Ischebeck. Berlin, Heidelberg: Springer Berlin Heidelberg, 2003, pp. 115–134. ISBN: 978-3-662-10557-3. DOI: 10.1007/978-3-662-10557-3_7.

[26] H. A. Bethe and C. L. Critchfield. "The Formation of Deuterons by Proton Combination". In: *Phys. Rev.* 54 (4 Aug. 1938), pp. 248–254. DOI: 10.1103/PhysRev.54.248.

[27] K. S. Hirata et al. "Observation in the Kamiokande-II detector of the neutrino burst from supernova SN1987A". In: *Phys. Rev. D* 38 (2 July 1988), pp. 448–458. DOI: 10.1103/PhysRevD.38.448.

[28] M. G. Aartsen et al. "Evidence for High-Energy Extraterrestrial Neutrinos at the IceCube Detector". In: *Science* 342 (2013), p. 1242856. DOI: 10.1126/science.1242856. arXiv: 1311.5238 [astro-ph.HE].

[29] T. Kajita, E. Kearns, and M. Shiozawa. "Establishing atmospheric neutrino oscillations with Super-Kamiokande". In: *Nuclear Physics B* 908 (2016). Neutrino Oscillations: Celebrating the Nobel Prize in Physics 2015, pp. 14 –29. ISSN: 0550-3213. DOI: http://dx.doi.org/10.1016/j.nuclphysb.2016.04.017.

[30] Itaru Shimizu. "Past and Present Experiments of Geoneutrinos". In: *Physics Procedia* 61 (2015), pp. 355 –358. ISSN: 1875-3892. DOI: http://dx.doi.org/10.1016/j.phpro.2014.12.075.

[31] A. Strumia and F. Vissani. "Neutrino masses and mixings and ..." In: (2010). arXiv: 0606054v3 [hep-ph].

[32] John N. Bahcall, Marc Kamionkowski, and Alberto Sirlin. "Solar neutrinos: Radiative corrections in neutrino-electron scattering experiments". In: *Phys. Rev. D* 51 (11 June 1995), pp. 6146–6158. DOI: 10.1103/PhysRevD.51.6146.

[33] B. Pontecorvo. "Neutrino Experiments and the Problem of Conservation of Leptonic Charge". In: *Sov. Phys. JETP* 26 (1968). [Zh. Eksp. Teor. Fiz.53,1717(1967)], pp. 984–988.

[34] V. Gribov and B. Pontecorvo. "Neutrino astronomy and lepton charge". In: *Physics Letters B* 28.7 (1969), pp. 493 –496. ISSN: 0370-2693. DOI: http://dx.doi.org/10.1016/0370-2693(69)90525-5.

[35] B. Pontecorvo. "Mesonium and anti-mesonium". In: *Sov. Phys. JETP* 6 (1957). [Zh. Eksp. Teor. Fiz.33,549(1957)], p. 429.

[36] Z. Maki, M. Nakagawa, and S. Sakata. "Remarks on the Unified Model of Elementary Particles". In: *Progress of Theoretical Physics* 28 (Nov. 1962), pp. 870–880. DOI: 10.1143/PTP.28.870.

[37] S.M. Bilenky, J. Hoek, and S.T. Petcov. "On the oscillations of neutrinos with Dirac and Majorana masses". In: *Physics Letters B* 94.4 (1980), pp. 495–498. DOI: http://dx.doi.org/10.1016/0370-2693(80)90927-2.

[38] L. Wolfenstein. "Neutrino oscillations in matter". In: *Phys. Rev. D* 17 (9 1978), pp. 2369–2374. DOI: 10.1103/PhysRevD.17.2369.

[39] S. P. Mikheev and A. Yu. Smirnov. "Resonance Amplification of Oscillations in Matter and Spectroscopy of Solar Neutrinos". In: *Sov. J. Nucl. Phys.* 42 (1985). [Yad. Fiz.42,1441(1985)], pp. 913–917.

[40] V. Barger et al. "Matter effects on three-neutrino oscillations". In: *Phys. Rev. D* 22 (11 1980), pp. 2718–2726. DOI: 10.1103/PhysRevD.22.2718.

[41] G. Bellini et al (Borexino collaboration). "Absence of a day-night asymmetry in the ^{7}Be solar neutrino rate in Borexino". In: (2012). arXiv: 1104.2150 [hep-ex].

[42] S. T. Petcov. "Exact analytic description of two neutrino oscillations in matter with exponentially varying density". In: *Phys. Lett.* B200 (1988), pp. 373–379. DOI: 10.1016/0370-2693(88)90791-5.

[43] Stephen J. Parke. "Nonadiabatic Level Crossing in Resonant Neutrino Oscillations". In: *Phys. Rev. Lett.* 57 (10 1986), pp. 1275–1278. DOI: 10.1103/PhysRevLett.57.1275.

[44] V. A. Kuzmin. "Detection of solar neutrinos by means of the 71Ga(nu, e-)71Ge reaction". In: *Sov. Phys. JETP* 22 (1966). [Zh. Eksp. Teor. Fiz.49,1532(1965)], pp. 1051–1056.

[45] J. N. Bahcall, M. H. Pinsonneault, and S. Basu. "Solar Models: Current Epoch and Time Dependences, Neutrinos, and Helioseismological Properties". In: *The Astrophysical Journal* 555.2 (2001), p. 990. DOI: 10.1086/321493.

[46] A. E. Chavarria on behalf of the Borexino Collaboration. "Solar Neutrinos in 2011". In: *XXXI Physics in Collision*. 2011. arXiv: 1201.6311 [astro-ph.SR].

[47] M. Altmann et al. "Complete results for five years of GNO solar neutrino observations". In: *Phys. Let. B* 616 (2005), pp. 174–190.

[48] V.N. Gavrin. "The Russian-American gallium experiment SAGE". In: *Phys. Uspekhi* 54 (2011), pp. 941–949.

[49] William R. Leo. *Techniques for Nuclear and Particle Physics Experiments: A How-to Approach*. 2., überarb. A. Springer-Verlag, Feb. 1994. ISBN: 3540572805.

[50] SNO Collaboration. "Direct Evidence for Neutrino Flavor Transformation from Neutral-Current Interactions in the Sudbury Neutrino Observatory". In: *Phys. Rev. Lett.* 89 (1 2002), p. 011301. DOI: 10.1103/PhysRevLett.89.011301.

[51] SNO Collaboration. "Electron energy spectra, fluxes, and day-night asymmetries of ^{8}B solar neutrinos from measurements with NaCl dissolved in the heavy-water detector at the Sudbury Neutrino Observatory". In: *Phys. Rev. C* 72 (5 2005), p. 055502. DOI: 10.1103/PhysRevC.72.055502.

[52] SNO Collaboration. "Measurement of the Total Active ^{8}B Solar Neutrino Flux at the Sudbury Neutrino Observatory with Enhanced Neutral Current Sensitivity". In: *Phys. Rev. Lett.* 92 (18 2004), p. 181301. DOI: 10.1103/PhysRevLett.92.181301.

[53] J.F. Amsbaugh et al. "An array of low-background ^{3}He proportional counters for the Sudbury Neutrino Observatory". In: *Nuclear Instruments and Methods in Physics Research Section A: Accelerators, Spectrometers, Detectors and Associated Equipment* 579.3 (2007), pp. 1054 –1080. ISSN: 0168-9002. DOI: http://dx.doi.org/10.1016/j.nima.2007.05.321.

[54] SNO Collaboration. "Independent Measurement of the Total Active ^{8}B Solar Neutrino Flux Using an Array of ^{3}He Proportional Counters at the Sudbury Neutrino Observatory". In: *Phys. Rev. Lett.* 101 (11 2008), p. 111301. DOI: 10.1103/PhysRevLett.101.111301.

[55] SNO Collaboration. "Combined analysis of all three phases of solar neutrino data from the Sudbury Neutrino Observatory". In: *Phys. Rev. C* 88 (2 2013), p. 025501. DOI: 10.1103/PhysRevC.88.025501.

[56] Super-Kamiokande Collaboration. "The Super-Kamiokande detector". In: *Nuclear Instruments and Methods in Physics Research Section A: Accelerators, Spectrometers, Detectors and Associated Equipment* 501.2-3 (2003), pp. 418 –462. ISSN: 0168-9002. DOI: http://dx.doi.org/10.1016/S0168-9002(03)00425-X.

[57] W. T. Winter et al. "The ^{8}B neutrino spectrum". In: *Phys. Rev. C* 73 (2 Feb. 2006), p. 025503. DOI: 10.1103/PhysRevC.73.025503.

[58] A. Gando et al. "^{7}Be Solar Neutrino Measurement with KamLAND". In: *Phys. Rev.* C92.5 (2015), p. 055808. DOI: 10.1103/PhysRevC.92.055808. arXiv: 1405.6190 [hep-ex].

[59] S. Abe et al. "Measurement of the ^{8}B solar neutrino flux with the KamLAND liquid scintillator detector". In: *Phys. Rev. C* 84 (3 Sept. 2011), p. 035804. DOI: 10.1103/PhysRevC.84.035804.

[60] G Alimonti et al. “Science and technology of Borexino: a real-time detector for low energy solar neutrinos”. In: *Astroparticle Physics* 16.3 (2002), pp. 205 –234. ISSN: 0927-6505. DOI: http://dx.doi.org/10.1016/S0927-6505(01)00110-4.

[61] R. S. Raghavan. “Neutrino mass, mixing and magnetic moment: Status and future”. In: *High-energy physics. Proceedings, 25th International Conference, Singapore, August 2-8, 1990. Vol. I+II.* Vol. C900802V1. [Conf. Proc.C900802V1,C900802V1:482(1990)]. 1990, pp. 482–488.

[62] G. Ranucci and E. Meroni. “Counting test facility for the Borexino experiment”. In: *International Journal of Modern Physics A* 29.16 (2014), p. 1442001. DOI: 10.1142/S0217751X14420019. eprint: http://www.worldscientific.com/doi/pdf/10.1142/S0217751X14420019.

[63] C. Arpesella et al. “Measurements of extremely low radioactivity levels in {BOREXINO}”. In: *Astroparticle Physics* 18.1 (2002), pp. 1 –25. ISSN: 0927-6505. DOI: http://dx.doi.org/10.1016/S0927-6505(01)00179-7.

[64] G. Alimonti et al. “The liquid handling systems for the Borexino solar neutrino detector”. In: *Nuclear Instruments and Methods in Physics Research Section A: Accelerators, Spectrometers, Detectors and Associated Equipment* 609.1 (2009), pp. 58 –78. ISSN: 0168-9002. DOI: http://dx.doi.org/10.1016/j.nima.2009.07.028.

[65] H Back et al. “Borexino calibrations: hardware, methods, and results”. In: *Journal of Instrumentation* 7.10 (2012), P10018.

[66] C. Coceva. “Pulse-shape discrimination with a glass scintillator”. In: *Nuclear Instruments and Methods* 21 (1963), pp. 93 –96. ISSN: 0029-554X. DOI: http://dx.doi.org/10.1016/0029-554X(63)90092-2.

[67] G. Bellini et al. “Cosmic-muon flux and annual modulation in Borexino at 3800 m water-equivalent depth”. In: *Journal of Cosmology and Astroparticle Physics* 2012.05 (2012), p. 015.

[68] Borexino Collaboration. “Neutrinos from the primary proton-proton fusion process in the Sun”. In: *Nature* 512.7515 (Sept. 2014). Article, pp. 383–386. ISSN: 0028-0836.

[69] O. Ju Smirnov. “An approximation of the ideal scintillation detector line shape with a generalized gamma distribution”. In: 595.2 (Oct 2008), pp. 410–418.

[70] G. Bellini et al. “Precision Measurement of the ^{7}Be Solar Neutrino Interaction Rate in Borexino”. In: *Phys. Rev. Lett.* 107 (14 Sept. 2011), p. 141302. DOI: 10.1103/PhysRevLett.107.141302.

[71] Richard Saldanha. "Precision Measurement of the 7BeSolar Neutrino Interaction Rate in Borexino". PhD thesis. Princeton University, 2012.

[72] M. Agostini et al. "Spectroscopy of geoneutrinos from 2056 days of Borexino data". In: *Phys. Rev. D* 92 (3 Aug. 2015), p. 031101. DOI: 10.1103/PhysRevD.92.031101.

[73] V. A. Kudryavtsev, L. Pandola, and V. Tomasello. "Neutron- and muon-induced background in underground physics experiments". In: *The European Physical Journal A* 36.2 (2008), pp. 171–180. ISSN: 1434-601X. DOI: 10.1140/epja/i2007-10539-6.

[74] National Institute of Standards and Technology, Gaithersburg, MD. 2010.

[75] G. Bellini et al. "Final results of Borexino Phase-I on low-energy solar neutrino spectroscopy". In: *Phys. Rev. D* 89 (11 June 2014), p. 112007. DOI: 10.1103/PhysRevD.89.112007.

[76] H. Back et al. "CNO and *pep* neutrino spectroscopy in Borexino: Measurement of the deep-underground production of cosmogenic ^{11}C in an organic liquid scintillator". In: *Phys. Rev. C* 74 (4 Oct. 2006), p. 045805. DOI: 10.1103/PhysRevC.74.045805.

[77] C. Arpesella et al. "First real time detection of 7Be solar neutrinos by Borexino". In: *Physics Letters B* 658.4 (2008), pp. 101 –108. ISSN: 0370-2693. DOI: http://dx.doi.org/10.1016/j.physletb.2007.09.054.

[78] C. Arpesella et al. "Direct Measurement of the ^{7}Be Solar Neutrino Flux with 192 Days of Borexino Data". In: *Phys. Rev. Lett.* 101 (9 Sept. 2008), p. 091302. DOI: 10.1103/PhysRevLett.101.091302.

[79] G. Alimonti et al. "The Borexino detector at the Laboratori Nazionali del Gran Sasso". In: *Nuclear Instruments and Methods in Physics Research Section A: Accelerators, Spectrometers, Detectors and Associated Equipment* 600.3 (2009), pp. 568 –593. ISSN: 0168-9002. DOI: http://dx.doi.org/10.1016/j.nima.2008.11.076.

[80] G. Bellini et al. "Observation of geo-neutrinos". In: *Physics Letters B* 687 (2010), pp. 299 –304. ISSN: 0370-2693. DOI: 10.1016/j.physletb.2010.03.051.

[81] G. Bellini et al. "Measurement of the solar ^{8}B neutrino rate with a liquid scintillator target and 3 MeV energy threshold in the Borexino detector". In: *Phys. Rev. D* 82 (3 Aug. 2010), p. 033006. DOI: 10.1103/PhysRevD.82.033006.

[82] G. Bellini et al. “Study of solar and other unknown anti-neutrino fluxes with Borexino at {LNGS}”. In: *Physics Letters B* 696.3 (2011), pp. 191 –196. ISSN: 0370-2693. DOI: http://dx.doi.org/10.1016/j.physletb.2010.12.030.

[83] G Bellini et al. “Muon and cosmogenic neutron detection in Borexino”. In: *Journal of Instrumentation* 6.05 (2011), P05005.

[84] G. Bellini et al. “Absence of a day-night asymmetry in the ^{7}Be solar neutrino rate in Borexino”. In: *Physics Letters B* 707 (2012). ISSN: 0370-2693. DOI: 10.1016/j.physletb.2011.11.025.

[85] G. Bellini et al. “First Evidence of *pep* Solar Neutrinos by Direct Detection in Borexino”. In: *Phys. Rev. Lett.* 108 (5 Feb. 2012), p. 051302. DOI: 10.1103/PhysRevLett.108.051302.

Acknowledgments

I would like to acknowledge all people that were involved in this analysis that made it possible to uncover the detector potential. Especially I would like to mention our maintenance team for making it possible to have a beautiful and clean dataset and amazing levels of the radiopurity and detector stability that were a keystone in all studies related with the detector.

I would like to acknowledge my advisors that were a great support in all tough moments of the analysis and helped to work out the most thin moments of the work.

It is impossible not to mention Simone Marcocci that did an incredible work creating probably the best monte-carlo simulation of a liquid scintillator detector ever and contributing heavily in the part of spectral fitting with monte-carlo PDFs.

I would like to thank the whole LNGS analysis group, that provided enormous practical contribution as well as moral support, such as Marcin Misiaszek that maintained all our software framework and created beautiful pulse-shape discrimination approaches, Nicola Rossi that made the crucial work of bismuth content establishment and Francesco Lombardi that made possible all works related with inner vessel shape.

It was a great pleasure to interact with JINR group from Dubna that contributed a lot in the final steps of the analysis performed, such as analytical fitting of low-energy part of the spectrum linked with restructurization of corresponding software.

Also I would like to acknowledge the coordinator of the of the analysis group, Gemma Testera, that made us maintain the general line of analysis that allowed to keep constant progress despite all present circumstances.

It was a great pleasure to work with data of this amazing detector in a very nice and dedicated team that made a great effort in the direction of understanding of such a mysterious part of particle physics such as solar neutrino and made us one step closer to understanding at least something about it.